3-2006

Structural Health Monitoring Considering Internal Beam Damage

Jessica B. Chronister

STRUCTURAL HEALTH MONITORING CONSIDERING INTERNAL BEAM DAMAGE

THESIS

Jessica B. Chronister, Second Lieutenant, USAF

AFIT/GA/ENY/06-M09

DEPARTMENT OF THE AIR FORCE
AIR UNIVERSITY

AIR FORCE INSTITUTE OF TECHNOLOGY

Wright-Patterson Air Force Base, Ohio

AFIT/GA/ENY/06-M09

STRUCTURAL HEALTH MONITORING
CONSIDERING INTERNAL BEAM DAMAGE

THESIS

Presented to the Faculty

Department of Aeronautics and Astronautics

Graduate School of Engineering and Management

Air Force Institute of Technology

Air University

Air Education and Training Command

In Partial Fulfillment of the Requirements for the

Degree of Master of Science in Astronautical Engineering

Jessica B. Chronister, BS

Second Lieutenant, USAF

March 2006

AFIT/GA/ENY/06-M09

STRUCTURAL HEALTH MONITORING

CONSIDERING INTERNAL BEAM DAMAGE

Jessica B. Chronister, BS
Second Lieutenant, USAF

Approved:

//signed//

_____ _____

Anthony N. Palazotto, Ph.D. (Chairman) date

//signed//

_____ _____

Richard G. Cobb, Ph.D. (Member) date

//signed//

_____ _____

Donald L. Kunz, Ph.D. (Member) date

AFIT/GA/ENY/06-M09

Abstract

The present study establishes a nondestructive method of damage detection and assessment in cantilever beams. The specimens used are twelve inch aluminum 2024-T3 beams with machined notches of varying lengths and locations. Laser Doppler vibrometry is used to obtain the frequency response of vibrating beams. Experimental methods are developed to detect the presence, location and extent of damage by direct observation of the eigenvector in the third through eighth modes. Models in MATLAB and ABAQUS are used to predict and validate the observed data. With this experimental method developed, the validity of the method is tested for specimens that have been exposed to a destructive corrosive environment. A corrosion experiment is developed and used to determine the validity of the damage detection method for corroded structures.

To my father, because we are always on the same wavelength

Acknowledgments

I would like to express my sincere gratitude to my thesis advisor, Dr. Anthony Palazotto, for his unending patience, invaluable guidance, and incomparable sense of humor. Thank you to Dr. Kunz and Dr. Cobb for the helpful comments and input as my committee, and also for Dr. Cobb's help with the laser vibrometer. I owe a special debt of gratitude to Jay Anderson and Wilber Lacy for catering to my every whim in the lab and for going the extra mile. Many thanks to Mark Derisso of AFRL for the financial support. Without the prior work of Aaron Chmiel, the ABAQUS expert, many aspects of this study would be incomplete. An additional thanks to Lt Col Scott Fawaz for answering many of my questions on corrosion. Thank you to my parents and my brother for always, always encouraging me. Thanks to the movie night crew for making AFIT a super-cool, fun place to be. Seriously. A final thanks goes to my wonderful husband, who is so supportive of everything I have ever done.

Jessica Beth Chronister

Table of Contents

Page

Page

List of Figures

Figure Page

Page

Page

Page

Page

Page

Page

Page

Page

Page

Page

List of Tables

Table Page

Page

STRUCTURAL HEALTH MONITORING

CONSIDERING INTERNAL BEAM DAMAGE

I. Introduction

1.1. Motivation: Structural Health Monitoring

The safety of a structure is paramount to all who design, build, use or maintain it. There is an ever-increasing desire to develop techniques to continuously monitor long-term service of such structures as aircraft, spacecraft, civil engineering structures and many other kinds of machinery (Fritzen, 2004:1). In contrast to time-consuming visual inspections or disassembly of a structure, Structural Health Monitoring (SHM) can provide information on remaining productive lifetime or time until next repair, and can even order an automatic shutdown if conditions require.

1.1.1. Philosophy.

SHM is defined by the literature as "an emerging technology that can be defined as continuous, autonomous, real time, in-service monitoring of the physical condition of a structure by means of embedded or attached sensors with minimum manual intervention" (Mal, 2004:1). According to one estimate, inspection and monitoring claims over 25% of the life cycle cost of an aircraft, to include pre-production, production and post-production costs (Mal, 2004:1). Reusable space-launch vehicles are another application that will require intensive monitoring in order to achieve a rapid turnaround time. The

life cycle cost of these and other aerospace structures could be reduced drastically through the integration of effective SHM systems.

1.1.2. Approaches.

Many methods of damage detection are being developed and investigated. Two approaches can be referred to as local and global. One local approach uses the wave propagation technique to determine the location of damage. An array of embedded or attached ultrasonic transducers, acting as both transmitters and receivers, analyze actively transmitted elastic waves and pinpoint damage by comparing these to baseline signals (Mal, 2004:2). Acoustic emission (AE), known as passive ultrasonic monitoring, also utilizes elastic and acoustic waves by monitoring the elastic waves initiated by the onset and growth of damage. One recent development of this practice includes the use of Lamb waves, which are guided, elastic waves in traction-free thin plates (Staszewski, 2004:251).

The local approach detects and characterizes small, hidden defects before they grow to a critical size, but it is dependent on the placement of transducers. Conversely, the global approach detects widespread or extensive damage over the entire structure. The global approach uses vibration induction of a structure and a comparison of changes in the frequency response function (FRF) before and after the damage occurs. System identification techniques can then be applied to the data to evaluate property changes, such as a reduction in stiffness. Baseline measurement data of the undamaged structure is key to this method. While this method is non-invasive and can detect the presence of damage in a structure, its reliability in finding the location of damage or the presence of a very small hidden flaw in a large, complex structure is unknown.

1.1.3. Relevance to the USAF.

Although SHM would obviously benefit the aging commercial aircraft fleet, which currently numbers over 100,000, it is perhaps even more valuable to the US Air Force with its increasing demand to keep aging aircraft (over 25 years) in service and the shifting emphasis on space power (Mal, 2004:1). Satellites, space structures and launch vehicles are all susceptible to structural damage from impact, foreign object debris (FOD) and fatigue (Doyle, 1995:272). These damaging effects, along with exposure to the space environment and advancements which increase spacecraft lifetime, make the periodic evaluation of a spacecraft's structural integrity an absolute necessity (Cobb, 1996:1). Many nondestructive evaluation techniques have been developed to detect changes inflicted by the space environment and changes due to structural fatigue. Some examples include X-ray photography, ultrasonic testing, dye penetration and magnetic resonance.

While advancing technology improves spacecraft service life, mission demand is forcing the Air Force to extend the service life of many of its aircraft to 40-60 years, which increases the risk of structural fatigue. Effective SHM systems may be the solution to reduce structural weight and cut maintenance costs for the USAF's aging aircraft (Schmidt 2004:101). All aging aircraft are particularly prone to suffer internal damage from fatigue and corrosion. According to Dr. Ajit Mal,

> Corrosion usually occurs when the aircraft is on the ground and fatigue is associated with pressurization/depressurization and landing cycles during flight. Fatigue results in the occurrence of cracks at stress concentration points and the presence of a corrosive environment exacerbates fatigue damage. (Mal, 2004:1)

The present study further investigates the use of previously researched methods of vibrational detection of notches in aluminum beams, embracing a global approach of SHM, and also explores the effects of corrosion on this method.

1.2. Background

Past theses by Capt Aaron Reifsnyder, USAF, and Ensign Frances Durham, USN, have explored the realm of SHM through studies on vibrometric detection of internal beam damage (Reifsnyder, 2001; Durham, 2004). Both studies involved twelve-inch cantilever aluminum 2024 beams with internal notches of various lengths. The Reifsnyder thesis focused on notches centered on the depth of a 0.125 inch deep beam, while Durham examined beams with notches located eccentrically on the depth of 0.25 inches. This past research sought to determine a method of damage detection that approximates the length and location of the notches. Reifsnyder's work aided in the development of laser vibrometer usage in damage detection, while Durham's study characterized internal damage based solely on changes in natural frequencies. Durham found an approximate correlation between notch length and percent deviation of a given eigenvalue from the notchless condition. However, these findings were not conclusive.

1.3. Problem Statement

The present study endeavors to create a better method of damage monitoring and detection. This study is broken into two sections: the first section directly develops this method, while the second section uses these findings to apply the method to structures exposed to the detrimental environment of corrosion. The remainder of this introductory chapter, as well as the written study, is separated into these sections.

The existence, extent and location of internal notches can be established through investigation of the eigenvectors in modes three through eight. An experimental approach using a scanning laser vibrometer examines the physical mode shapes of a beam to refine this method. Analytical values for natural frequencies and mode shapes are found using a MATLAB program that is simple in concept but very valuable for this work.

After the development of this improved experimental mode of damage detection, a better numerical model was needed to verify the MATLAB analytical results, to compare with the experimental values, and to validate assumptions made about mode shapes and interference due to contact between sides of the notch. The new model was created using ABAQUS, a finite element modeling tool. The ABAQUS model helped to verify experimental results and aided in the understanding of when contact between sides of the notch occurs.

With this reliable damage detection technique generated, the decision was made to study a detrimental environment. The second half of this thesis focuses on the characterization of damage location in which the structure is exposed to a damaging environment. The environment chosen for the present study was a corrosive environment. The structural effects of corrosion on a specimen were researched, and a corrosion experiment was developed. Finally, the results of this corrosion study were compared to the non-corroded results from the first part of the study.

1.4. Past Approaches to Beam Analysis

1.4.1. Background.

Modal frequency analysis of damaged beams and plates has been an oft-researched topic in the past two decades. Modal parameters such as natural frequencies, mode shapes and modal damping ratios all change with the presence of surface or internal damage. The determination of these parameters is a straightforward process accomplished through standard vibrations testing. Finite element modeling, mode shape analysis, experimental comparisons of natural frequency changes and damage index estimation using laser vibrometry are just some of the research topics covered.

1.4.2. Finite Element Modeling.

When a structure is damaged, shifts in eigenvalues and variations in eigenvectors indicate the change in dynamic response. Yuen used finite element modeling (FEM) of a beam in an attempt to relate changes in eigenparameters to the location and size of damage. His study was modeled after an earlier method developed by Adams and Cawley in which location damage on a plate was deduced from sensitivity analysis (Adams, 1979:49-57). Adams and Cawley used a finite element model of a plate and assumed that the modulus of elasticity at the damaged location was equal to zero. The sensitivity of eigenvalue change was then evaluated for each of the model's elements, with analytical results that matched well with experimental conclusions (Yuen, 1985:302).

In Yuen's study, a cantilevered beam of uniform cross-section was chosen for simplicity, and the eigenvalues and eigenvectors of the dynamic system were investigated. Consistent with the Adams and Cawley study, Yuen assumed that damage

in the structure would affect only the stiffness matrix. As such, he modeled a change in stiffness as a reduction of modulus of elasticity, and introduced damage to each element of his model in turn by reducing the modulus of elasticity by 50 percent. Yuen found that the percentage changes in the eigenvalues for a damaged structure were generally small but measurable. His data also suggests that the eigenvector changes significantly in the region between the damage and the fixed end, while the change is less discernable between the damage and the free end.

A more recent study investigates the detection of a delamination element in a multilayered composite cantilevered beam using a spectral finite element model and the wave propagation technique, which utilizes the local approach to SHM. The dynamic stiffness matrix is again found, but this time it is transformed and solved for unit impulse at each frequency, which yields the FRF (Palacz, 2005:46). The results of this study show that the delamination does cause additional wave reflections, even if said delamination was as small as 5% of the beam length (Palacz, 2005:51). The additional wave reflections indicate to the tester the presence of beam damage, meaning that as long as the damage is at least as large as 5% of the beam length, this wave propagation technique is an effective means of damage detection. Continued research uses a wave propagation technique and separates the global structural dynamics of a specimen from the local stresses that dominate around a crack-tip region (Doyle, 1995:272). A global/local approach is used to simplify the effects of these singular stresses at the crack tip by treating uniform segments as connected waveguides and the crack as a local stiffness. While this study proves useful for local SHM techniques, one conclusion was

that for many problems, the local details at the crack tip do not affect the overall dynamics (Doyle, 1995:279).

1.4.3. Damage Detection from Mode Shapes.

The amount by which a natural frequency is reduced and the mode shape changed depends upon the location and extent of damage, particularly the location with respect to the mode shape. The existence of a crack or notch at a location in the beam leads to a reduction in stiffness, which is of particular importance when the crack is at a region of high curvature (Salawu, 1995:719). Changes in the curvature mode shapes are localized in the damaged area, with larger areas of damage causing increased changes in the curvature mode shape. Through this, abnormal curvature mode shapes indicate the presence of damage.

For a cantilevered beam, curvature and displacement mode shapes are different. For example, in the first mode the maximum curvature occurs at the fixed end, where the displacement is lowest. For this reason, Pandey, Biswas and Samman used a central difference equation to numerically find the curvature mode shapes of a cantilevered beam (Pandey, 1991:321). The curvature mode shapes could then be compared to those of a baseline undamaged structure, and the deviant region of the mode shape could be ascertained as the defective area.

1.4.4. Natural Frequency Changes.

While mode shape analysis is very useful and is the method used in the present study, the most commonly researched parameter used for damage detection is the natural frequency shift. The popularity of this method is likely due to the fact that natural frequencies are easy to measure and that a baseline measurement can be continually

compared to other measurements to detect changes. Furthermore, it is inexpensive and time efficient to monitor natural frequencies in most structures (Kim, 2003:146). Dimarogonas states in his review that for small cracks in a cracked beam, the decrease in natural frequency is proportional to the square of the crack depth ratio *a/h* where *a* is crack depth and *h* is the height of the beam cross-section, directly relating crack depth to natural frequency shift (Dimarogonas, 1996:832). Ideally, this natural frequency shift would have to be greater than five percent to confidently predict damage location (Salawu, 1995:718).

Cawley and Ray advanced the early knowledge in this arena with tests on free-free isotropic steel beams by comparing frequency changes produced by cracks to those produced by manufactured slots of equivalent depth. Slots, like the notches used in the present experiment, referred to machined inclusions in the beam. Cracks were created by fatigue loading in a Mayes 25 kN servo-hydraulic testing machine (Cawley, 1988:367). Natural frequency changes were predicted to increase with increasing slot width (Cawley, 1988:366). This hypothesis was supported by their research, which confirmed that the amount of frequency change is a function of slot width to depth ratio. They also discovered that when slots of a given depth are found through the frequency shift, a crack of the same size may not be as easily found. It is therefore preferred to manufacture the narrowest cut possible when manufacturing slots or notches (Cawley, 1988:370). This recommendation was heeded in the present experiment.

Rizos, Aspragathos and Dimarogonas further advanced the process of crack location detection by initiating transverse surface cracks on beams of rectangular cross sections (Rizos, 1990:381). A thin saw cut would be made, and the crack expanded to

the desired depth by fatigue loading. The beam was actuated by a harmonic vibration exciter at one of the natural frequencies. The mode shapes were then measured by placing accelerometers along the beam length. They were able to locate the notch location by comparison of mode shapes and notch depth from stiffness measurements with a maximum error of less than 8 percent, and in most cases less than 5 percent (Rizos, 1990:381). Their method, while undesirable to locate cracks of a depth ratio less than 10 percent, is a useful method to monitor crack growth.

For a beam with simply supported ends, the fundamental natural frequency is affected the least in cases where the crack location (c) to beam length (L) ratio was equal to 1/16, according to a study presented by Owolabi, Swamidas and Seshadri. This frequency experienced the largest decrease when the crack was located in the center of the beam (c/L = 8/16). One explanation is "that the dynamic bending moment was the largest at the middle point (where the amplitude of the first mode is greatest) for the first mode" (Owolabi, et al, 2003:10). However, this holds for only the first mode. Modes 1 and 3 are sensitive to inclusions near a beam's center, while modes 2 and 4 are not, due to their mode shapes. In general, at least three modes are needed in order to detect damage when its location in a beam is unknown and the crack localization becomes more accurate as more modes are used (Kim, 2003:154-5). A method that requires only one or two modes would be very beneficial to damage detection by creating an ease of use that requires less testing, possibly leading to earlier detection.

1.4.5. Laser Vibrometry.

The ratio of strain energy in an undamaged beam to that of one suspected to contain a crack is a crucial element of V.K. Sharma's damage index estimation study.

This ratio, termed the Strain Energy Ratio (SER) offers information on the location and size of suspected damage, as it is expected to be 1 over undamaged areas and other than 1 in a region where a crack or damage is present (Sharma, 2005:3).

Sharma's experiment used a simply supported rectangular steel beam to which a varying-frequency harmonic unit load was applied. The beam measured 1 m (39.37 in) in length by 5 mm (0.197 in) in thickness by 1 cm (.394 in) in width. An FE model of 80 elements was used to best match experimental data to be provided by a scanning laser Doppler vibrometer. The damage in the beam was modeled as a reduction of thickness over one element of the FE model. The results of this testing show that the cumulative SER is "proportional to the damage extent" (Sharma, 2005:7). The present study provides a new way of using laser Doppler vibrometry to detect beam damage that is especially useful when no baseline data is known.

The present study also uses a laser Doppler vibrometer, but takes a global approach by using vibration testing and modal analysis of a baseline specimen and comparing it to results from damaged specimens. Notchless and notched beams that have been exposed to varying degrees of corrosion (from zero to two weeks immersion) are also examined and compared. Eigenvalues, eigenvectors and damping characteristic are evaluated. The ability of locating the internal damage within the beam is then established. Additionally, an estimation of the effect of corrosion on damping properties is presented.

This method of evaluation has been studied and verified through the course of this and two prior theses. The method was used to determine notch location and length in 12"x1.5"x0.125" beams with a notch centered on the depth of the beam and spanning the

entire width, in 12”x1.5”x0.25” beams with notches eccentrically located on the depth, spanning the entire width, and on 12”x1.5”x0.25” beams with notches again centered on the depth, spanning the entire width. With this method established and understood, the next undertaking is to examine how it holds with specimens under varying conditions. Thermal changes, different boundary conditions, vacuum environment, and corrosion environment are all possible hurdles to the usefulness of the developed method. The environment examined in the current study is the corrosion environment.

1.5. Corrosion

1.5.1. Background.

Corrosion is defined as a “deterioration of a metal due to its reaction with the surrounding aqueous environment” (Corrosion Testing Laboratories, Inc, 2005:1). Aluminum is the most widely used non-ferrous metal on a volume basis, and is very commonly used in structures because of its high thermal and electrical conductivity, low mechanical properties and good workability. The service life of aluminum structures can be over 30 years, due primarily to a self-forming, microscopically thin, external layer of hydrated aluminum oxide that provides corrosion resistance.

The layer is comprised of a thin, inner barrier layer and a thicker, more permeable bulk outer layer. This oxide film is stable in solutions with a pH from 4.0 to 8.5. Any corrosion resistance an aluminum object may have is dependent upon this self-renewing film, so two highly corrosive situations for an aluminum structure are ones in which the structure is constantly abraded, rubbing away the protective oxide layer, or when there is a depletion of oxygen in the environment. When the oxide layer is perforated at a certain location, an accelerated attack occurs at that location because the exposed aluminum is

attacked more rapidly than the oxide. This causes a form of attack known as *pitting* and occurs under alkaline conditions. When the aqueous environment is acidic, the oxide layer is attacked more quickly than the aluminum, which results in general attack (Corrosion Doctors, 2005:2). *General corrosion* is a form of attack that affects the entire exposed area, although it may not be perfectly uniform.

1.5.2. Relevance to the USAF.

Corrosion is a major issue for the USAF because it can be expensive to remove from aircraft, it threatens fight safety, and it leads to a reduction in mission readiness and completion. Corrosion is the most expensive maintenance issue and costs the Air Fore one to three billion dollars annually (Ferrer, 2002:452). A corroded aircraft part must either be replaced or have the corroded portion removed by grinding it off mechanically (Ferrer, 2002:452). This is assuming that the corrosion damage is external, which it often is not. Corrosion is a very real problem, as aircraft and spacecraft are sometimes stationed in the most humid of environments, such as the F-15s at Eglin AFB, FL, where the mean maximum humidity is 88%, or the spacecraft at Kennedy Space Center in Florida, where the mean maximum humidity for the month of January is 99%.

Although general corrosion was observed most often by Ferrer and Kelly (Ferrer, 2002:457) in their analysis of lap joints, and most studies of aircraft skins reveal general corrosion and exfoliation corrosion as the dominant forms, pitting can also be a large source of deterioration on aircraft skins. *Exfoliation corrosion* is defined as a type of corrosion "that attacks the exposed material end grain and can work its way parallel to the metal surface . . . causing splitting of material layers, leading to a stratified appearance" (http://composite.about.com/library/glossary/e/bldef-e2070.htm, 2006).

Exfoliation is a form of *intergranular corrosion*, and it is most commonly found in aluminum alloys (Ferrer, 2002:459).

Actual corrosive environments are very complex and can be difficult or impossible to recreate in a laboratory environment. According to the ASTM Standard Practice for Laboratory Immersion Corrosion Testing of Metals, "Experience has shown that all metals and alloys do not respond alike to the many factors that affect corrosion and that 'accelerated' corrosion tests give indicative results only, or may even be entirely misleading" (ASTM G31, 2005:1). Comparing laboratory results to actual in-service performance can be problematic for a number of reasons, just a few of which are:

1) By their very nature, accelerated corrosion tests are designed to deviate from actual service exposure to produce results in significantly shortened time frames.
2) In general, laboratory tests are more simplistic and standardized, with fewer variables than actual service conditions.
3) Multiple failure mechanisms/modes and their interactions in the field are not easily reproduced in the laboratory. Artificially accelerating one corrosion mode may retard another mode.
4) Small coupon size, sample geometries, finite number of samples can affect laboratory studies compared to the "real world".
5) The "acceleration" of corrosion by adjusting a few selected variables in laboratory tests usually does not represent the complex interplay of multiple variables under actual service conditions.
6) Laboratory specimens usually deviate from production parts/components used in actual service, especially when details pertaining to the surface condition are considered

(Corrosion Club, 2005:1-2)

Despite these complicating factors, laboratory corrosion tests can be very useful in determining the general change in properties after a specimen is corroded. Although no perfect relationship can be established between immersion time and time in service, one possibility is to relate known ranges of corrosion rates in immersed and air conditions. For example, the corrosion rates for aluminum in seawater typically range

from 1 to 50 mils per year, while the range for normal outdoor air (urban exposure) is 0-0.5 mils per year (Shackelford, 1995:277-280). Using this data and assuming a linear relationship, it may be possible to get a very general approximation of corrosion damage accrued in an outdoor environment when compared to the experimental immersion data. While there is no simple way to relate laboratory results to system lifetime predictions, immersion tests are still the fastest and most economical means for conducting corrosion research.

1.5.3. Results of Prior Aluminum 2024 Tests.

Seawater is the most abundant corrosive medium in the world, and its composition is substantially the same across the world. The total dissolved solids vary from as low as 8,000 ppm to 60,000 ppm, but the nominal dissolved solids, used in seawater equations, is about 34,500 ppm. About 25,000 ppm is assumed to be sodium chloride. The pH of seawater ranges from 7.7 to 8.3 in surface waters (The Hendrix Group Reporter, 1998:3).

One study by Zhang and Frankel in 2000 investigated the anisotropy of localized corrosion in aluminum 2024-T3, an aluminum commonly found in aircraft structures, and the one used in the present study. A foil-penetration technique exposed one side of a thin foil of aluminum 2024-T3 to a corrosive solution at open circuit or under potential control. A sensor on the backside of the foil determined the time required to fully penetrate foils of different thicknesses by any means of corrosion (pitting or intergranular attack). The results of said study revealed a strong anisotropy in the growth kinetics of localized corrosion in AA2024-T3. Growth in the short transverse direction was much slower than in either the longitudinal or long transverse direction (see Figure 1).

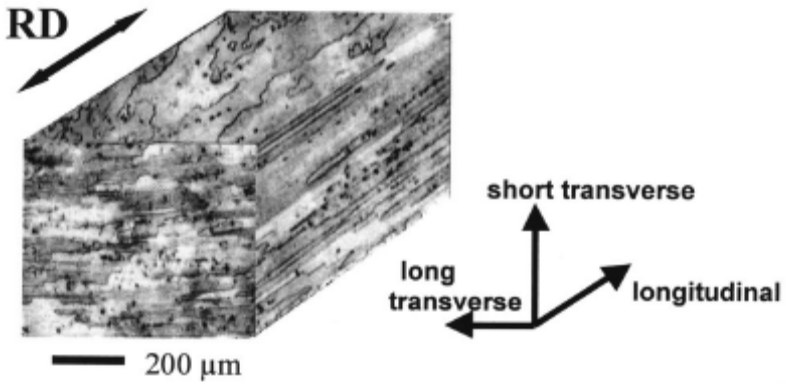

Figure 1. Orientation of aluminum 2024-T3 sample (Zhang, 2000:268)

This difference was a result of microstructural anisotropy. Intergranular path length was strongly related to orientation, while pitting potential was nearly independent of sample orientation (Zhang, 2000:268-269).

In addition to the anisotropy of AA2024-T3, investigations have shown a certain susceptibility of this alloy to pitting and intergranular attack in a sodium chloride environment. This susceptibility is worsened by a varied existence of inclusions and defects in large commercial (or military) structures. The passive oxide film further complicates the corrosion process and predictions pertaining to it (Leblanc, 2002:B239). One result from a further study by Zhang and Frankel in 2002 states,

> When the unpenetrated samples were dissembled from the cell, no penetrated pits were visible on the back side as expected. However, many penetrated pits were found on the unexposed surface of these same unpenetrated samples after they were left in laboratory air for several weeks. Localized corrosion apparently continued as a result of the aggressive environment trapped within occluded regions of the samples, and did not dry out quickly on removal from the bulk solution.
>
> (Zhang, 2002:B512)

Although this phenomenon was not investigated further in the Zhang study, this continuation of corrosion after a structure has left the corroded environment is very

applicable to real-world structures like aircraft and spacecraft, as well as the present experiment.

1.6. Preview

In the following chapter, the detection features of damage location will be discussed, describing the experiment, the frequency data generated, an overview of the finite element model, and the damping data calculated. The third chapter will expand upon the effects of corrosion upon damage detection. It will cover the corrosion experiment, the frequency data, and damping features as well. The final chapter will present conclusions and suggestions for further study.

II. Features of Damage Location

2.1. Experiment

The experiment was conducted on a total of 23 beams for this study. The first 13 cases were done to validate and refine experimental methods of previous theses, while the remaining 10 beams were tested after being placed in a corrosive environment to check the validity of this method for corroded specimens. All experiments were conducted in the Vibration Laboratory (Lab number 257) of the Air Force Institute of Technology at Wright-Patterson Air Force Base, Dayton, Ohio. The following sections of this chapter will discuss frequency data, finite element modeling with the program ABAQUS, and damping features. This section will outline the theory behind laser Doppler vibrometry and the setup and use of experimental equipment.

2.1.1. Theory Behind Laser Doppler Vibrometry.

Laser vibrometry uses the Doppler effect to measure vibrations. Light scattered from a moving object exhibits a slight frequency change. A high-precision interferometer inside the laser vibrometer detects small frequency shifts of the backscattered laser light. The interferometer does this by splitting the light into two parts: the reference beam, pointed directly to the photo detector, and the measurement beam pointing to the test object. Light from the measurement beam is scattered by the moving surface of the vibrating object. Frequency and phase changes are evident in the backscattered light according to the velocity and displacement of the object. The superposition of this light with the reference beam creates a modulated detector output

signal revealing the Doppler shift in frequency. A decoder in the vibrometer provides a voltage which is proportional to the velocity of the vibration parallel to the measurement beam. This voltage is digitized and processed as the vibrometer signal (*Corporate Video on Vibrometers*).

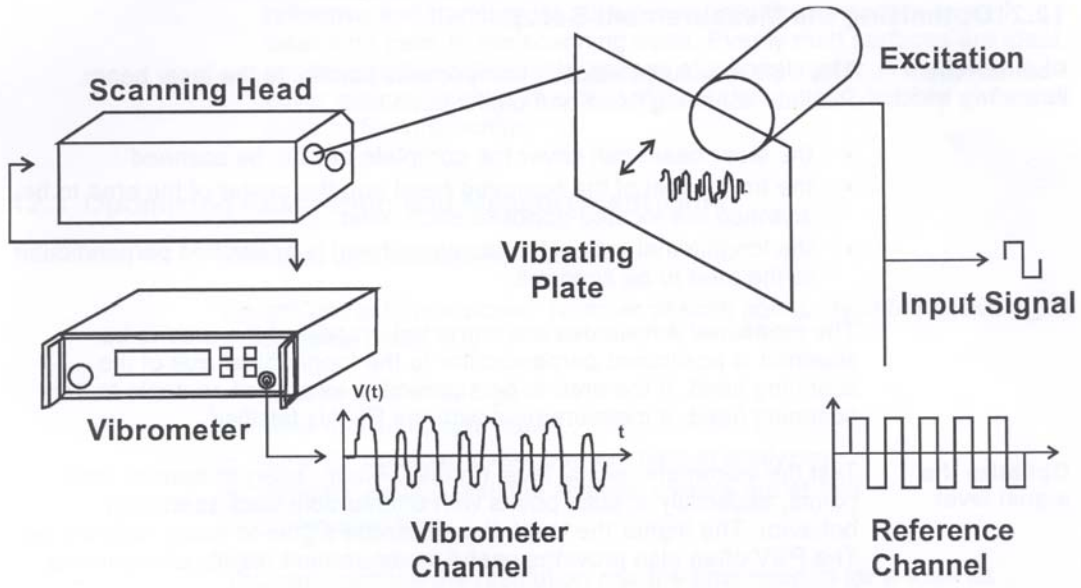

Figure 2. Basic schematic of Laser Doppler Vibrometer (Polytec Theory Manual, 12-1)

A heterodyne inferometer in the scanning head uses a Bragg cell to generate a high-frequency carrier signal. In the digital demodulation, a mixing process converts the carrier signal into two quadrature signals, *I* and *Q*. This signal pair is easier to process than the carrier signal because it lies in the base band, but it carries the same information. The signals are sinusoidal with the same amplitude and a phase shift of 90 degrees. According to the following figure, the *I* and *Q* signals can represent a rotating pointer with an angle of rotation equal to the interferometric phase difference, $\Delta\varphi$.

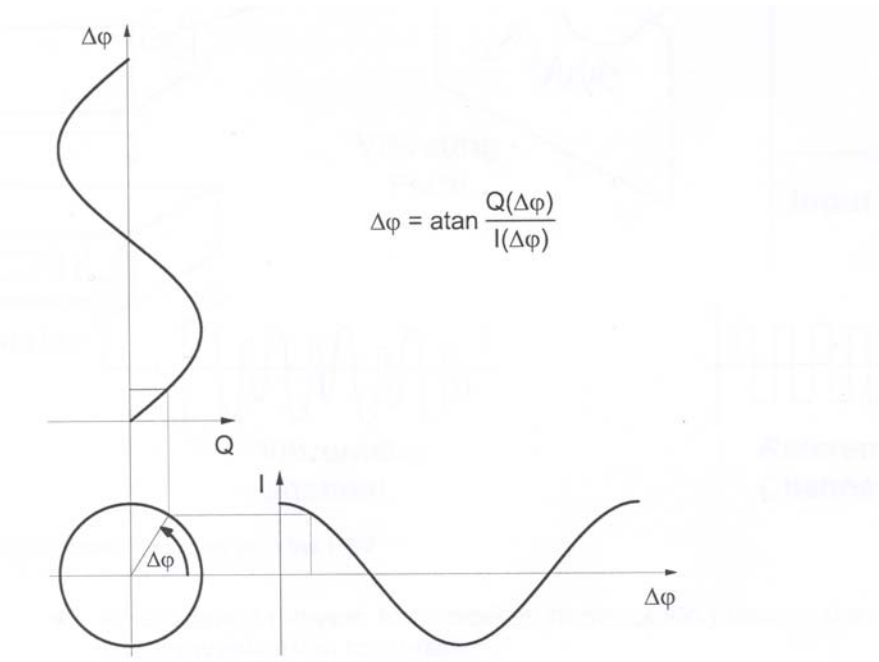

Figure 3. Graphic representation of I and Q (Polytec Theory Manual, 11-1)

I and *Q* are defined as follows:

$$I(\Delta\varphi) = A\cos(\Delta\varphi) \tag{1}$$

$$Q(\Delta\varphi) = A\sin(\Delta\varphi) \tag{2}$$

and

$$\frac{Q(\Delta\varphi)}{I(\Delta\varphi)} = \frac{\sin(\Delta\varphi)}{\cos(\Delta\varphi)} = \tan(\Delta\varphi) \tag{3}$$

Applying the inverse tangent to Equation 3 yields

$$\Delta\varphi = \tan^{-1}\left(\frac{Q(\Delta\varphi)}{I(\Delta\varphi)}\right) \tag{4}$$

And the phase difference is proportional to the displacement of the object (Δx) as follows:

$$\Delta\varphi = \frac{4\pi}{\lambda}\Delta x \tag{5}$$

where λ is the wavelength of the laser. Hence, the Doppler frequency shift is:

$$\Delta f(t) = \frac{4u(t)}{\lambda} \tag{6}$$

where *u(t)* is the velocity of the tested specimen.

Periodic functions can be described as a sum of trigonometric functions, called a Fourier series. Non-periodic functions are described by an integral of trigonometric functions, and are known as a Fourier integral. A Fourier transformation splits a time signal into a sum of vibrations with different frequencies. The generation of a frequency spectrum using the Polytec software uses the Fast Fourier Transformation (FFT) process to generate the corresponding frequency spectrum. For more information on this process, refer to the Polytec Theory Manual.

2.1.2. Experimental Equipment.

The specimens designed and lab equipment used replicate the Durham thesis experiment as closely as possible. To aid in the ability to compare experiment results to those of the Durham experiment, the laser vibrometer, actuator and amplifier are all the same components used by Durham. The beam design and environmental constraints are employed in the same fashion as in the Durham experiment.

2.1.2.1 Specimen Design.

The beams used in this study are made of Al 2024-T3. This material was chosen to match the beams used in the Reifsnyder and Durham studies. Although Reifsnyder found residual stresses in this material due to the cold working process, the effect of these stresses on beam dynamics is considered minimal for notches up to 16 cm (6.299 in) in length. Thus, the longest notches used in the present study are 16 cm (6.299 in). Al 2024-T3 has a density of 2837.5 kg/m^3 and a modulus of elasticity of 73.084 GPa.

Beam dimensions are identical to those of the beams used in the Durham study in order to facilitate comparison between the data (Durham Appendix C). The beams are 38.1 cm (15 in) long, 3.81 cm (1.5 in) wide, and 0.635 cm (0.25 in) deep. During the experiment, 7.62 cm (3 in) of the beam are clamped, leaving an effective length of 30.48 cm (12 in). The thirteen uncorroded beams contain 4 cm (1.575 in), 8 cm (3.150 in), 12 cm (4.724 in) and 16 cm (6.299 in) notches, and one notchless case. These notch lengths account for 13%, 26%, 39%, 52% and 0% of the notch length, respectively. All notches are centered on the depth of the beam and run the entire width, as indicated in Figure 4. For each notch length, there are three cases: one beam notched at the free end, one notched at the center of the length and one notched at the clamped end. These, plus the notchless beam, yield a total of thirteen specimens for the uncorroded beams.

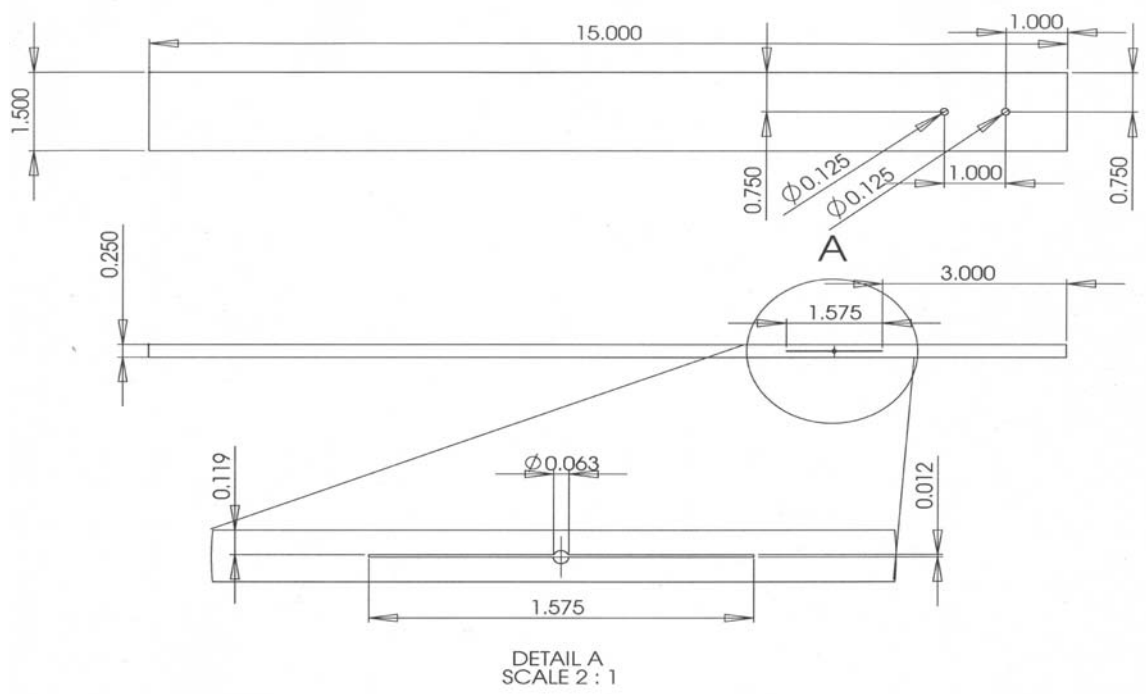

Figure 4. Sample of technical drawing for the 4 cm (1.575 in) clamped end notch.

These centrally notched beams will be compared to previously determined data for eccentrically notched beams. The basic difference in these notch locations is illustrated in Figure 5.

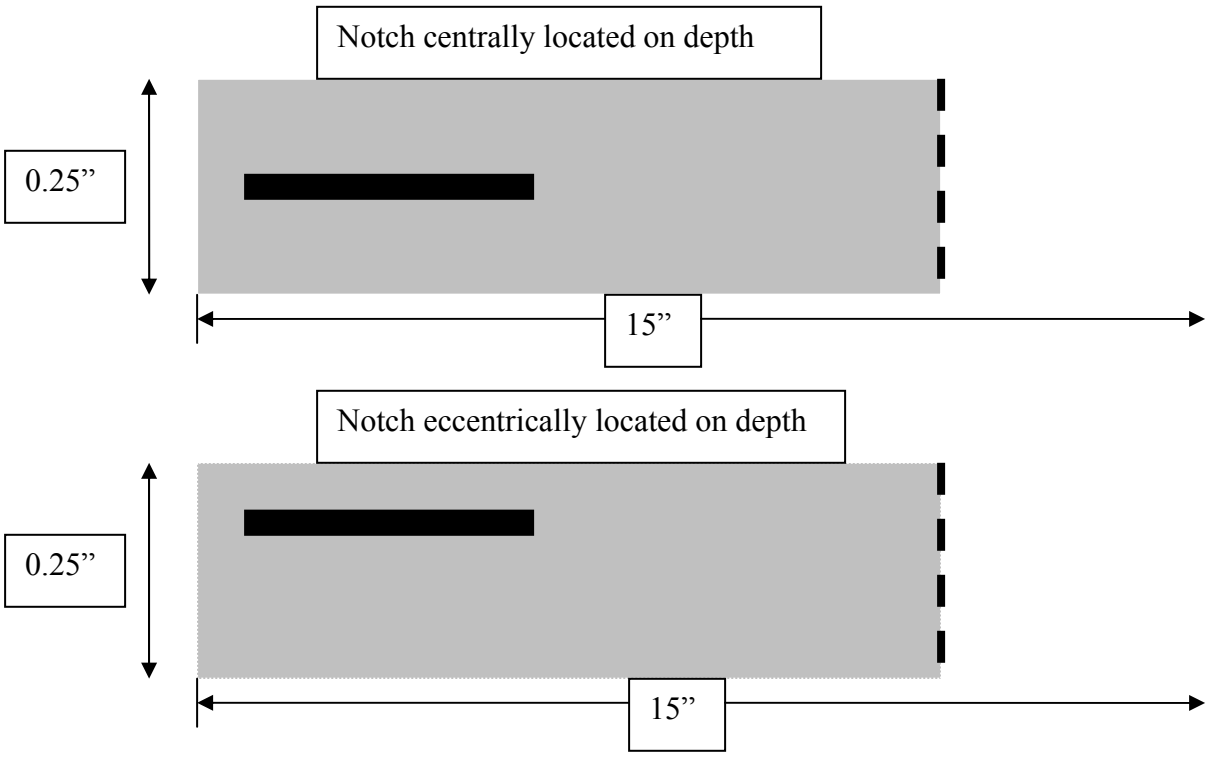

Figure 5. Central and eccentric notch location on beam depth

Notches are machined using an electrical discharge machining (EDM) cutting wire, which passes an ultra-high current through a thin wire to burn away the aluminum. A starter hole of $1/6^{th}$ cm (.0656 in) is cut in the middle of the future notch and the wire is pulled to either side as a liquid coolant floods the area to prevent thermal conduction from the wire to the rest of the aluminum. Notch dimensions and starter hole dimensions again are the same as in the previous study for the sake of comparison.

Finally, all beams contain two holes in the clamp area, each 0.125 inch in diameter, centered on the width, through the entire depth, at locations centered 1 inch and

2 inches from the clamp end. These holes are placed so pins can be inserted through the clamp and the beam, in hopes of enhancing the clamped condition. Please see Appendix D for technical drawings of the beams.

Figure 6. Centrally notched beams. From top to bottom: 4 cm (1.575 in) free end notch, 4 cm (1.575 in) middle notch, 4 cm (1.575 in) clamped end notch, 8 cm (3.150 in) free end notch, 8 cm (3.150 in) middle notch, 8 cm (3.150 in) clamped end notch, 12 cm (4.724 in) free end notch, 12 cm (4.724 in) middle notch, 12 cm (4.724 in) clamped end notch, 16 cm (6.299 in) free end notch, 16 cm (6.299 in) middle notch, 16 cm (6.299 in) clamped end notch.
NOTE: beams are 15 inches long, perspective in the photograph makes them appear longer.

2.1.2.2 Experimental Test Equipment.

The support system for the experiment consists of a stainless steel Newport Research Corporation Model 45 cylindrical test stand affixed to a Newport Research Corporation Model 100 magnetic base with two socket head cap screws. The clamp is specifically designed for these beams, and contains two pins to engage in the corresponding holes in the beams. This ensures that the end of the beam is always flush with the edge of the clamp, that there is always the same length of beam exposed for each test, and that the cantilever condition is as close to perfectly perpendicular as possible. The clamp is tightened by clamping the plate using four socket head cap screws, each tightened to 38.5 inch-lb. The beam can never be perfectly clamped, but the pins and torque measurements help to give the best experimental clamp possible under laboratory conditions and lend a degree of repeatability to the procedure. Finally, the support system is secured to a pneumatic shaker table with the magnetic base.

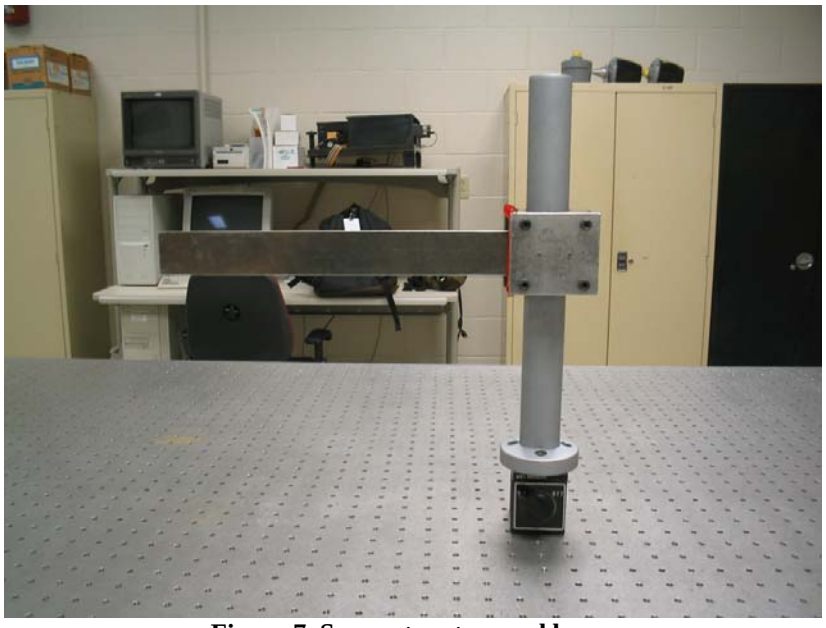

Figure 7. Support system and beam

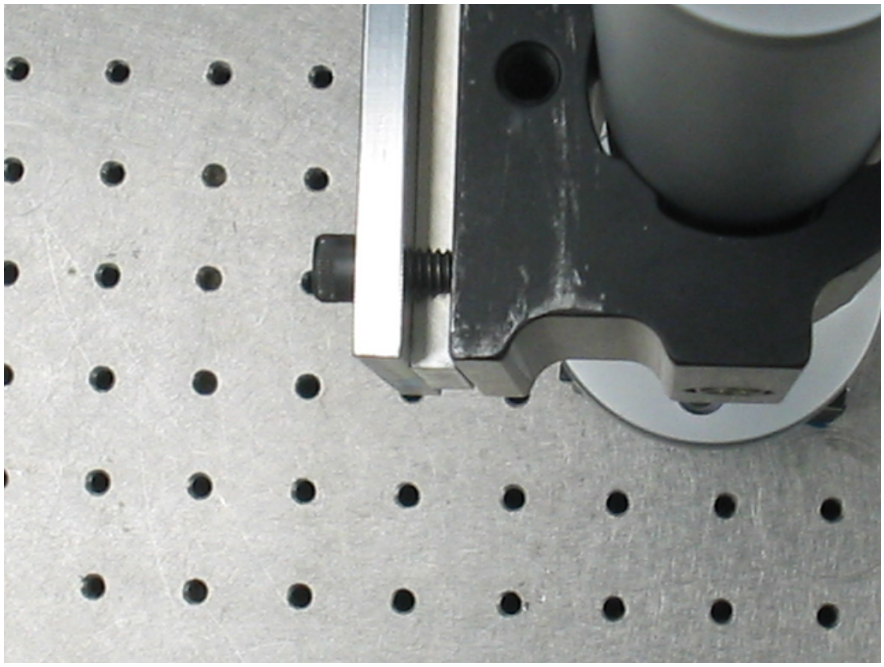

Figure 8. Properly clamped beam: end of beam flush with end of clamp

The support system was tested with the laser vibrometer to see if it introduced vibrations or deflections into the data. No natural frequencies of the test stand or the clamp were between 45 and 8000 Hz, which is the range of natural frequencies of the beams. Very small peaks, possibly resulting from background noise, were found between 2.5 and 10 Hz for both the test stand and the clamp. For the test stand, movement ranged between 20 micrometers to 10 micrometers per second, and only twisting motion was characterized. For the clamp, the movement ranged from 500 nanometers to 4 micrometers, and the most movement was found at the side opposite the specimen root. All of this information was contained in the frequency response function acquired by the laser vibrometer.

The actuator for all experiments is an Atlas Sound PD-60T acoustic horn attached to a Newport Research Corporation Model 100 magnetic base. This excitation method is chosen due to its external nature, which precludes changes in damping or vibration data a

piezoelectric patch may present. The signal used is a burst chirp produced by the Polytec software and amplified by a 220 DN Bogen amplifier. The horn is placed at a distance of 2-3 mm from the beam, centered on the beam width and placed 2.3 cm (0.90 in) from the free end of the beam. It is important for the horn to be placed at the exact center of the width to minimize the torsion modes introduced into the data.

Figure 9. Acoustic horn actuator

Figure 10. Bogen amplifier

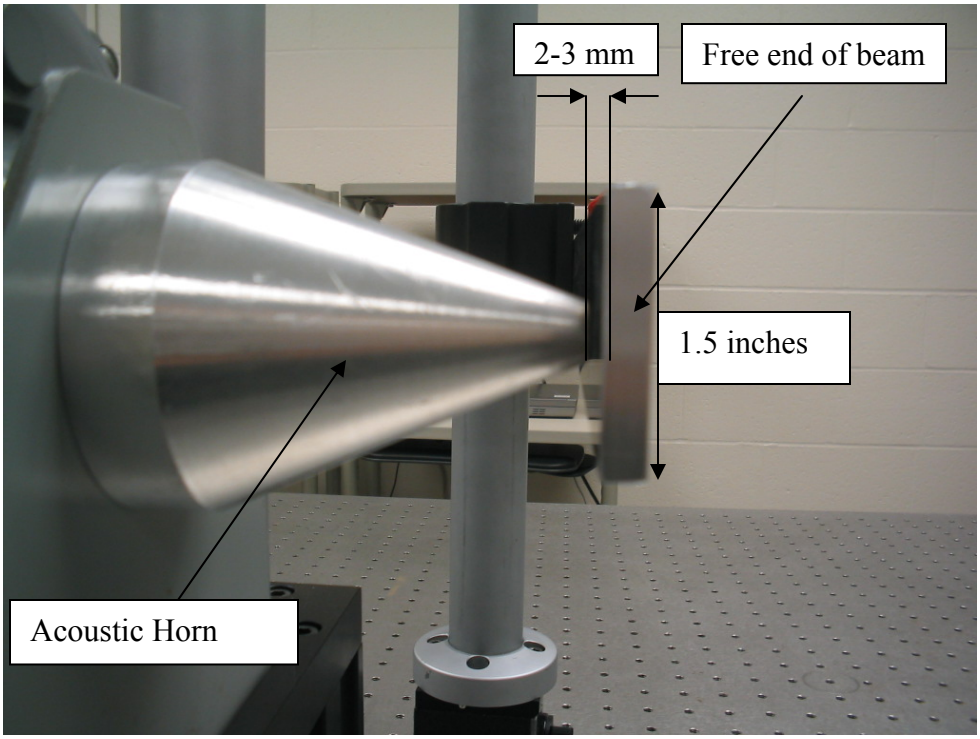

Figure 11. Horn placement

2.1.2.3 Laser Vibrometer Setup and Procedure.

All three scanning heads, "TOP," "LEFT," and "RIGHT," must be turned on, although only the "TOP" scanning head will be used to collect the data. These Polytec PSV-400 Scanning Heads are all supported by 3051 Manfrotto Tripods. The tripod supporting the "TOP" scan head can be leveled by ensuring that all three legs are the same length. Please refer to Figures 12 and 13 for an illustration of the equipment setup. When the aluminum beam is set in the support system as earlier detailed, the laser from the top scan head should be perpendicular to the aluminum beam and parallel to the floor. The laser beam should be positioned so as to hit the center of the aluminum beam when the laser and camera are turned on. For best results, place the object at a distance that is 14 mm + n205 mm, where n is an integer, to test the object at a maximum of the laser signal. In between maxima are minima of laser intensity where temporal fluctuations of laser signal intensity appear, causing problems in the measured intensity. If an object is measured at a minimum, the resulting data may be misleading. The beam should be positioned at any one of these maxima between five and ten feet from the scanning head.

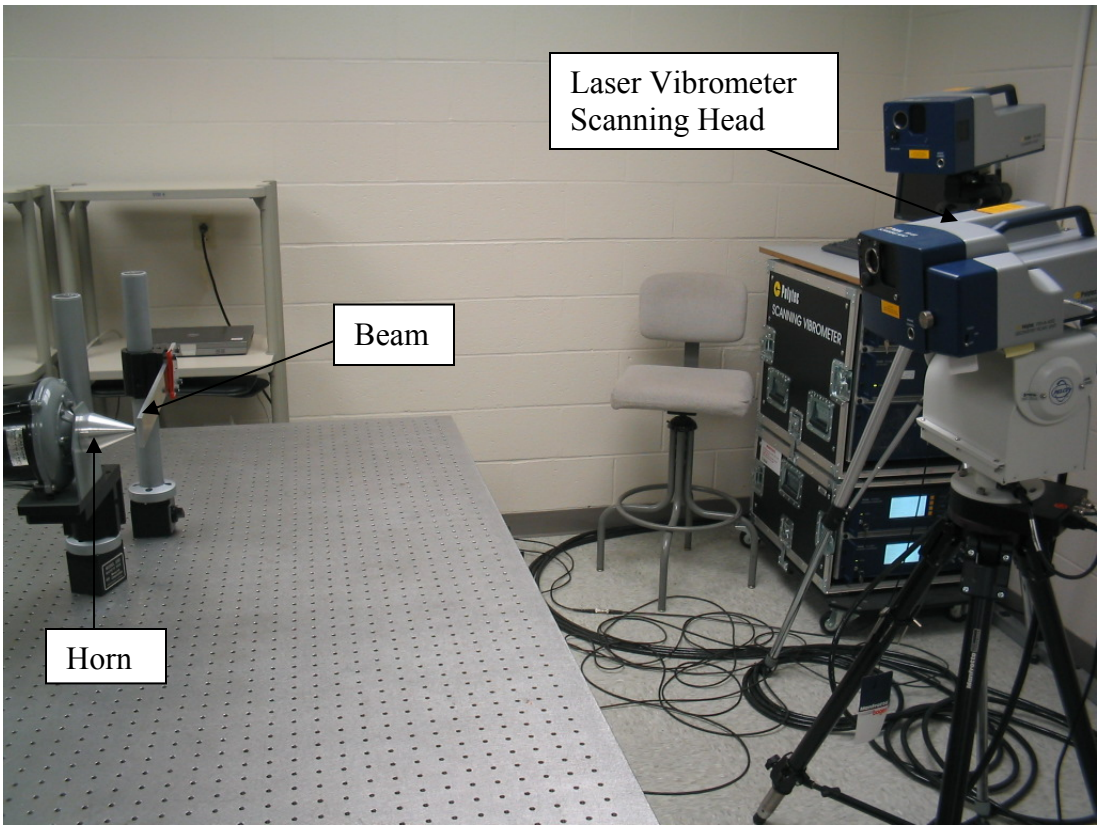

Figure 12. Horn, beam and scanning head configuration

The scanning heads are all connected to a Polytec OF V-5000 Vibrometric Controller (located under the computer in the lab). The scan heads are turned on by turning the silver keys to the "on" positions on the controller. Scan heads should be turned on at least 30 minutes prior to the experiment to ensure they are sufficiently warmed up, and the shutter should be opened in order to run the experiment. The Bogen amplifier was placed on the ground, away from the pneumatic shaker table, to prevent the introduction of vibrations from the cooling fan. The "SIGNAL 1" output from the "GENERATOR OUTPUTS" category on the Junction Box should be connected to the "HIZ INPUTS" inlet on the back of the Bogen amplifier with a signal cable. This same signal should also be connected to an input channel of the Junction Box as a reference. The

output wires from "COM" and "25V 4-5Ω" on the back of the Bogen amplifier should be connected to the horn input with another signal cable.

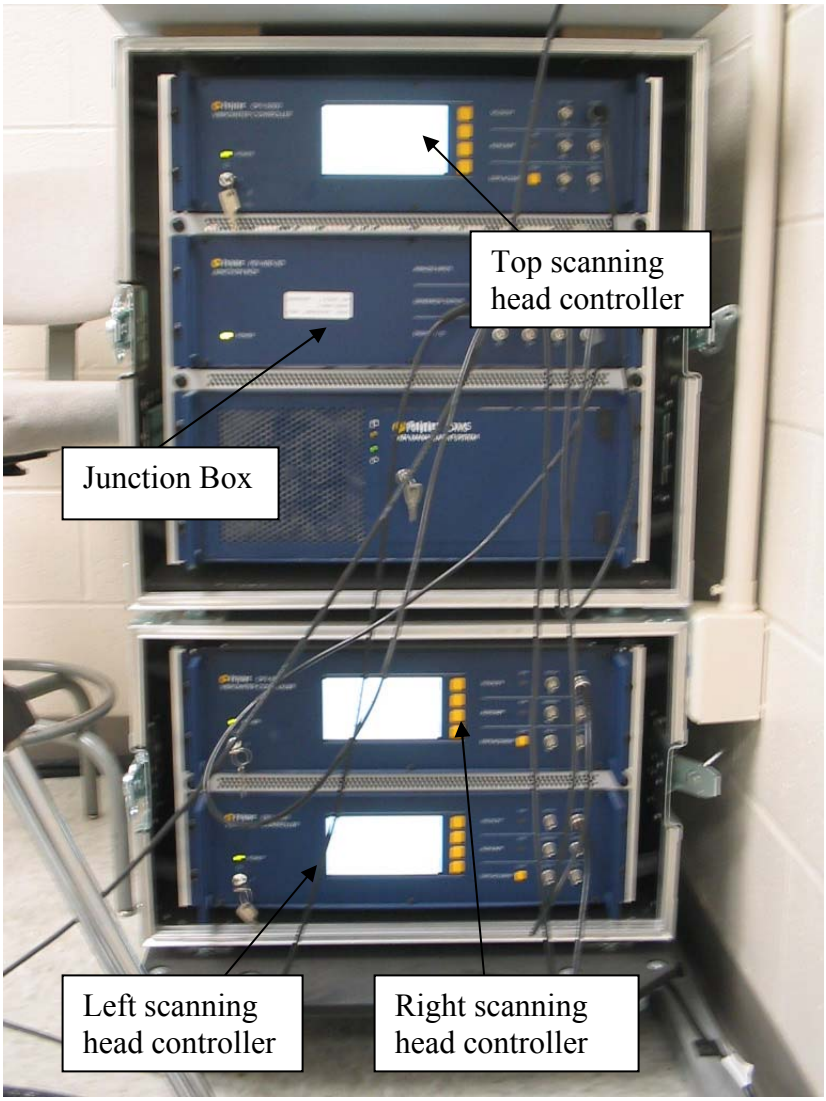

Figure 13. Junction box and vibrometric controllers in Lab 257

The software used for data acquisition in this experiment is the PSV 8.2 program. Once it is opened, the user must get into the acquisition mode by clicking the icon. In the acquisition mode, the user can select the device and generator for the experiment as explained in Appendix E. With the aid of a camera in the top scanning head, the software is used to align the object coordinates with respect to the surroundings so the scanning

head recognizes the approximate area to be tested. The grid defining the points to be scanned is also defined at this stage. For the present study, a global grid of 24 points in the x-direction and 17 points in the y-direction was used, yielding an area over the beam defined by 90 scan points.

The remaining software preparation concerns the general settings, channels used, filtering, frequency ranges, windowing, trigger type, vibrometer specifications and generator settings. Fast Fourier Transfer (FFT) was chosen as the measurement mode, no filtering or windowing was used, frequency ranges changed for each beam, and channel, vibrometer and generator settings were chosen as outlined in Appendix E. For a detailed User's Manual and an explanation of the importance of the chosen settings and the issues surrounding each one, please refer to Appendix E.

2.2. Frequency Data

2.2.1. MATLAB Predictions.

The Cobb-Durham-Chmiel-Chronister code (CDCC code) written in MATLAB is a good tool to approximate the general location of bending modes in the frequency spectrum, and yields graphically the first eight eigenvectors. This code was based on a finite element approach. For a theoretical development of this code, please refer to Appendix A.

The most important feature of the CDCC code is the fact that no actual attempt to model the notch in the beam was carried out. Instead, the notched portion of the beam was modeled as having a different effective moment of inertia, defined as

$$I_{notched\_region} = \frac{b(h_u^{\,3} + h_l^{\,3})}{12} \tag{7}$$

where h_u and h_l are the heights of the upper and lower sublaminates in the notched region. This reduction in the moment of inertia reduced the stiffness of the model, effectively representing the damaged area. In effect, this equation models a beam in the following fashion:

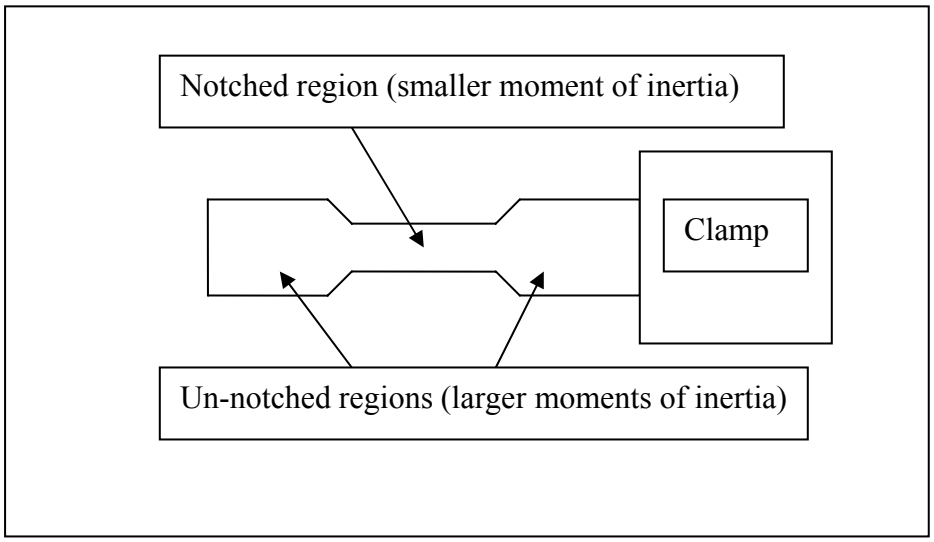

Figure 14. MATLAB modeling of a notched beam

The finite element model in the CDCC code used a simple beam model with 36 elements along the length of the beam. Elements in the region of the notch were 0.26247 inches long, regardless of notch length, while the remaining elements were spread evenly over the remaining (un-notched) length of the beam. One notable exception to this is the "transition" area on either end of the notch. There are three transition elements on either end of the notched region where the moment of inertia is linear stepped from the notched value to the un-notched value in order to curtail any discontinuities. The size of these transition elements is also 0.26247 inches, the same size as the elements in the notched region.

2.2.2. Experimental Data Acquisition.

Using the Polytec software, a user can obtain many forms of the acquired data. The first data generated is the FRF, which can be used to identify peaks that represent different bending and torsion modes of the scanned structure. From the FRF, natural frequencies can be obtained and tabulated. From these, animations of the modes can be observed in video form. From these videos, the mode shapes can be captured by freezing the animation.

To retrieve data for analysis purposes, the user must be in presentation mode of PSV 8.2. This can be done by clicking the  icon. Once in this mode, results of a previous scan can be opened from the File option. Clicking the  icon and choosing "Average Spectrum" presents the FRF of the scan, allowing the user to highlight frequency bands of interest. To define bands, click the  icon and use the mouse to highlight peaks in the FRF. The program will determine the peak magnitude value and the frequency at which this value occurs. Below is the FRF generated by the notchless beam data with the peaks representing bending modes highlighted.

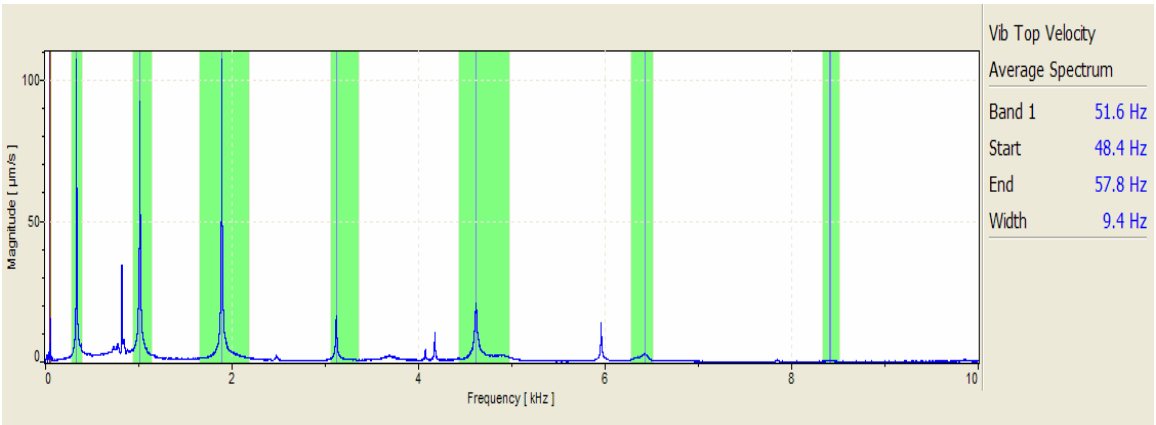

Figure 15. FRF generated by the Polytec software for the notchless beam. Highlighted peaks represent bending modes.

In order to assess whether a given frequency represents bending or torsion, the animation function can be utilized. The  button "plays" an animation of a given mode. The window to the left states which frequency is being represented in the animation. To rotate the view and see the eigenvector, click the  icon and "grab" the image with the mouse. Refer to Figures 16-18 for animation and mode shape examples.

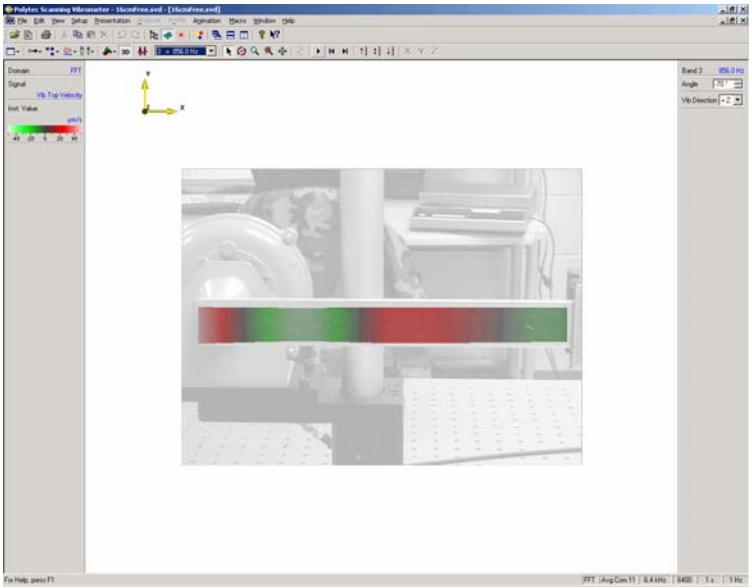

Figure 16. Animation mode for the 16 cm (6.299 in) free end notch. View is aimed directly at beam, as the laser does.

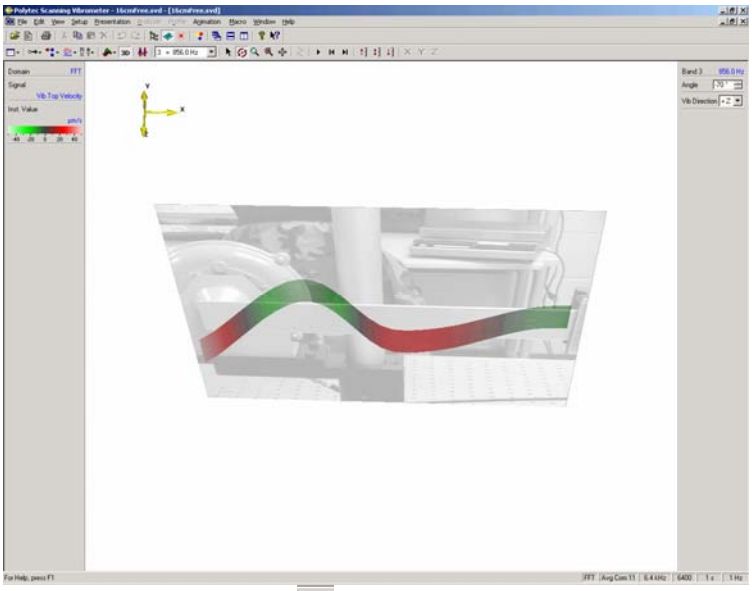

Figure 17. Using the icon, view can be rotated down.

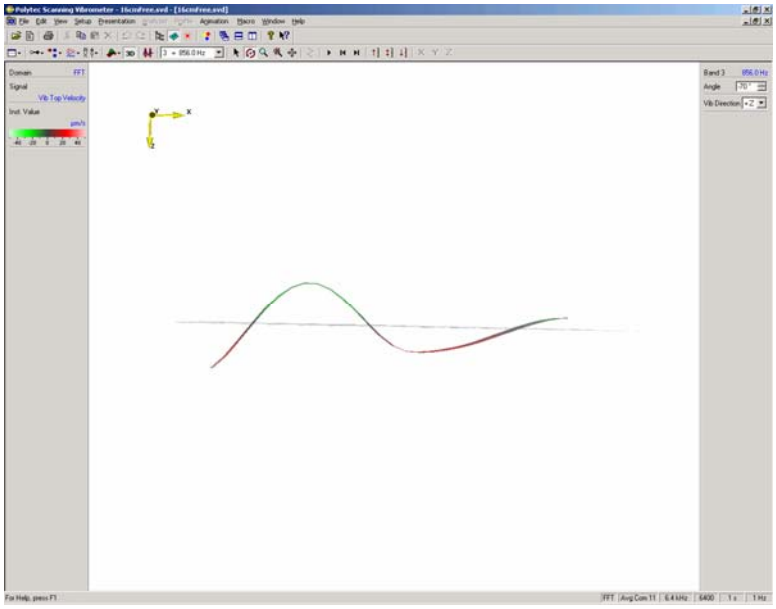

Figure 18. View is tilted all the way down. This shows the eigenvector.

2.2.3. Results.

The current section outlines the changes in natural frequencies and a comparison of eigenvector curvatures. The experimental natural frequencies found for each beam will be compared to the CDCC code frequencies, frequencies for all notched beams will

be compared to the notchless case, and finally frequency shifts will be compared to data from past research. Mode shape analysis through curvature comparison will show the results of plotting mode shapes for each notched case on top of mode shapes for the notchless case.

2.2.3.1.Changes in Natural Frequencies.

The resonant frequencies for the first eight bending modes of the notchless aluminum beam are included in Table 1. The experimental values are compared to both the MATLAB theoretical values and the frequencies yielded by the ABAQUS model. The absolute value of the percent difference ranges from 1.32% to 5.93% for MATLAB, and from 1.47% to 6.75% for the ABAQUS predictions for this beam. The experimental frequencies are lower than the predicted values except for in the third mode for both cases. This indicates that the experimental beam has a lower stiffness than the theoretical "perfect" case, which is not surprising.

Table 1. Experimental and theoretical values for the first 8 natural frequencies of the notchless beam

Mode	1	2	3	4	5	6	7	8
Experimental data (Hz):								
	52.5	333.75	1020	1893.75	3106.25	4586.25	6401.25	8426.43
MATLAB predicted data (Hz):								
	55.808	349.745	979.3	1919.04	3172.3	4739	6619.2	8813
Percent difference:								
	5.93%	4.57%	-4.16%	1.32%	2.08%	3.22%	3.29%	4.39%
Average MATLAB percent difference:					3.62%			
ABAQUS predicted data (Hz):								
	56.302	352.02	983.53	1922.1	3166.1	4707.3	6535	8635.9
Percent difference:								
	6.75%	5.19%	-3.71%	1.47%	1.89%	2.57%	2.05%	2.43%
Average ABAQUS percent difference:					3.26%			

The average MATLAB percent difference, when averaged across all modes and all cases, is 10.12%. This number could be misleading, however, because in looking at specific modes as outlined in Table 2, the MATLAB data varied from the experimental data by

0.28% to 84.44%. The MATLAB predictions and percent difference from experimental modes are assembled in Table 2.

Table 2. Modal frequencies and MATLAB predicted frequencies for centrally notched beams

	[1]EXPERIMENTAL MODAL FREQUENCIES (Hz) [2]MATLAB-predicted modal frequencies (Hz) [3]Percent difference (%)							
Mode	1	2	3	4	5	6	7	8
Notchless	[1]52.5 [2]55.808 [3]5.93%	333.75 349.745 4.57%	1020 979.3 -4.16%	1893.75 1919.04 1.32%	3106.25 3172.3 2.08%	4586.25 4739 3.22%	6401.25 6619.2 3.29%	8426.43 8813 4.39%
Clamped End								
4 cm (1.575 in)	[1]53.125 [2]33.793 [3]-57.2%	326.563 295.145 -10.64%	973.438 861.9 -12.9%	1704.69 1658.32 -2.80%	2815.63 2725.3 -3.31%	4254.69 4135.4 -2.88%	6006.25 5853.5 -2.61%	7871.88 7793.9 -1.00%
8 cm (3.150 in)	[1]52.5 [2]29.035 [3]-80.8%	285 275.871 -3.31%	741.25 738.74 -0.34%	1632.5 1536.09 -6.28%	2610 2530.1 -3.16%	3747.5 3682.4 -1.77%	5381.25 5263.9 -2.23%	7110 6949.5 -2.31%
12 cm (4.724 in)	[1]50 [2]27.109 [3]-84.4%	237.5 229.795 -3.35%	732.5 714.89 -2.46%	1386.25 1352.19 -2.52%	2322.5 2281.5 -1.80%	3418.75 3352.9 -1.96%	4775 4737.2 -0.80%	6271.25 6251.9 -0.31%
16 cm (6.299 in)	[1]46.25 [2]26.328 [3]-75.7%	217.5 193.347 -12.49%	646.25 650.22 0.61%	1292.5 1248.96 -3.49%	2062.5 2016.6 -2.28%	3193.75 3113.4 -2.58%	4260 4248.2 -0.28%	5780 5682.3 -1.72%
Middle								
4 cm (1.575 in)	[1]53.125 [2]50.963 [3]-4.24%	342.188 276.038 -23.96%	1000 926.01 -16.5%	1934.38 1660.02 -16.5%	2851.56 287.6 -0.14%	4628.13 4265.6 -8.50%	5640.63 5836 3.35%	8117.19 8009.6 -1.34%
8 cm (3.150 in)	[1]52.0313 [2]46.285 [3]-12.4%	332.5 238.15 -39.62%	910.625 804.08 -13.3%	1743.75 1579.83 -10.4%	2356.25 2474.8 4.79%	3650 3781.2 3.47%	5135 5355.4 4.12%	6730 7008.8 3.98%
12 cm (4.724 in)	[1]51.25 [2]41.744 [3]-22.8%	335 221.051 -51.55%	610 664.16 8.15%	1441.25 1425.79 -1.08%	2357.5 2303.4 -2.35%	3417.5 3336.6 -2.42%	4598.75 4689.4 1.93%	6332.5 6306.2 -0.42%
16 cm (6.299 in)	[1]49 [2]36.567 [3]-34.0%	319 205.368 -55.33%	558 569.76 2.06%	1228 1197.89 -2.51%	2123 2054.1 -3.35%	3284 3027.6 -8.47%	4340 4136.2 -4.93%	5674 5534.7 -2.52%
Free End								
4 cm (1.575 in)	[1]53.125 [2]60.569 [3]12.29%	339.063 357.615 5.19%	1017.19 869.86 -16.9%	1859.38 1679.99 -10.7%	2995.31 2830.5 -5.82%	4414.06 4124.8 -7.01%	6150 5845.7 -5.21%	8185.94 7915.7 -3.41%
8 cm (3.150 in)	[1]53.75 [2]60.33 [3]10.91%	330 296.149 -11.43%	968.75 772.6 -25.4%	1781.25 1543.3 -15.4%	2852.5 2526.6 -12.90%	3737.5 3773 0.96%	5245 5287.3 0.80%	7058.75 7034.4 -0.35%
12 cm (4.724 in)	[1]53.75 [2]57.428 [3]6.40%	300 251.437 -19.31%	921.25 740.3 -24.4%	1475 1386.65 -6.37%	2260 2297.9 1.65%	3461.25 3491.6 0.87%	4866.25 4796.1 -1.46%	6268.75 6385.9 1.83%
16 cm (6.299 in)	[1]52 [2]51.276 [3]-1.41%	284 247.816 -14.60%	856 660.72 -29.6%	1267 1325.29 4.40%	2132 2181.7 2.28%	3291 3219.7 -2.21%	4174 4440.1 5.99%	5737 5946 3.51%

The percent difference in Table 2 is calculated as follows:

$$\%difference = \frac{\omega_{MATLAB} - \omega_{experimental}}{\omega_{MATLAB}} \tag{8}$$

where ω is the modal frequency.

According to Table 2, the largest percent difference is found in the first or second mode in most cases. Without exception, the largest percent difference for all cases is in modes one through three. In general, the percent difference decreases drastically as the mode number increases, indicating that the code better predicts the higher modes. This trend is an indication that the somewhat crude MATLAB technique of combining inertias is justifiable since the beams' resonant frequencies increase.

Table 3 shows the first eight resonant frequencies for all notched beams tested, excluding the corroded beams, and shows the percent change from the notchless case. The percent deviation from the notchless case is calculated according to Equation 9

$$\%deviation = \frac{\omega_{notched\_beam} - \omega_{notchless\_beam}}{\omega_{notchless\_beam}} \times 100\% \tag{9}$$

where ω is the modal frequency. Overall, for each location and particular mode, modal frequency decreases as notch length increases, as would be expected. The only cases in which the data in Table 3 did not exhibit this trend were the second and fifth modes for the 12 cm (4.724 in) middle notched beams, and the first mode for the 4 cm (1.575 in), 8 cm (3.150 in), and 12 cm (4.724 in) free end notched beams. For the free end notch cases, the modal frequencies were very close to the preceding values in the first mode, which may make it difficult to see the trend of decreasing modal frequency with increasing notch length. From the 4 cm (1.575 in) free end notch to the 8 cm (3.150 in)

free end notch, the modal frequency increased by a mere 0.625 Hz, from the 8 to 12 cm (3.150 to 4.724 in) notch, the modal frequencies remained the same, and for the 16 cm (6.299 in) free end notch, the frequency dropped by 1.75 Hz, agreeing with the rest of the data.

Table 3. Experimental modal frequencies for centrally notched beams

	[1]EXPERIMENTAL MODAL FREQUENCIES (Hz) [2]Deviation from notchless beam (%)							
Mode	1	2	3	4	5	6	7	8
Notchless	52.5	333.75	1020	1893.75	3106.25	4586.25	6401.25	8426.43
Clamped End								
4 cm (1.575 in)	[1]53.125 [2]1.19%	326.56 -2.15%	973.438 -4.56%	1704.69 -9.98%	2815.63 -9.36%	4254.69 -7.23%	6006.25 -6.17%	7871.88 -6.58%
8 cm (3.150 in)	[1]52.5 [2]0.00%	285 -14.6%	741.25 -27.3%	1632.5 -13.8%	2610 -16.0%	3747.5 -18.3%	5381.25 -15.9%	7110 -15.6%
12 cm (4.724 in)	[1]50 [2]-4.76%	237.5 -28.8%	732.5 -28.2%	1386.25 -26.8%	2322.5 -25.2%	3418.75 -25.5%	4775 -25.4%	6271.25 -25.6%
16 cm (6.299 in)	[1]46.25 [2]-11.9%	217.5 -34.8%	646.25 -36.6%	1292.5 -31.8%	2062.5 -33.6%	3193.75 -30.4%	4260 -33.5%	5780 -31.4%
Middle								
4 cm (1.575 in)	[1]53.125 [2]1.19%	342.188 2.53%	1000 -1.96%	1934.38 2.15%	2851.56 -8.20%	4628.13 0.91%	5640.63 -11.9%	8117.19 -3.67%
8 cm (3.150 in)	[1]52.031 [2]-0.89%	332.5 -0.37%	910.625 -10.7%	1743.75 -7.92%	2356.25 -24.1%	3650 -20.4%	5135 -19.8%	6730 -20.1%
12 cm (4.724 in)	[1]51.25 [2]-2.38%	335 0.37%	610 -40.2%	1441.25 -23.9%	2357.5 -24.1%	3417.5 -25.5%	4598.75 -28.2%	6332.5 -24.9%
16 cm (6.299 in)	[1]49 [2]-6.67%	319 -4.42%	558 -45.3%	1228 -35.2%	2123 -31.7%	3284 -28.4%	4340 -32.2%	5674 -32.7%
Free End								
4 cm (1.575 in)	[1]53.125 [2]1.19%	339.063 1.59%	1017.19 -0.28%	1859.38 -1.81%	2995.31 -3.57%	4414.06 -3.75%	6150 -3.93%	8185.94 -2.85%
8 cm (3.150 in)	[1]53.75 [2]2.38%	330 -1.12%	968.75 -5.02%	1781.25 -5.94%	2852.5 -8.17%	3737.5 -18.5%	5245 -18.1%	7058.75 -16.23
12 cm (4.724 in)	[1]53.75 [2]2.38%	300 -10.1%	921.25 -9.68%	1475 -22.1%	2260 -27.2%	3461.25 -24.5%	4866.25 -24.0%	6268.75 -25.6%
16 cm (6.299 in)	[1]52 [2]-0.95%	284 -14.9%	856 -16.1%	1267 -33.1%	2132 -31.4%	3291 -28.2%	4174 -34.8%	5737 -31.9%

The experimental natural frequencies are compared to the experimental data from the eccentrically notched beams in Table 4. This data is the same as that found in the Durham study, except for the natural frequencies of the 12 cm (4.724 in) clamped end notch and the 16 cm (6.299 in) clamped end, middle, and free end notches. These cases

were re-tested due to the questionable nature of the previously found data. After re-testing, the new data agreed much better with the analytical results.

Table 4. Comparison of modal frequencies for centrally and eccentrically notched aluminum 2024-T3 beams of the same dimensions

[1]EXPERIMENTAL MODAL FREQUENCIES FOR CENTERED NOTCHES (Hz) [2]Experimental modal frequencies for eccentrically notched beams (Hz) [3]Percent difference (%)								
Mode	1	2	3	4	5	6	7	8
Notchless	[1]52.5 [2]52.92 [3]-0.8%	333.75 330.91 0.85%	1020 1053 -3.24%	1893.75 1869 1.31%	3106.25 3093 0.43%	4586.25 4590 -0.08%	6401.25 6306 1.49%	8426.43 8450 -0.28%
Clamped								
4 cm (1.575 in)	[1]53.13 [2]50.94 [3]4.1%	326.563 318.2 2.56%	973.438 955.7 1.82%	1704.69 1747 -2.48%	2815.63 2858 -1.50%	4254.69 4212 1.00%	6006.25 6279 -4.54%	7871.88 8169 -3.77%
8 cm (3.150 in)	[1]52.5 [2]50.63 [3]3.6%	285 296.9 -4.18%	741.25 871.9 -17.63%	1632.5 1747 -7.01%	2610 2850 -9.20%	3747.5 3760 -0.33%	5381.25 4031 25.09%	7110 5725 19.48%
12 cm (4.724 in)	[1]50 [2]50 [3]0%	237.5 270.313 -13.82%	732.5 900 -22.87%	1386.25 1647.5 -18.85%	2322.5 2571.88 -10.74%	3418.75 3953.13 -15.63%	4775 5009.38 -4.91%	6271.25 7663 -22.19%
16 cm (6.299 in)	[1]46.25 [2]47.5 [3]-2.7%	217.5 243.75 -12.07%	646.25 862.5 -33.46%	1292.5 1487.5- 15.09%	2062.5 2490.63 -20.76%	3193.75 3735.94 -16.98%	4260 5076.25 -19.16%	5780 6867.1 -18.81%
Middle								
4 cm (1.575 in)	[1]53.13 [2]51.88 [3]2.34%	342.188 331.3 3.18%	1000 812.5 18.75%	1934.38 1853 4.21%	2851.56 2887 -1.24%	4628.13 4309 6.90%	5640.63 5844 -3.61%	8117.19 8159 -0.52%
8 cm (3.150 in)	[1]52.03 [2]50.94 [3]2.10%	332.5 328.1 1.32%	910.625 775 14.89%	1743.75 1878 -7.70%	2356.25 2459 -4.36%	3650 4013 -9.95%	5135 5744 -11.86%	6730 7703 -14.46%
12 cm (4.724 in)	[1]51.25 [2]50.31 [3]1.83%	335 317.5 5.22%	610 710 -16.39%	1441.25 1638 -13.65%	2357.5 2678 -13.59%	3417.5 3850 -12.66%	4598.75 5473 -19.01%	6332.5 7308 -15.40%
16 cm (6.299 in)	[1]49 [2]50.31 [3]-2.7%	319 295 7.52%	558 623.4 -11.72%	1228 1388 -13.03%	2123 2445 -15.17%	3284 3805 -15.86%	4340 5006.25 -15.35%	5674 6172.5 -8.79%
Free								
4 cm (1.575 in)	[1]53.13 [2]52.81 [3]0.59%	339.063 328.1 3.23%	1017.19 1009 0.81%	1859.38 1828 1.69%	2995.31 2972 0.78%	4414.06 4322 2.09%	6150 6178 -0.46%	8185.94 8134 0.63%
8 cm (3.150 in)	[1]53.75 [2]52.5 [3]2.33%	330 325 1.52%	968.75 987.5 -1.94%	1781.25 1731 2.82%	2852.5 2903 -1.77%	3737.5 3966 -6.11%	5245 5481 -4.50%	7058.75 6881 2.52%
12 cm (4.724 in)	[1]53.75 [2]52.5 [3]2.33%	300 306.3 -2.10%	921.25 942.5 -2.31%	1475 1666 -12.95%	2260 2291 -1.37%	3461.25 2550 26.33%	4866.25 3700 23.97%	6268.75 5023 19.87%
16 cm (6.299 in)	[1]52 [2]52.5 [3]-1.0%	284 300 -5.63%	856 963.8 -12.59%	1267 1442.5 -13.85%	2132 1865 12.52%	3291 2962.5 9.98%	4174 3793 9.13%	5737 4965 13.46%

Table 4 gives the natural frequencies of both beams and shows the percent difference between the two. The percent difference ranges from 0% for the first mode of the 12 cm (4.724 in) clamped end notch, to 33.46% for the third mode of the 16 cm (6.299 in) clamped end notch. If the comparison of the two notchless beams (theoretically identical) is taken as the spread of data, the frequency of a given mode can reasonably range from 0 to 3.24% difference for a theoretically similar beam. If this is the case, the spread of data exceeds the differences in modal frequencies between centrally and eccentrically notched beams for the 4 cm (1.575 in) notches in 71% of all cases, and six of the eight measured modes for the 8 cm (3.150 in) free end notched case. Thus, it would be difficult to differentiate between a centered and un-centered notch if the notch is 4 cm (1.575 in) or possibly shorter in length.

Also worth considering is a comparison of modal frequencies to the modal frequencies of another previous study, specifically the one in which the beams were also centrally notched, but the beam depth was 0.125 in. All other dimensions were the same except for beam and notch depth. In both cases beams were machined from aluminum 2024-T3. These frequencies are compiled in Table 5. As expected, when the depth of the beam is halved, the natural frequency for a given mode is also halved. The notches in each case have a depth of 0.012". For the 0.25" deep beam, this is 4.8% of the beam depth, while for the 0.125" deep beam, it is 9.6% of the beam depth. The previously mentioned hypothesis that natural frequency decrease is proportional to the square of the crack depth ratio (Dimarogonas, 1996:832) is unsupported in this research. This is most likely due to two main factors. Either the manufactured notches do not behave as cracks,

or the notches in the present study are too large to be considered small cracks, as they span the entire width of each beam.

Table 5. Comparison of modal frequencies for centrally notched beams 0.25" in depth and 0.125" in depth

[1]EXPERIMENTAL MODAL FREQUENCIES FOR CENTERED NOTCHES (Hz) [2]Experimental modal frequencies for centrally notched beams 0.125 inches deep (Hz) [3]Percent difference (%)								
Mode	1	2	3	4	5	6	7	8
Notchless	[1]52.5 [2]28.37 [3]46%	333.75 177.78 46.73%	1020 497.68 51.21%	1893.75 975.53 48.49%	3106 1612.45 48.09%	4586.25 2408.85 47.48%	6401.25 3364.22 47.44%	8426.43 4479.16 46.84%
Clamped								
4 cm (1.575 in)	[1]53.13 [2]27.73 [3]48%	326.563 169.9 47.97%	973.438 474.87 51.22%	1704.69 965.5 43.36%	2815.63 1387.33 50.73%	4254.69 2077.33 51.18%	6006.25 3092.67 48.51%	7871.88 3946.33 49.87%
8 cm (3.150 in)	52.5 n/a	285 n/a	741.25 n/a	1632.5 n/a	2610 n/a	3747.5 n/a	5381.25 n/a	7110 n/a
12 cm (4.724 in)	[1]50 [2]25.13 [3]50%	237.5 146.63 38.26%	732.5 369.13 49.61%	1386.25 682.8 50.74%	2322.5 1039.33 55.25%	3418.75 1656.33 51.55%	4775 2289.67 52.05%	6271.25 2949 52.98%
16 cm (6.299 in)	[1]46.25 [2]24.22 [3]47.63	217.5 137.1 36.97%	646.25 300.3 53.53%	1292.5 563.17 56.43%	2062.5 1026 50.25%	3193.75 1449 54.63%	4260 1977 53.59%	5780 2755.67 52.32%
Middle								
4 cm (1.575 in)	[1]53.13 [2]27.73 [3]47.8%	342.188 170.57 50.15%	1000 456.23 54.38%	1934.38 899.23 53.51%	2851.56 1535.67 46.15%	4628.13 1977.67 57.27%	5640.63 3053 45.87%	8117.19 3785.67 53.36%
8 cm (3.150 in)	[1]52.03 [2]28.13 [3]45.9%	332.5 169 49.17%	910.625 390.87 57.08%	1743.75 725.8 58.38%	2356.25 1283 45.55%	3650 1846.67 49.41%	5135 2477 51.76%	6730 3483.33 48.24%
12 cm (4.724 in)	[1]51.25 [2]27.47 [3]46.4%	335 161.33 51.84%	610 366.13 39.98%	1441.25 635.7 55.89%	2357.5 1080.67 54.16%	3417.5 1729.33 49.4%	4598.75 2377.67 48.30%	6332.5 2991 52.77%
16 cm (6.299 in)	[1]49 [2]26.82 [3]45.3%	319 152.43 52.22%	558 324.87 41.78%	1228 577.3 52.99%	2123 1024.33 51.75%	3284 1403.33 57.27%	4340 1982.33 54.32%	5674 2820.33 50.29%
Free								
4 cm (1.575 in)	[1]53.13 [2]28.91 [3]45.6%	339.063 175.27 48.31%	1017.19 471.73 53.62	1859.38 931.77 49.89%	2995.31 1485 50.42%	4414.06 2213.33 49.86%	6150 3116 49.33%	8185.94 4151 49.29%
8 cm (3.150 in)	[1]53.75 [2]29.3 [3]45.5%	330 166.93 49.42%	968.75 421.63 56.48%	1781.25 774.33 56.53%	2852.5 1359.67 52.33%	3737.5 1779.33 52.39%	5245 2533.33 51.70%	7058.75 3476.67 50.75%
12 cm (4.724 in)	[1]53.75 [2]29.04 [3]46.0%	300 154.3 48.57%	921.25 406.27 55.90%	1475 658.2 55.38%	2260 1090.33 51.76%	3461.25 1748.33 49.49%	4866.25 2369 51.32%	6268.75 3084.33 50.80%
16 cm (6.299 in)	[1]52 [2]28.26 [3]45.7%	284 146.77 48.32%	856 336.6 60.68%	1267 561.47 55.69%	2132 1046.33 50.92%	3291 1535 53.36%	4174 2263.67 45.77%	5737 2750 52.07%

2.2.3.2.Comparison of Mode Shapes.

The eigenvector curvature comparison was accomplished by obtaining the experimental eigenvector from the animation feature of the Polytec laser vibrometer software, importing it to Excel, and creating a MATLAB m-file to plot the mode shape. The mode shape for each mode was plotted against the corresponding mode shape of the notchless beam. By lining the mode shapes directly atop one another, the deviation from the notchless mode shape shows the location and approximate extent of damage.

The key to comparing eigenvectors (mode shapes) is to note the location at which the curvature of a mode shape for a notched beam (representing a damaged structure) changes from the curvature of the same mode shape for a notchless beam (representing an undamaged structure). Curvature is defined as the derivative of slope, so the change in slope between two points that are close together on the eigenvector can be examined to graphically determine curvature, as in Figure 19. The curvature is shown as the change in slope for a particular mode shape between two points that are close together. Note that the red plot, representing the third mode eigenvector of the notched beam, has a change in slope that is much less than the blue plot (notchless beam) between points 1 and 2. Likewise, the change in slope between points 3 and 4 is much greater for the blue plot than the change in slope for the red plot. These different amounts of change in the slope of the eigenvector indicate the beginning and end of the notched location. This matches very well with the known notch location, indicated by a bold line on the abscissa.

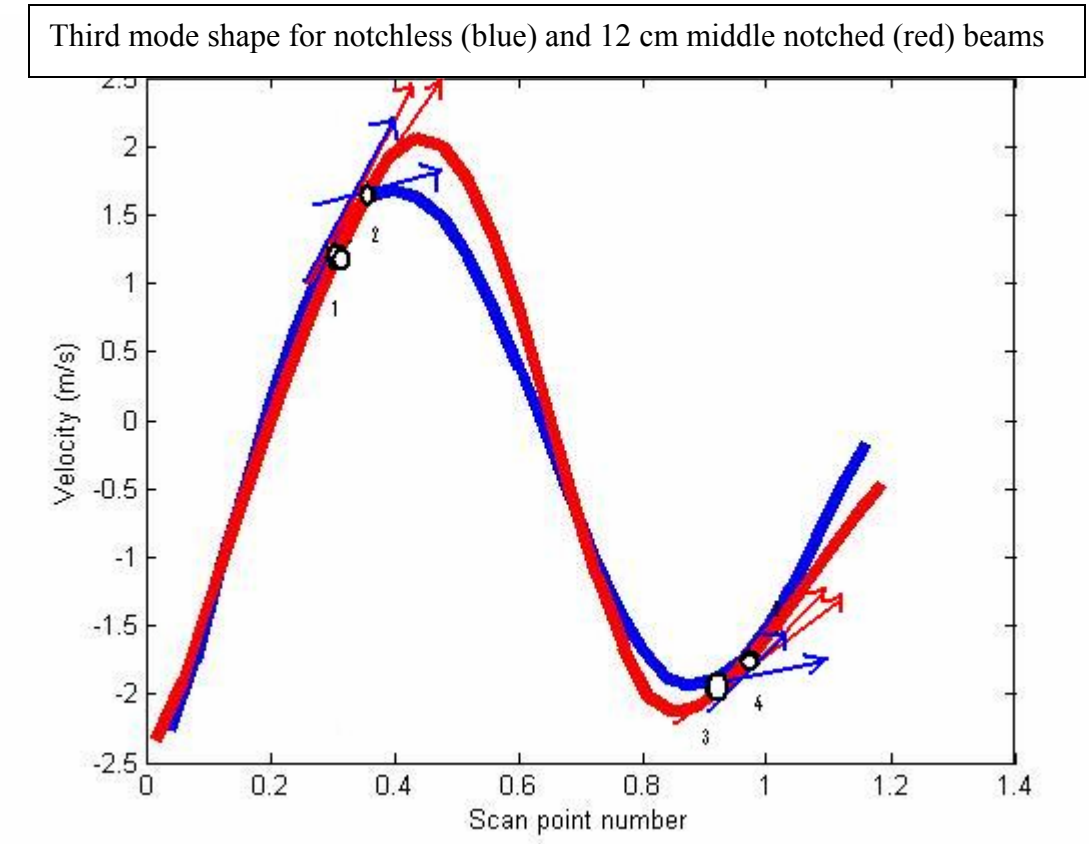

Figure 19. Curvature change. The change in slope (curvature equals change in slope) is much less for the red plot (notched beam) than for the blue plot (notchless beam) between points 1 and 2 and points 3 and 4.

Figures 20 through 32 show all experimental mode shapes for the 4 cm (1.575 in) clamped end notched beam, the 12 cm (4.724 in) middle notched beam and mode four for all beams. For a complete catalog of all mode shapes, please refer to Appendix I. Please note that the *right side* of the plots represent the clamped end of the mode shapes. As such, the root of the cantilever is not always effectively captured by the scanning vibrometer. The very small region between the horizontal zero line and the start of the mode shape (on the right) will have to be visualized by the reader. Please note that the notchless mode shape for mode seven is not good for a valid comparison due to some

torsion in that mode. Because it was not a pure bending mode, the mode shape reflects the torsion by being enlarged in magnitude around scan point number 0.4 on the x-axis.

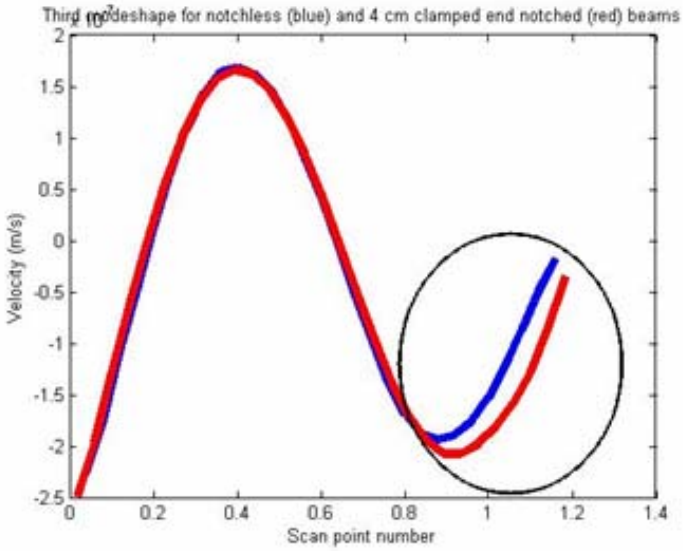

Figure 20. Third mode shapes for notchless and 4 cm (1.575 in) clamped end notch

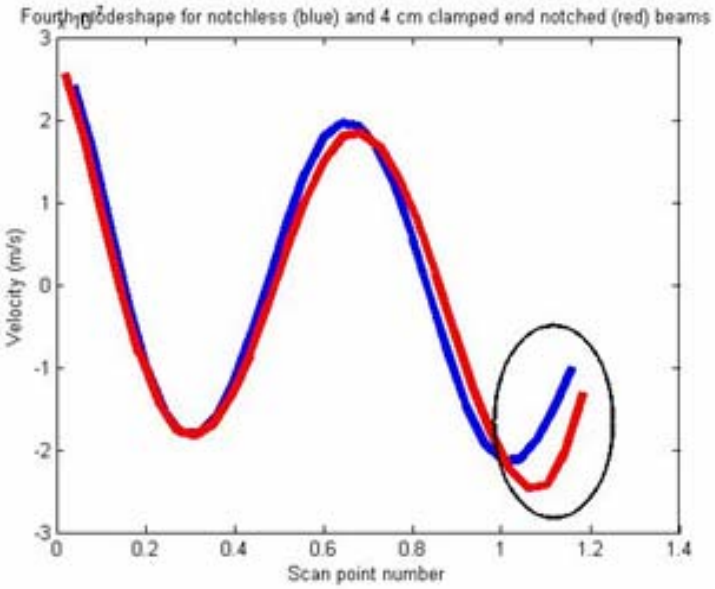

Figure 21. Fourth mode shapes for notchless and 4 cm (1.575 in) clamped end notch

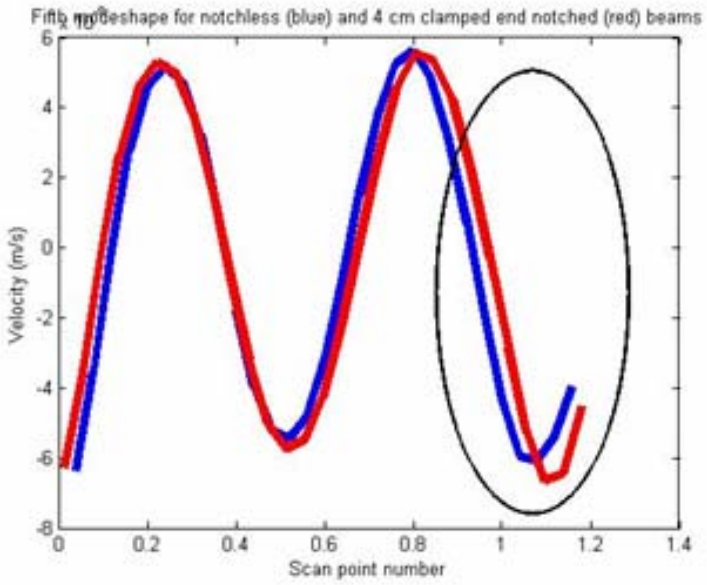

Figure 22. Fifth modeshape for notchless and 4 cm (1.575 in) clamped end notch

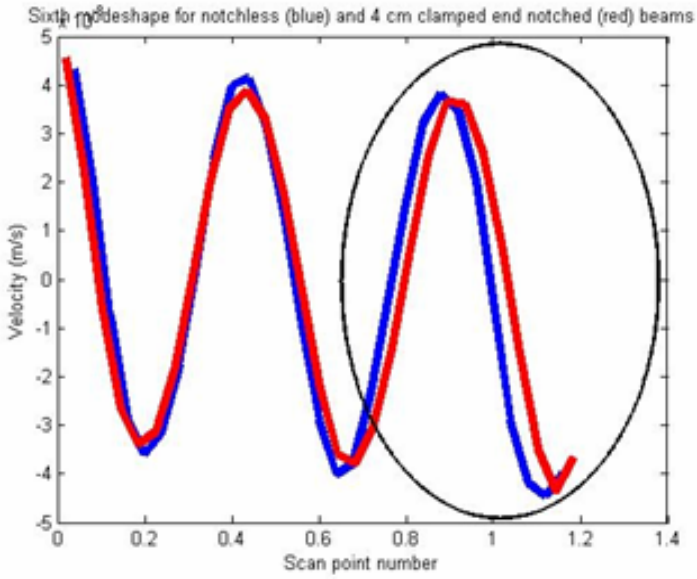

Figure 23. Sixth mode shape for notchless and 4 cm (1.575 in) clamped end notch

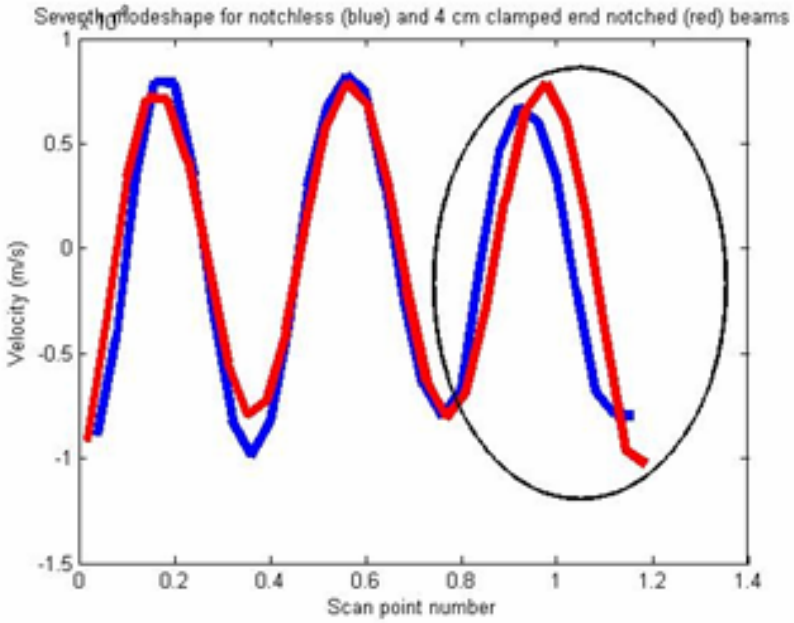

Figure 24. Seventh mode shape for notchless and 4 cm (1.575 in) free end notch

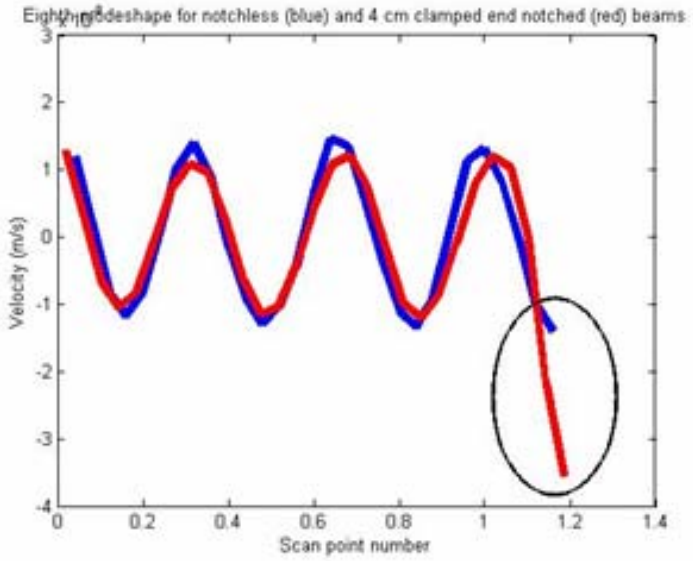

Figure 25. Eighth mode shape for notchless and 4 cm (1.575 in) free end notch

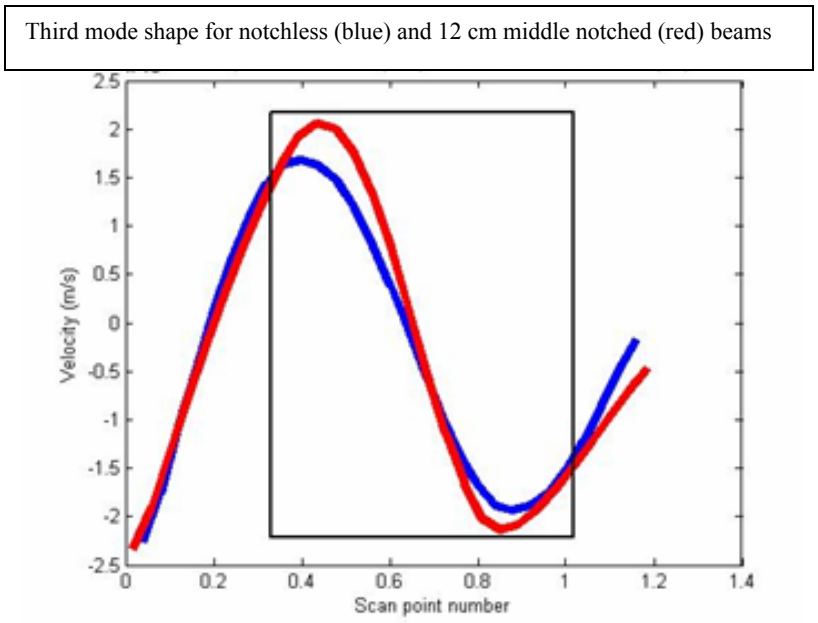

Figure 26. Third mode shape for notchless and 12 cm (4.724 in) middle notched beam

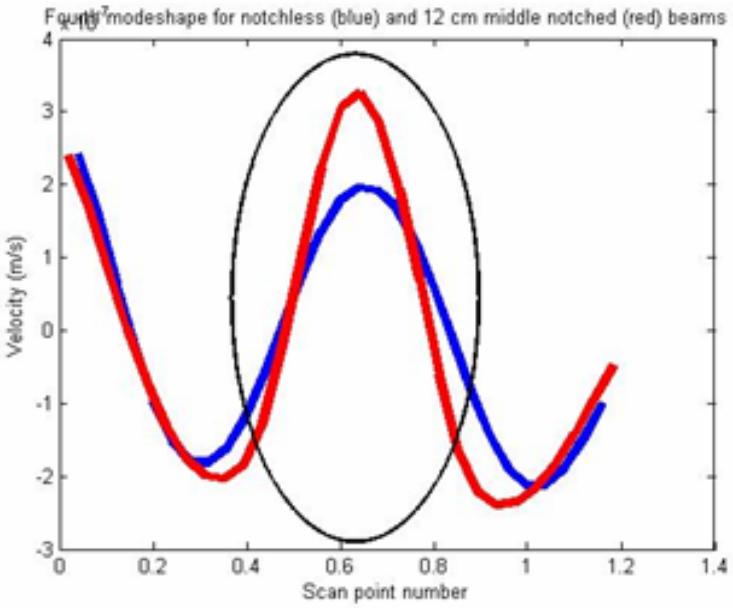

Figure 27. Fourth mode shape for notchless and 12 cm (4.724 in) middle notched beam

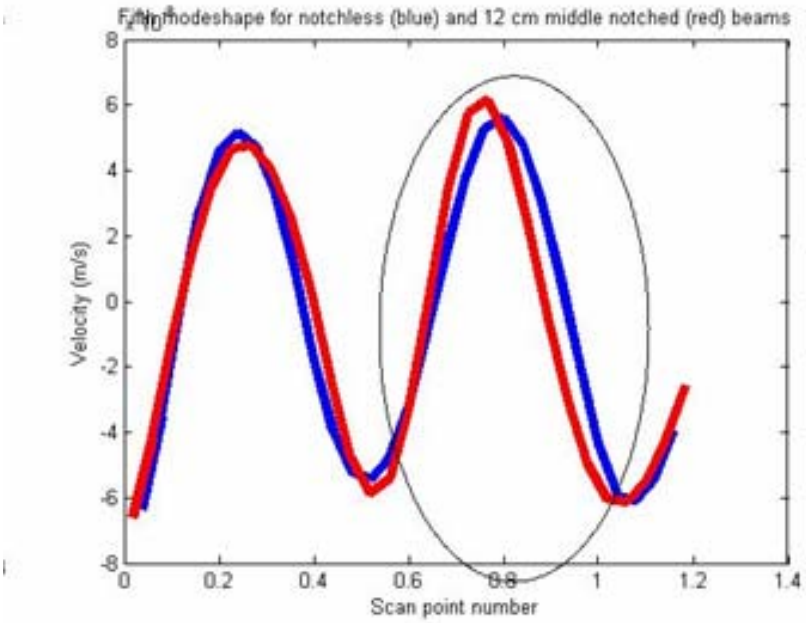

Figure 28. Fifth mode shape for notchless and 12 cm (4.724 in) middle notched beam

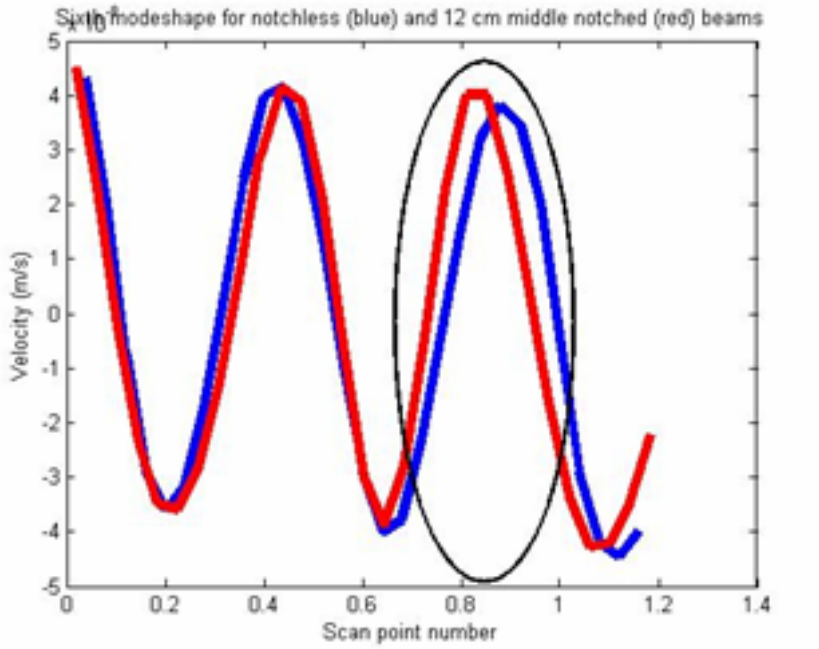

Figure 29. Sixth mode shape for notchless and 12 cm (4.724 in) middle notched beam

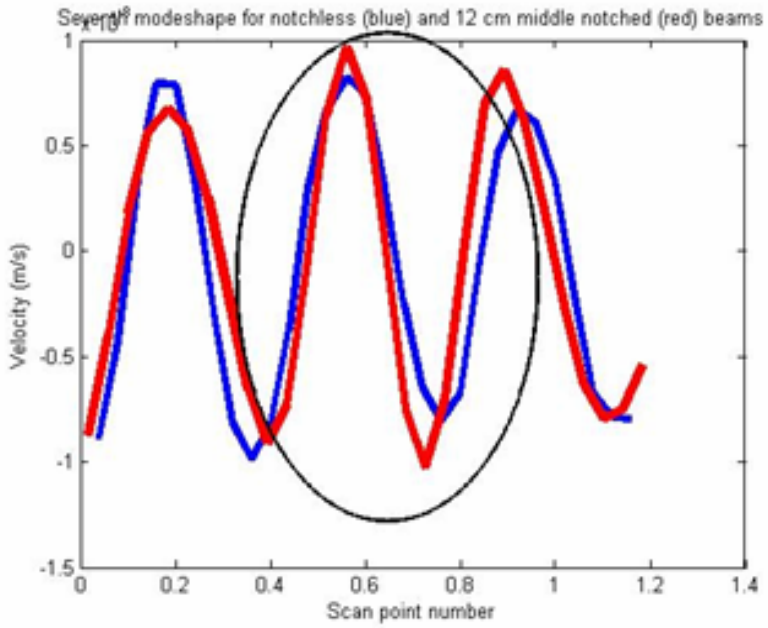

Figure 30. Seventh mode shape for notchless and 12 cm (4.724 in) middle notched beam

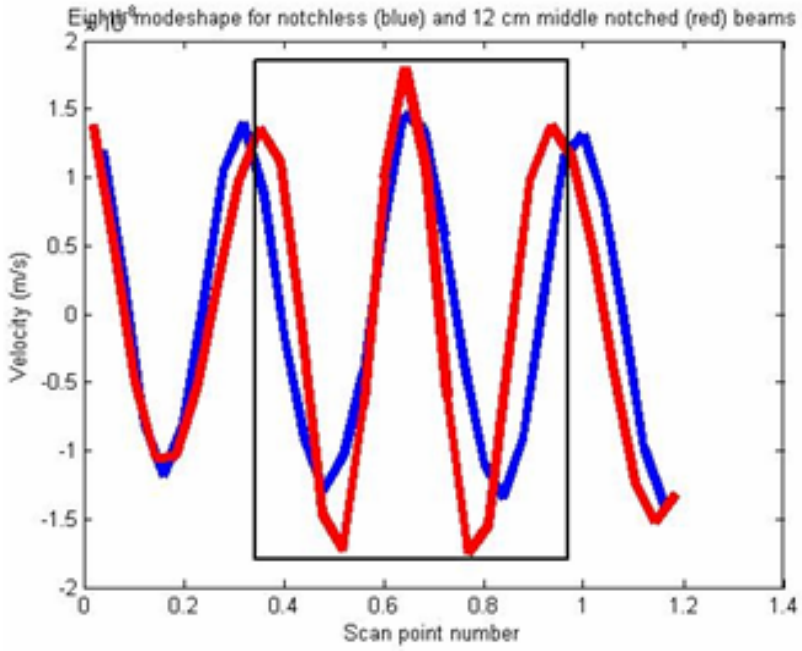

Figure 31. Eighth mode shape for notchless and 12 cm (4.724 in) middle notched beam

The following figure shows the fourth mode for all beams.

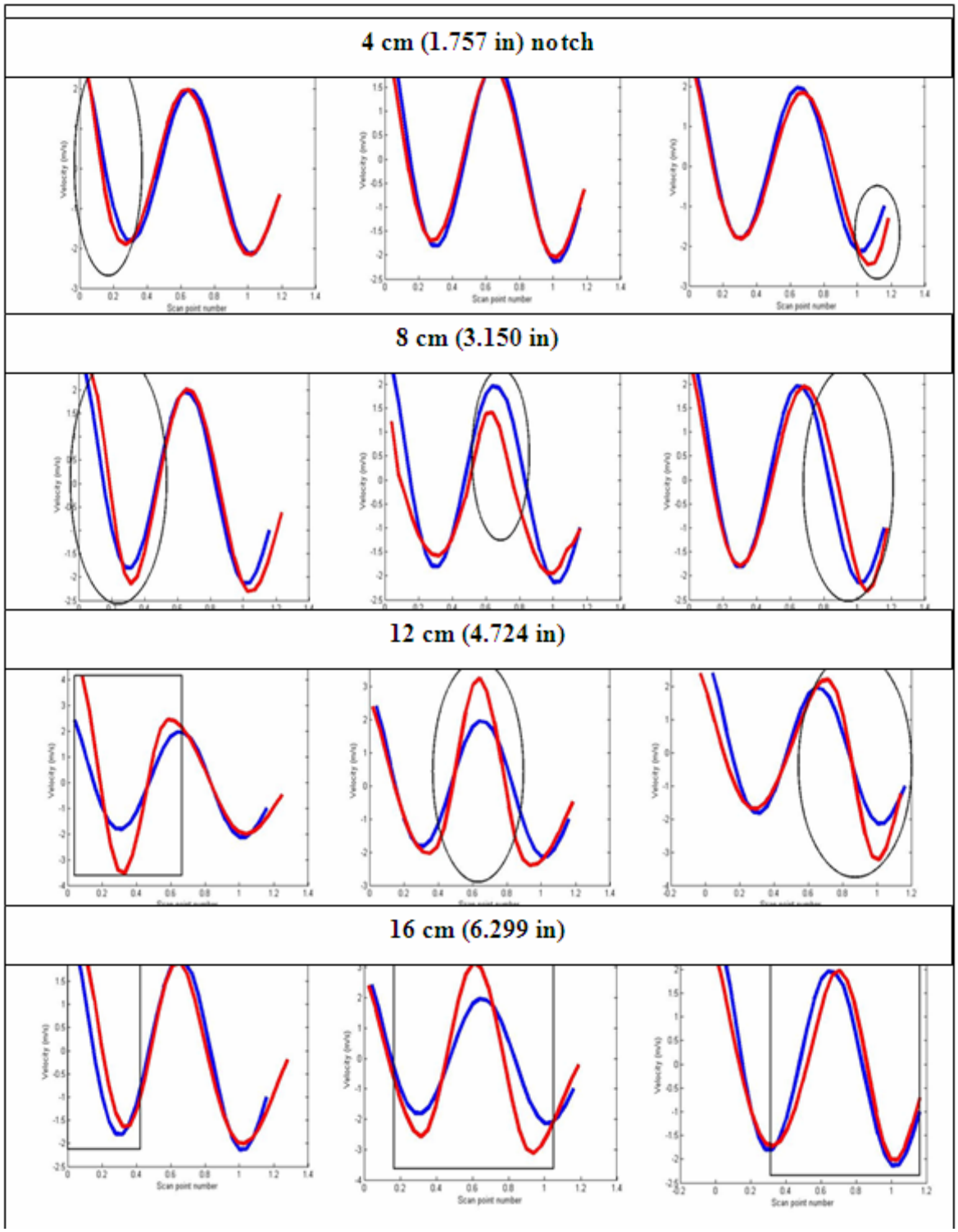

Figure 32. Fourth mode shape for all beams. Note how deviation increases as notch length increases.

The curvature change in the eigenvector is a valuable tool for locating damage. It is safe to assume that if this method works for centered notches, it should also work for eccentric notches because the "thin beam" on one side of the notch is much more likely to act independently of the global beam than in the case of a centered notch. When observing the experimental data (all centrally notched beams) with regards to eigenvectors' curvature change, this technique worked for the fourth, fifth or sixth mode for all beams except the 8 cm middle notched beam. For this case, it was determined that although the damage location can not be pinpointed with the centrally notched beam, it can for the eccentrically notched beam. In fact, the resulting eigenvectors from the eccentrically notched beam experiments are so different that it is very obvious where the onset of damage is, as shown in the following figures. The clamp is on the left of these plots.

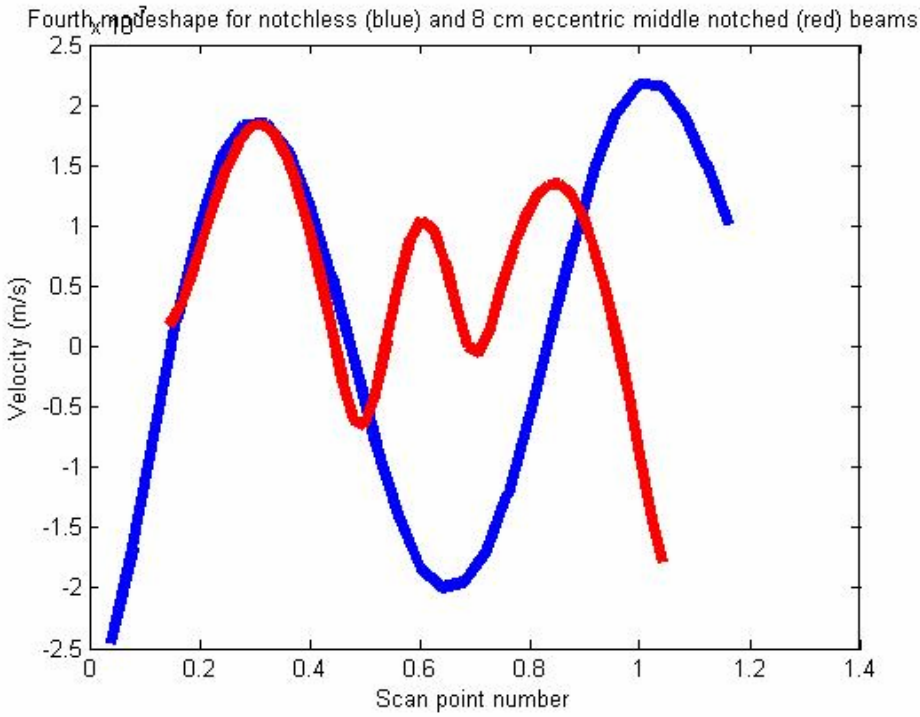

Figure 33. Fourth mode eigenvector for the notchless and eccentrically, 8 cm middle notched beam.

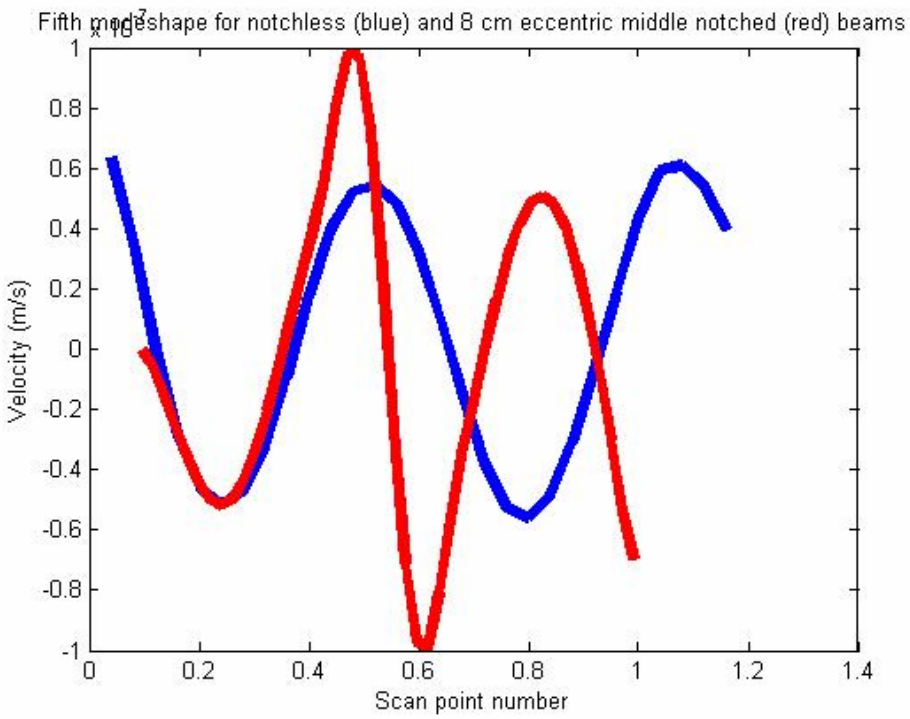

Figure 34. Fifth mode eigenvector for the notchless and eccentrically, 8 cm middle notched beam.

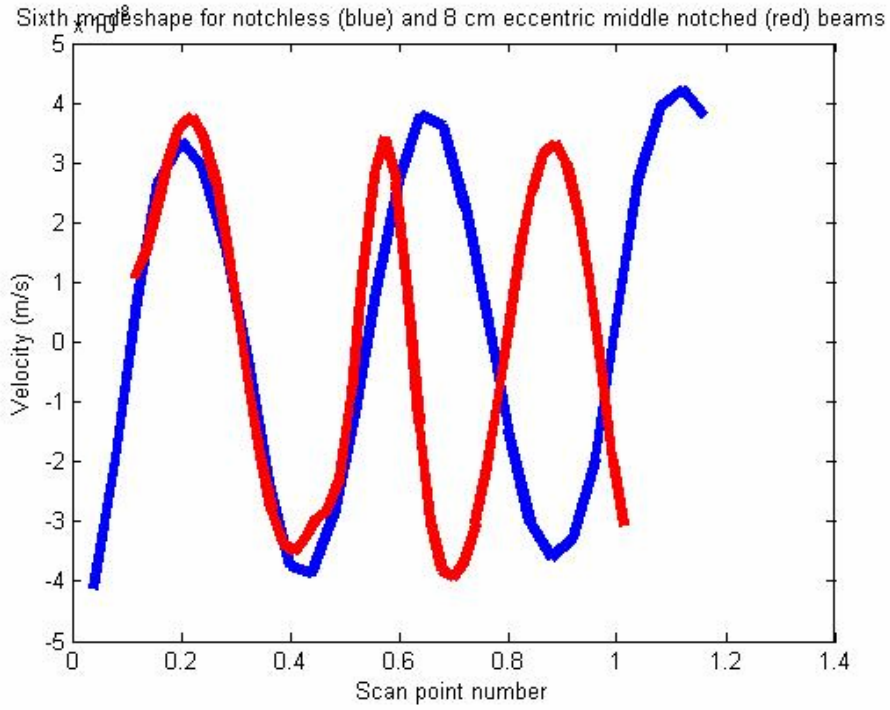

Figure 35. Sixth mode eigenvector for the notchless and eccentrically, 8 cm middle notched beam.

These plots show that in all the data available, the eigenvector curvature comparison method works in all cases of the centered notch save one, and for the only one in which it does not, it clearly shows the presence of damage for an off-centered notch.

2.2.4. Trends.

The experimental natural frequencies found for the beams corresponded well with analytical results, and compared as expected with the results of prior studies. These experimental modal frequencies were plotted and fit with a least-squares curve-fit line to best characterize trends. As is seen in the following graphs, all curves look essentially the same in the first two modes. For the clamped end notches, it is not until mode three that the 52% beam length and 39% beam length notch curves break away from the notchless case. The 26% beam length notch curve deviates from the notchless at the fourth mode, and the 13% beam length notch curve is not easily distinguished from the notchless curve until mode five. For the middle notch curves, results are almost the same save for greater distance between the 13% and 26% notch curves. The 26% notch curve also breaks away from the notchless case at mode three for the middle notch scenario. Overall, the 13% notch curve is very close to the notchless case the whole time while the 26% notch tracks more closely with the 39% and 52% notch curves. For the free end notches, the 39% and 52% notch curves break away from the notchless curve at mode three, the 26% curve breaks away at the fifth mode, and the 13% notch curve tracks closely with the notchless curve the whole time.

From the evident trends, the research shows that for notches 13% of the beam length, it is very difficult to detect damage from frequency shifts alone. In order to detect

damage from frequency changes, one must look to the higher modes. For best results, the data suggests investigating modes five and higher.

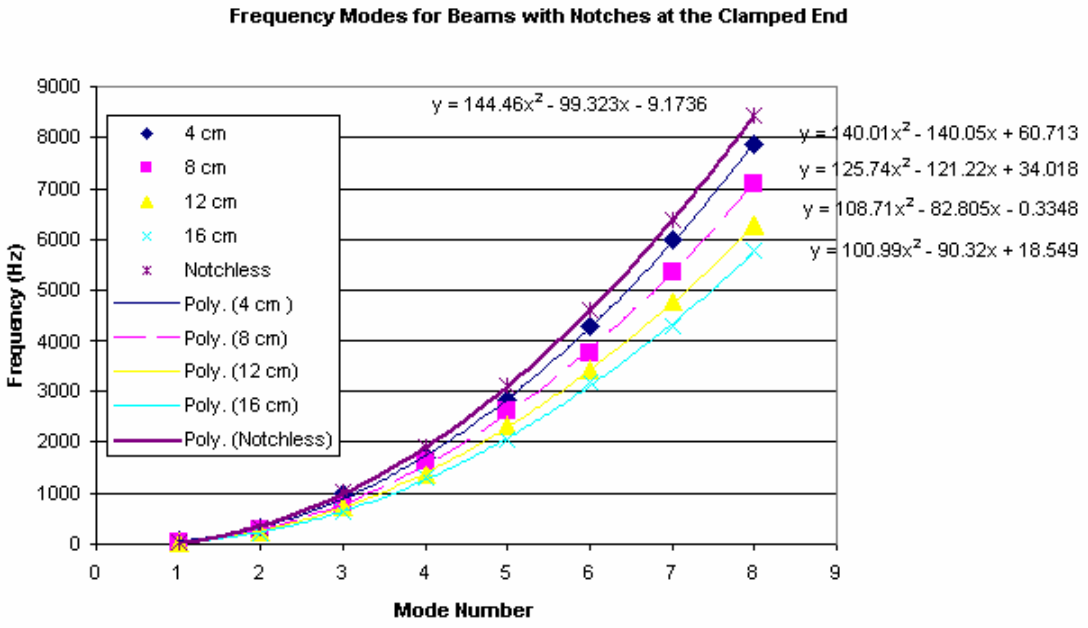

Figure 36. Frequency modes for beams with notches at the clamped end and the notchless beam

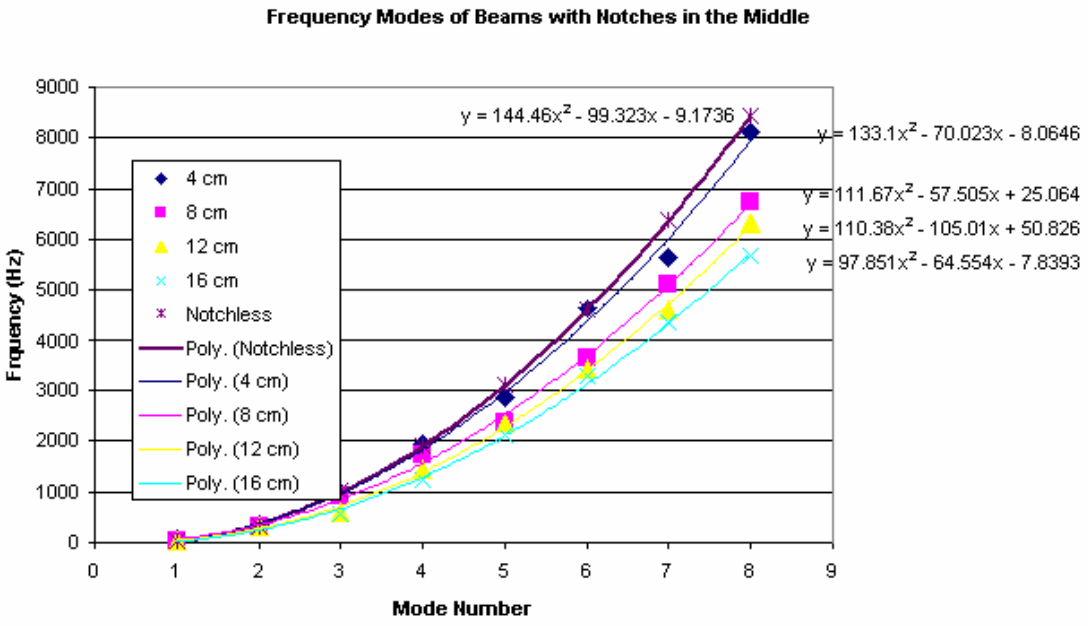

Figure 37. Frequency modes for beams with notches at the middle and the notchless beam

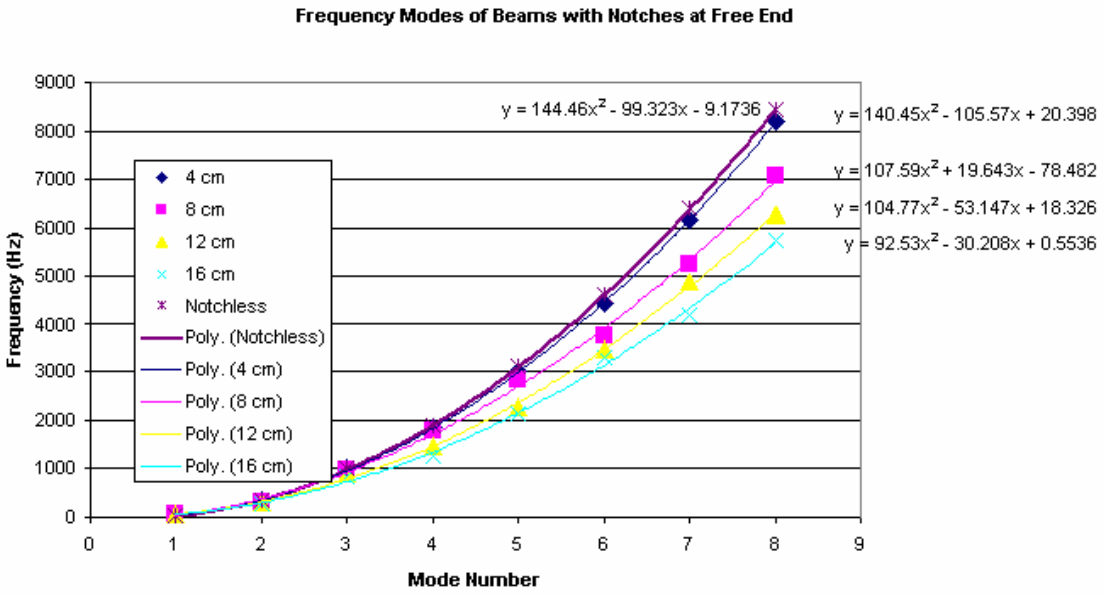

Figure 38. Frequency modes for beams with notches at the free end and notchless beam

Table 6. Modal frequencies obtained from the least-squares curve-fit of the experimental modal frequencies

	CURVE-FIT MODAL FREQUENCIES (Hz) Deviation from notchless beam (%)					
Mode	3	4	5	6	7	8
Notchless	992.9974	1904.894	3105.711	4595.448	6374.105	8441.682
Clamped End						
4 cm (1.575 in)	900.653 -9.30%	1740.673 -8.62%	2860.713 -7.89%	4260.773 -7.28%	5940.853 -6.80%	7900.953 -6.41%
8 cm (3.150 in)	802.018 -19.23%	1560.978 -18.05%	2571.418 -17.20%	3833.338 -16.58%	5346.738 -16.12%	7111.618 -15.76%
12 cm (4.724 in)	729.6402 -26.52%	1407.805 -26.10%	2303.39 -25.83%	3416.395 -25.66%	4746.82 -25.53%	6294.665 -25.43%
16 cm (6.299 in)	656.499 -33.89%	1273.109 -33.17%	2091.699 -32.65%	3112.269 -32.27%	4334.819 -31.99%	5759.349 -31.77%
Middle						
4 cm (1.575 in)	979.7664 -1.33%	1841.443 -3.33%	2969.32 -4.39%	4363.397 -5.05%	6023.674 -5.50%	7950.151 -5.82%
8 cm (3.150 in)	857.579 -13.64%	1581.764 -16.96%	2529.289 -18.56%	3700.154 -19.48%	5094.359 -20.08%	6711.904 -20.49%
12 cm (4.724 in)	729.216 -26.56%	1396.866 -26.67%	2285.276 -26.42%	3394.446 -26.13%	4724.376 -25.88%	6275.066 -25.67%
16 cm (6.299 in)	679.1577 -31.61%	1299.561 -31.78%	2115.666 -31.88%	3127.473 -31.94%	4334.982 -31.99%	5738.193 -32.03%
Free End						
4 cm (1.575 in)	967.738 -2.54%	1845.318 -3.13%	3003.798 -3.28%	4443.178 -3.31%	6163.458 -3.30%	8164.638 -3.28%
8 cm (3.150 in)	948.757 -4.46%	1721.53 -9.63%	2709.483 -12.76%	3912.616 -14.86%	5330.929 -16.37%	6964.422 -17.50%
12 cm (4.724 in)	801.815 -19.25%	1482.058 -22.20%	2371.841 -23.63%	3471.164 -24.47%	4780.027 -25.01%	6298.43 -25.39%
16 cm (6.299 in)	742.6996 -25.21%	1360.202 -28.59%	2162.764 -30.36%	3150.386 -31.45%	4323.068 -32.18%	5680.81 -32.71%

The trends evidenced by the curvature comparisons of the eigenvectors are encouraging. This method of damage detection appears to be more reliable than looking at frequency shift alone, particularly in the detection of smaller notches. The best indication of damage when investigating mode shape comparisons is a change in curvature between the two eigenvectors, indicating the onset of damage. From the data garnered in this experiment, changes in magnitude in the amplitude always indicate a

damage region, while some changes in the x-direction are occasionally due to scaling the mode shape to compare it with another case. One notable caveat is to make sure changes in the amplitude are due to the actual mode shape, not to imperfections in graphically representing a torsion mode. This can always be clarified by watching the animation of the natural frequency with the PSV software.

Additionally, it is found that smaller notches improve the ability to pinpoint the extent of damage. This is very useful for real-world applications, as most users would want to know immediately if his structure has a crack, and would not want to be notified for the first time when the damage is already 12 cm (4.724 in) long! In the present study, it was much easier to detect the extent of damage when the notch was 4 cm (1.575 in) or 8 cm (3.150 in) long. The larger notches tended to influence the whole mode shape more, making it difficult to ascertain the exact location or extent of damage.

From the data presented, the fourth and fifth modes appear to be the best indicators of damage. Usually damage can be detected from mode three or higher, and in many cases damage can even be detected from the second mode shape, but the mode shape that appears to show damage most readily for most cases is the fourth mode shape.

To mathematically verify that mode shape curvature change is an effective tool for locating the presence of damage, the curvature at the known beginning and end of a notch, along a mode shape, must be compared for the notched and notchless cases. The following figures show the fourth mode shape for the notchless and 12 cm (4.724 in) free end notched beam.

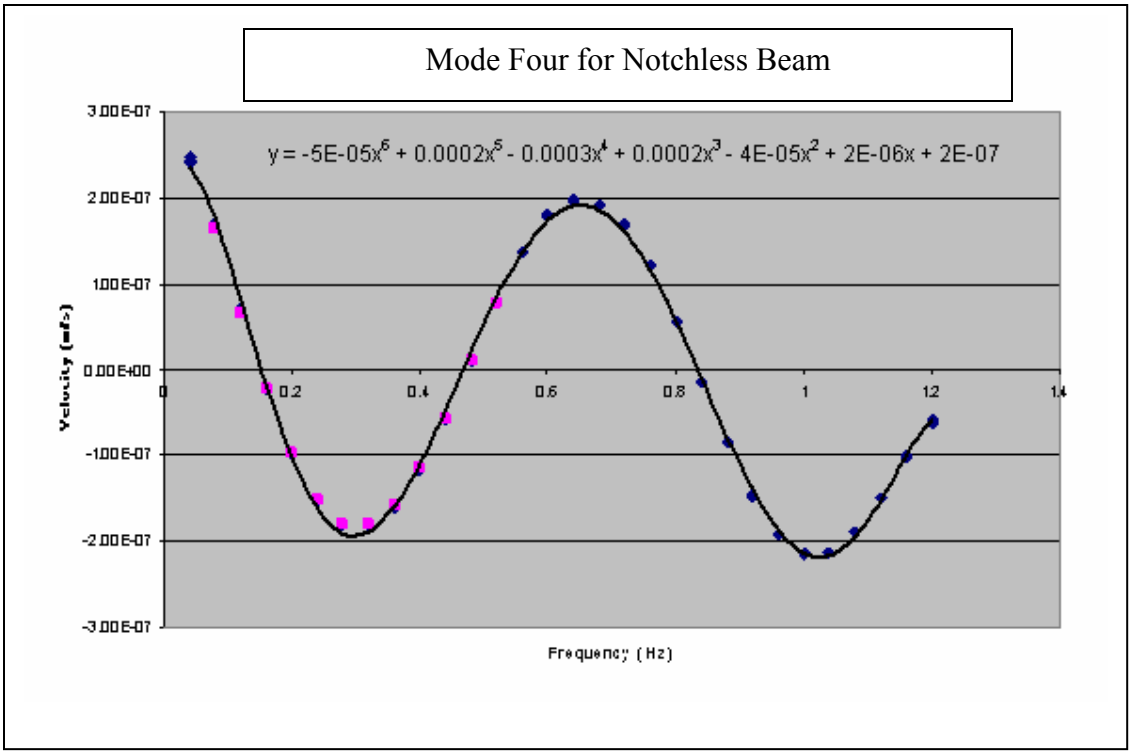

Figure 39. Fourth mode for notchless beam.

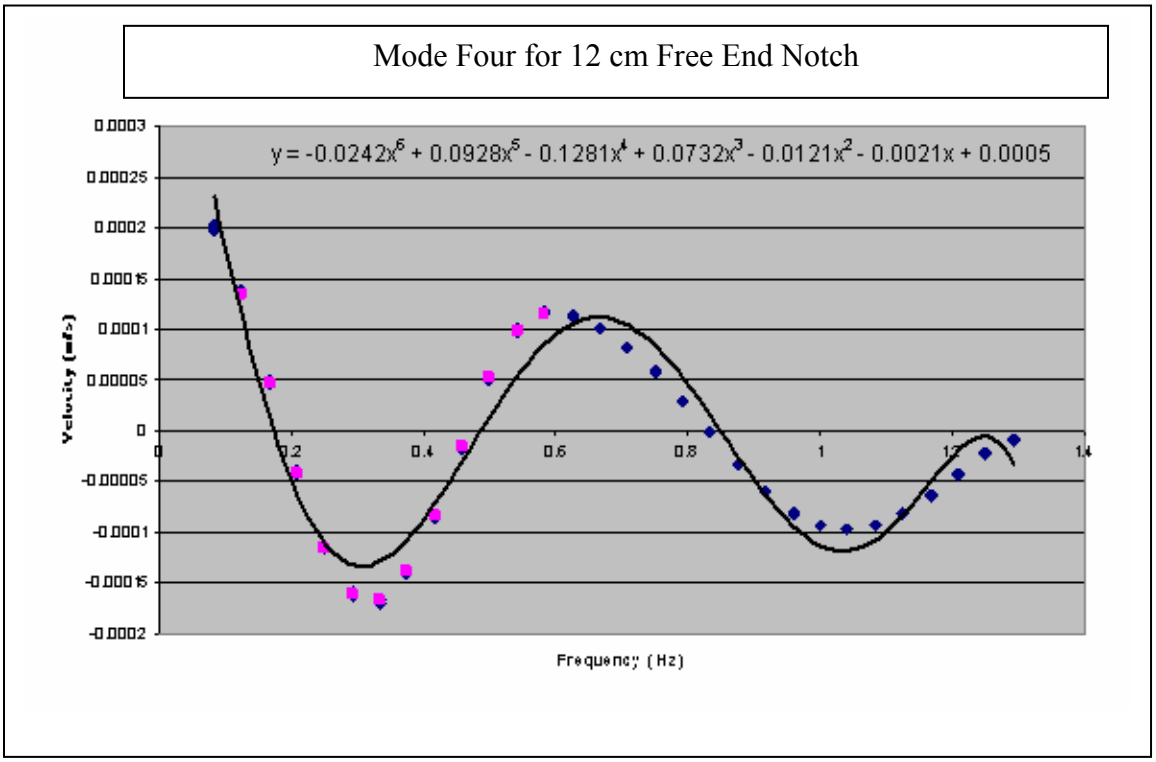

Figure 40. Fourth mode for 12 cm (4.724 in) free end notched beam. Pink area represents notch location.

From the equations shown in Figures 39 and 40, a scientific approach to determining curvature change is easily attained. By finding the second derivative of the curve-fit functions at known notch end points, 0.125 and 0.58333, one can determine if the curvature changes with the presence of a notch. Recall that the numbers on the x-axis represent scan point number, and do not have a unit associated with them.

Table 7. Second derivative for each function

Notchless	
y=	-5E-05x^6 + 0.0002x^5 - 0.0003x^4 + 0.0002x^3 - 4E-05x^2 + 2E-06x + 2E-07
y"=	-3/2000*x^4+0.004*x^3-0.0036*x^2+0.0012*x-1/12500
12 cm (4.724 in) free end notched beam	
y=	-0.0242x^6 + 0.0928x^5 - 0.1281x^4 + 0.0732x^3 - 0.0121x^2 - 0.0021x + 0.0005
y"=	-.726*x^4+1.856*x^3-1.5372*x^2+.4392*x-.0242

Table 8. Curvature values at notch end points

Notchless	y"(0.125)=	0.000021196	y"(0.58333)=	0.000015298
Notched	y"(0.125)=	0.010129004	y"(0.58333)=	-0.00673026

The curvature values differ between the notched and notchless case for both end points. The notched curvature at scan point 0.58333 is negative, while the curvature at this point for the notchless case is positive. This validates the visual inspection hypothesis that curvature change indicates damage presence.

2.3. Finite Element Modeling with ABAQUS

The CDCC code gives a good approximation of modal frequency values, excepting the first mode, but the theory behind it is not correct; rather it is a simple approximation of characterizing decreased stiffness due to the presence of damage. When the need for a better numerical model arose, ABAQUS seemed a good candidate.

2.3.1. Motivation.

While the experimental frequency results compared well with the MATLAB theoretical results, a percent difference of up to 84.4% was exhibited, with consistently high percent differences in the first mode. The experimental data was consistently different from first-mode MATLAB approximations, yielding a need for another analytical model. An ABAQUS model was then designed to provide another set of analytical results, graphically represent bending modes, and convene a study on the likelihood of contact between sides of the notch.

2.3.2. ABAQUS Specifications.

Two ABAQUS finite element models were designed for use in this study. ABAQUS is a powerful finite element analysis tool which allows a much more refined model than the CDCC code and allows the user to view expected beam and notch dynamic behavior. The two models used in this study were the plane strain model and the three-dimensional restricted model, both developed by Aaron Chmiel (Chmiel, 2005:6). In both cases, cantilevered beams with centered notches, eccentric notches and centered notches on a thinner depth were all modeled to compare with current and previous experimental results. Both cases yielded very similar results, never differing by more than 2%. A summary of the theory behind each method is outlined in Appendix B.

For the plane strain model in ABAQUS, there were no elements in the width direction and elements were approximately 0.02 inches in depth. Along the length of the beam there were different dimensions for the elements; elements in the notched regions were 0.04 inches long, while the remaining elements were 0.1 inches long. In some cases even longer elements were used so as to not exceed available storage space. For the 3-D

restrained model, the dimensions were the same as in the two-dimensional model, but with a width of 0.1 inches.

Because the results of the two models are very similar, and the plane strain model is slightly faster computationally, plane strain results are used for comparison with the experimental and CDCC results. To see the number of elements used for each analysis, see Table 9.

Table 9. Number of elements used in the ABAQUS models

		4cm	8cm	12cm	16cm
3D Restrained	clamp	25155	29055	32610	36165
	middle	25155	28875	32430	36345
	free	25515	29235	32790	36525
Plane Strain	clamp	2609	2817	2786	2754
	middle	2837	2829	2786	2754
	free	2861	2841	2798	2778

2.3.3. ABAQUS Results.

When averaged across all modes, the ABAQUS percent differences from the experimental modal frequencies range from 1.87% for the 16 cm (6.299 in) clamped end notch to 6.12% for the 8 cm (3.150 in) middle notch (see Table 10). Also, the percent difference in the first mode is drastically reduced from the CDCC results in the first mode. Percent difference between experimental data and the ABAQUS prediction in mode one ranges from 5.20% for the 16 cm (6.299 in) middle notch to 7.70% for the 4 cm (1.575 in) free end notch.

The ABAQUS models show the global mode shapes as well as the movement of the individual small beams on either side of the notch. For a complete overview of the ABAQUS models, please refer to Appendix B. The images in Figures 41 through 72

depict the first eight bending modes for the 4 cm (1.575 in) middle notched beam and the 16 cm (6.299 in) middle notched beam as modeled by ABAQUS.

Table 10. Experimental and ABAQUS-predicted modal frequencies

	EXPERIMENTAL MODAL FREQUENCIES (Hz) ABAQUS-predicted modal frequencies (Hz) Percent difference (%)							
Mode	1	2	3	4	5	6	7	8
Notchless	52.5 56.302 6.75%	333.75 352.02 5.19%	1020 983.53 -3.71%	1893.75 1922.1 1.47%	3106.25 3166.1 1.89%	4586.25 4707.3 2.57%	6401.25 6535 2.05%	8426.43 8635.9 2.43%
Clamped End								
4 cm (1.575 in)	53.125 56.792 6.46%	326.563 344.73 5.27%	973.438 916.36 -6.23%	1704.69 1714.5 0.57%	2815.63 2804 -0.41%	4254.69 4232.9 -0.51%	6006.25 5972.4 -0.57%	7871.88 7937.2 0.82%
8 cm (3.150 in)	52.5 55.767 5.86%	285 291.88 2.36%	741.25 777.74 4.69%	1632.5 1619.3 -0.82%	2610 2628.7 0.71%	3747.5 3746.2 -0.03%	5381.25 5355.7 -0.48%	7110 7072.4 -0.53%
12 cm (4.724 in)	50 53.309 6.21%	237.5 241.69 1.73%	732.5 766.66 4.46%	1386.25 1398.7 0.89%	2322.5 2353.5 1.32%	3418.75 3444.2 0.74%	4775 4803.2 0.59%	6271.25 6358.6 1.37%
16 cm (6.299 in)	46.25 49.586 6.73%	217.5 219.35 0.84%	646.25 678.48 4.75%	1292.5 1299 0.50%	2062.5 2073.4 0.53%	3193.75 3208.6 0.46%	4260 4294.8 0.81%	5780 5797.9 0.31%
Middle								
4 cm (1.575 in)	53.125 56.94 6.70%	342.188 358.35 4.51%	1000 952.39 -5.00%	1934.38 1943.2 0.45%	2851.56 2846.9 -0.16%	4628.13 4661.6 0.72%	5640.63 5645.1 0.08%	8117.19 8206.4 1.09%
8 cm (3.150 in)	52.0313 56.285 7.56%	332.5 358.25 7.19%	910.625 792.1 -15.0%	1743.75 1809.6 3.64%	2356.25 2441.1 3.48%	3650 3776.9 3.36%	5135 5421.5 5.28%	6730 6972.6 3.48%
12 cm (4.724 in)	51.25 54.567 6.08%	335 350.26 4.36%	610 657.16 7.18%	1441.25 1454.3 0.90%	2357.5 2407.6 2.08%	3417.5 3490 2.08%	4598.75 4624.1 0.55%	6332.5 6450.7 1.83%
16 cm (6.299 in)	49 51.686 5.20%	319 327.65 2.64%	558 596.75 6.49%	1228 1224.2 -0.31%	2123 2121.5 -0.07%	3284 3297.4 0.41%	4340 4389 1.12%	5674 5717 0.75%
Free End								
4 cm (1.575 in)	53.125 57.558 7.70%	339.063 357.45 5.14%	1017.19 983.64 -3.41%	1859.38 1878.1 1.00%	2995.31 3035.5 1.32%	4414.06 4493.7 1.77%	6150 6271.5 1.94%	8185.94 8309.7 1.49%
8 cm (3.150 in)	53.75 57.821 7.04%	330 344.24 4.14%	968.75 898.09 -7.87%	1781.25 1778.2 -0.17%	2852.5 2846.8 -0.20%	3737.5 3757.9 0.54%	5245 5290.2 0.85%	7058.75 7081 0.31%
12 cm (4.724 in)	53.75 57.351 6.28%	300 315.45 4.90%	921.25 876.11 -5.15%	1475 1492.3 1.16%	2260 2321 2.63%	3461.25 3519.3 1.65%	4866.25 4897.2 0.63%	6268.75 6381 1.76%
16 cm (6.299 in)	52 55.459 6.24%	284 297.38 4.50%	856 776.05 -10.3%	1267 1272.7 0.45%	2132 2158.8 1.24%	3291 3332.3 1.24%	4174 4241.4 1.59%	5737 5776.2 0.68%

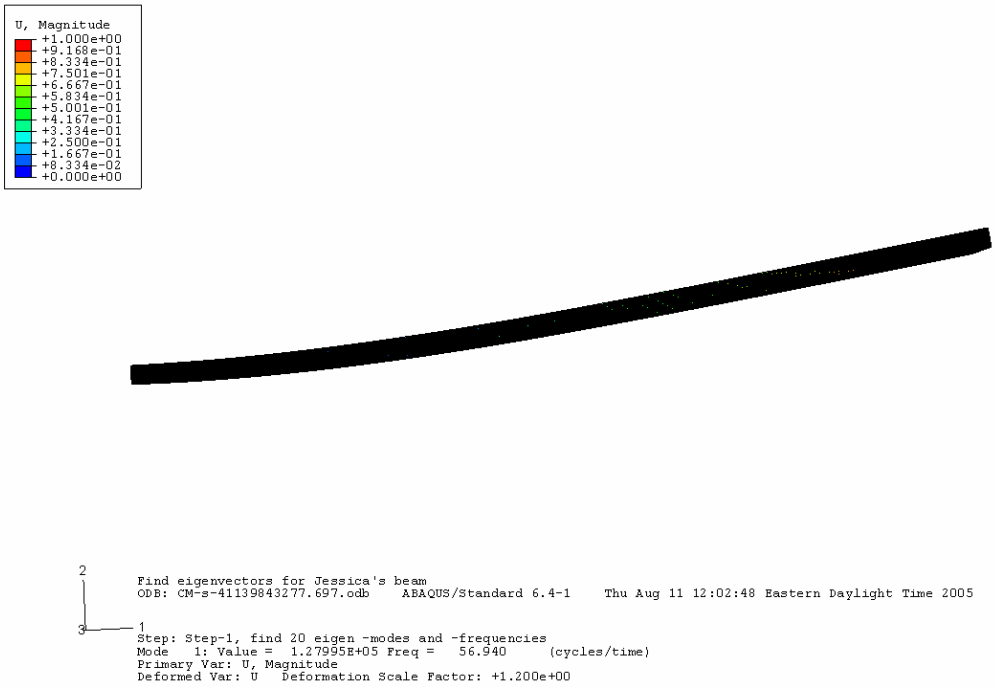

Figure 41. First mode, 4 cm (1.575 in) middle notch

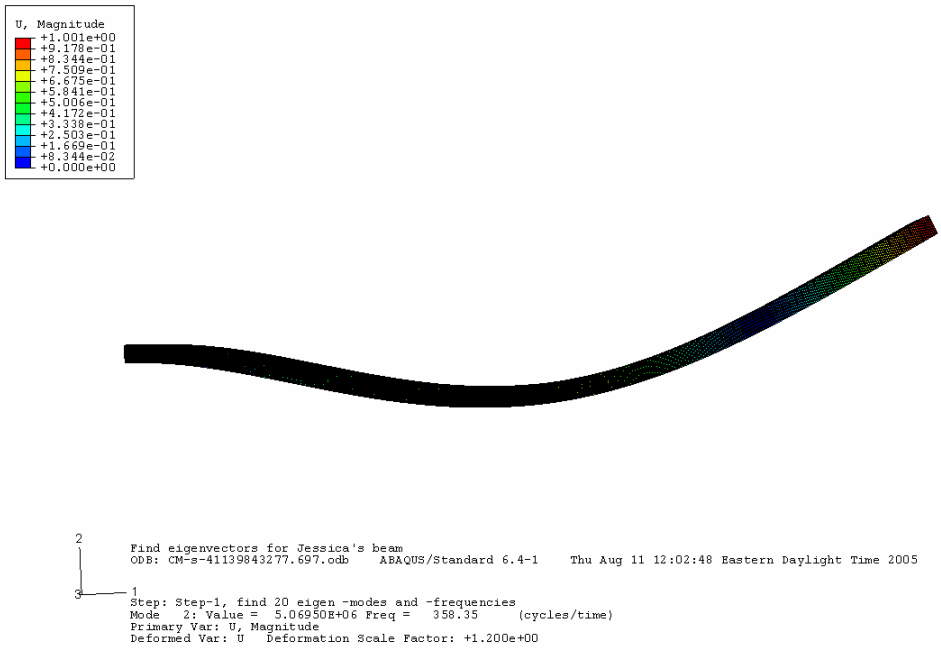

Figure 42. Second mode, 4 cm (1.575 in) middle notch

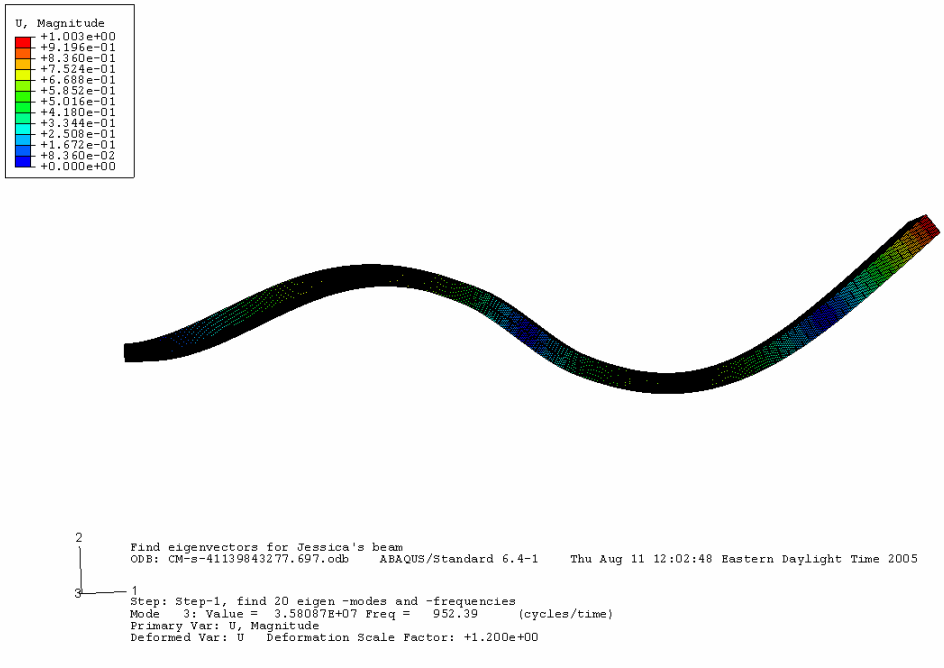

Figure 43. Third mode, 4 cm (1.575 in) middle notch

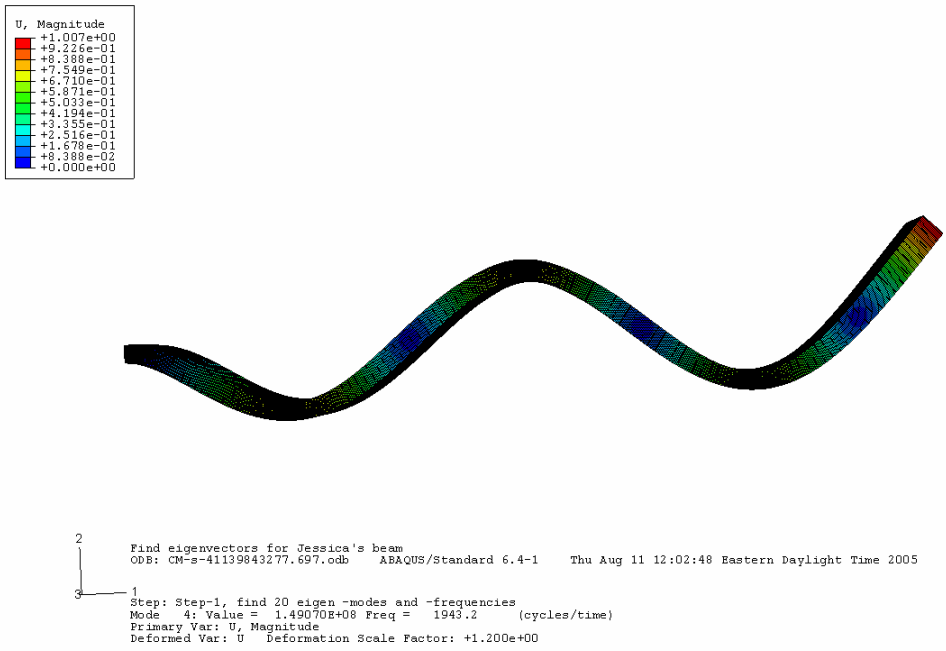

Figure 44. Fourth mode, 4 cm (1.575 in) middle notch

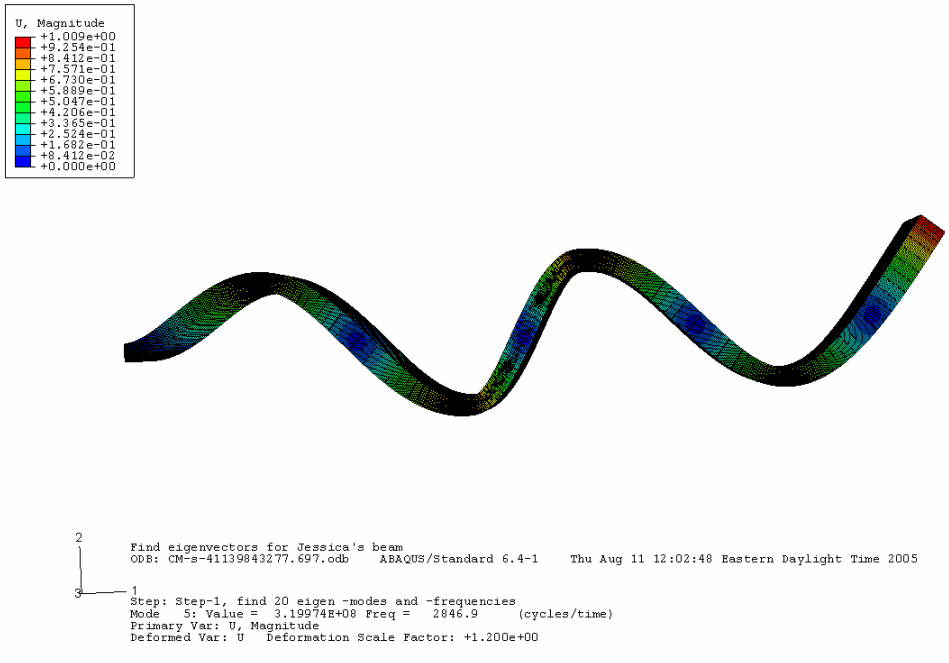

Figure 45. Fifth mode, 4 cm (1.575 in) middle notch

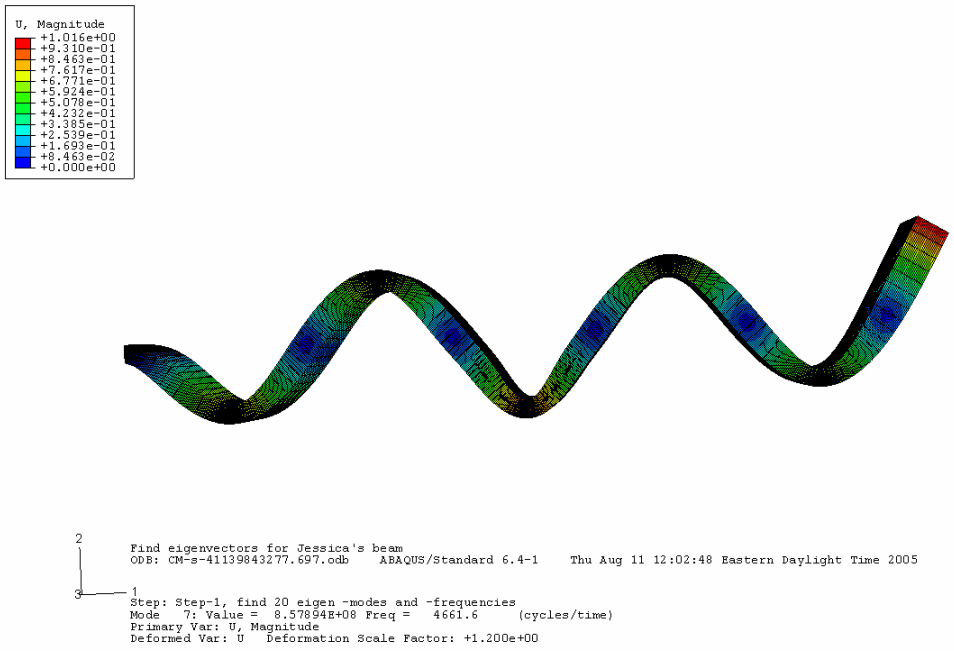

Figure 46. Sixth mode, 4 cm (1.575 in) middle notch

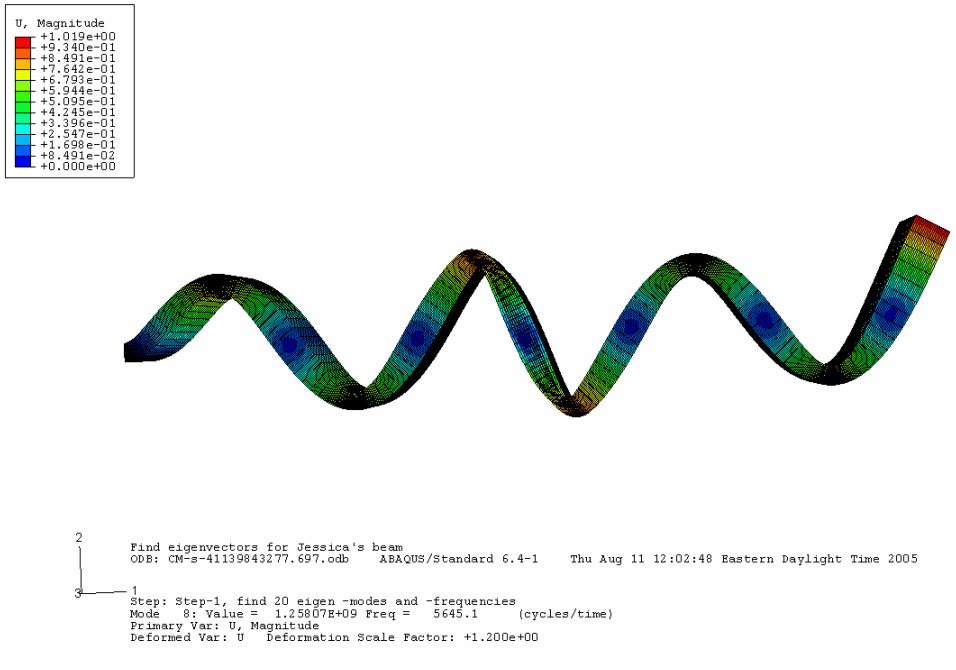

Figure 47. Seventh mode, 4 cm (1.575 in) middle notch

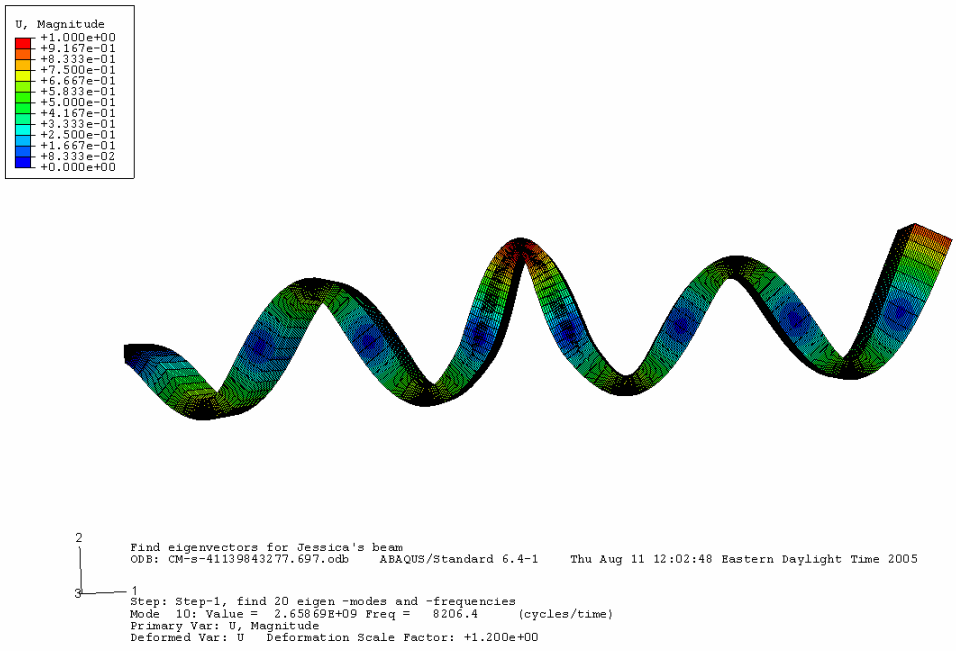

Figure 48. Eighth mode, 4 cm (1.575 in) middle notch

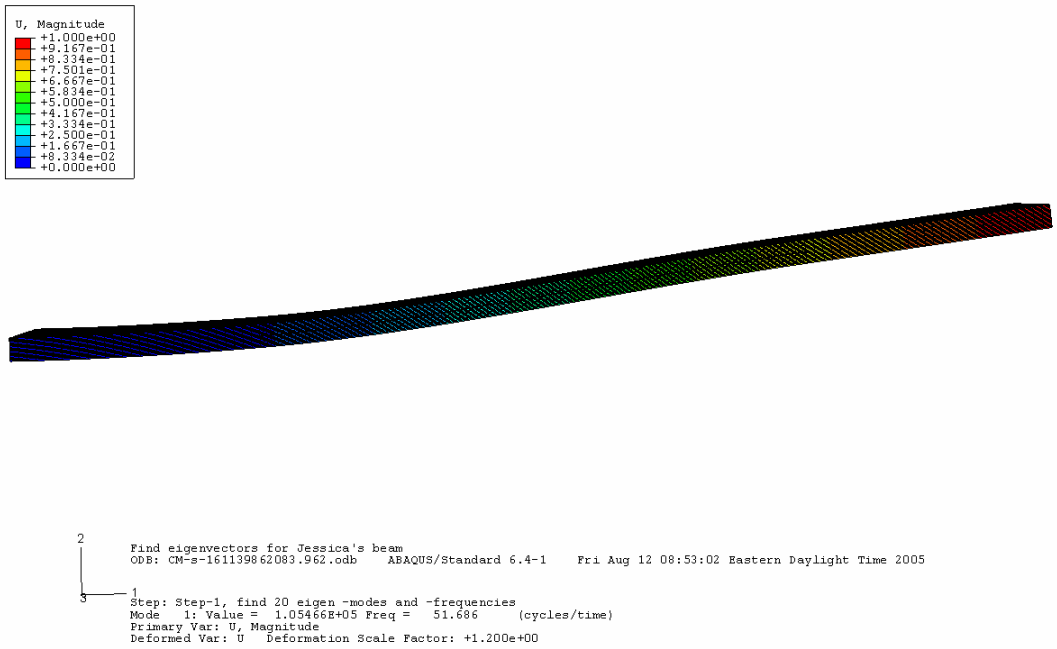

Figure 49. First mode, 16 cm (6.299 in) middle notch

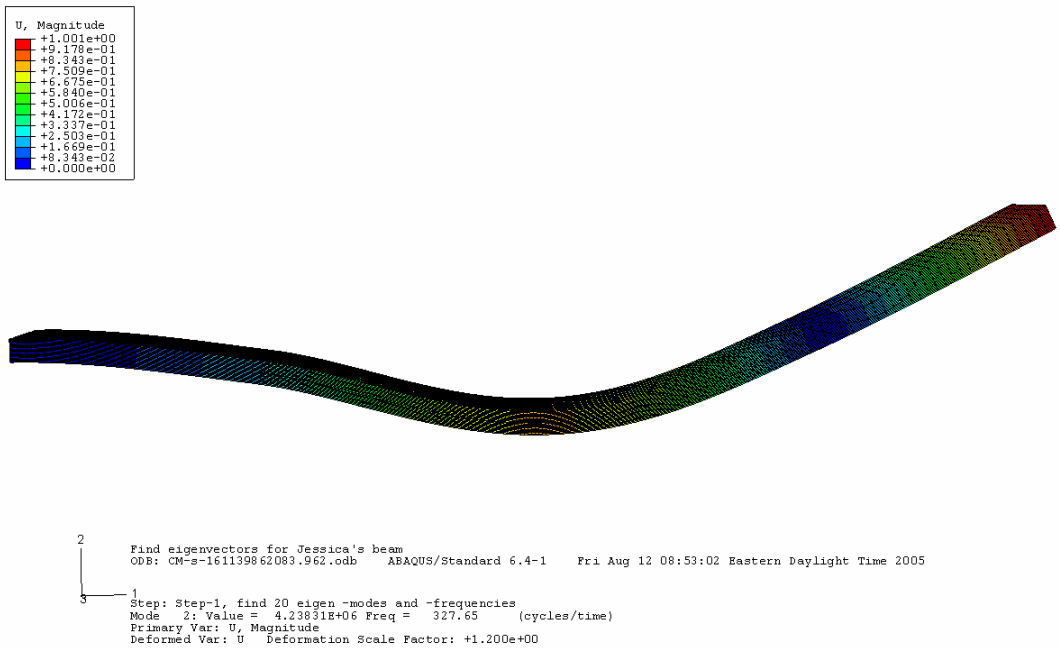

Figure 50. Second mode, 16 cm (6.299 in) middle notch

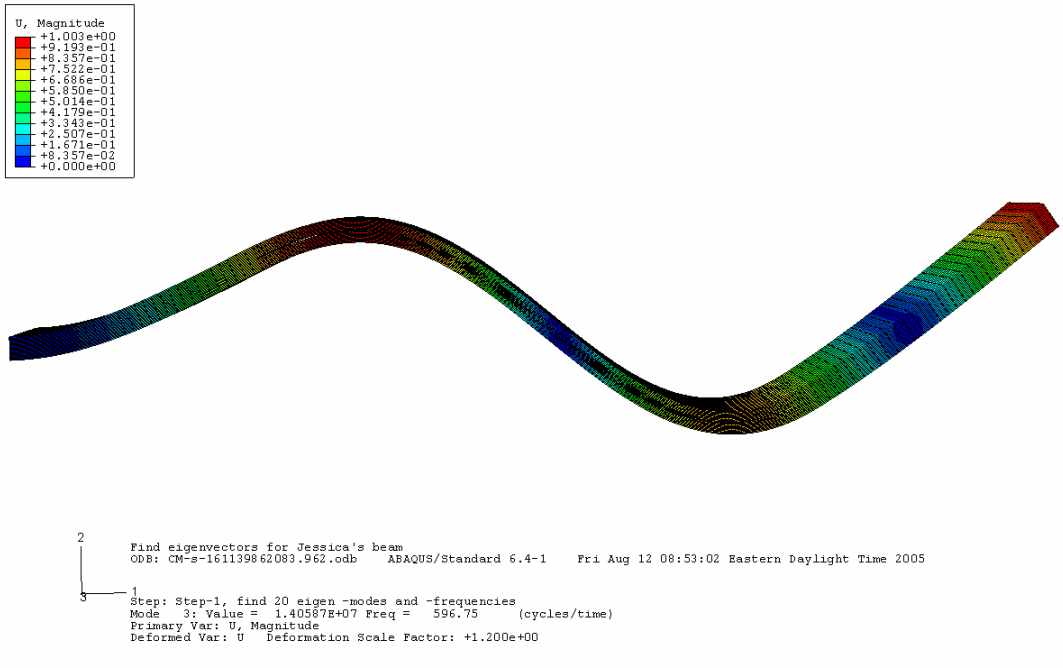

Figure 51. Third mode, 16 cm (6.299 in) middle notch

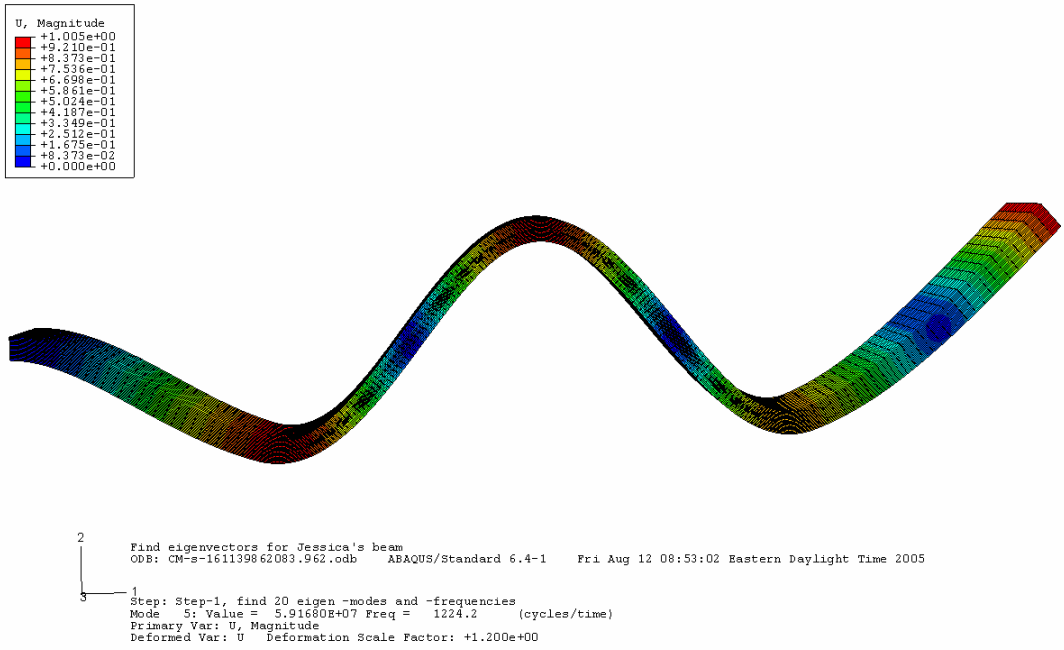

Figure 52. Fourth mode, 16 cm (6.299 in) middle notch

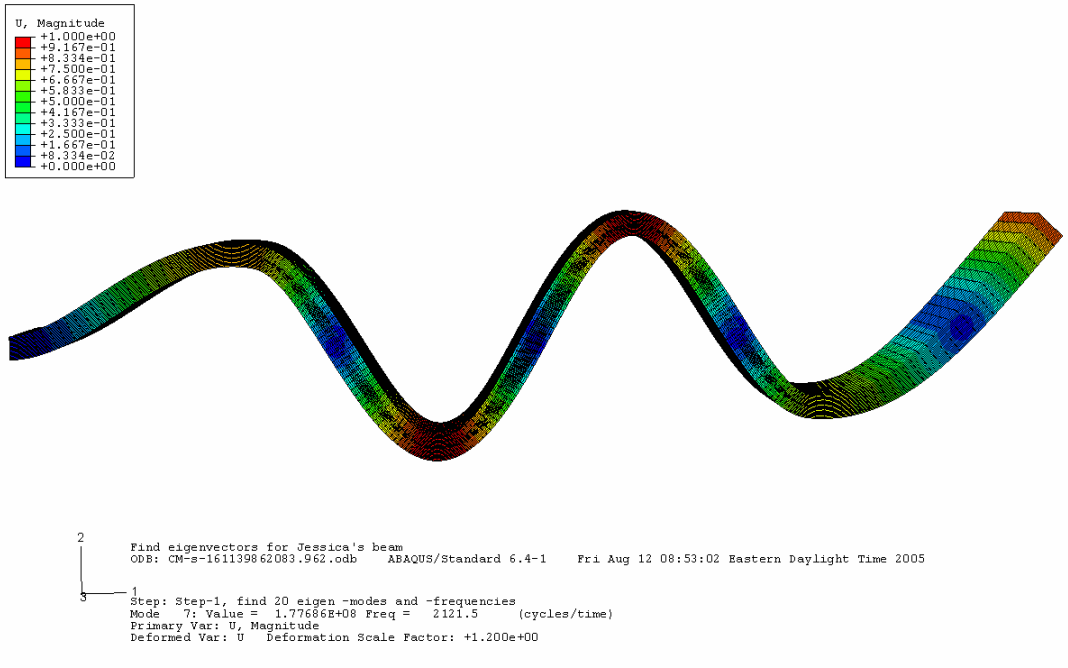

Figure 53. Fifth mode, 16 cm (6.299 in) middle notch

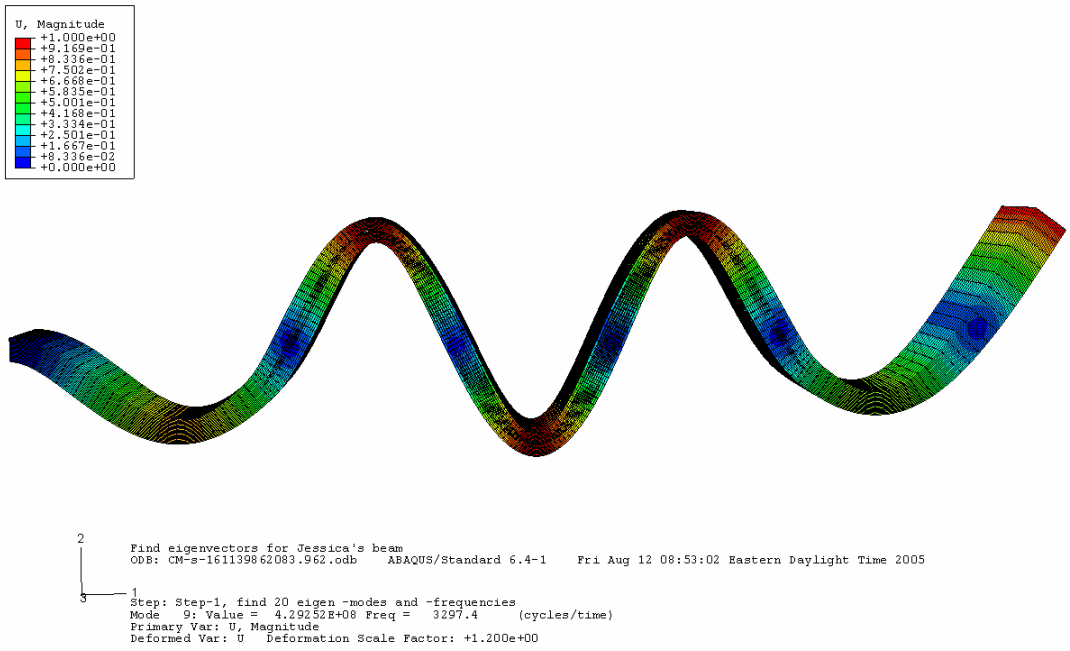

Figure 54. Sixth mode, 16 cm (6.299 in) middle notch

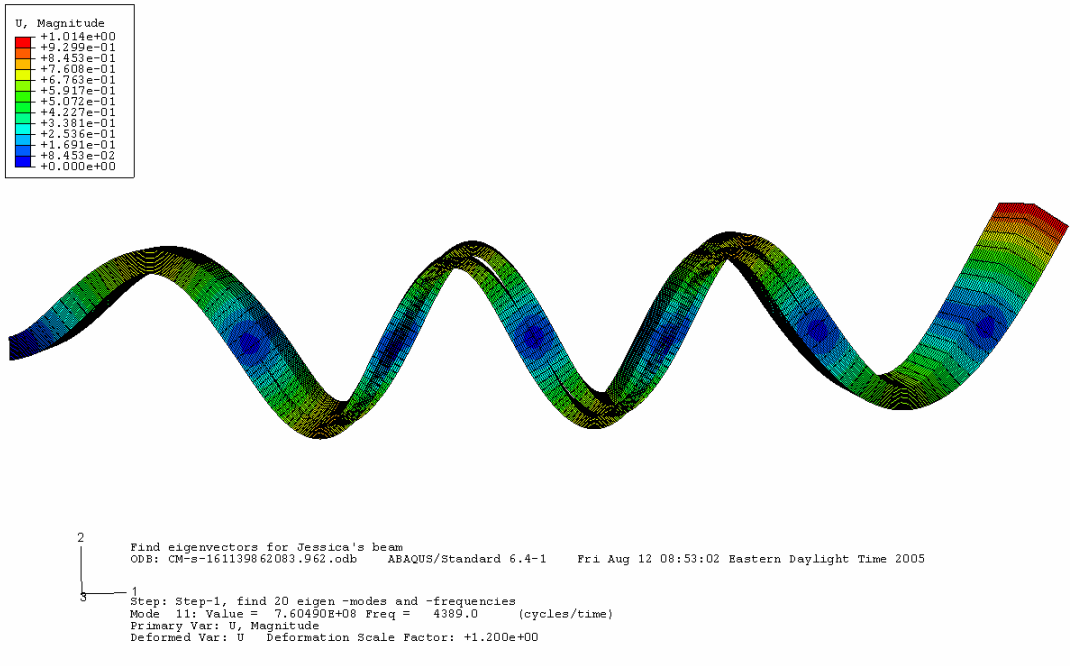

Figure 55. Seventh mode, 16 cm (6.299 in) middle notch

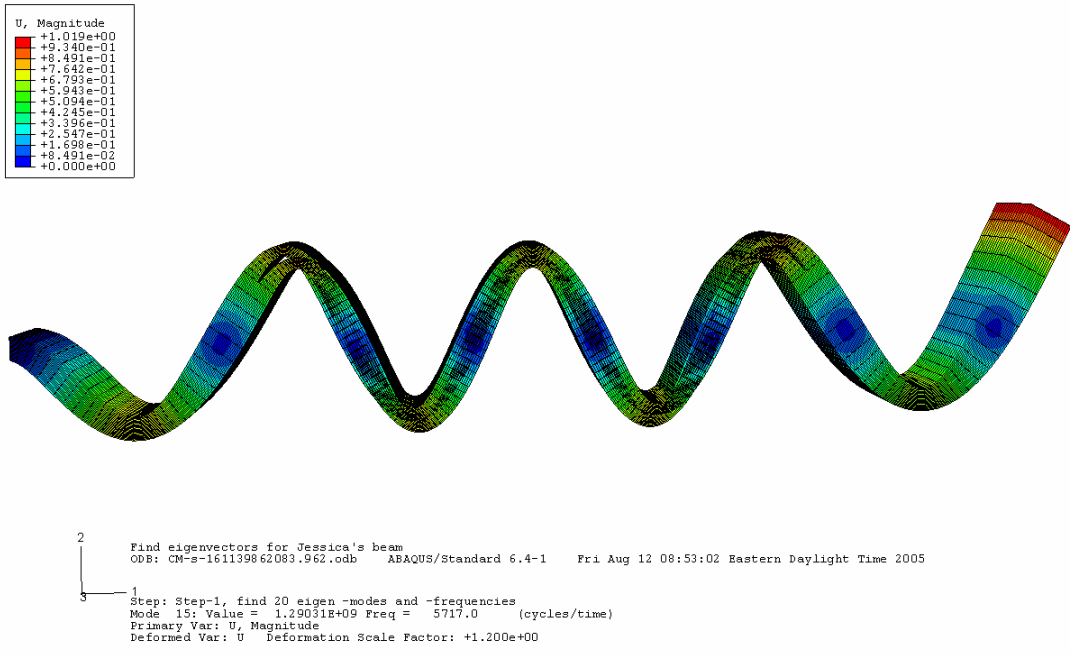

Figure 56. Eighth mode, 16 cm (6.299 in) middle notch

Further analysis with ABAQUS revealed the likelihood of contact between the sides of the notch, which would be a possible cause of interference. This investigation started with the examination of small beam frequencies in the CDCC code, where the part of the beam on the either side of the centered or eccentric notch was considered a small beam. Using the boundary conditions of clamped-clamped, clamped-simple and simple-simple, the first eight natural frequencies of these small beams were generated. When it appeared that one of these small beam natural frequencies was close to a natural frequency of the global structure, interference was a possibility. ABAQUS was used to verify this hypothesis, and was very useful in presenting modes in which the small beams had mode shapes independent of those of the global structure. See Figure 57 for an example of this.

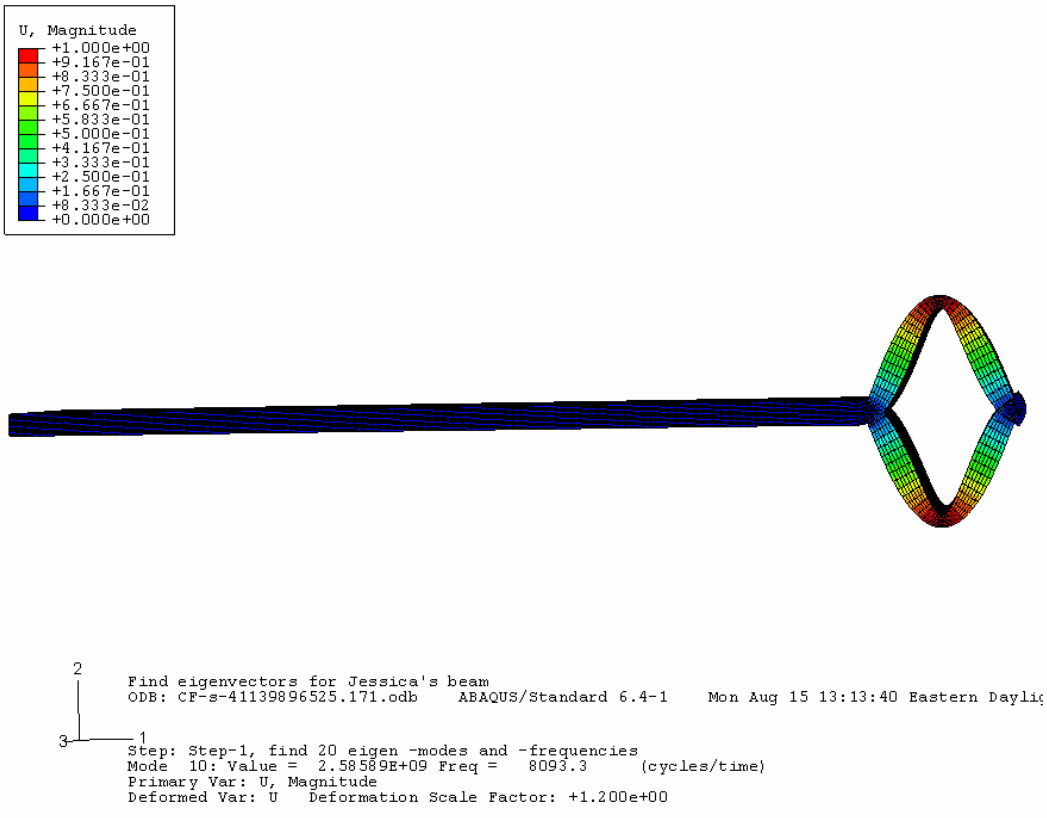

Figure 57. Example of small beam independent natural frequency.

Figure 57 illustrates the behavior of small beams independent of global structural behavior. This figure portrays a 4 cm (1.575 in) free end centered notch. Note that for this particular case, the frequency is not close to a natural frequency of the large beam, so interference would not be a problem at a specific mode of the whole beam.

Through the ABAQUS models, it was found that the thinner small beams above eccentric notches tend to move independently of the rest of the beam, while the thicker small beam moves with the global beam. In the cases of centered notches, a greater amount of bending was seen in the region of the notch, but because of mass symmetry about the notch, "the two sides of the beam move in unison, rather than separating, as they do with the eccentric notch" (Chmiel, 2005:8). See Figure 58 to illustrate this point.

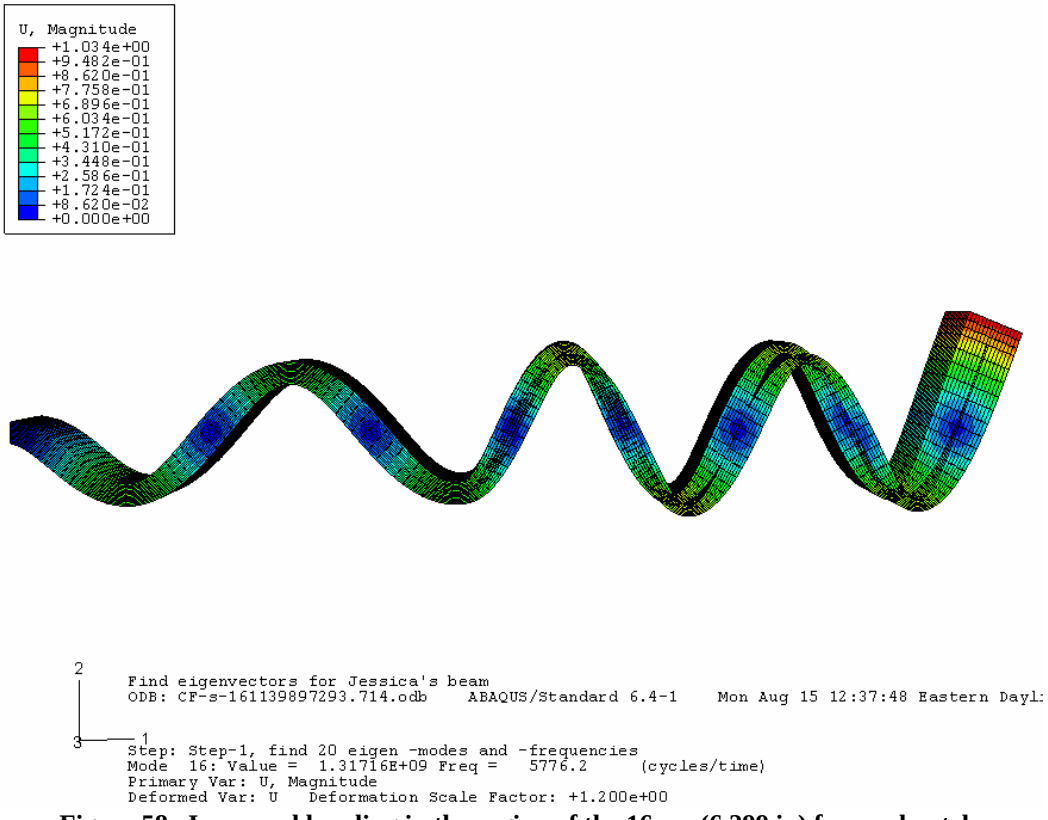

Figure 58. Increased bending in the region of the 16 cm (6.299 in) free end notch

Because obvious differences in small beam and global mode shapes exist, the behavior of these small beams raised the question of interference between the sides of the notch.

The ABAQUS model of the eccentrically notched beams were examined by applying a forcing function to the end of each beam of the form

$$F = A\sin(\omega t) \tag{10}$$

where A is the amplitude and ω is frequency. The eccentrically notched beams were used because the thinner section on one side of the notch would be more likely to vibrate on its own independent of the global structure. Amplitudes of 10, 20, 30, 40, 50 and 100 were used with a frequency 95% of a given natural frequency. This reduction of frequency was implemented to prevent infinite resonance in the model. The analysis was run by Aaron Chmiel with ABAQUS/Standard for 0.1 seconds with output of the displacements written each 0.01 second.

The results showed that contact depended on both length and location of a given notch. Larger notches require much less amplitude to produce contact than do shorter notches. Furthermore, free end notches require a lower amplitude to create contact than notches located at the clamped end. It was found that contact could not be produced with an amplitude up to 100 for a 4 cm (1.575 in) notch. For a 12 cm (4.724 in) notch located at the clamped end, contact occurred at amplitudes of 50 or higher. For a 12 cm (4.724 in) notch at the free end, contact occurred when the amplitude was 30 or higher. For the 16 cm (6.299 in) middle notch, contact occurred at amplitudes of 20 and higher, while an amplitude of only 10 was required to produce contact in the free end 16 cm (6.299 in) notched beam.

2.4. Damping Features

The damping of each beam is determined and characterized experimentally according to the ASTM Standard Test Method for Measuring Vibration-Damping Properties of Materials. This method utilizes the half-power bandwidth method (ASTM E 756-05, 2005:6). The damping ratio is converted to a quality factor, Q, through the following relationship:

$$Q = \frac{1}{2\zeta} \tag{11}$$

where ζ is the damping ratio. For a discussion of theory behind damping analysis, please refer to Appendix C.

2.4.1. Damping Results.

The Q values for the notchless beam and all notched beams are compiled in the following table. The system Q values are determined, not the material Q values. This includes the beam, the clamp, the test stand, magnetic base, and table. The values in Table 11 are normalized by finding the difference from the notchless case. This hopefully offsets any possible clamp inconsistencies that could hinder damping analysis, in an attempt to isolate the Q value of the beam.

Table 11. Q values for uncorroded beams

Q VALUES FOR UNCORRODED BEAMS Difference from notchless case								
Mode	1	2	3	4	5	6	7	8
Notchless	54.124	166.9	145.714	236.75	517.667	229.3	320.05	561.8
Clamped End								
4 cm (1.575 in)	35.1854 18.94	96.0588 70.84	66.6712 79.04	77.5 159.25	156.444 361.22	851 -621.7	429 -108.95	291.556 270.24
8 cm (3.150 in)	57.0652 -2.94	142.5 24.4	35.3571 110.36	408.25 -171.5	153.529 364.14	468.5 -239.2	316.529 3.52	284.4 277.4
12 cm (4.724 in)	56.1798 -2.06	215.909 -49.01	53.8603 91.85	154 82.75	464.6 53.07	427.375 -198.08	318.333 1.72	82.5132 -85.31%
16 cm (6.299 in)	38.2231 17.90	217.5 -50.6	88.5343 57.18	323.25 -86.5	515.75 1.92	245.692 -16.39	387.273 -67.22	231.2 330.6
Middle								
4 cm (1.575 in)	50.1226 4.00	95.0556 71.84	117.647 28.07	214.889 21.86	77.0811 440.59	149.290 80.01	245.261 74.79	197.976 363.82
8 cm (3.150 in)	273.842 -219.72	277.083 -110.18	39.7642 105.95	134.154 102.60	181.231 336.44	304.167 -74.87	38.0370 282.01	258.846 302.95
12 cm (4.724 in)	42.7083 11.42	119.643 47.26	83.5616 62.15	240.167 -3.42	235.8 281.87	341.8 -112.5	170.333 149.72	140.733 421.07
16 cm (6.299 in)	44.9541 9.17	132.917 33.98	80.8696 64.84	245.6 -8.85	424.6 93.07	328.4 -99.1	361.667 -41.62	943.333 -381.53
Free End								
4 cm (1.575 in)	47.0177 7.11	89.2368 77.66	127.125 18.59	169 67.75	83.1944 434.47	259.647 -30.35	212.069 107.98	372.091 189.71
8 cm (3.150 in)	42.3228 11.80	122.222 44.68	61.7070 84.01	57.4516 179.30	114.12 403.55	339.818 -110.52	149.857 170.19	371.526 190.27
12 cm (4.724 in)	41.9922 12.13	157.895 9.01	29.1551 116.56	295 -58.25	226 291.67	346.1 -116.99	152.063 167.99	164.974 396.83
16 cm (6.299 in)	63.4146 -9.29	118.333 48.57	73.1624 72.55	181 55.75	426.4 91.27	274.25 -44.95	347.833 -27.78	150.974 410.83

2.4.2. Trends.

According to ASTM standard E756-05, aluminum has a damping ratio that is frequency dependent. Therefore, it is expected that the Q value would increase as frequency increases. The trend from the data is that this holds true. However, the difference from the notchless Q value for each mode is determined above, and two interesting trends present themselves. First, it seems that the greatest difference from the notchless Q value is always seen in the 5th mode for the 4 cm (1.575 in) and 8 cm (3.150

in) notch lengths. This is true with one exception; see Table 12. Furthermore, for the 12 cm (4.724 in) and 16 cm (6.299 in) notch lengths, the greatest difference from the notchless Q values occurs in the 8th mode every time. This is useful because it presents the idea that damping characteristics could be a means of determining damage. This could prove especially useful in the case of notches even smaller in length than the ones used in the present study, as there is no evidence as of yet that the eigenvector curvature change method would work for such small notches.

Table 12. Modes in which the greatest difference from the notchless case Q value occurs.

	Free	Middle	Clamp
4 cm	5th	5th	6th
8 cm	5th	5th	5th
12 cm	8th	8th	8th
16 cm	8th	8th	8th

Some inconsistencies are found in the damping data, and these are due to many factors. Air inside of the notch could provide resistance to movement, increasing damping. Contact of the notch sides, which is a known possibility, would also affect the damping. The clamp condition was also far from perfect, and is probably a major source of error. While great care was taken to ensure that all four bolts were tightened evenly each time, no torque wrench was used until after all pertinent data was acquired. The use of a torque wrench to measure the given torque on each bolt would greatly improve the repeatability of the clamp condition and would likely make the damping data more meaningful. As it stands, the damping effects due to clamp inconsistencies are unknown.

III. Effects of Corrosion on the Detection of Damage Location

3.1 Corrosion Experiment

The following chapter outlines the development of the experiment aimed at monitoring the impact of corrosion on the detection of damage location. Experimental equipment, physical corrosion results, frequency results, and damping features will be discussed and compared to the data from Chapter Two.

3.1.1 Development of Corrosion Experiment.

A single notch length and location was selected for the test beams in the corrosion effect portion of the experiment. Identical members with varying times of exposure provide the data for analysis. There were a total of five exposure times, so two beams were manufactured for each exposure time: one notchless beam and one beam with an 8 cm (3.150 in) notch in the middle of the length. Only one notched beam was chosen so as to not change too many factors of the experiment at once. This case was chosen because an 8 cm (3.150 in) notch was hypothesized to be large enough to see a curvature change in the eigenvector, but small enough to be an applicable damage size to be of concern in real-world scenarios. Furthermore, the 8 cm (3.150 in) notch should have ample surface area inside the notch for corrosion to occur. Table 13 gives a summary of tests and exposure times.

Table 13. Summary of corrosion times for each corrosion test, yielding a total of 10 corroded beams for the experiment

Notchless Beam	8-cm Middle Notched Beam
24 hour test	24 hour test
48 hr test	48 hr test
120 hr test	120 hr test
168 hr (1 week) test	168 hr (1 week) test
336 hr (2 week) test	336 hr (2 week) test

The corrosion experiment was developed in accordance with the ASTM standard practices for Preparing, Cleaning, and Evaluating Corrosion Test Specimens, for Laboratory Immersion Corrosion Testing of Metals, and for Exposing and Evaluating Metals and Alloys in Surface Seawater (ASTM G1-03; ASTM G31-72; ASTM G52-00). Multiple time periods were chosen in order to characterize the effects of differing corrosion exposure times on a specimen. The corrosive solution was a saltwater mix, chosen to simulate a saltwater that spacecraft or aircraft would be exposed to in a humid coastal region, such as Florida.

3.1.2 Experimental Equipment.

The following section discusses the lab equipment used for the corrosion experiment. Tank preparation, specimen preparation, in-test monitoring and removal, cleaning, and testing with the laser vibrometer will be covered.

3.1.2.1 Tank Preparation.

The tank used for the corrosion portion of the present study was a 29-gallon high glass fish tank procured from Gerber's Saltwater Warehouse in Moraine, OH. The tank has a glass lid and dimensions of 30 ¼" x 12 ½" x 18 ¾". The tank was prepared by washing with an organic glass cleaner. While the tank can hold up to 29 gallons, no more than 25 gallons were ever used. The water used was Reverse Osmosis (RO) 18 mega-

Ohm pure water acquired from the environmental branch of the AFIT lab. The tank would be filled to an approximate height with the water, then the water height would be measured in the lab and these measurements converted to a volume. Instant Ocean™, the salt mix chosen for this experiment, was then added in a ratio of 1.5 lb Instant Ocean™ per 5 gallons of RO water.

Instant Ocean™ is a saltwater mix commonly used in saltwater fish tanks but originally developed by the United States Navy for research purposes. It is now produced by Marineland Labs in Moorpark, CA. When properly mixed, Instant Ocean™ produces saltwater with a specific gravity of 1.022, a salinity of 35 parts per thousand, and a pH of approximately 8.0 to 8.2. After the mix was added to the water, it was agitated until completely dissolved. The pump and heater were then added to the tank to ensure constant agitation and as constant temperature as possible. The pump was also purchased from Gerber's Saltwater Warehouse in Moraine, OH with a serial number of 8Q-F88. The heater was a 100-Watt Heater, also from Gerber's, with a model number of 1551012. Both devices were attached to the tank with self-contained suction cups. The heater was placed on the bottom of the tank in the middle, while the heater was placed on the wall of the tank, set to 73 degrees. After the heater and pump ran for at least one hour, salinity, temperature and pH were measured as baseline conditions.

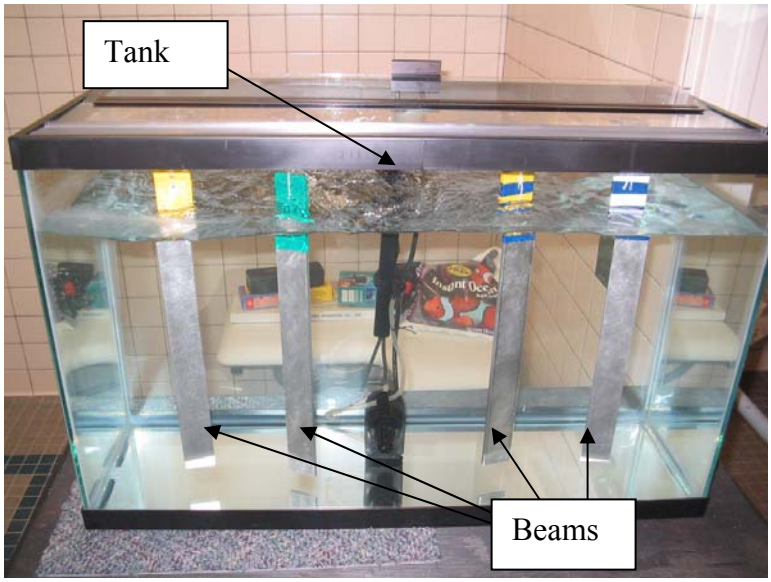

Figure 59. Corrosion test setup

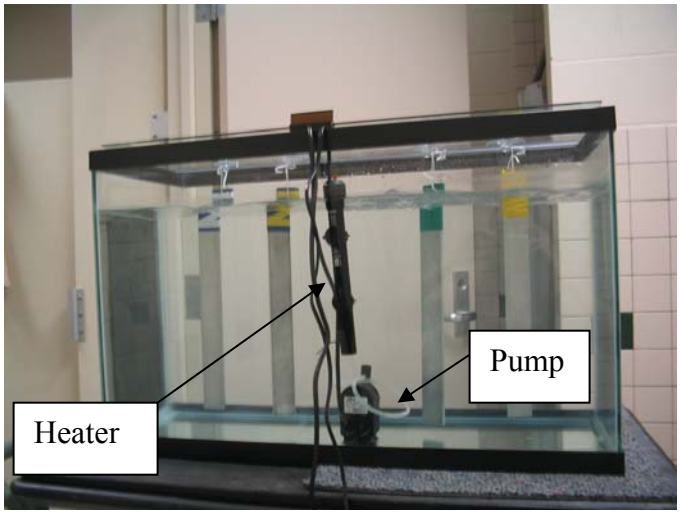

Figure 60. Pump and heater placement

The beam hanging support system consisted of suction cups with hooks attached to the glass lid of the tank. Three suction cups were rated by the manufacturer to hold up to 5 lbs, and the smallest suction cup could hold up to 3 lbs, well beyond the total weight of each beam. These four cups were affixed to the inside lid on a clean, dry surface, spaced equally along the length of the tank. Each metal hook was coated in electrical

tape to prevent the hooks themselves from becoming corroded and to preclude any kind of electrical interaction with the beams or resulting galvanic corrosion. This precaution was helpful, but perhaps overzealous as the hooks never came in contact with the water and were well over three inches from the water's surface at all times. The final element of the hanging support system was a nylon rope looped through the pre-existing holes in the beams and tied around the hooks.

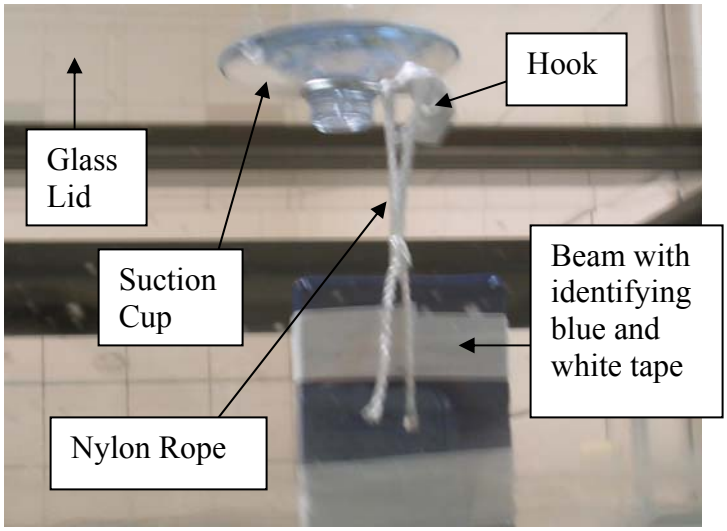

Figure 61. Beam hanging support system

3.1.2.2 Specimen Preparation.

The beams to be corroded were prepared in accordance with the ASTM International Standard Practice for Preparing, Cleaning, and Evaluating Corrosion Test Specimens (ASTM G1-03, 2005:1-8). Distinguishing marks were placed on all beams in the form of a very small (1 mm x 3 mm) piece of colored electrical tape placed on the thin edge that would not be immersed. This tape never left the beam, so any small effects it would have on the mass measurement would remain constant. All beams were tested with the laser vibrometer to ascertain pre-corrosion natural frequencies. Each beam was

abraded with abrasive paper for a total of four minutes with No. 220 abrasive paper. The edges as well as faces were abraded to remove any burrs and to remove any external dirt or foreign material. Next, each beam was degreased with acetone and water and hot-air dried, to clean and remove any additional traces of unknown substances in accordance with the ASTM standard. Ideally, the beams would all be prepared at the same time and stored in a desiccator, but the only desiccator in the lab was unavailable, so each beam was prepared as close to immersion time as possible and placed in the corrosive bath not later than an hour after preparation.

After cleaning and drying, each beam was weighed to the nearest one-tenth of a gram on the scale in the Vibration Laboratory and measured to the nearest ten-thousandth of an inch. The width and depth for each beam was measured at the middle and free end of the length with calipers. Preliminary pictures were taken of each beam to note any pre-existing discolorations or marks. Observations were recorded prior to the immersion and the surface areas, to include notches and holes, were calculated. The final preparation step was to mask off the last three inches of the beam (the part of the beam that would be clamped during the vibration testing) with electrical tape to prevent or hinder corrosion in this area. The color of the tape used for each beam matched the pre-existing identifying tape. The beams were suspended from the support rack with nylon rope as earlier outlined. To prevent the beams from touching the base of the tank if the rope stretches, beams were hung so at least one inch of water was between the beam and the tank bottom.

3.1.2.3 In-Test Monitoring.

For each test period, the salinity, temperature and pH level of the water was recorded periodically. These measurements are shown in Appendix H. The 24-hour and 48-hour tests were run simultaneously, as were the 7-day and 14-day tests. To do this, four beams were placed in the tank at the start of the experiment, with two predetermined as the 24-hour beams and two predetermined as 48-hour beams. At the end of 24 hours, the 24-hour beams were removed, leaving the 48-hour beams in the tank for one more day. The 7-day and 14-day tests were performed in a likewise fashion. This was done to conserve the very pure (and expensive) RO water. As long as the pH level stays fairly constant throughout the test, this method is perfectly acceptable. For all tests except the two-week test, the pH stayed constant. The pH varied by 0.2 for the two week test, but for such a long test duration, it is likely that the pH level would have changed by that amount even if the other two beams were not present.

The time duration for each test was carefully recorded. The date and time at the start of each test was recorded, along with initial environmental conditions. For each periodic checkup of water salinity, temperature, and pH level, the time and date was recorded according to the same timepiece.

3.1.2.4 Removal, Cleaning and Testing with Laser Vibrometer.

Upon the completion of a test period, the specimens were removed from the corrosive saltwater bath and examined. Photographs were taken of salt deposits and observations were recorded (please see Appendices G and H for photographs and observations, respectively). The specimens were then re-tested with the laser vibrometer before cleaning. The beams were then cleaned by scrubbing the outside with a medium-

stiffness plastic bristle brush and tap water to remove corrosion products and salt deposits. The beams were scrubbed vigorously on all faces and edges, and the notch was exposed to warm water, but nothing was placed in or through the notch to clean it.

The beams were then tested a third time with the laser vibrometer to see the frequency response when the corrosion product is cleaned off externally but may still exist in the notch. For the first two exposure times, the beam notches were cleaned out with air compressed to 100 psi blown through the notch, and tested a fourth time. For the longer exposure times, corrosion product in the notch was such that it could not be blown out of the notch and the only way to remove it would be chemical cleaning with Nitric acid. The process to acquire Nitric acid would have taken so long that the results would not have been meaningful due to increased exposure time to corrosive material in the notch.

Although the beams were tested three to four times each, the results used for all cases are the pre-corrosion natural frequencies and the cleaned beams with unclean notch natural frequencies. This was done to best compare these results to real-word situations. If an aircraft or spacecraft is exposed to a humid environment and becomes corroded, external corrosion product is easily removed through use and daily cleanings. One never sees an operational aircraft with built up salt deposits due to weeks of neglect, as the test beams exhibited. However, any corrosion that takes place in notches or internal damage is unseen and most likely impossible to reach with external cleanings. For this reason, the two cases of greatest interest are the uncorroded results and the corroded and cleaned results where the notch remains unclean.

3.1.3 Physical Results.

Obvious, first level results of corrosion testing are provided by physical examination. Pitting, intergranular attack, and other evidence of exposure to a corrosive environment are usually observable with the naked eye or are clearly evident in a microscopic examination of the corroded specimen.

3.1.3.1 Mass Loss.

The mass loss is assembled in Table 14 below. Mass loss was exhibited in every case, excepting the longer duration (one week and two week) middle notched cases. For these cases, there is an obvious buildup of corrosion product stuck inside the notch. This buildup was not removed from within the notch because, as previously explained, internal cracks and notches would not be cleaned out in practical applications and any corrosion product present would simply be left in the crack. The mass loss for all notchless cases never exceeds 0.2 grams, and ranges only from 0.1 to 0.2 grams. This indicates that a scale with greater precision would have been desirable.

Table 14. Mass loss for corroded beams.
NOTE: negative mass loss is mass gain, courtesy of built-up corrosion product in a notch

		Mass Before (g)	Mass After (g)	Mass Loss (g)
24 hr	Notchless	259.0	258.9	0.1
	Middle Notch	254.7	254.5	0.2
48 hr	Notchless	258.8	258.6	0.2
	Middle Notch	255.4	255.0	0.4
120 hr	Notchless	259	258.9	0.1
	Middle Notch	255.2	255	0.2
1 week	Notchless	258.6	258.5	0.1
	Middle Notch	255.3	255.6	-0.3
2 week	Notchless	258.7	258.6	0.1
	Middle Notch	255.5	256.3	-0.8

Table 15. Mass loss and fourth, fifth and sixth mode natural frequencies for uncorroded and corroded beams

Time	*Color*	*Beam*	*Mass Loss*	*4th mode frequency*	*5th mode frequency*	*6th mode frequency*
0 hr	N/A	Notchless	0	1893.75	3106.25	4586.25
24 hr	Yellow	Notchless	0.1	1779.69	2867.19	4950
48 hr	Blue	Notchless	0.2	1900	3134.38	4628.13
120 hr	Red	Notchless	0.1	1904.69	3137.5	4629.69
1 week	WhiteRed	Notchless	0.1	1906.25	3134.38	4621.88
2 week	White	Notchless	0.1	1787.5	2898.44	4892.19
0 hr	N/A	Notched	0	1743.75	2356.25	3650
24 hr	Green	Notched	0.2	1780	2381.25	3695
48 hr	Red	Notched	0.4	1790	2393.75	3706.25
120 hr	RedWhite	Notched	0.2	1798.75	2398.75	3710
1 week	BlueGreen	Notched	-0.3	1792.19	2392.19	3709.38
2 week	YellowBlue	Notched	-0.8	1559.38	2290.63	3518.75

The above table shows mass loss as related to frequency in the fourth, fifth and sixth modes. These modes were chosen because they are the three best modes to characterize internal damage based on frequency shift and eigenvector curvature comparison.

3.1.3.2 Physical Appearance.

The following figures show photographs and microscope images of corroded beams. Figures 62, 64 and 65 were microscope images, and Figure 63 is a photograph taken with a digital camera.

Figure 62 shows the portion of a corroded beam that was masked off. The tape covered the left side of the picture and a double layer was ensured. Note how some corrosion damage is present in this taped off section. It appears that the corrosive environment seeped through the end of the tape. According to this and other specimens, general corrosion occurred in small parts of masked-off regions.

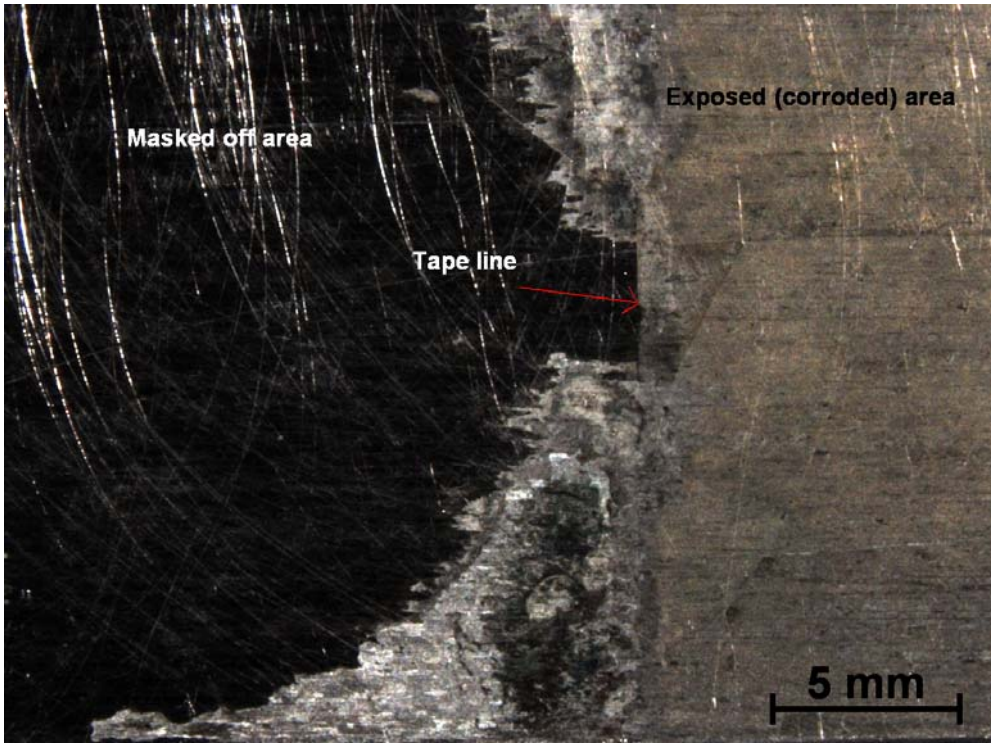

Figure 62. Line between exposed and unexposed beam

In Figure 63, the beam was wrapped with the protective tape leaving a small area around the upper hole exposed. Note that this area was not submerged in the water; it was merely exposed to the very humid air above the water. Although this region was not immersed, it still shows the same extent of general corrosion as the fully immersed region. This is very significant for relating experimental immersion data to real life applications.

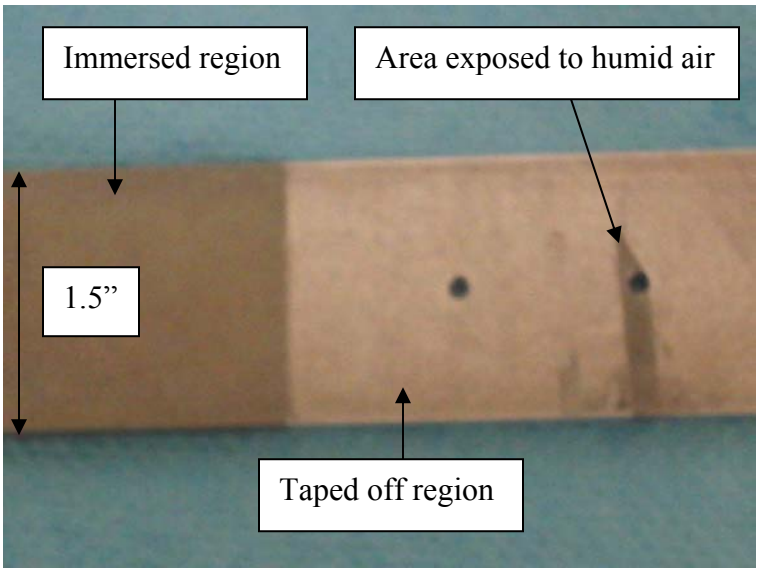

Figure 63. Tape line and exposed tape region exhibiting general corrosion. Beam shown was exposed to corrosive environment for 24 hours.

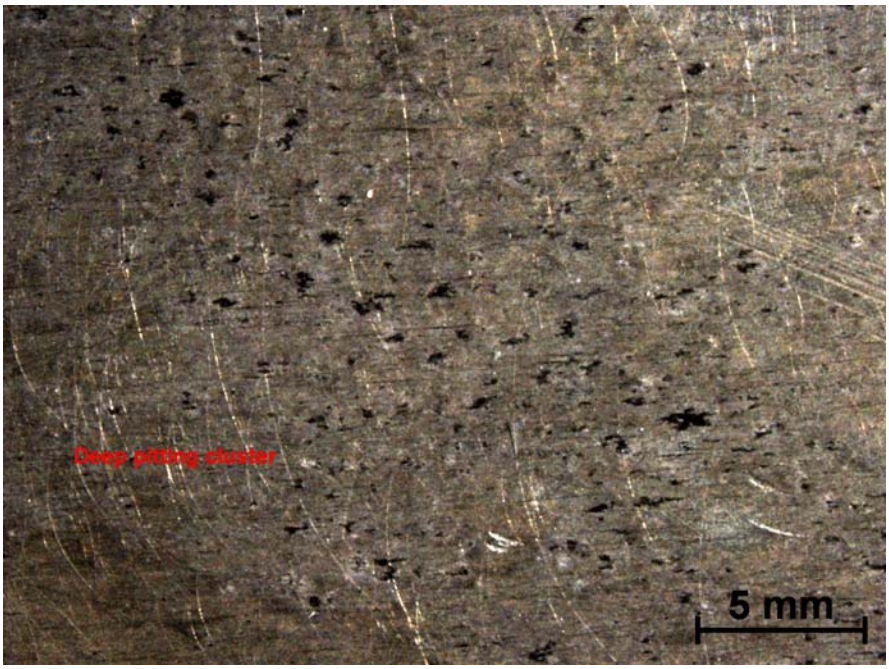

Figure 64. Example of deep pitting corrosion

Figure 64 shows an example of pitting corrosion. These deep pits were exposed after cleaning and appeared under the previous location of salt deposits on the beam.

Many of the beams showed moderate pitting, but the case shown in Figure 64 is an example of deep pitting corrosion. These images are presented to give the reader an idea of what is physically meant when the terms "pitting" and "granular attack" are used in the lab observations; they are not necessarily used to correlate pitting concentration to changes in frequency or mode shape curvature changes. However, these relations would be an interesting topic for further study.

Figure 65 shows an example of inter-granular attack, a localized attack along the grains of the metal.

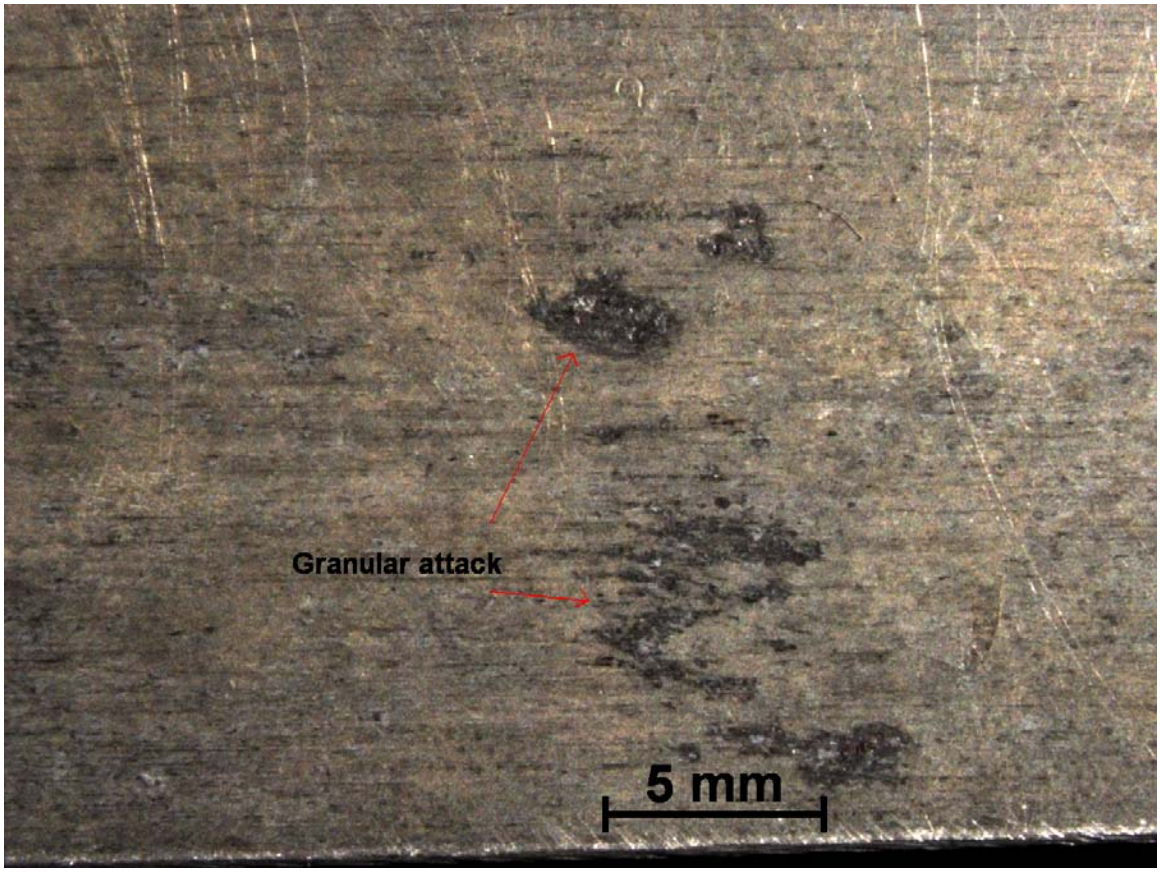

Figure 65. Example of granular attack corrosion

3.1.3.3 Relation to Real-Time Equivalents.

It is very difficult to compare results of laboratory immersion tests to the corrosion of actual structures in their service lifetime, due to the many factors delineated in the introductory chapter of this study (ASTM G31, 2005:1). Corrosion, by nature, is an unpredictable process, appearing in different forms and different amounts to structures of the same material in the same environment. Nevertheless, an attempt to relate the corrosion found in the present immersion data to normal outdoor urban air exposure will be attempted.

The typical aluminum corrosion rate in sea water ranges from 1 to 50 mils per year (Shackelford, et al, 1995:280). The corrosion rate for the present study is found by calculating the surface area for a beam, converting it to meters squared, then using this, along with mass loss and immersion duration to obtain a corrosion rate. The following equations prove helpful:

$$Surface\_Area_{m^2} = 0.000645 \times Surface\_Area_{in^2} \tag{12}$$

$$Corrosion\_rate = \frac{grams}{meters^2 \times day} \tag{13}$$

$$\frac{mm}{year} = 21.6 \times \frac{grams}{meters^2 \times day} \tag{14}$$

The corrosion rates obtained are found in Table 16.

The corrosion rates found exceeded the typical corrosion rates for aluminum in sea water. The corrosion rates for this experiment ranged from 8.96 mm/year to 106.49 mm/year. This is likely due to the fact that specimens are kept in a constantly agitated, temperature regulated environment with a warm temperature of 72 to 74 degrees. Sea water temperature changes in a cyclic pattern from night to day, as well as with the

seasons, with an average temperature well below 74 degrees for November through April in Daytona Beach, FL (http://www.nodc.noaa.gov/dsdt/wtg12.html, 1). In order to compare these corrosion rates with known ranges for sea water and urban air, the outliers of 106.4935 mm/year will be thrown out, and the values of 62.7155 mm/year will be assumed 50, the maximum for the given scale.

Table 16. Corrosion rate for experimental immersion

		Mass Loss (g)	Surface Area (m^2)	Corrosion rate ($g*m^{-2}*day^{-1}$)	Corrosion rate (mm/year)
24 hr	Notchless	0.1	0.034441259	2.903494366	62.7154783
	Middle Notch	0.2	0.040565856	4.930254646	106.4935003
48 hr	Notchless	0.2	0.034441259	2.903494366	62.7154783
	Middle Notch	0.4	0.040565856	4.930254646	106.4935003
120 hr	Notchless	0.1	0.034441259	0.580698873	12.54309566
	Middle Notch	0.2	0.040565856	0.986050929	21.29870007
1 week	Notchless	0.1	0.034441259	0.414784909	8.959354043
	Middle Notch	-0.3	0.040565856	-1.056483138	-22.82003579
2 week	Notchless	0.1	0.034441259	0.207392455	4.479677021
	Middle Notch	-0.8	0.040565856	-1.408644184	-30.42671438

Table 17. Corrosion rate equivalents between sea water and outdoor urban air exposure

Corrosion Duration	Beam	Sea water Corrosion rate (mm/year)	Outdoor urban air Corrosion rate (mm/year)
24 hr	Notchless	50	0.5
	Middle Notch	N/A	N/A
48 hr	Notchless	50	0.5
	Middle Notch	N/A	N/A
120 hr	Notchless	12.5	0.125
	Middle Notch	21.3	0.213
1 week	Notchless	8.96	0.090
	Middle Notch	N/A	N/A
2 week	Notchless	4.5	0.045
	Middle Notch	N/A	N/A

The range of corrosion rates for aluminum in normal outdoor air (urban exposure) are 0 to 0.5 mm/year (Shackelford, et al, 1995:276). If a linear relationship is assumed for both scales, corrosion rates can be related from sea water to urban air exposure, as shown in Table 17.

3.2 Frequency Data

For the corrosion experiment, all beams were tested with the laser vibrometer before corrosion, after corrosion and before cleaning, and after corrosion and cleaning. In all notched cases the cleaned data included external cleaning, but no internal cleaning of the notch was done in order to replicate real life conditions. While aircraft are routinely cleaned to eliminate corrosion byproducts, unknown internal notches or cracks are largely unaffected by the cleaning regimen.

3.2.1 Changes in Natural Frequency.

The experimental natural frequencies for each beam are tabulated in Table 18 for the pre-corrosion and post-corrosion beams, as well as the percent difference between the two. The percent difference is calculated as follows:

$$\%difference = \frac{\omega_{pre-corrosion} - \omega_{post-corrosion}}{\omega_{pre-corrosion}} \tag{15}$$

where ω is natural frequency.

Table 18. Pre- and post-corrosion experimental modal frequencies

[1]EXPERIMENTAL MODAL FREQUENCIES BEFORE CORROSION (Hz) [2]Experimental Modal Frequencies After Corrosion (Hz) [3]Percent difference (%)								
Mode	1	2	3	4	5	6	7	8
24 hour								
Notchless	[1]50 [2]50 [3]0%	312.5 320.313 -2.5%	951.6 975 -2.46%	1700 1779.69 -4.69%	2791 2867.19 -2.73%	4968.75 4950 0.38%	6326.56 6304.69 0.35%	8553.13 8185.94 4.29%
Notched	[1]48.75 [2]52.5 [3]-7.69%	313.75 326.25 -7.57%	863.75 867.5 -0.43%	1591.25 1780 -11.9%	2272.5 2381.25 -4.79%	3695 3695 0%	5501.25 5293.75 3.77%	6570 6818.75 -3.79%
48 hour								
Notchless	[1]53.125 [2]53.125 [3]0%	332.813 334.375 -0.47%	1015.63 1020.31 -0.46%	1889.06 1900 -0.58%	3112.5 3134.38 -0.70%	4595.31 4628.13 -0.71%	6329.69 6418.75 -1.41%	8382.81 8431.25 -0.58%
Notched	[1]50 [2]52.5 [3]-5.00%	320 338.75 -5.86%	867.5 886.25 -2.16%	1630 1790 -9.82%	2290 2393.75 -4.53%	3510 3706.25 -5.59%	4888.75 5325 -8.92%	5733.75 6850 -19.5%
120 hour								
Notchless	[1]50 [2]53.125 [3]-6.25%	317.88 335.938 -5.91%	960.938 1021.88 -6.34%	1753.13 1904.69 -8.65%	2909.38 3137.5 -7.84%	4364.06 4629.69 -6.09%	6904.69 6389.06 7.47%	8353.13 8442.19 -1.07%
Notched	[1]48.75 [2]52.5 [3]-7.69%	313.75 340 -8.37%	866.3 882.5 -1.87%	1585 1798.75 -13.5%	2260 2398.75 -6.14%	3460 3710 -7.23%	5465 5331.25 2.45%	6623 6867.5 -3.69%
1 week								
Notchless	[1]51.8125 [2]53.125 [3]-2.53%	334.375 334.375 0.00%	1012.5 1021.88 -0.93%	1890.63 1906.25 -0.83%	3117.19 3134.38 -0.55%	4615.63 4621.88 -0.14%	6429.69 6375 0.85%	8412.5 8442.19 -0.35%
Notched	[1]51.25 [2]53.125 [3]-3.66%	333.75 339.063 -1.59%	880 885.938 -0.67%	1755 1792.19 -2.12%	2358.75 2392.19 -1.42%	3651.25 3709.38 -1.59%	5206.25 5315.63 -2.10%	6743.75 6850 -1.58%
2 week								
Notchless	[1]53.125 [2]50 [3]5.88%	334.375 320.313 4.21%	1018.75 967.188 5.06%	1896.88 1787.5 5.77%	3126.56 2898.44 7.30%	4609.38 4892.19 -6.14%	6353.13 6326.56 0.42%	8420.31 8167.19 3.01%
Notched	[1]50 [2]50 [3]0.00%	325 320.313 1.44%	866.25 832.813 3.86%	1676.25 1559.38 6.97%	2331.25 2290.63 1.74%	3538.75 3518.75 0.57%	5007.5 5382.81 -7.49%	6047.5 6623.44 -9.52%

Theoretically, it is expected that ω would increase as the amount of mass lost increases in accord with the one dimensional equation:

$$\omega = \sqrt{\frac{k}{m}} \tag{16}$$

where k and m represent mass and stiffness, respectively. In the present system, K and M are actually matrices of values, but the concept still applies. It is unknown how corrosion affects the stiffness, but as long as the natural frequency shifts up, the mass loss is more significant than any possible decrease in stiffness. This trend is not clearly represented in the 24 hour case, but is definitely evident for all other corrosion times.

It is slightly more difficult to hypothesize the expected behavior for the notched beams as two possibilities present themselves. Initially, it was believed that the presence of a notch would introduce a greater surface area exposed to a corrosive environment, thus increasing mass loss. If this were the only result, it would naturally follow that the natural frequency would shift up as mass decreases, and would shift more than a modal frequency for a notchless beam under the same corrosive exposure time. However, corrosion product in the form of loosely adhering pieces of metal or salt deposits tend to clog up the notch. As corrosion time increases, the amount of mass trapped in the notch approaches and exceeds the amount of mass lost, resulting in a net gain of mass. The presence of matter in this notch makes the beam respond more like the notchless beam. Figures 66 and 67 illustrate the presence of corrosion product in a notch.

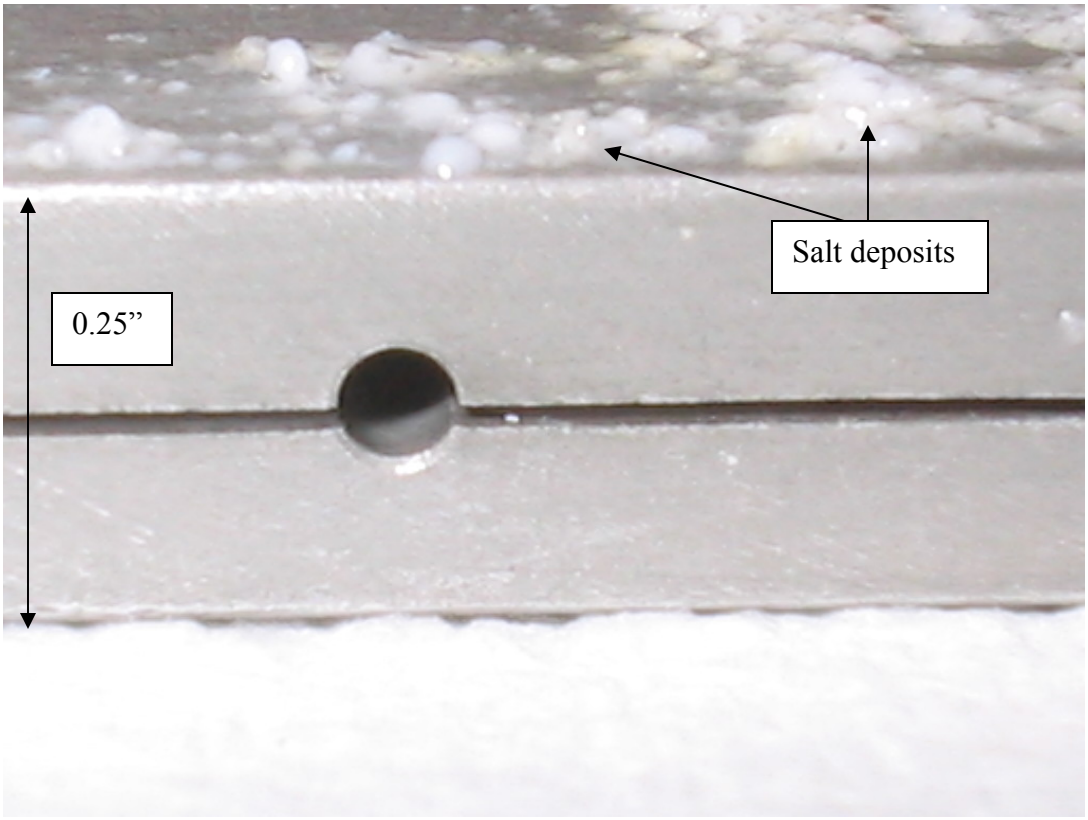

Figure 66. 24 hour corroded beam, zoomed in on the notch. No corrosion product is visible within the notch. Note the presence of sat deposits on the top surface of the beam, however.

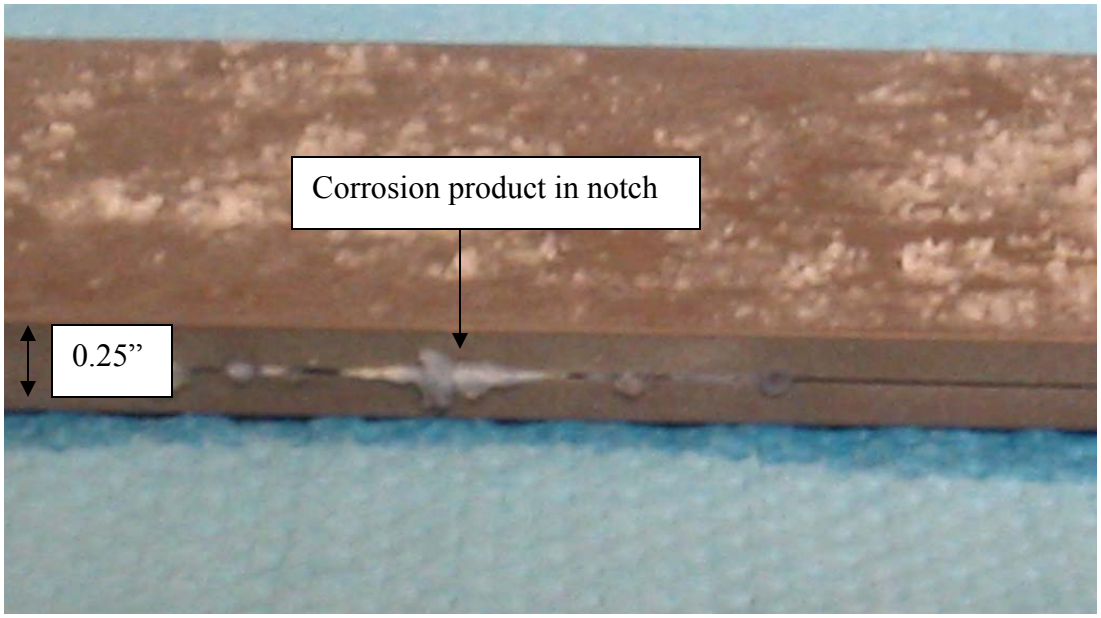

Figure 67. Corrosion product trapped in notch.
Beam shown is the one week corroded beam.

According to Table 18, the 24 hour, 48 hour and 120 hour scenarios are all characterized by a frequency increase, indicating that mass loss exceeds mass increase in the notch. However, for the one week and two week time spans, the trend is of a frequency decrease. This is graphically represented in Figures 68 and 69.

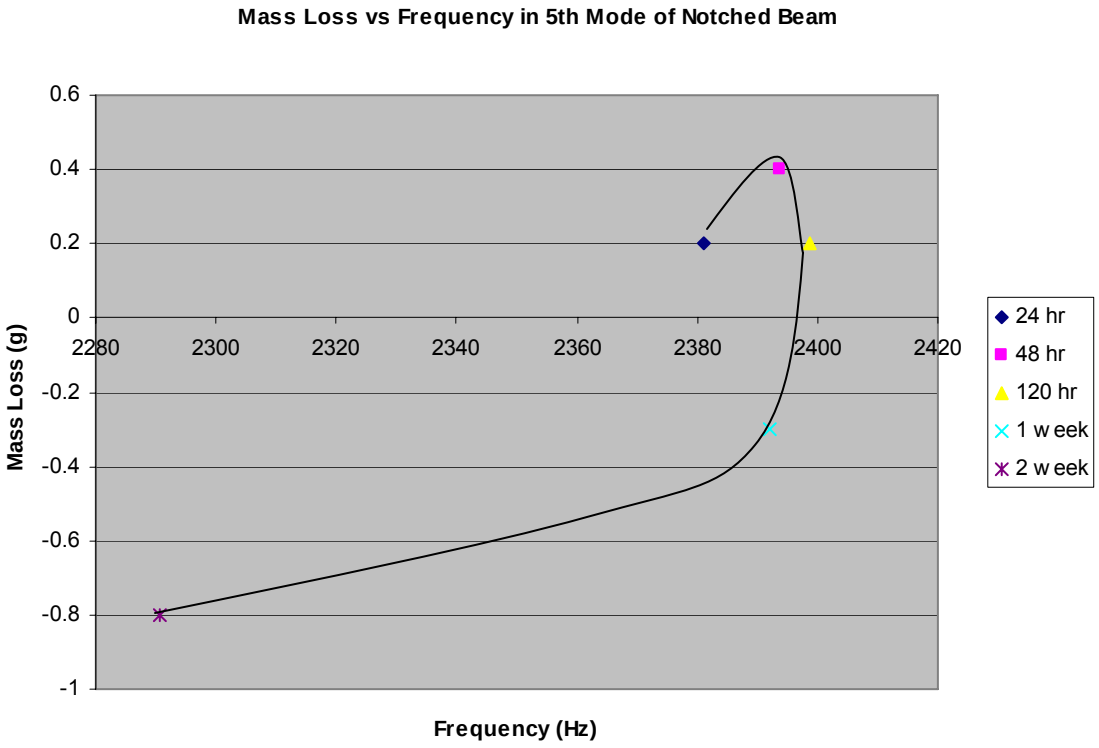

Figure 68. Mass loss plotted versus natural frequency for the fifth mode

The mass loss versus frequency for all cases are plotted for mode five in Figure 68 and mode six in Figure 69. These modes were chosen because they are two of the best modes for damage detection in both natural frequency shift and mode shape comparison.

In both plots, a distinct trend is evident. Corrosion produces an increasing mass loss for the 24 and 48 hour corrosion periods. While the net mass loss is still positive for the 120 hour corrosion duration, it is less than the 48 hour mass loss, indicating that corrosion product is starting to build up in the notch. The one week and two week natural

frequencies decrease from this value, while the total mass loss increases in the negative direction (indicating a net mass increase). From the trends presented in this data, the mass increase due to corrosion product in the notch starts to outweigh the decrease in mass due to corrosion between two and five days. Sometime between five and seven days, the total mass loss becomes negative, indicating that there is a mass increase in the specimen due to corrosion product in the notch.

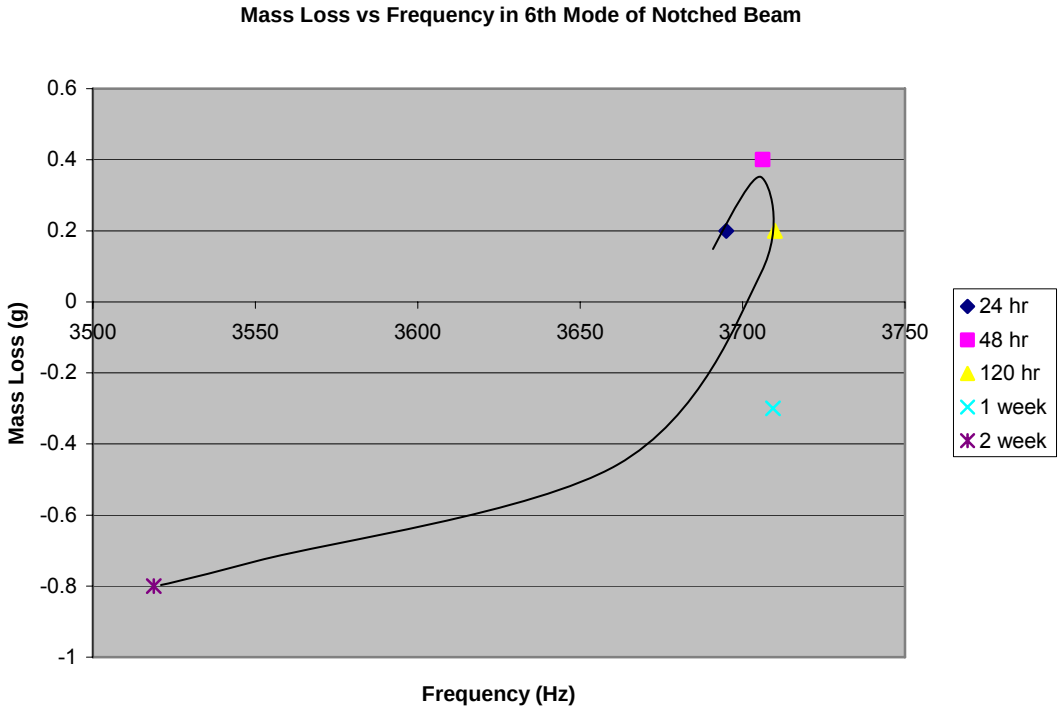

Figure 69. Mass loss plotted versus natural frequency for sixth mode

Table 19 shows the comparison of natural frequencies for notchless, notched and corroded notched beams for the different exposure times. If the examination of frequency is to be used to locate damage, the change must also be observed when the damaged structure is corroded. The results of this table show that in 70% of cases, the frequency shifts down from the notchless to the notched case. After corrosion, the

frequency shifts up, but not nearly to the same frequency as the notchless case. Therefore, it is still possible to detect damage from frequency shift in modes three and higher, but corrosion does hinder this process. Notable exceptions to this trend include modes three through six of the beam that was exposed to a corrosive environment for two weeks. In these cases, the natural frequency shifted down from the notchless to notched beam, and also shifted down from the notched to the corroded and notched beam. Modes six and seven for the 24 hour exposure tests, as well as mode seven for the 120 hour exposure tests also continued to shift downward in frequency after corrosion. However, mode four for the 24 and 120 hour exposure times shifted down from the notchless to the notched beams, but shifted back up higher than the notchless modal frequency after corrosion and cleaning.

Table 19. Comparison of modal frequencies for notchless, notched and notched corroded beams.

[1]MODAL FREQUENCY FOR NOTCHLESS BEAM (Hz) [2]Modal Frequency for notched beam (Hz) [3]Modal Frequency for notched, corroded and cleaned beam (Hz)						
Mode	3	4	5	6	7	8
24 hour	[1]951.6 [2]863.75 [3]867.5	1700 1591.25 1780	2791 2272.5 2381.25	4968.75 3695 3692	6326.56 5501.25 5293.75	8553.13 6570 6818.75
48 hour	[1]1015.63 [2]867.5 [3]886.25	1889.06 1630 1790	3112.5 2290 2393.75	4595.31 3510 3706.25	6329.69 4888.75 5325	8382.81 5733.75 6850
120 hour	[1]960.938 [2]866.3 [3]882.5	1753.13 1585 1798.75	2909.38 2260 2398.75	4364.06 3460 3710	6904.69 5465 5331.25	8353.13 6623 6867.5
1 week	[1]1012.5 [2]880 [3]885.938	1890.63 1755 1792.19	3117.19 2358.75 2392.19	4615.63 3651.25 3709.38	6429.69 5206.25 5315.63	8412.5 6743.75 6850
2 week	[1]1018.75 [2]866.25 [3]832.81	1896.88 1676.25 1559.38	3126.56 2331.25 2290.63	4609.38 3538.75 3518.75	6353.13 5007.5 5382.81	8420.31 6047.5 6623.44

	3					

3.2.2 Comparison of Mode Shapes.

The comparison of mode shapes for pre- and post-corrosion conditions of a given beam clearly demonstrate the random nature of corrosion. The mode shapes differed from the notchless case to varying degrees for different modes. Overall, the corroded mode shapes were obtained from data that appeared to have more interference. It was more difficult to obtain a clear mode shape that was pure bending, and some mode shapes obtained exhibited some torsion features. These features may be indicative of an asymmetric mass loss due to the corrosion process. In general, the notched mode shapes behaved less like the notched condition and more like the notchless case, but it is still possible to differentiate the notched, corroded beam from the notchless, uncorroded beam. Figures 70 through 73 show the difference between pre- and post-corrosion mode shapes for the 24 hour corrosion durations. Both the notchless and the 8 cm (3.150 in) middle notched beam mode shapes are compared. In all cases, the clamp is on the right side of the plot and is shown as a black box. The approximate location of the notch is outlined as a bold black line on the abscissa.

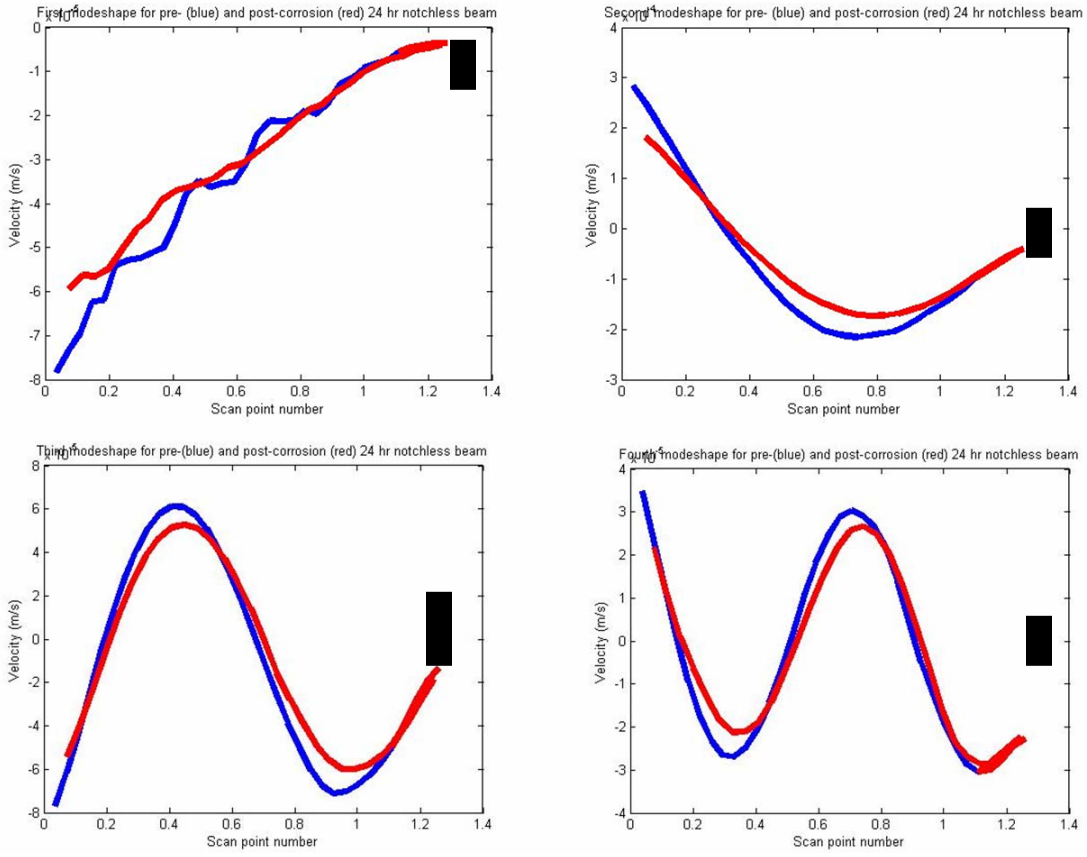

Figure 70. Corrosion comparison of mode shapes for modes one through four of the 24 hour notchless beam. The blue plot is the uncorroded mode shape; red indicates the corroded one.

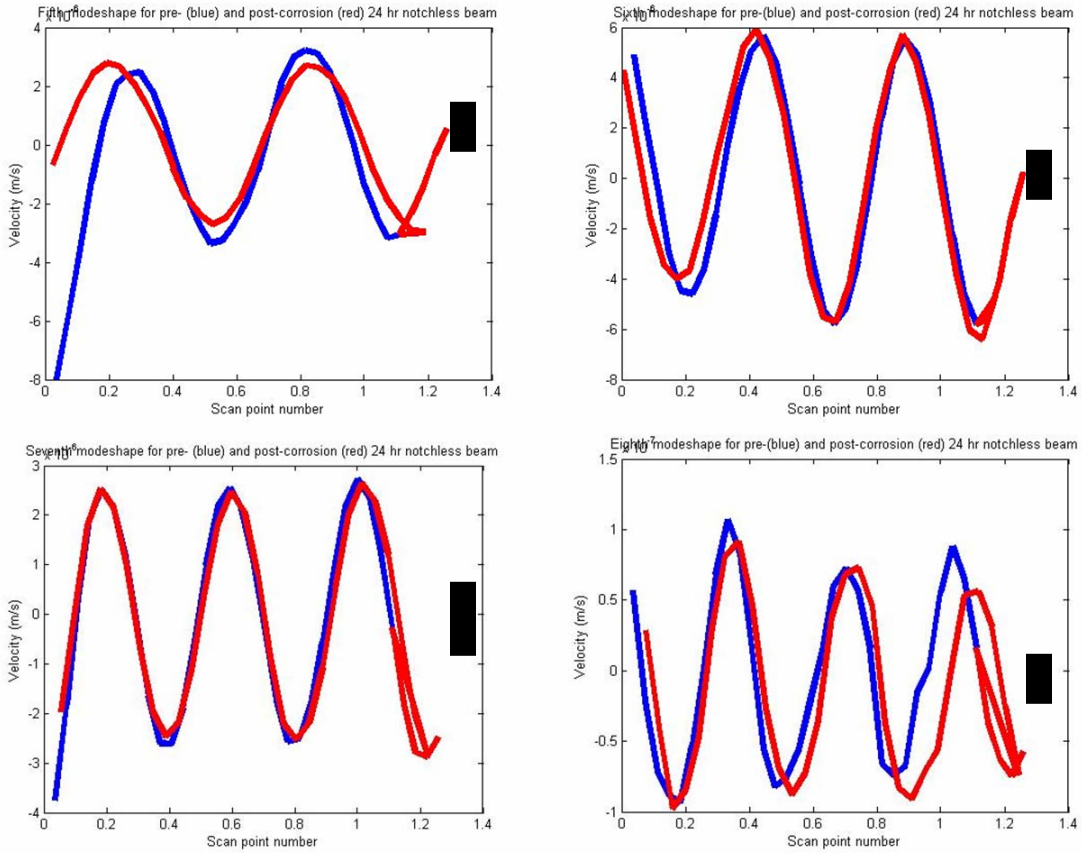

Figure 71. Corrosion comparison of mode shapes for modes five through eight of the 24 hour notchless beam. The blue plot is the uncorroded mode shape; red indicates the corroded one.

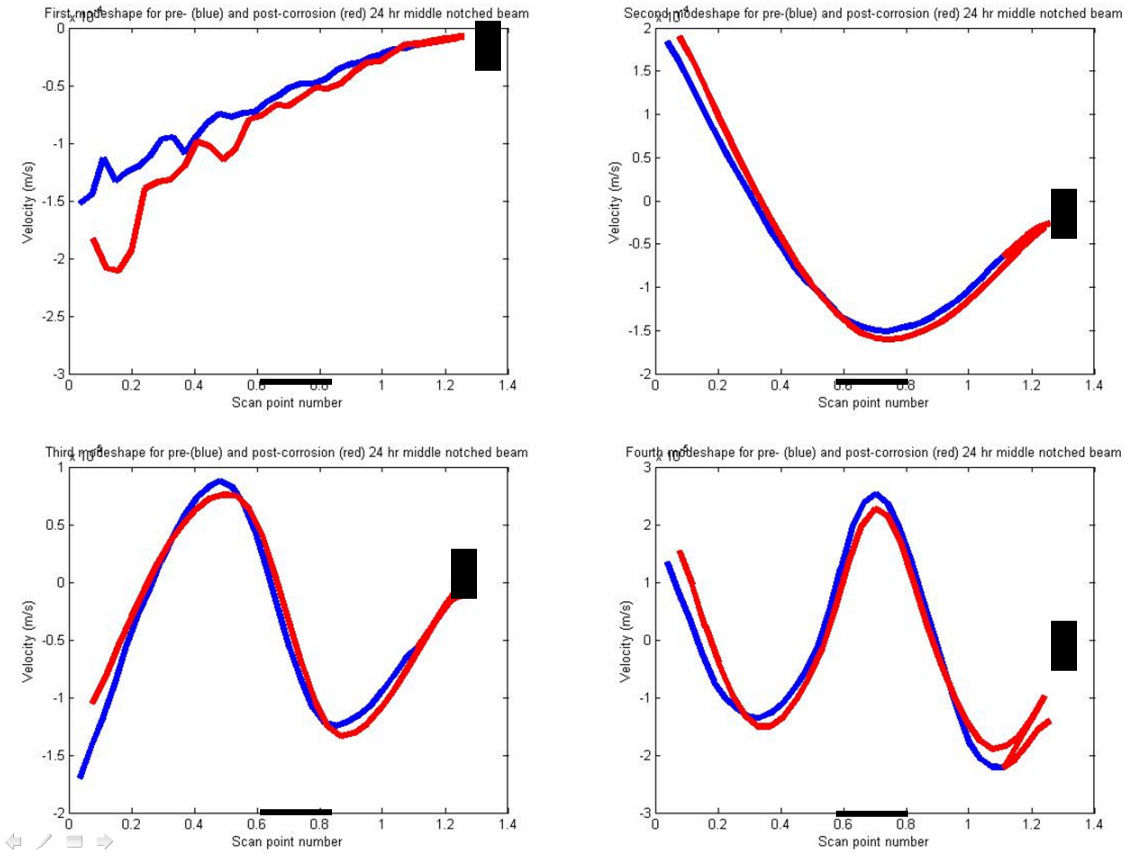

Figure 72. Corrosion comparison of mode shapes for modes one through four of the 24 hour middle notched beam. The blue plot is the uncorroded mode shape; red indicates the corroded one.

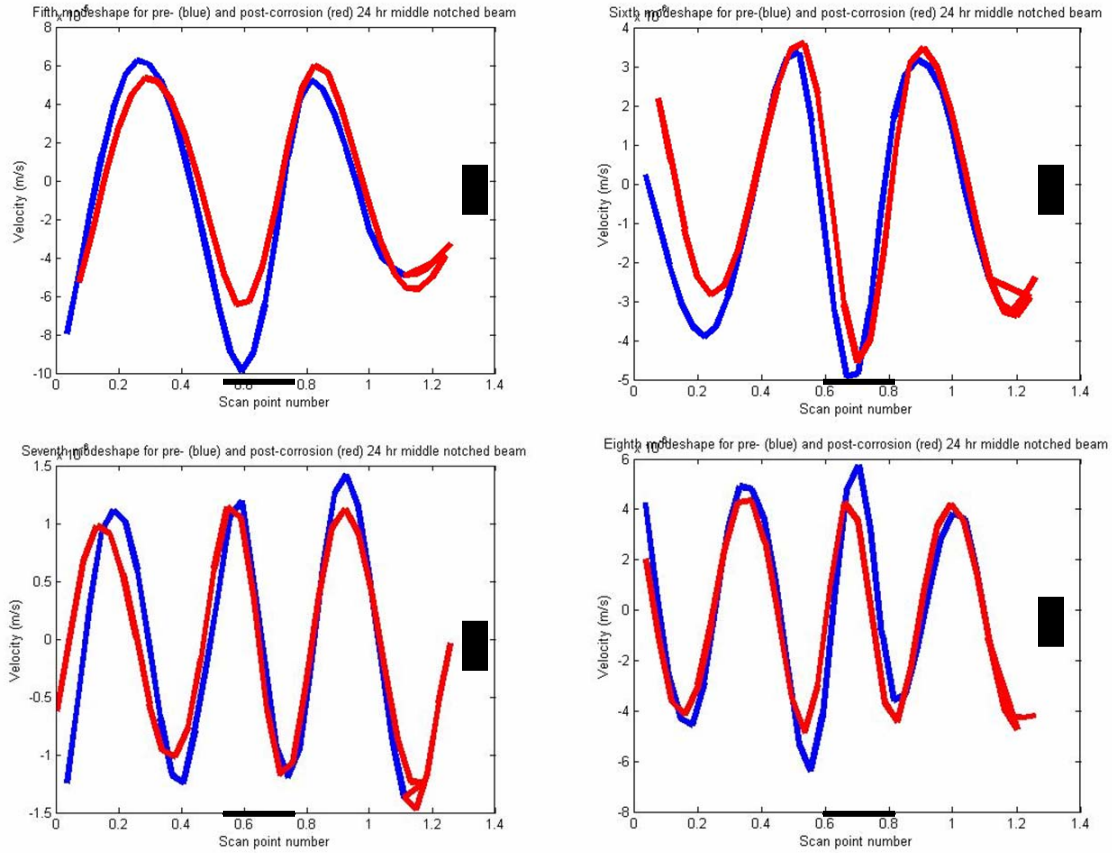

Figure 73. Corrosion comparison of mode shapes for modes five through eight of the 24 hour middle notched beam. The blue plot is the uncorroded mode shape; red indicates the corroded one.

It is clear that even 24 hours in a corrosive environment changes the frequency response of a structure. Most corroded mode shapes are the same general shape as their baseline counterparts, but some deviation is present. Any deviation is likely to reduce the effectiveness of mode shape curvature comparisons as a useful means of damage detection. Modes four, five and six from Figures 68 and 69 are good examples of

corroded mode shapes that will still differ enough from the notchless ones to show the presence of damage. Figures 74 through 77 show the two week exposure time corrosion comparisons.

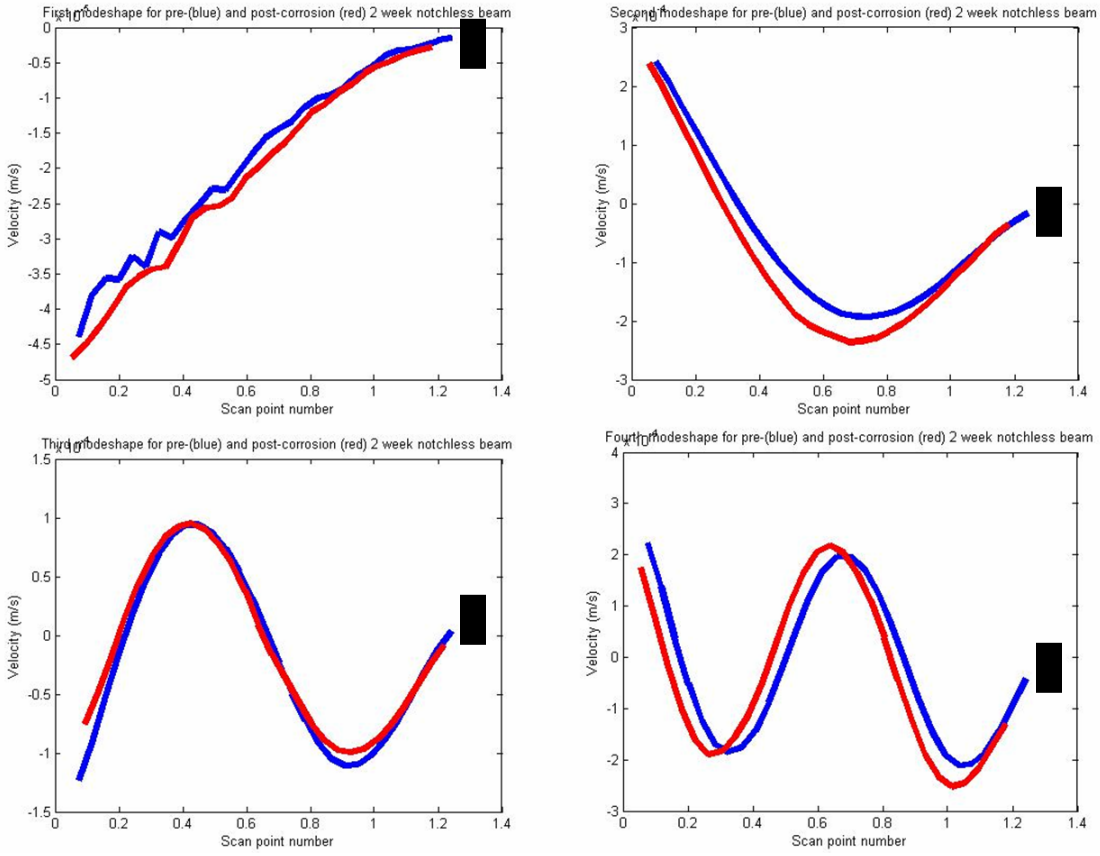

Figure 74. Corrosion comparison of mode shapes for modes one through four of the 2 week notchless beam. The blue plot is the uncorroded mode shape; red indicates the corroded one.

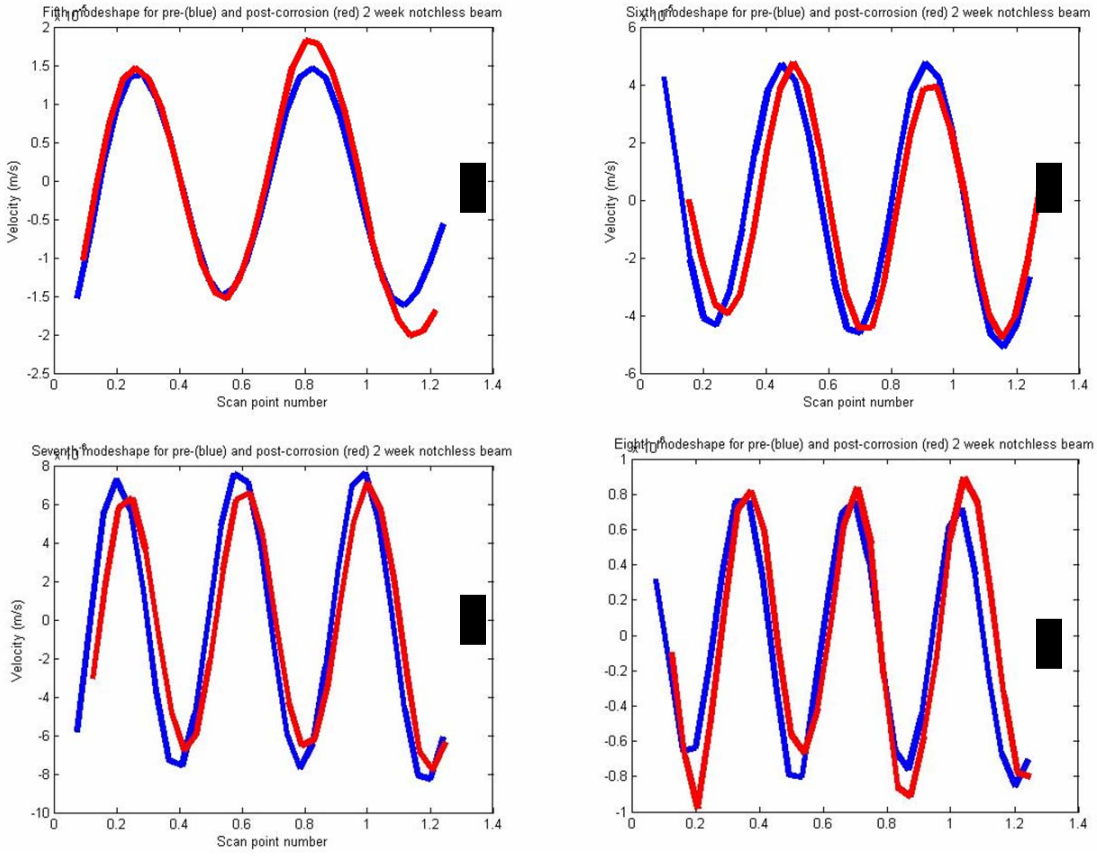

Figure 75. Corrosion comparison of mode shapes for modes five through eight of the 2 week notchless beam. The blue plot is the uncorroded mode shape; red indicates the corroded one.

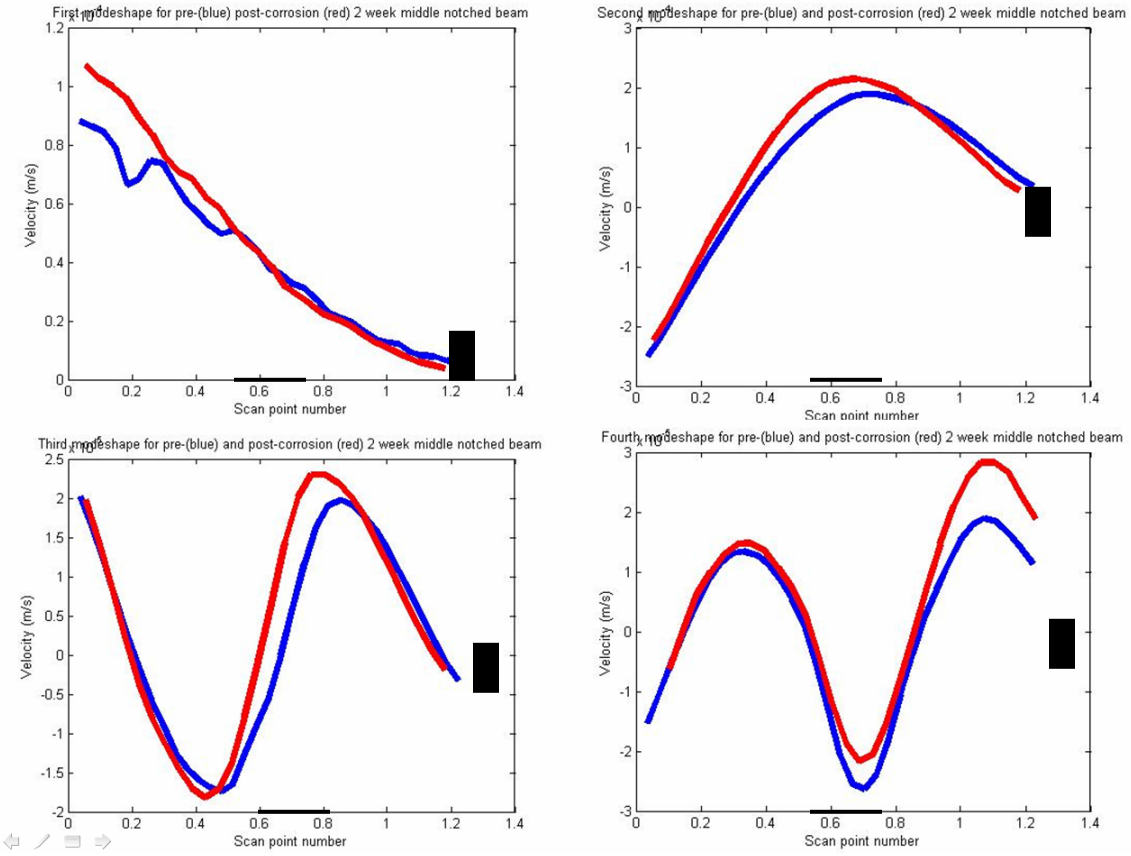

Figure 76. Corrosion comparison of mode shapes for modes one through four of the 2 week middle notched beam. The blue plot is the uncorroded mode shape; red indicates the corroded one.

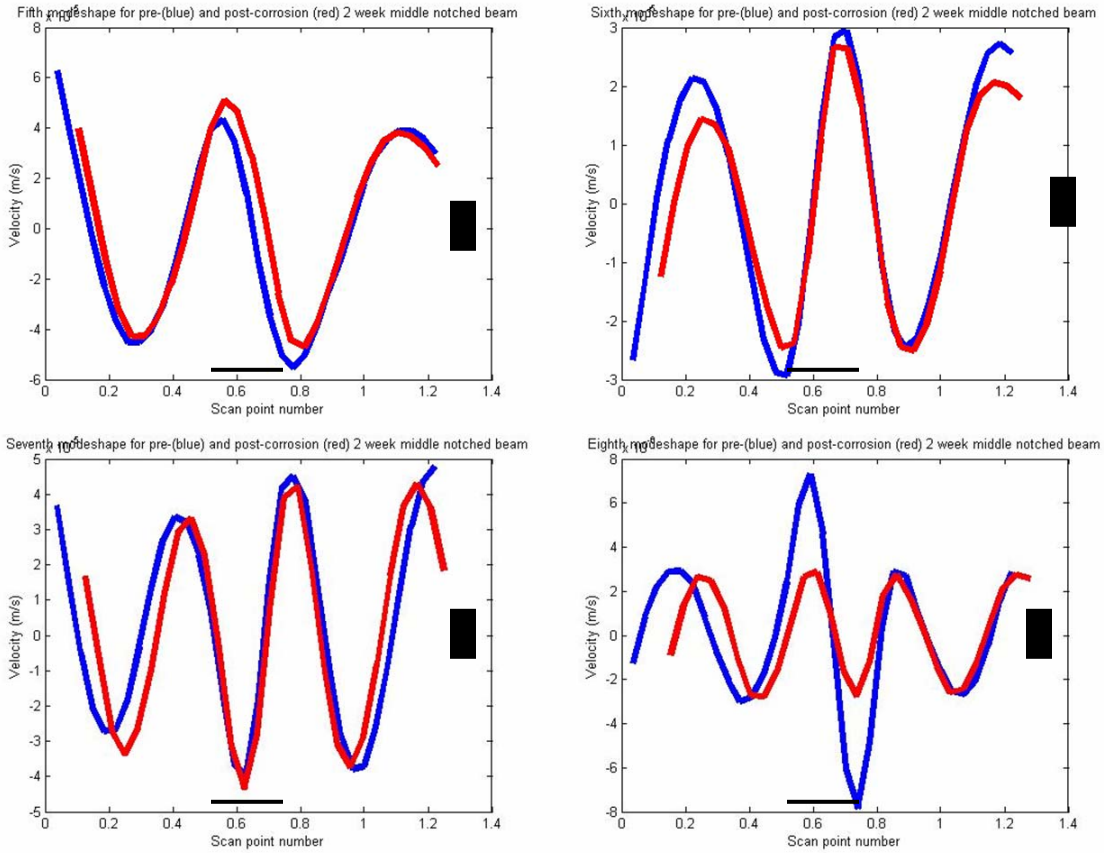

Figure 77. Corrosion comparison of mode shapes for modes five through eight of the 2 week middle notched beam. The blue plot is the uncorroded mode shape; red indicates the corroded one.

Unfortunately, with a longer corrosion time comes an increase in notch residue. This causes the middle notched beams to behave much more like a notched beam for some modes. For modes three, four, five and seven, it appears to still be possible to detect damage location from mode shapes, although direct comparison to the uncorroded, notchless mode shape would be necessary. However, for modes six and especially eight,

the mode shapes appear to be identical to notchless mode shapes, which would make damage detection from this data impossible.

3.3 Damping Features

The general trend which presents itself is that the normalized Q values decrease after corrosion, indicating that damping increases. In 67% of all modes for all cases, and 73% of the time for modes three through eight, the normalized Q values decrease. One would expect the damping to increase with the presence of corrosion by-products in the notch of a notched beam. It is possible that the structural makeup of the beams could be affected by the corrosive immersion, which could change the material properties.

The normalized Q values used in the following tables are calculated by subtracting the specimen Q values from the uncorroded notchless beam Q values. This normalization will hopefully offset the reality that the system Q, not just the Q for the beam, was captured.

Table 20. Normalized Q values before and after corrosion for one day. Modes one through eight are listed.

ONE DAY						
	Notchless			Middle		
	Before	After	Difference	Before	After	Difference
Mode	Q	Q		Q	Q	
1	17.85714	31.0559	13.19876	45.99057	58.33333333	12.3427673
2	148.8095	84.28947	-64.5201	98.0625	102.2727273	4.21022727
3	83.47368	48.99497	-34.4787	31.87454	29.20875421	-2.66578454
4	170	84.7619	-85.2381	227.2857	197.7777778	-29.5079365
5	146.8947	27.04717	-119.848	206.6364	183.1538462	-23.4825175
6	50.19192	37.5	-12.6919	69.71698	307.9166667	238.199686
7	45.51799	41.75497	-3.76302	90.18033	252.0952381	161.91491
8	77.75455	94.09195	16.33741	234.6429	162.3571429	-72.2857143

Table 21. Normalized Q values before and after corrosion for two days. Modes one through eight are listed.

TWO DAYS						
	Notchless			Middle		
	Before	After	Difference	Before	After	Difference
Mode	Q	Q		Q	Q	
1	37.41549	43.19512	5.779629	58.82353	64.81481481	5.9912854
2	104	104.5	0.5	133.3333	109.2903226	-24.0430108
3	101.6	127.5	25.9	85.04902	47.65053763	-37.398482
4	269.8571	211.1111	-58.746	326	137.6923077	-188.307692
5	141.5	184.3529	42.85294	254.4444	239.4	-15.0444444
6	270.2941	201.2174	-69.0767	234	285.0769231	51.0769231
7	150.7143	49.75969	-100.955	305.5625	190.1785714	-115.383929
8	598.7857	281.0333	-317.752	86.87879	214.0625	127.183712

Table 22. Normalized Q values before and after corrosion for five days. Modes one through eight are listed.

FIVE DAYS						
	Notchless			Middle		
	Before	After	Difference	Before	After	Difference
Mode	Q	Q		Q	Q	
1	50	38.78102	-11.219	40.96639	61.76470588	20.7983193
2	144.1818	95.97143	48.21039	136.4348	106.25	-30.1847826
3	95.13861	127.75	-32.6114	40.33019	83.25471698	42.9245283
4	219.125	238.125	-19	264.1667	85.66666667	-178.5
5	111.8846	261.5	-149.615	282.5	239.9	-42.6
6	218.2	201.3043	16.89565	133.0769	463.75	330.673077
7	89.67532	81.91026	7.765068	97.58929	156.7941176	59.2048319
8	N/A	402	N/A	183.9722	124.8727273	-59.0994949

Table 23. Normalized Q values before and after corrosion for one week. Modes one through eight are listed.

ONE WEEK						
	Notchless			Middle		
	Before	After	Difference	Before	After	Difference
Mode	Q	Q		Q	Q	
1	18.74909	36.89583	18.14674	40.6746	37.68085106	-2.99375211
2	90.37838	90.37838	0	119.2143	105.96875	-13.2455357
3	144.7143	113.5556	-31.1587	36.66667	48.40983607	11.7431694
4	315.1667	127.0667	-188.1	117	44.8	-72.2
5	346.3333	125.36	-220.973	294.875	217.4545455	-77.4204545
6	242.9474	171.1852	-71.7622	331.9091	218.1764706	-113.73262
7	103.7097	77.7439	-25.9658	192.8148	183.3103448	-9.50446999
8	210.325	496.5882	286.2632	110.5574	142.7083333	32.1509563

Table 24. Normalized Q values before and after corrosion for two weeks. Modes one through eight are listed.

TWO WEEKS						
	Notchless			Middle		
	Before	After	Difference	Before	After	Difference
Mode	Q	Q		Q	Q	
1	41.50781	34.96503	-6.54278	60.97561	40.6504065	-20.3252033
2	123.8519	100.0938	-23.7581	130	94.20588235	-35.7941176
3	113.2222	99.71134	-13.5109	78.75455	46.52513966	-32.2294058
4	379.4	137.5385	-241.862	88.21053	55.67857143	-32.5319549
5	156.35	152.5263	-3.82368	233.1	120.5789474	-112.521053
6	307.2667	78.90323	-228.363	208.1765	90.23076923	-117.945701
7	113.4464	79.0875	-34.3589	178.8571	56.07291667	-122.784226
8	161.9231	92.80682	-69.1163	59.29412	94.61428571	35.3201681

As previously discussed, it was determined that the Q values captured for the experiment were actually for the entire system, including the beam, test stand, clamp and table. An attempt to isolate the beam Q values was made by clamping the beam directly to the table, but these values were on the same order of magnitude as the previous ones, evidently capturing the system Q. In an attempt to eliminate some of the external system effects, the Q values were normalized by finding the percent difference from the notchless, uncorroded beam Q values. The normalized Q values for the beam clamped directly to the table are in the following table.

Table 25. Normalized Q values for notchless beam without test stand

Notchless Beam without Test Stand		
Mode	wn	Q
1	45.31	67%
2	278.1	61%
3	800	65%
4	1541	41%
5	3892	-25%
6	4736	73%
7	6058	84%
8	7459	-232%

Overall, the beam clamped directly to the table showed a greater deviation from the notchless case than did the pre-corrosion notchless beams. These larger normalized Q values indicate less damping, which implies that a small degree of damping is introduced by the test stand and clamp. However, it is difficult to find the beam Q values independent of the system values. The main conclusion drawn from the damping analysis is that corroded specimens exhibit an increase in damping after corrosion has occurred. Further research is necessary to establish a numerical relationship between the increase in damping and the duration of corrosion exposure.

IV. Conclusions

4.1 Detection Features of Damage Location

The aim of the present study was to determine the best method of damage detection using vibration methods and the frequency response of a structure. This was accomplished through extensive testing of various notched and notchless aluminum beams, encompassing data and results from two prior studies as well. It has been determined that mode shape analysis considering curvature change of the eigenvector is the best method to detect internal notches in cantilever beams of the given dimensions and material properties. While frequency shift can also be a good indicator of the presence of damage, the use of eigenvector curvature comparison is a better indicator of the extent and location of damage. It is important to note that this method, while very effective, can and should be implemented into future SHM measures to detect damage. However, the method itself is not well designed for remote SHM. While it is feasible to have an acoustic horn and laser vibrometers present to detect damage in grounded aircraft or spacecraft, it is not very realistic to have a whole laser vibrometer equipment setup orbiting with a satellite in space.

Of the two analytical models used, the ABAQUS model was reliably more consistent with the experimental data. However, the MATLAB code did yield good estimations, and was much less time-intensive than constructing the ABAQUS models. Furthermore, by changing beam dimensions and boundary conditions through the

MATLAB code, selections of frequencies at which interference was caused by notch contact were approximated. Through the ABAQUS model, it was verified when contact occurs between faces of an eccentric notch, according to the forcing function in Equation 10, $F = A\sin(\omega t)$. The eccentric rather than centric notch was examined because less energy would be required to bring about contact through a thinner beam portion in the case of the eccentric notch. As long as amplitude values of the loading function are below the values required for contact with an eccentric notch, the centered notch should not exhibit contact either.

While past research has associated the crack depth ratio (*a/h*) as an important factor in damage detection through frequency shift, the experiments performed did not support this. Rather, the importance of notch length was established as a better predictor of frequency shift. Only two crack depth ratios were used in the data encompassed by the present study, while four different notch lengths were characterized. Perhaps if different notch depths were studied, the stated hypothesis could be better established.

For notches 4 cm (1.575 in) in length, comparing frequency shift did not yield a distinction between centered and eccentric notched specimens. In general, frequency shift was more useful for detecting damage when the damage region was 39% or 52% of the beam length. Fortunately, the mode shape curvature comparison method detects the location and extent of damage best for the 4 cm (1.575 in) and 8 cm (3.150 in) notches. A final conclusion about the mode shape comparison method is that it is a better indicator of damage when examining the amplitude of a mode shape. The general x-direction of a mode shape occasionally varies when plotted directly on top of a corresponding mode

shape, and may not always indicate the presence of damage, but according to experimental results, large variations in the amplitude always indicate damage.

The final conclusion from this portion of the research is the problem of clamp repeatability. The torque measurements of the bolts in the clamp were only established after the data was acquired, because the decision to study damping was made after the acquisition of data. Some of the damping data was inconclusive due to the varying amount of damping provided by the clamp. If damping analysis is performed in future research, it is recommended that torque measurements of the clamp be established as a standard to be used for all testing before the commencement of data acquisition.

4.2 Detection Features of Damage Location with Corrosion

One conclusion from the corrosion experiments is the determination of when the mass increase due to residual corrosion product buildup in a notch outweighs the mass loss due to corrosion. Between two and five days, the rate of mass increase due to corrosion by-products in the notch becomes apparent. Between five and seven days, the total amount of mass gained becomes greater than the total amount of mass lost, resulting in a net mass increase. Ideally, more corrosion cases are necessary to provide a more accurate picture as to the effect of corrosion on damping data. It was found that damping increases after corrosion. Technique issues with the experiment (in particular clamping torque variances) as well as the random nature of the manifestations of corrosion (pitting, granular attack) are barriers to establishing tight correlations between experimental findings and real world service life predictions. This makes it difficult to establish relationships between experimental findings and service life predictions.

Corrosion is a process that becomes more destructive with time. Not only does the exposure time in a corrosive environment increase the amount of attack, but even after removal from the environment, residual traces of corrosion product continue to attack the material. Because of this, SHM on structures exposed to a corrosive environment, such as humid coastal air, should be performed often.

The purpose of the corrosion experiment is to determine if mode shape analysis is effective for use with corroded structures. It has been found that it can still be a reliable method to detect cracks 8 cm (3.150 in) long. The presence of corrosion does influence the frequency response of a structure, and the balance of mass loss and mass increase in the notch does complicate matters. However, it is still possible to distinguish damage presence and location through the examination of the mode shapes of corroded members. It was also found that damping decreased after a structure was corroded. Further research with the use of notches smaller than the shortest ones in the present experiment would prove to be very useful to the development of this method of SHM in use with structures exposed to corrosion. Ideally, the study of notches even smaller than 4 cm (1.575 in) would aid in the process of detecting damage as early as possible.

Furthermore, experiments performed for longer than two weeks could provide even more insights. With a greater number of exposure times, more definitive trends could be examined, particularly in the balance of mass loss versus mass increase due to corrosion by-products. Perhaps a better correlation to real world situations could also be drawn, and a spectrum of corrosion intensity could be established. In this fashion, researchers could more easily relate time in a corrosive bath to days or months in corrosive air.

4.3 Proposed Topics for Further Study

To continue the study of this method and prove its effectiveness, a blind study should be done in which the notch location in unknown, and using the curvature change method, the user attempts to locate the damage and determine its extent. In addition to this, future research should attempt to determine just how accurately the eigenvector must be known. For example, the number of scan points used with the scanning vibrometer would give a good idea of just how coarse or fine the grid of the known eigenvector is, and a study on just how fine this grid needs to be for the method to be valid would be an effective way to evaluate the sensitivity of this method. Furthermore, it should be determined how many eigenvectors are needed, and if just one or many eigenvectors are required to determine damage detection when the location is unknown.

Possible topics for future research regarding this method of SHM can be categorized into four groups: boundary condition changes, environmental changes, technique changes, and structural changes to the specimens. Boundary condition changes include the investigation of different boundary conditions such as clamp-clamp, free-free or simply supported conditions. The usefulness of both the frequency shift and mode shape analysis methods can be tested for each of these conditions to determine which works best for each case, and if one method is more reliable than the other for structural health monitoring of actual spacecraft and aircraft.

Environmental changes would include a continuation of the corrosion study. More samples per corrosion time and a few more exposure times would help to make the study more comprehensive and would yield more results from which to characterize trends. Another useful environment change would be the investigation of other

detrimental environments besides corrosion, such as extreme heat or cold. If the damage detection methods developed work in extreme temperatures, they could be a very useful means of SHM in spacecraft. One more environmental change, also useful for the development of SHM in spacecraft, would be a vacuum environment. Testing to determine the practicality of vibrations testing in a vacuum environment would be a key consideration in choosing a SHM method for spacecraft.

Another interesting topic for further study is the use of a local approach for damage detection and assessment. The wave propagation technique is the common local approach used to pinpoint damage location. The use of this technique, either alone or in combination with a global method, has a great deal of potential as an effective SHM tool.

Some structural changes to the specimens would also provide enlightening research. In real world applications, it is always most desirable to find and fix damage before it becomes too extensive. The earlier internal damage is detected the more likely it is that remediation procedures can be effectively applied to reduce the threat of catastrophic failure. With this in mind, beams can be designed with notches even smaller than 4 cm (1.575 in) in length. Another possibility is to include notches that do not span the entire width of the beam. Perhaps notches of the same length, spanning different percentages of the beam depth, can be investigated. One more alternative is the possibility of machining thinner notches. A depth of 0.012" was chosen for the present study to compare to previous results, but as technology advances, the ability to machine even smaller notches will undoubtedly present itself. An additional topic worthy of further examination is the study of the developed damage detection technique on actual cracks, which can be introduced a number of ways. One common way to induce a crack

is by machining a small notch and then fatigue loading the member until a crack occurs and extends to a desired length. The results of this research can be compared to those of the notched beams to determine if mode shape analysis works as well for cracks as it does for notches.

Appendix A: MATLAB Program

This appendix will cover classical beam theory as developed by Mierovitch, some of the theory behind the CDCC code, and the code itself.

Classical Beam Theory

A fourth-order differential equation with two boundary conditions at each end, as developed by Meirovitch (1975:207-213), can be used to find the natural frequencies of an isotropic, cantilevered beam. The "simple-beam theory" is used, in which the rotation of a differential element is considered insignificant in comparison to vertical translation. This theory holds when the beam length to height ratio is 10 or greater, as is the case in the present study. Even when the notches are considered and modeled as two different beams, the thickest sublaminate is only 7.6% of the beam length (4 cm (1.575 in) length in the most extreme case).

In this approach, a one-dimensional differential beam element in flexure will be kept in equilibrium by a shear and a bending moment at both ends and an externally applied transverse load. The shearing force, bending moments and externally applied forces are all considered to be functions of time.

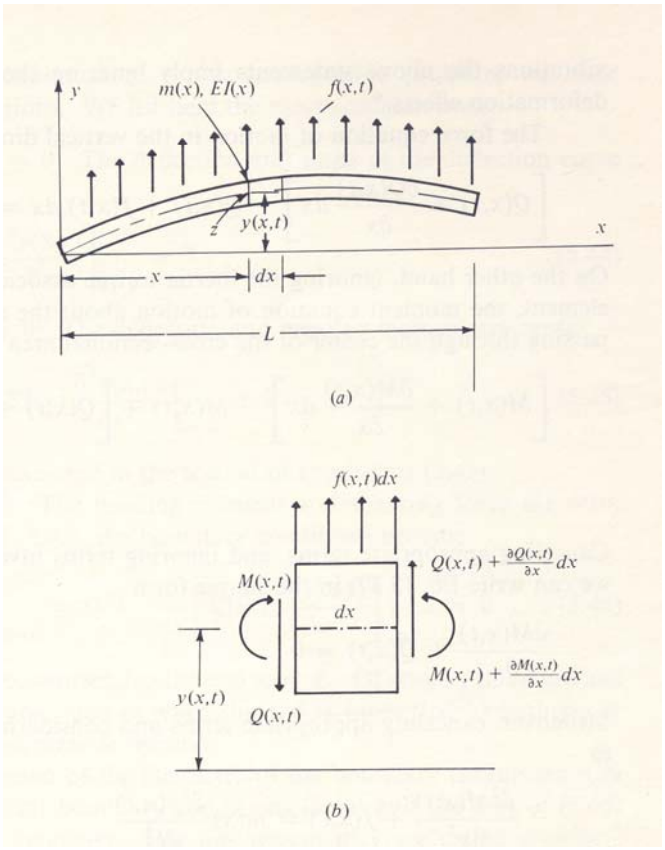

Figure 78. Differential Beam Element (Meirovitch 1975:207)

When the forces are balanced according to the force equation of motion $F = ma$, the equation of motion becomes

$$\left[Q(x,t) + \frac{\partial Q(x,t)}{\partial x}dx\right] - Q(x,t) + f(x,t)dx = m(x)dx\frac{\partial^2 y(x,t)}{\partial\, t^2} \tag{17}$$

where $Q(x,t)$ is the transverse shearing force, $f(x,t)$ is the applied external load, $m(x)$ is the mass per unit length, $y(x,t)$ is transverse displacement during vibration and x is the distance along the beam length from 0 to L. The moment equation of motion then becomes

$$\left[M(x,t) + \frac{\partial M(x,t)}{\partial x}dx\right] - M(x,t) + \left[Q(x,t) + \frac{\partial Q(x,t)}{\partial x}dx\right]dx + f(x,t)dx\frac{dx}{2} = 0 \tag{18}$$

where *M(x,t)* is the reaction moment about the rotational axis. When the element is small, the dx^2 terms are negligible. Eliminating these terms and canceling terms in Equation (18) yields

$$\frac{\partial M(x,t)}{\partial x} + Q(x,t) = 0 \tag{19}$$

Thus Equation (17) and Equation (19) can combine to form

$$-\frac{\partial^2 M(x,t)}{\partial x^2} + f(x,t) = m(x)\frac{\partial^2 y(x,t)}{\partial t^2} \tag{20}$$

which is satisfied over the domain $0 < x < L$. Recall the relation between bending moment and bending deformation

$$M(x,t) = EI(x)\frac{\partial^2 y(x,t)}{\partial x^2} \tag{21}$$

where *E* is the modulus of elasticity and *I(x)* is the moment of inertia of the cross-sectional area at a given distance *x*. Recall for a rectangular beam that the moment of inertia is defined as

$$I = \frac{bh^3}{12} \tag{22}$$

with *b* as the base or width of the beam cross-section and *h* as the height. Combining Equation (20) and Equation (21) and assuming no damping yields the fourth-order differential boundary-value equation of motion

$$-\frac{\partial^2}{\partial x^2}\left[EI(x)\frac{\partial^2 y(x,t)}{\partial x^2}\right] + f(x,t) = m(x)\frac{\partial^2 y(x,t)}{\partial t^2} \qquad 0 < x < L \tag{23}$$

To find the natural frequencies of the cantilevered beam, the applied external force must be equal to zero.

The boundary conditions for the clamped end at $x = 0$ are zero displacement and zero slope:

$$y(0,t) = 0 \tag{24}$$

$$\left.\frac{\partial y(x,t)}{\partial x}\right|_{x=0} = 0 \tag{25}$$

Likewise, boundary conditions for the free end at $x = L$ are that the curvature and its derivative are zero:

$$\left. EI(x)\frac{\partial^2 y(x,t)}{\partial x^2}\right|_{x=L} = 0 \tag{26}$$

$$\left.\frac{\partial}{\partial x}\left[EI(x)\frac{\partial^2 y(x,t)}{\partial x^2}\right]\right|_{x=L} = 0 \tag{27}$$

Considering the free vibration defined as $f(x,t) = 0$, the solution to Equation (23) is separable in space and time, so the separation of variables method is used where

$$y(x,t) = Y(x)F(t) \tag{28}$$

and $F(t)$ is the harmonic oscillation with a frequency of ω. $Y(x)$ is an x-dependent displacement function. Thus, the eigenvalue problem formulation reduces to the differential equation

$$\frac{d^2}{dx^2}\left[EI(x)\frac{d^2Y(x)}{dx^2}\right] = \omega^2 m(x)Y(x) \qquad 0 < x < L \tag{29}$$

where the function $Y(x)$ must satisfy the previously stated boundary conditions.

For a uniform beam of constant modulus of elasticity, moment of inertia and mass over the range $0 < x < L$, the differential equation reduces to

$$\frac{d^4Y(x)}{dx} - \beta^4 Y(x) = 0 \tag{30}$$

where

$$\beta^4 = \frac{\omega^2 m}{EI} \tag{31}$$

The general solution to Equation (30) is

$$Y(x) = C_1 \sin \beta x + C_2 \cos \beta x + C_3 \sinh \beta x + C_4 \cosh \beta x \tag{32}$$

where C_i are unknown coefficients that can be found by solving the boundary conditions. Using the free-end boundary conditions

$$\left.\frac{d^2Y(x)}{dx^2}\right|_{x=L} = 0 \tag{33}$$

$$\left.\frac{d^3Y(x)}{dx^3}\right|_{x=L} = 0 \tag{34}$$

the following simultaneous equations are obtained

$$C_1(\sin \beta L + \sinh \beta L) + C_2(\cos \beta L + \cosh \beta L) = 0 \tag{35}$$

$$C_1(\cos \beta L + \cosh \beta L) - C_2(\sin \beta L - \sinh \beta L) = 0 \tag{36}$$

Equation (36) can be solved for C_2 in terms of C_1 and inserted into Equation (32) to yield

$$Y(x) = \frac{C_1}{\sin \beta L - \sinh \beta L}[(\sin \beta L - \sinh \beta L)(\sin \beta x - \sinh \beta x) + (\cos \beta L + \cosh \beta L)(\cos \beta x - \cosh \beta x)] \tag{37}$$

and

$$C_1[(\sin \beta L + \sinh \beta L)(\sin \beta L - \sinh \beta L) + (\cos \beta L + \cosh \beta L)^2] = 0 \qquad (38)$$

In order for a nontrivial solution to exist, $C_1 \neq 0$ and the characteristic equation must be

$$\cos \beta L \cosh \beta L = -1 \qquad (39)$$

Equation (39) can be solved numerically to find an infinite set of resonant eigenvalues β_r. When no forcing function exists, the resonant modes are the same as the natural modes. To find the natural frequencies from the resonant eigenvalues, the following relation, with material properties expressed in English units, is used:

$$\omega_n = \beta_r^2 \sqrt{\frac{EI}{mL^4}} \qquad r = 1, 2, \ldots \qquad (40)$$

The displacement function equation (Equation (37)) can then be expressed as

$$Y_r = \frac{C_1}{(\sin \beta_r L - \sinh \beta_r L)}[(\sin \beta_r L - \sinh \beta_r L)(\sin \beta_r x - \sinh \beta_r x) + (\cos \beta_r L + \cosh \beta_r L)(\cos \beta_r x - \cosh \beta_r x)] \qquad (41)$$

which represents the natural modes.

The resonant eigenvalues for an isotropic cantilevered beam are as follows

Mode	*Resonant Eigenvalues*
1	1.875
2	4.694
3	7.855
4	10.966
5	14.137
6	17.279
7	20.42
8	23.562

Table 26. Resonant Eigenvalues for Vibration Modes

The mode shapes for the first eight bending modes are as follows

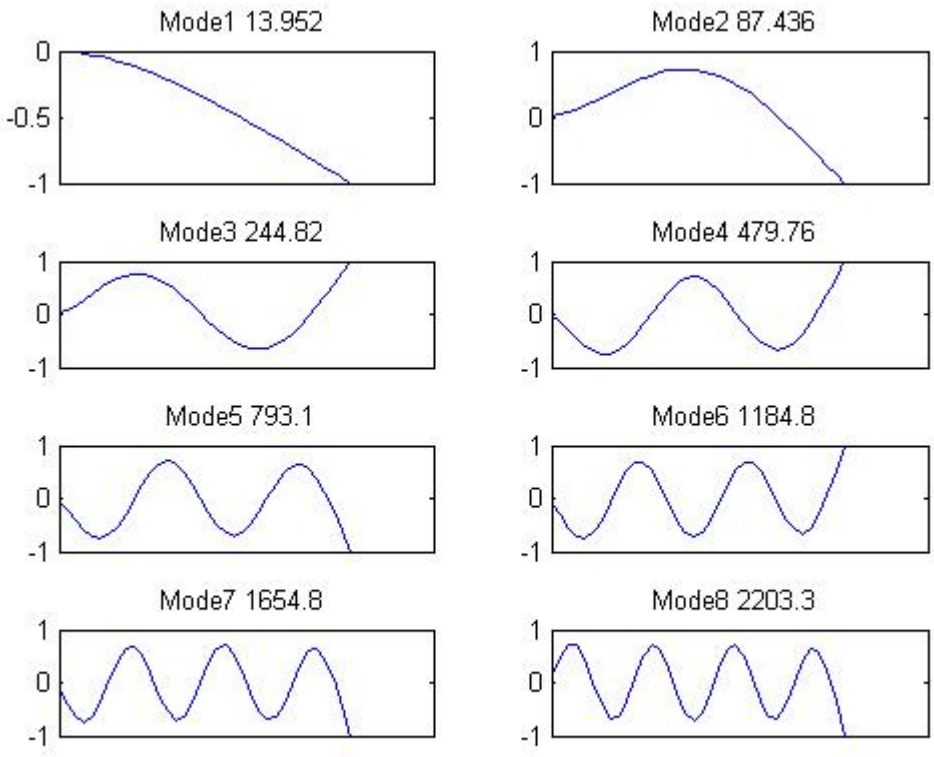

Figure 79. First eight mode shapes for a cantilever beam.
Corresponding frequencies refer to a 12-inch aluminum 2024-T3 beam.

MATLAB Code

The CDCC code was written in MATLAB, and yields a very good approximation of the location of bending modes in the frequency spectrum. This code was based on a finite element approach, the main concepts of which are outlined on the following pages. This outline is developed as according to Mech 719 class notes, taught by Dr. Cobb. Recall from Bernoulli-Euler beam theory a beam element:

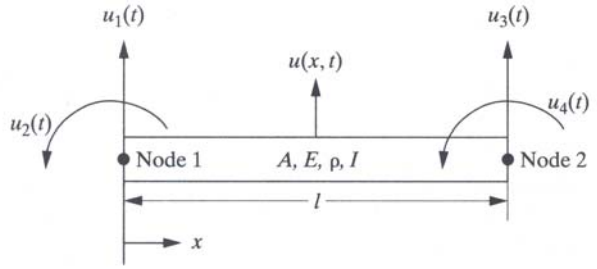

Figure 80. Finite element model beam element (Inman, 2001: 547)

This element illustrates the two transverse coordinates, $u_1(t)$ and $u_3(t)$, and two slope coordinates, $u_2(t)$ and $u_4(t)$, used to illustrate the vibration of the beam.

The equation of motion obtained from a Lagrange function for this beam element is

$$\rho A \frac{\partial u}{\partial t^2} + EI \frac{\partial^4 u}{\partial x^4} = 0 \tag{42}$$

One can then use the Rayleigh Ritz Method or Assumed Modes Method to choose admissible functions, which are functions that satisfy the boundary conditions for a solution in the form of

$$u(x,t) = \sum_{i=1}^{4} \psi_i(x) \upsilon_i(t) \tag{43}$$

The functions of $\psi_i(x)$ satisfy the following boundary conditions

$$\psi_1(0) = 1 \qquad \psi_1'(0) = \psi_1(L) = \psi_1'(L) = 0 \tag{44}$$

$$\psi_2'(0) = 1 \qquad \psi_2(0) = \psi_2(L) = \psi_2'(L) = 0 \tag{45}$$

$$\psi_3(L) = 1 \qquad \psi_3(0) = \psi_3'(0) = \psi_3'(L) = 0 \tag{46}$$

$$\psi_4'(L) = 1 \qquad \psi_4(0) = \psi_4'(0) = \psi_4(L) = 0 \tag{47}$$

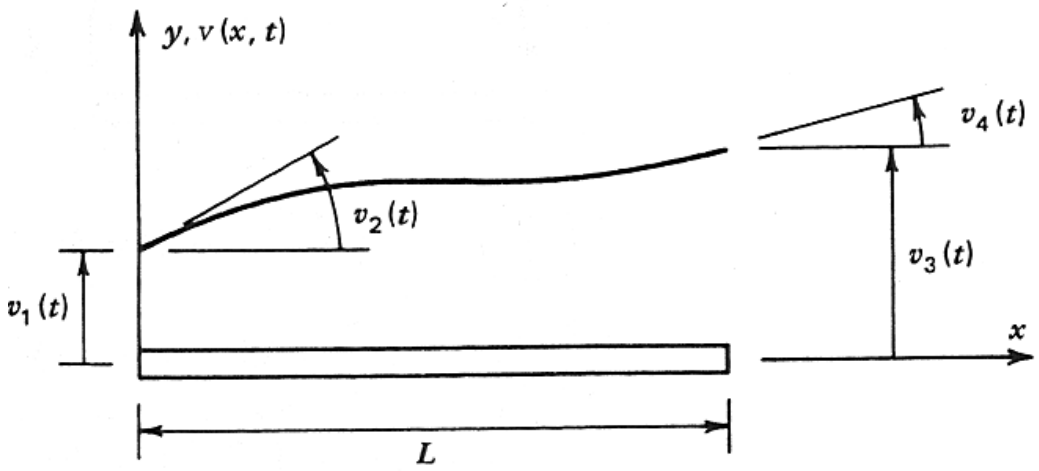

Figure 81. Assumed Modes Method
Note: "v" in the figure is "u" in Equation 43

The mode shape for a cantilevered beam in accordance with Bernoulli-Euler beam theory is

$$u(x) = c_1 + c_2\left(\frac{x}{L}\right) + c_3\left(\frac{x}{L}\right)^2 + c_4\left(\frac{x}{L}\right)^3 \tag{48}$$

where the c_i constant values are specific to each mode. The first four mode shape functions are as follows.

$$\psi_1 = 1 - 3\left(\frac{x}{L}\right)^2 + 2\left(\frac{x}{L}\right)^3 \tag{49}$$

$$\psi_2 = x - 2L\left(\frac{x}{L}\right)^2 + L\left(\frac{x}{L}\right)^3 \tag{50}$$

$$\psi_3 = 3\left(\frac{x}{L}\right)^2 - 2\left(\frac{x}{L}\right)^3 \tag{51}$$

$$\psi_4 = -L\left(\frac{x}{L}\right)^2 + L\left(\frac{x}{L}\right)^3 \tag{52}$$

When one takes the solution from Equation (43) and plugs it into Equation (42), the solution can then be integrated over the length of the beam and multiplied by each ψ_i to yield an equation in the same form as

$$[m]\ddot{u} + [k]u = 0 \tag{53}$$

Thus, the elemental *k* and *m* matrices are found to be

$$k_{ij} = \int_0^L EI\psi_i''\psi_j'' dx \tag{54}$$

$$m_{ij} = \int_0^L \rho A \psi_i \psi_j dx \tag{55}$$

The elemental matrices of each beam element in the model can then be combined to form the mass and stiffness matrices of the whole structure. The following matrix is then formed:

$$\begin{bmatrix} 0 & I \\ -M^{-1}K & -M^{-1}C \end{bmatrix} \tag{56}$$

where *M*, *K* and *C* represent the mass, stiffness and damping matrices, respectively, for the whole system. The eigenvalues and eigenvectors of this matrix are the resonant frequencies and mode shapes for the structure. The code uses this method to determine the first eight natural frequencies for a beam of given specifications and to plot the mode shapes for these frequencies.

To account for the notch in the experimental beams, no actual attempt to model the notch was attempted. Rather, the notched portion of the beam was modeled as having a different effective moment of inertia, defined as

$$I_{notched\_region} = \frac{b(h_u^{\,3} + h_l^{\,3})}{12} \tag{57}$$

where h_u and h_l are the heights of the upper and lower sublaminates in the notched region. This reduction in the moment of inertia reduced the stiffness of the model, effectively representing the damaged area. The specifications of the CDCC code, previously mentioned in section 2.2.1, are summarized below.

Model Specifications:

- 36 elements along beam length
- Elements in notched region were 0.26247 inches long, regardless of notch length. Remaining elements were spread evenly over the remaining (un-notched) length of the beam.
- Exception is the "transition" area on either end of the notch→ three transition elements on either end of the notched region. Moment of inertia is linearly stepped from the notched value to the un-notched value to avoid discontinuities. The size of these transition elements is also 0.26247 inches, the same size as the elements in the notched region.

CDCC Code

```
% FEM analytical solution
% Written by Dr Richard Cobb
% Modified by Frances Durham
% Modified by Aaron Chmiel, June 2005
% Modified by Jessica Chronister, Nov 2005

% This code computes the natural frequencies and mode shapes of a
% cantilevered, simple, free-free, and clamped beam with or without
% an eccentric notch, and no damping.

clear % clears the workspace

beam_length = 12; % Length of beam in inches
h=.25 ;         % thickness of beam in inches
h_u=h/2-0.006;  % thickness of portion of beam above the notch in
inches
h_l=h/2-0.006;% thickness of portion of beam below the notch in inches
b=1.5;          % Width of beam in inches
E = 10000000;   % lb-f/in^2 (psi)
rho = 0.0975/32.174/12; % Density of beam material in lb*s^2/in^4
n_els = 36;             % Number of elements in beam
n_nodes = n_els + 1;    % Number of nodes in beam
j = n_nodes*2;          % reference value
n_crack_tip_els = 3;    % number of transitional elements

location = input('Location of crack (0) no crack, (1) clamped end, (2)
middle, (3) free end: ');

% if there is no crack
if (location==0)
    beam_length_cm = input('Length of beam in cm: ');
    beam_length = beam_length_cm/2.54; % converts the length of the
beam to inches
    h = 1/16;                          % thickness of the beam in
inches
% If there is a crack
else
    crack_length_cm = input('Length of crack in cm: ');
    crack_length = crack_length_cm/2.54;% convert crack length to
inches
    n_crack_els = crack_length_cm*3/2;  % sets number of elements in
crack
    L_crack = crack_length/n_crack_els; % length of crack elements
    L_crack_tip_els=L_crack;            % length of transitional
elements
end

% set inital values
A(1:n_els) = b*h;               % crosssectional area of beam
I(1:n_els) = b*(h^3)/12;        % moment of inertia
L(1:n_els) = beam_length/n_els;  % inital length of elements

% crack at fixed end
if (location==1)
```

```
    L_undamaged = (beam_length - crack_length-
n_crack_tip_els*L_crack_tip_els)/(n_els-n_crack_els-n_crack_tip_els);
    L(1:n_crack_els) = L_crack;
    L(n_crack_els+1:n_crack_els+n_crack_tip_els) = L_crack_tip_els;
    L(n_crack_els+n_crack_tip_els+1:n_els) = L_undamaged;
    crackel1=1;
    crackel2=n_crack_els;
    for k=1:n_crack_els
            I(k) = b*(h_u^3+h_l^3)/12;
            A(k) = b*(h_u+h_l);
    end
    slope = (I(n_crack_els+1)-I(n_crack_els))/(n_crack_tip_els+1);
    for k=1:n_crack_tip_els
        I(n_crack_els+k) = I(n_crack_els)+k*slope;
    end
end
% crack in the middle
if (location==2)
    L_undamaged = (beam_length-crack_length-
2*n_crack_tip_els*L_crack_tip_els)/(n_els-n_crack_els-
2*n_crack_tip_els);
    n_els_undamaged = n_els-n_crack_els-2*n_crack_tip_els;
    L(1:n_els_undamaged/2)=L_undamaged;
    L(n_els_undamaged/2+1:n_els_undamaged/2+n_crack_tip_els) =
L_crack_tip_els;

L(n_els_undamaged/2+n_crack_tip_els+1:n_els_undamaged/2+n_crack_tip_els
+n_crack_els) = L_crack;
    L(n_els-n_els_undamaged/2-n_crack_tip_els+1:n_els-
n_els_undamaged/2) = L_crack_tip_els;
    L(n_els-n_els_undamaged/2:n_els) = L_undamaged;
    crackel1=n_els_undamaged/2+n_crack_tip_els+1;
    crackel2=crackel1+n_crack_els;
    for
k=n_els_undamaged/2+n_crack_tip_els+1:n_els_undamaged/2+n_crack_tip_els
+n_crack_els
        I(k) = b*(h_u^3+h_l^3)/12;
        A(k) = b*(h_u+h_l);
    end
    slope = (I(1)-
I(n_els_undamaged/2+n_crack_tip_els+1))/(n_crack_tip_els+2);
    for k = 1:n_crack_tip_els
        I(n_els_undamaged/2+k) = I(n_els_undamaged/2)-k*slope;
        I(n_els_undamaged/2+n_crack_tip_els+k) =
I(n_els_undamaged/2+n_crack_tip_els+n_crack_els)+k*slope;
    end
end
% crack at the free end
if (location==3)
    L_undamaged = (beam_length - crack_length-
(n_crack_tip_els+1)*L_crack_tip_els)/(n_els-n_crack_els-
n_crack_tip_els);
    L(1:n_els-n_crack_tip_els-n_crack_els-2) = L_undamaged;
    L(n_els-n_crack_tip_els-n_crack_els-1:n_els-n_crack_els-2) =
L_crack_tip_els;
    L(n_els-n_crack_els-1:n_els-1) = L_crack;
```

```
    L(n_els) = L_crack_tip_els;
    crackel2 = n_els-1;
    crackel1 = crackel2-n_crack_els;
    for k = n_els-n_crack_els-1:n_els-1
        I(k) = b*(h_u^3+h_l^3)/12;
        A(k) = b*(h_u+h_l);
    end
    slope = (I(1)-I(n_els-1))/(n_crack_tip_els+1);
    for k = 1:n_crack_tip_els
        I(n_els-n_crack_els-1-k) = I(n_els-1)+(n_crack_tip_els-
k)*slope;
    end
end

% set position of nodes
pos(1) = 0;
for k = 1:n_els-1
    pos(k+1) = pos(k)+L(k);
end

% create mass and stiffness matrices
M = zeros(j);K = zeros(j);
for i = 1:2:j-3
    k = (i+1)/2;
    mel = (rho*A(k)*L(k)/420)*[156 22*L(k) 54 -13*L(k);...
                               22*L(k) 4*(L(k)^2) 13*L(k) -
3*(L(k)^2);...
                               54 13*L(k) 156 -22*L(k);...
                               -13*L(k) -3*(L(k)^2) -22*L(k)
4*(L(k)^2)];

    kel = (E*I(k)/(L(k)^3))*[12 6*L(k) -12 6*L(k);...
                            6*L(k) 4*(L(k)^2) -6*L(k) 2*(L(k)^2);...
                            -12 -6*L(k) 12 -6*L(k);...
                            6*L(k) 2*(L(k)^2) -6*L(k) 4*(L(k)^2)];

    M(i:i+3,i:i+3) = M(i:i+3,i:i+3) + mel; % insert values into mass
matrix
    K(i:i+3,i:i+3) = K(i:i+3,i:i+3) + kel; % insert values into
stiffness matrix
end

% Apply Boundary Condition
bound = input('Boundary condition (1) cantilever, (2) clamped, (3)
simple, (4) free: ');

if (bound == 1)      % Cantilever
    M = M(3:j,3:j);  % removes first two rows and columns from mass
matrix
    K = K(3:j,3:j);  % removes first two rows and columns from
stiffness matrix
    f = 1:2:2*n_els; % index. used to take proper values from
eigenvector
elseif (bound == 2)     % Clamped on both ends
    M = M(3:j-2,3:j-2); % removes first two, and last two rows and
columns from mass matrix
```

```
    K = K(3:j-2,3:j-2); % removes first two, and last two rows and
columns from stiffness matrix
    f = 1:2:2*n_els-2;  % index. used to take proper values from
eigenvector
    pos = pos(1:n_els-1); % shortens pos for proper plotting
elseif (bound == 3)   % Simple support both ends
    M = M(2:j,2:j);   % removes first row and column from mass matrix
    K = K(2:j,2:j);   % removes first row and column from stiffness
matrix
    M(:,j-2) = [];    % removes column from mass matrix
    M(j-2,:) = [];    % removes row from mass matrix
    K(:,j-2) = [];    % removes column from stiffness matrix
    K(j-2,:) = [];    % removes row from stiffness matrix
    f = 2:2:2*n_els-1;% index. used to take proper values from
eigenvector
    pos = pos(1:n_els-1); % shortens pos for proper plotting
elseif (bound == 4)  % Free both ends
    f = 1:2:2*n_els; % index. used to take proper values from
eigenvector
    %disp('FREE BEam')
elseif (bound == 5)     % Clamped on right, simple on left
    M = M(2:j-2,2:j-2); % removes first, and last two rows and columns
from mass matrix
    K = K(2:j-2,2:j-2); % removes first, and last two rows and columns
from stiffness matrix
    f = 1:2:2*n_els;    % index. used to take proper values from
eigenvector
end

A = [M^-1*K];              % create matrix
[asize,other] = size(A);   % find size of A, used for reference
[V,D] = eig(A);            % Find eigenvectors/values
for i = 1:asize
   Doh(i) = D(i,i);
   Dohabs(i) = sqrt(Doh(i))/2/pi;
end

% Plot Mode shapes and frequencies
figure(2)
% 1st mode plot
subplot(4,2,1)
M1=V(:,asize);
m1hz=sqrt(D(asize,asize))/2/pi;
mode1=M1(f);
mode1=mode1/max(abs(mode1));
plot(pos,mode1);
title(sprintf('Mode1 %3.3f ',m1hz))
set(gca,'XTick',[])
% 2nd mode plot
subplot(4,2,2)
M2=V(:,asize-1);
m2hz=sqrt(D(asize-1,asize-1))/2/pi;
mode2=M2(f);
mode2=mode2/max(abs(mode2));
plot(pos,mode2);
title(sprintf('Mode2 %3.3f ',m2hz))
```

```
set(gca,'XTick',[])
% 3rd mode plot
subplot(4,2,3)
M3=V(:,asize-2);
m3hz=sqrt(D(asize-2,asize-2))/2/pi;
mode3=M3(f);
mode3=mode3/max(abs(mode3));
plot(pos,mode3);
title(sprintf('Mode3 %3.2f ',m3hz))
set(gca,'XTick',[])
% 4th mode plot
subplot(4,2,4)
M4=V(:,asize-3);
m4hz=sqrt(D(asize-3,asize-3))/2/pi;
mode4=M4(f);
mode4=mode4/max(abs(mode4));
plot(pos,mode4);title(sprintf('Mode4 %3.2f ',m4hz))
set(gca,'XTick',[])
% 5th mode plot
subplot(4,2,5)
M5=V(:,asize-4);
m5hz=sqrt(D(asize-4,asize-4))/2/pi;
mode5=M5(f);
mode5=mode5/max(abs(mode5));
plot(pos,mode5);
title(sprintf('Mode5 %3.1f ',m5hz))
set(gca,'XTick',[])
% 6th mode plot
subplot(4,2,6)
M6=V(:,asize-5);
m6hz=sqrt(D(asize-5,asize-5))/2/pi;
mode6=M6(f);
mode6=mode6/max(abs(mode6));
plot(pos,mode6);
title(sprintf('Mode6 %3.1f ',m6hz))
set(gca,'XTick',[])
% 7th mode plot
subplot(4,2,7)
M7=V(:,asize-6);
m7hz=sqrt(D(asize-6,asize-6))/2/pi;
mode7=M7(f);
mode7=mode7/max(abs(mode7));
plot(pos,mode7);
title(sprintf('Mode7 %3.1f ',m7hz))
set(gca,'XTick',[])
% 8th mode plot
subplot(4,2,8)
M8=V(:,asize-7);
m8hz=sqrt(D(asize-7,asize-7))/2/pi;
mode8=M8(f);
mode8=mode8/max(abs(mode8));
plot(pos,mode8);
title(sprintf('Mode8 %3.1f ',m8hz))
set(gca,'XTick',[])

% Calculate node and anitnode crossings
```

```
if (location ~= 0) % ignore if no crack
% 2nd mode
i=0;
p=0;
mode2_crossedanti=0;
mode2_crossednode=0;
for k=2:n_els-1
    if mode2(k-1)<=mode2(k) & mode2(k+1)<=mode2(k)
        i=i+1;
        mode2_maxcurve(i)=pos(k);
        if k>=crackel1 & k<=crackel2
            mode2_crossedanti=mode2_crossedanti+1;
        end
    elseif mode2(k-1)>=mode2(k) & mode2(k+1)>=mode2(k)
            i=i+1;
            mode2_maxcurve(i)=pos(k);
        if k>=crackel1 & k<=crackel2
            mode2_crossedanti=mode2_crossedanti+1;
        end
    end
    if mode2(k)<=0 & mode2(k+1)>=0
        p=p+1;
        mode2_nodes(p)=pos(k);
        mode2_crossednode=mode2_crossednode+1;
    elseif mode2(k)>=0 & mode2(k+1)<=0
        p=p+1;
        mode2_nodes(p)=pos(k);
        mode2_crossednode=mode2_crossednode+1;
    end
end
% 3rd mode
i=0;
p=0;
mode3_crossedanti=0;
mode3_crossednode=0;
for k=3:n_els-1
    if mode3(k-1)<=mode3(k) & mode3(k+1)<=mode3(k)
        i=i+1;
        mode3_maxcurve(i)=pos(k);
        if k>=crackel1 & k<=crackel2
            mode3_crossedanti=mode3_crossedanti+1;
        end
    elseif mode3(k-1)>=mode3(k) & mode3(k+1)>=mode3(k)
            i=i+1;
        if k>=crackel1 & k<=crackel2
            mode3_crossedanti=mode3_crossedanti+1;
        end
            mode3_maxcurve(i)=pos(k);
    end
    if mode3(k)<=0 & mode3(k+1)>=0
        p=p+1;
        mode3_nodes(p)=pos(k);
        mode3_crossednode=mode3_crossednode+1;
   elseif mode3(k)>=0 & mode3(k+1)<=0
            p=p+1;
            mode3_nodes(p)=pos(k);
```

```
        mode3_crossednode=mode3_crossednode+1;
    end
end
% 4th mode
i=0;
p=0;
mode4_crossedanti=0;
mode4_crossednode=0;
for k=2:n_els-1
    if mode4(k-1)<=mode4(k) & mode4(k+1)<=mode4(k)
        i=i+1;
        mode4_maxcurve(i)=pos(k);
        if k>=crackel1 & k<=crackel2
            mode4_crossedanti=mode4_crossedanti+1;
        end
    elseif mode4(k-1)>=mode4(k) & mode4(k+1)>=mode4(k)
            i=i+1;
            mode4_maxcurve(i)=pos(k);
        if k>=crackel1 & k<=crackel2
            mode4_crossedanti=mode4_crossedanti+1;
        end
    end
    if mode4(k)<=0 & mode4(k+1)>=0
        p=p+1;
        mode4_nodes(p)=pos(k);
        mode4_crossednode=mode4_crossednode+1;
    elseif mode4(k)>=0 & mode4(k+1)<=0
            p=p+1;
            mode4_nodes(p)=pos(k);
        mode4_crossednode=mode4_crossednode+1;
    end
end
% 5th mode
i=0;
p=0;
mode5_crossedanti=0;
mode5_crossednode=0;
for k=2:n_els-1
    if mode5(k-1)<=mode5(k) & mode5(k+1)<=mode5(k)
        i=i+1;
        mode5_maxcurve(i)=pos(k);
        if k>=crackel1 & k<=crackel2
            mode5_crossedanti=mode5_crossedanti+1;
        end
    elseif mode5(k-1)>=mode5(k) & mode5(k+1)>=mode5(k)
            i=i+1;
            mode5_maxcurve(i)=pos(k);
        if k>=crackel1 & k<=crackel2
            mode5_crossedanti=mode5_crossedanti+1;
        end
    end
    if mode5(k)<=0 & mode5(k+1)>=0
        p=p+1;
        mode5_nodes(p)=pos(k);
        mode5_crossednode=mode5_crossednode+1;
    elseif mode5(k)>=0 & mode5(k+1)<=0
```

```
            p=p+1;
            mode5_nodes(p)=pos(k);
        mode5_crossednode=mode5_crossednode+1;
    end
end
% 6th mode
i=0;
p=0;
mode6_crossedanti=0;
mode6_crossednode=0;
for k=2:n_els-1
    if mode6(k-1)<=mode6(k) & mode6(k+1)<=mode6(k)
        i=i+1;
        mode6_maxcurve(i)=pos(k);
        if k>=crackel1 & k<=crackel2
            mode6_crossedanti=mode6_crossedanti+1;
        end
    elseif mode6(k-1)>=mode6(k) & mode6(k+1)>=mode6(k)
            i=i+1;
            mode6_maxcurve(i)=pos(k);
        if k>=crackel1 & k<=crackel2
            mode6_crossedanti=mode6_crossedanti+1;
        end
    end
    if mode6(k)<=0 & mode6(k+1)>=0
        p=p+1;
        mode6_nodes(p)=pos(k);
        mode6_crossednode=mode6_crossednode+1;
    elseif mode6(k)>=0 & mode6(k+1)<=0
            p=p+1;
            mode6_nodes(p)=pos(k);
        mode6_crossednode=mode6_crossednode+1;
    end
end
% 7th mode
i=0;
p=0;
mode7_crossedanti=0;
mode7_crossednode=0;
for k=2:n_els-1
    if mode7(k-1)<=mode7(k) & mode7(k+1)<=mode7(k)
        i=i+1;
        mode7_maxcurve(i)=pos(k);
        if k>=crackel1 & k<=crackel2
            mode7_crossedanti=mode7_crossedanti+1;
        end
    elseif mode7(k-1)>=mode7(k) & mode7(k+1)>=mode7(k)
            i=i+1;
            mode7_maxcurve(i)=pos(k);
        if k>=crackel1 & k<=crackel2
            mode7_crossedanti=mode7_crossedanti+1;
        end
    end
    if mode7(k)<=0 & mode7(k+1)>=0
        p=p+1;
        mode7_nodes(p)=pos(k);
```

```
        mode7_crossednode=mode7_crossednode+1;
    elseif mode7(k)>=0 & mode7(k+1)<=0
            p=p+1;
            mode7_nodes(p)=pos(k);
        mode7_crossednode=mode7_crossednode+1;
    end
end
% 8th mode
i=0;
p=0;
mode8_crossedanti=0;
mode8_crossednode=0;
for k=2:n_els-1
    if mode8(k-1)<=mode8(k) & mode8(k+1)<=mode8(k)
        i=i+1;
        mode8_maxcurve(i)=pos(k);
        if k>=crackel1 & k<=crackel2
            mode8_crossedanti=mode8_crossedanti+1;
        end
    elseif mode8(k-1)>=mode8(k) & mode8(k+1)>=mode8(k)
            i=i+1;
            mode8_maxcurve(i)=pos(k);
        if k>=crackel1 & k<=crackel2
            mode8_crossedanti=mode8_crossedanti+1;
        end
    end
    if mode8(k)<=0 & mode8(k+1)>=0
        p=p+1;
        mode8_nodes(p)=pos(k);
        mode8_crossednode=mode8_crossednode+1;
    elseif mode8(k)>=0 & mode8(k+1)<=0
            p=p+1;
            mode8_nodes(p)=pos(k);
        mode8_crossednode=mode8_crossednode+1;
    end
end
% compile node crossings for each mode
nodes_crossed(1)=0;
nodes_crossed(2)=mode2_crossednode;
nodes_crossed(3)=mode3_crossednode;
nodes_crossed(4)=mode4_crossednode;
nodes_crossed(5)=mode5_crossednode;
nodes_crossed(6)=mode6_crossednode;
nodes_crossed(7)=mode7_crossednode;
nodes_crossed(8)=mode8_crossednode;
% Compile antinode crossing for each mode
antinodes_crossed(1)=0;
antinodes_crossed(2)=mode2_crossedanti;
antinodes_crossed(3)=mode3_crossedanti;
antinodes_crossed(4)=mode4_crossedanti;
antinodes_crossed(5)=mode5_crossedanti;
antinodes_crossed(6)=mode6_crossedanti;
antinodes_crossed(7)=mode7_crossedanti;
antinodes_crossed(8)=mode8_crossedanti;
end  % ends node and antinode if statement
```

Appendix B: ABAQUS Model

Two ABAQUS finite element models were designed for use in this study, a plane strain analysis model, and a three-dimensional restricted model. Both models yielded results which matched closely with one another, never differing by more than 2%. The first half of this appendix will give a very basic definition of the difference between the two models, and the second half will show all ABAQUS models.

Two Methods:

Plane Strain Analysis

The plane strain analysis evaluates a two-dimensional plane strain finite element model in which the strain in the z-direction (perpendicular to the beams oscillatory motion) is neglected. This model breaks the structure into two-dimensional elements on the surface of the beam.

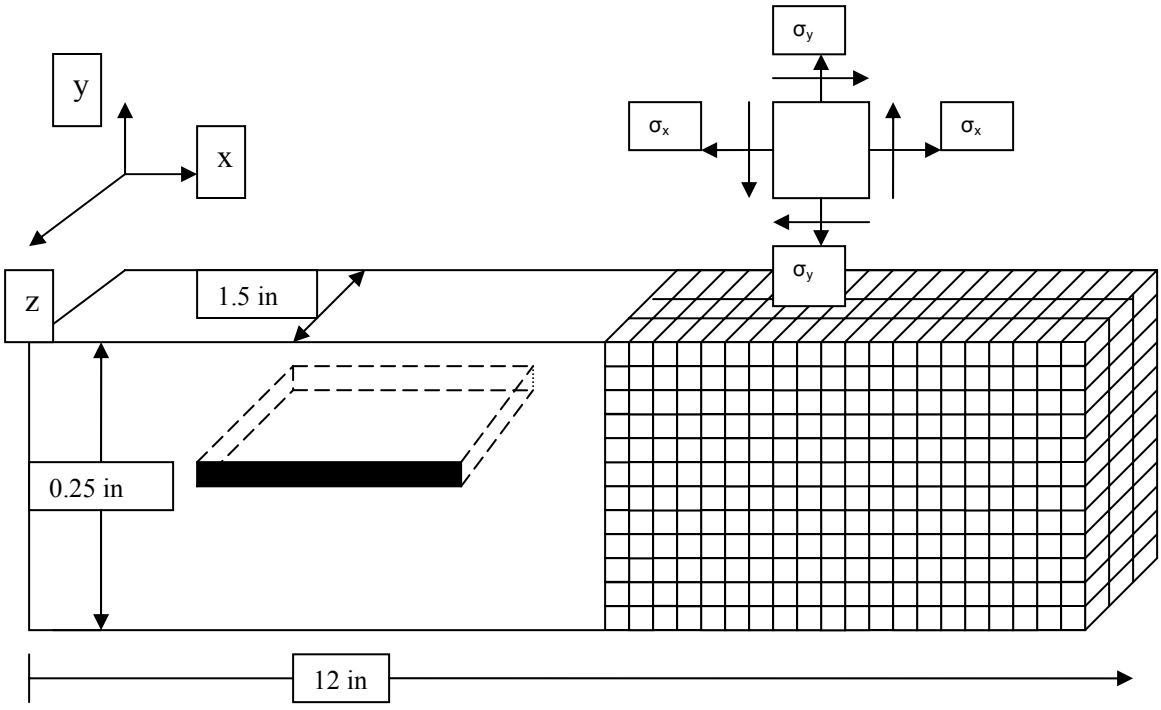

Figure 82. Plane strain model in ABAQUS.

With this model, the elements are only on the surface of the beam. The beam is free to move as it would when an actuator causes vibration in the y-direction, and the strain from each of these elements is used to find the natural frequencies.

For this model in ABAQUS, there were no elements in the width direction and elements were approximately 0.02 inches in depth. Along the length of the beam there were different dimensions for the elements; elements in the notched regions were 0.04 inches long, while the remaining elements were 0.1 inches long. In some cases even longer elements were used so as to not exceed available storage space.

Three-Dimensional Restricted Analysis

The three-dimensional restricted analysis used the same basic theory as the plane strain model, but with three-dimensional brick elements. Motion of these brick elements was restrained in the z-direction at the yellow surface and the one parallel to it. The brick elements inside the beam were free to move. The plane strain on the surfaces of the brick elements was calculated. For this model, the dimensions were the same as in the two-dimensional model, but with a width of 0.1 inches. This method obviously required many more elements, which in turn gave it a longer run time. Because the results of the two models were very close, and the plane strain model was slightly faster computationally, plane strain results were used for comparison with the experimental and CDCC results.

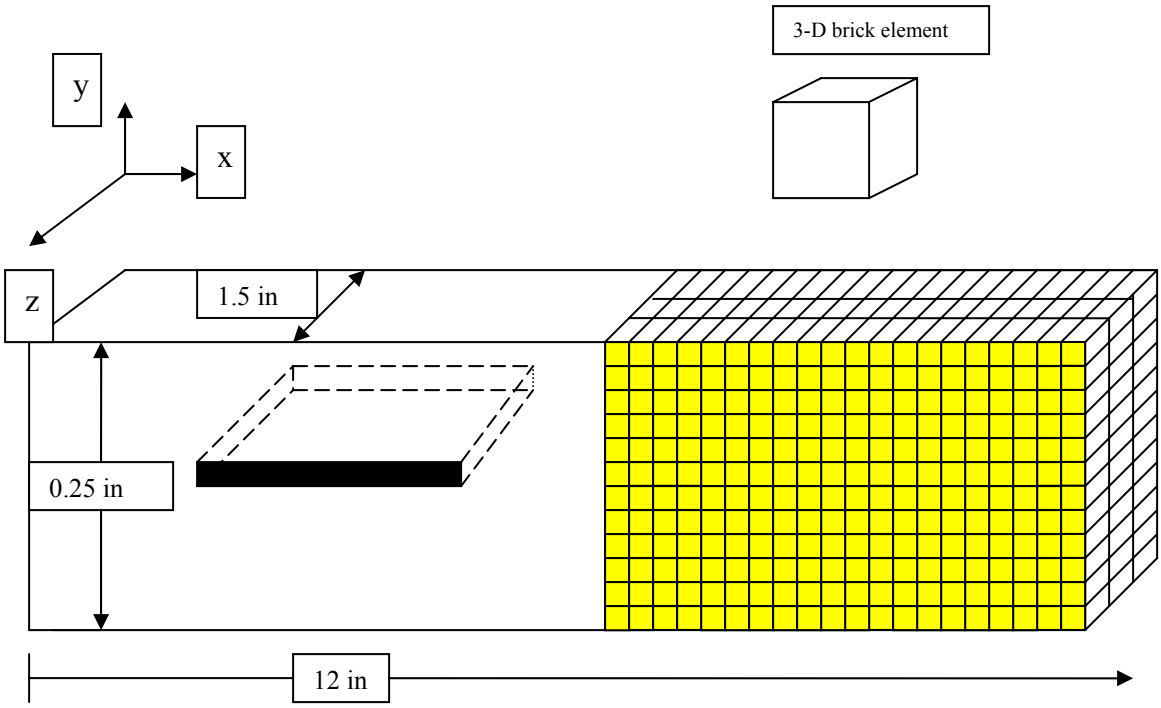

Figure 83. 3-dimensional restricted movement model in ABAQUS

3D Restrained Model Results:

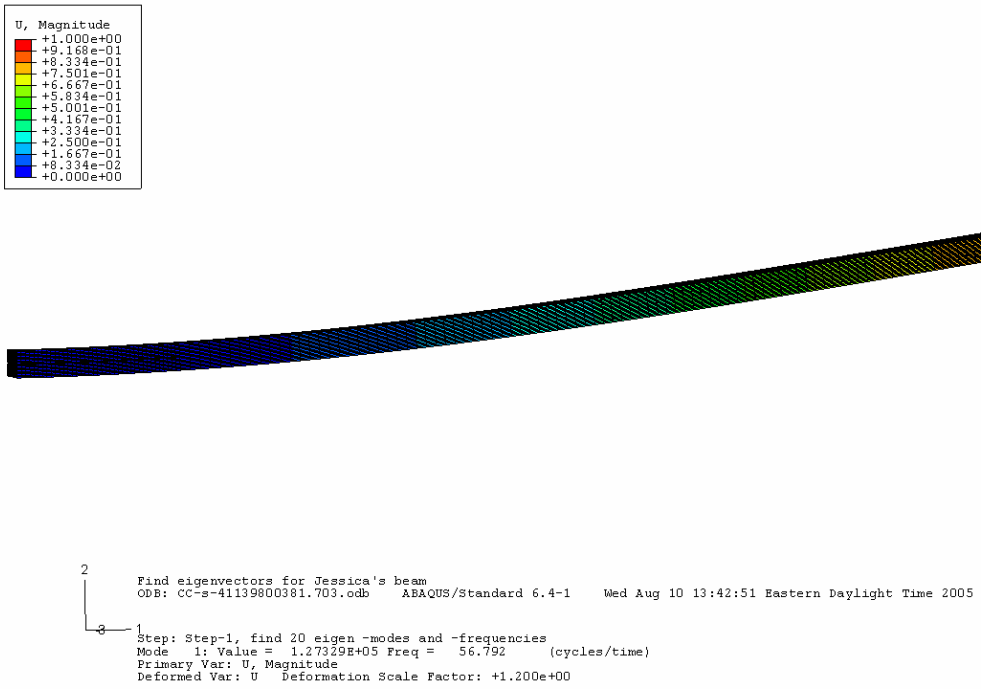

Figure 84. First mode, 4 cm (1.575 in) clamped end notch

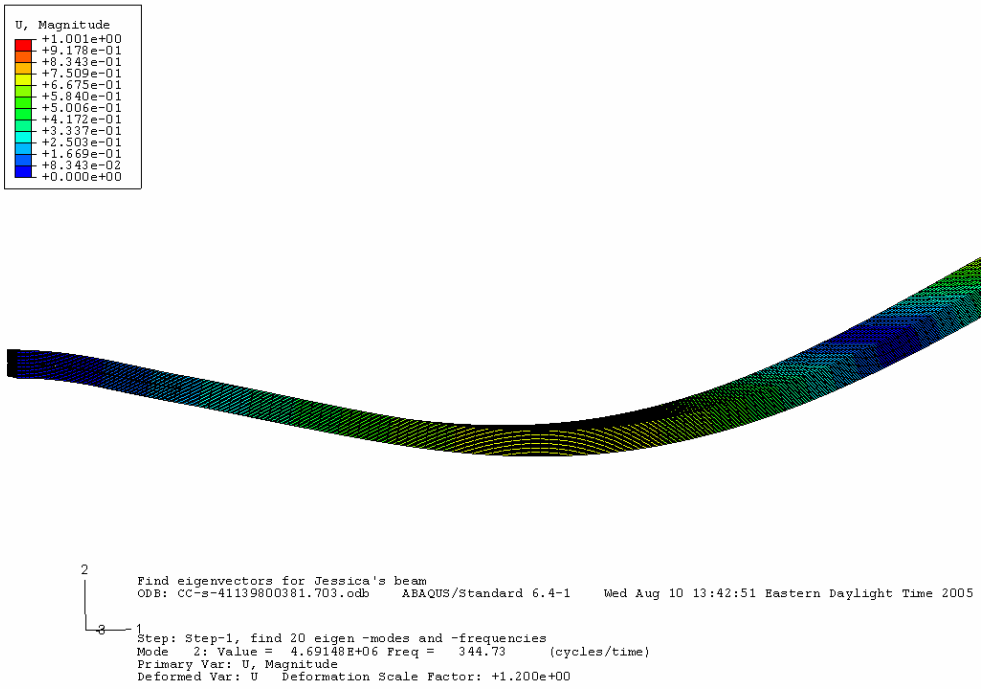

Figure 85. Second mode, 4 cm (1.575 in) clamped end notch

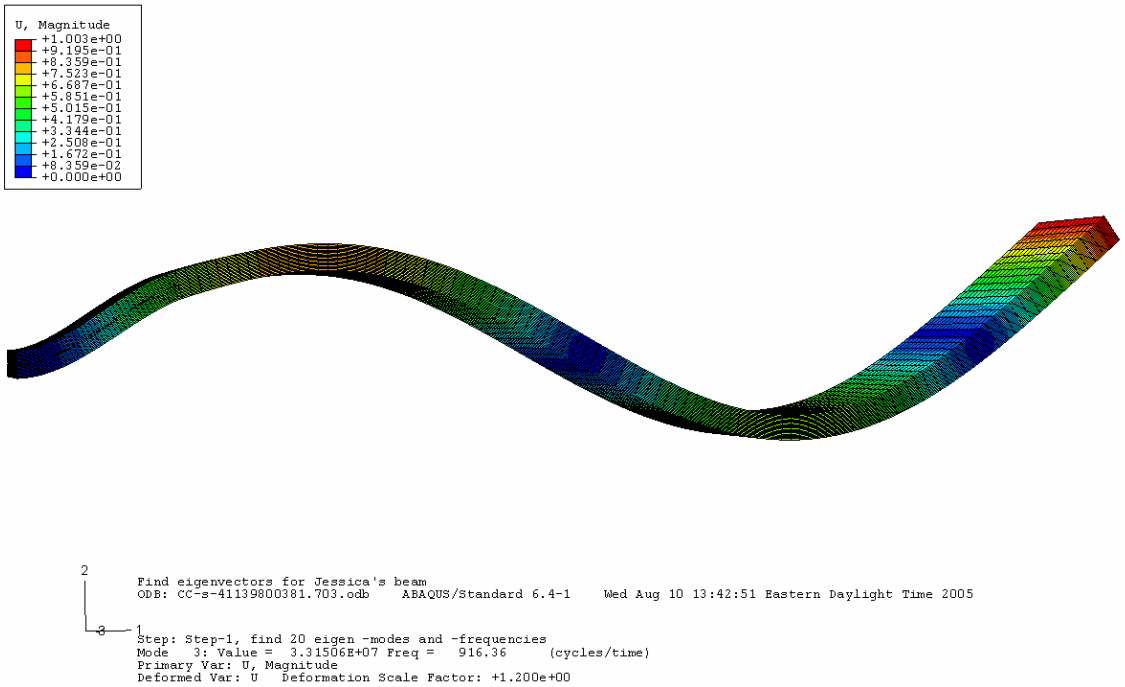

Figure 86. Third mode, 4 cm (1.575 in) clamped end notch

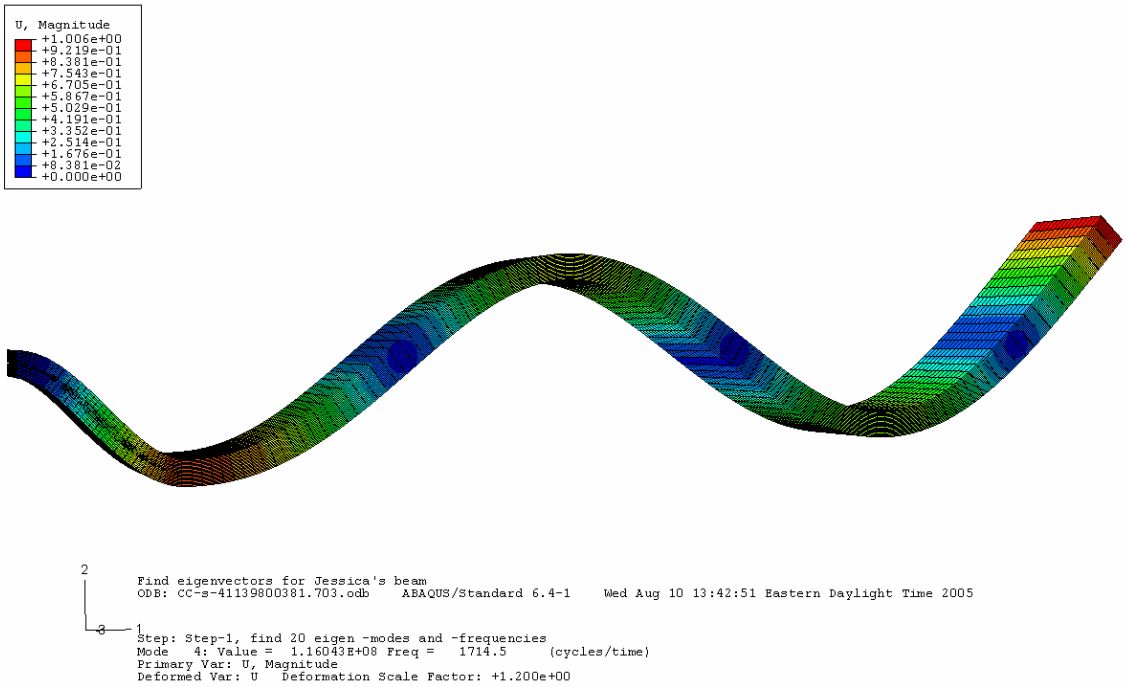

Figure 87. Fourth mode, 4 cm (1.575 in) clamped end notch

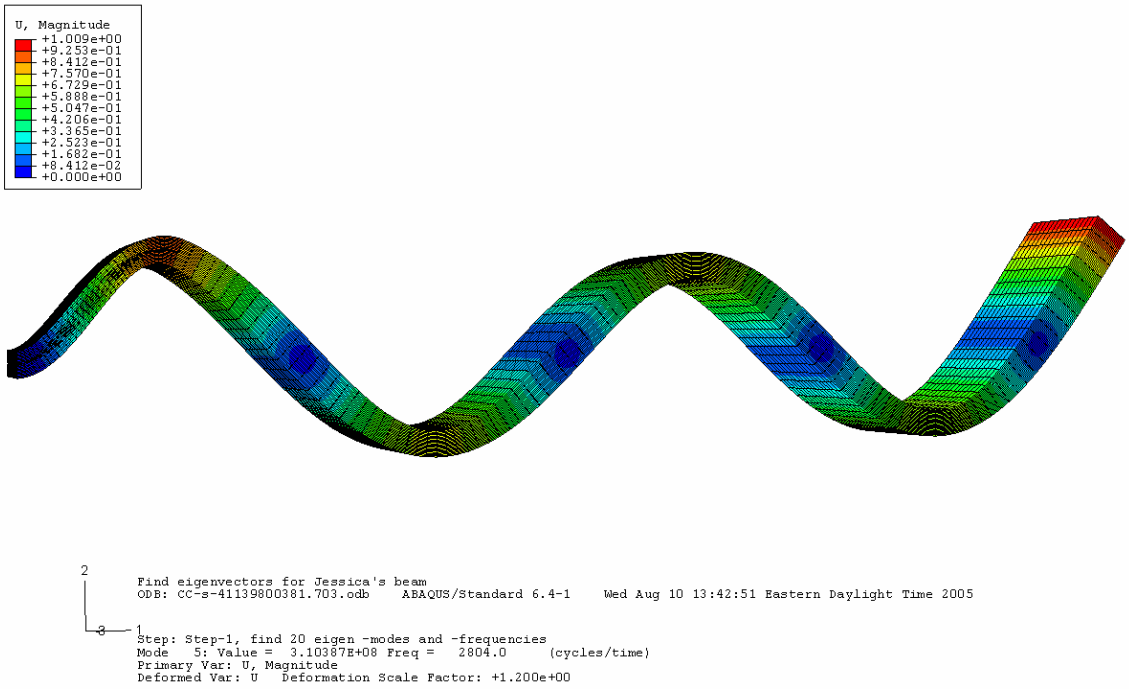

Figure 88. Fifth mode, 4 cm (1.575 in) clamped end notch

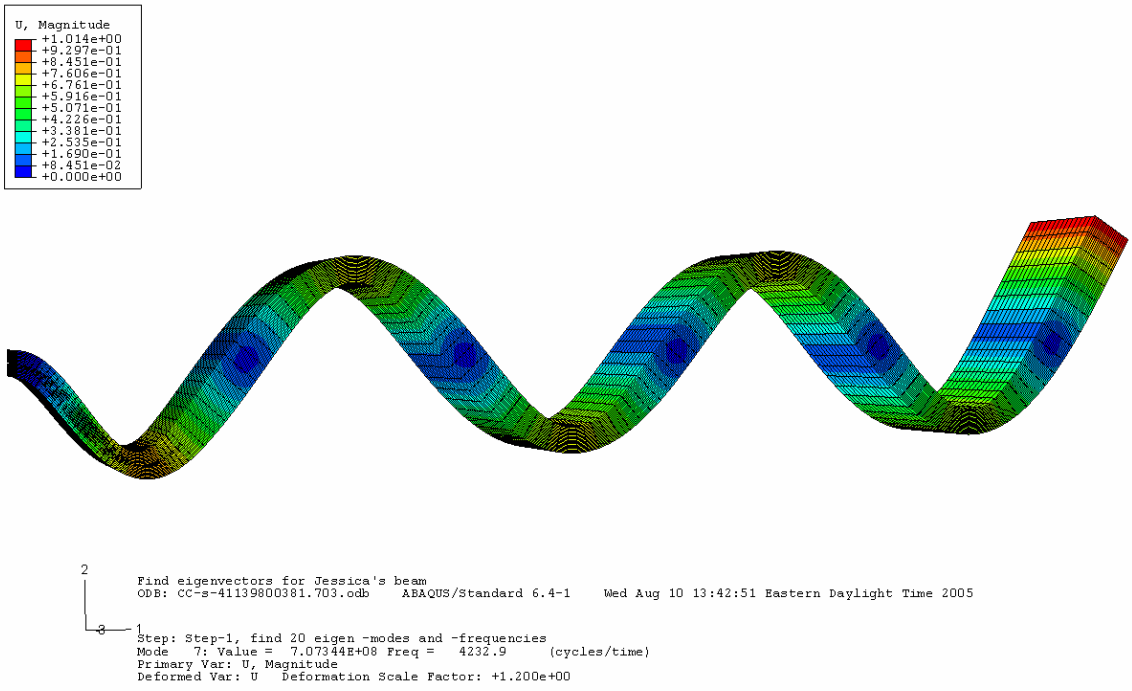

Figure 89. Sixth mode, 4 cm (1.575 in) clamped end notch

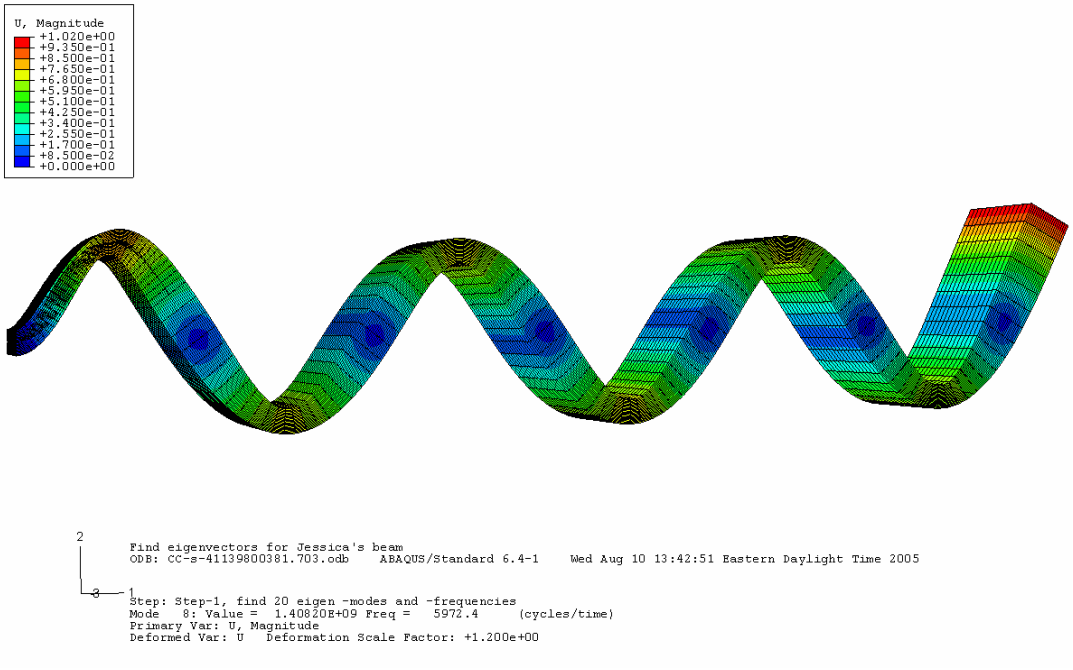

Figure 90. Seventh mode, 4 cm (1.575 in) clamped end notch

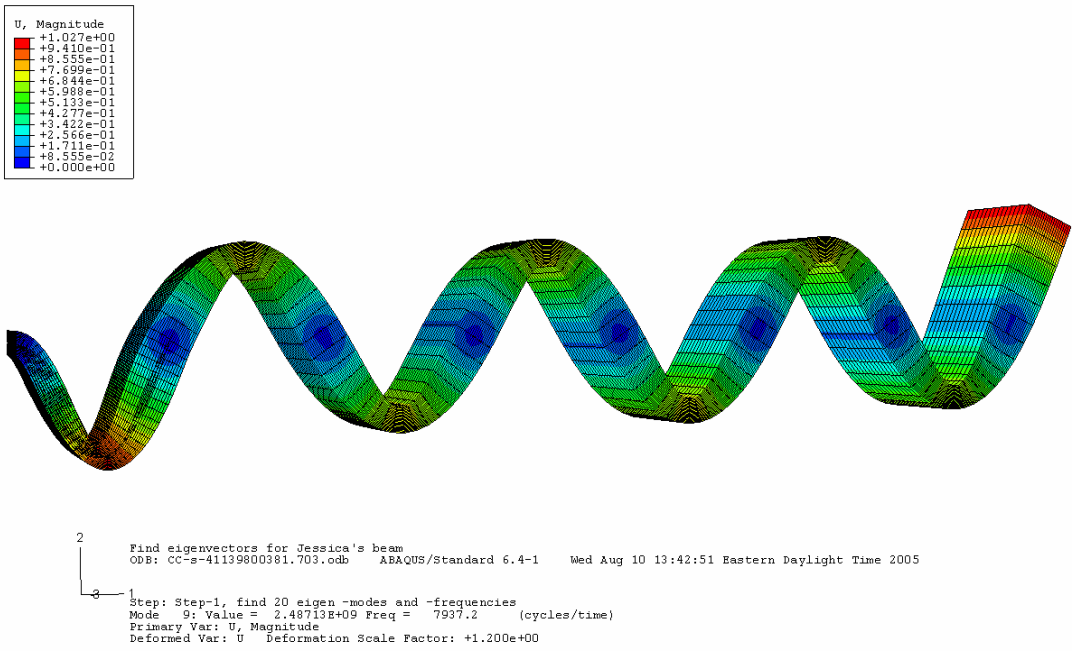

Figure 91. Eighth mode, 4 cm (1.575 in) clamped end notch

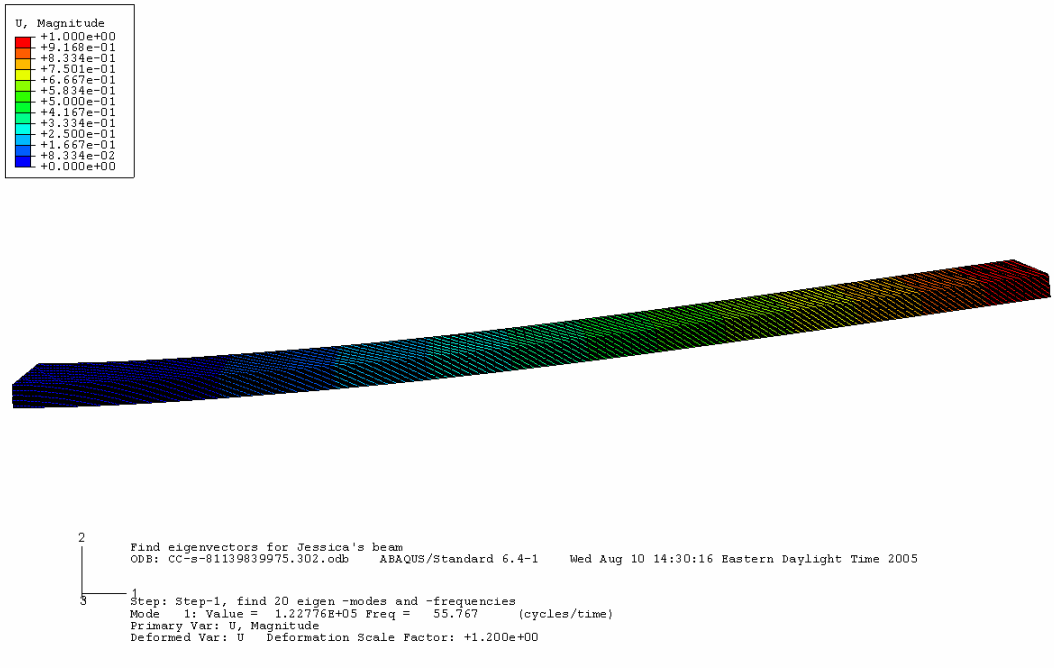

Figure 92. First mode, 8 cm (3.150 in) clamped end notch

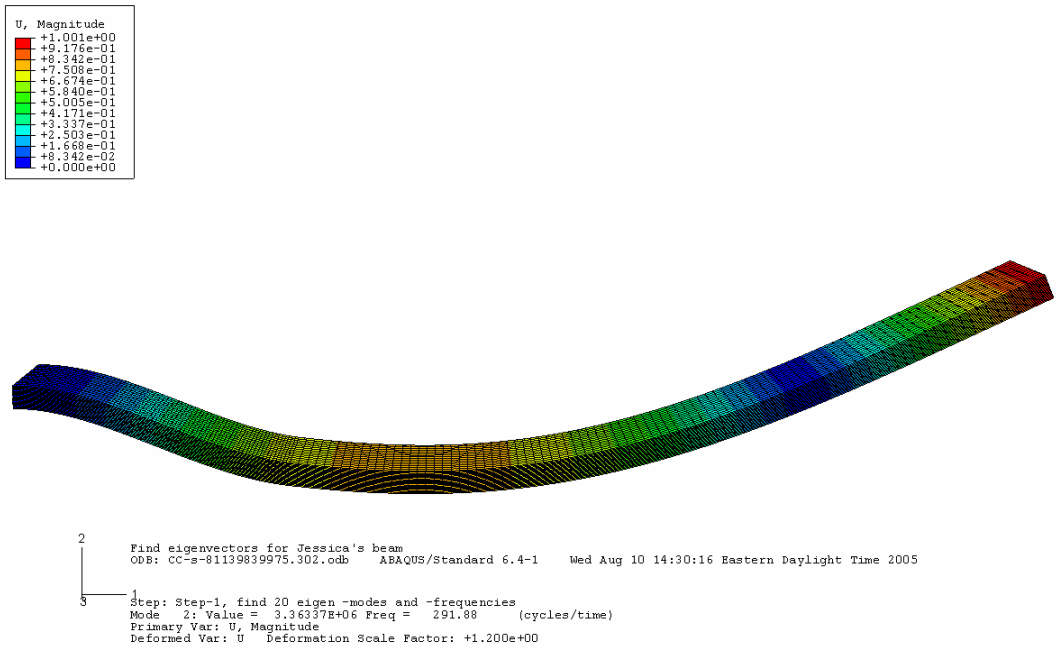

Figure 93. Second mode, 8 cm (3.150 in) clamped end notch

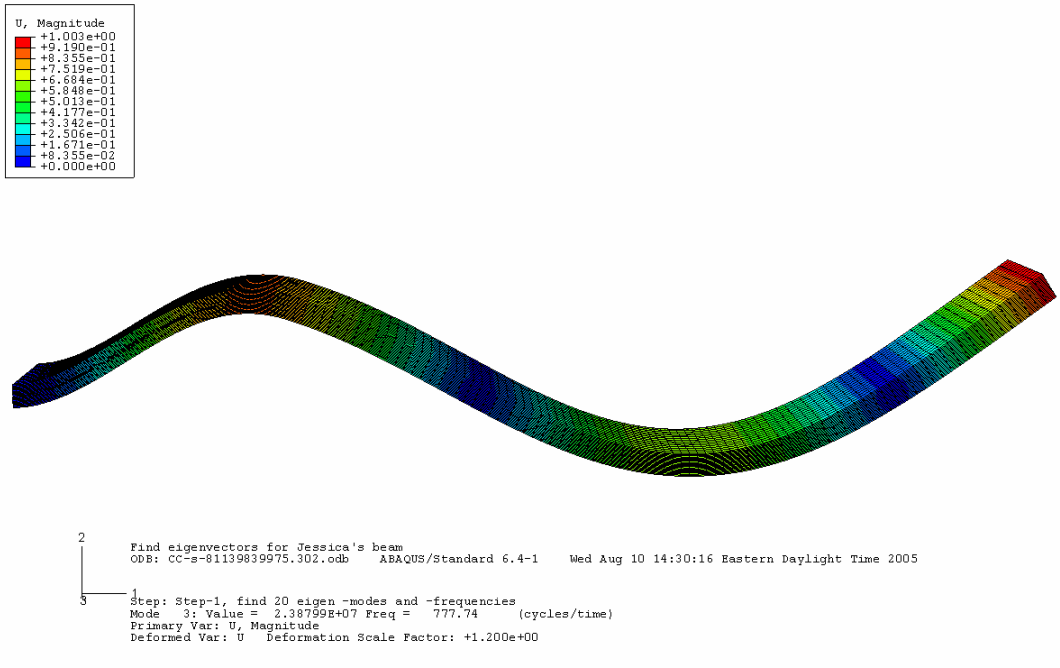

Figure 94. Third mode, 8 cm (3.150 in) clamped end notch

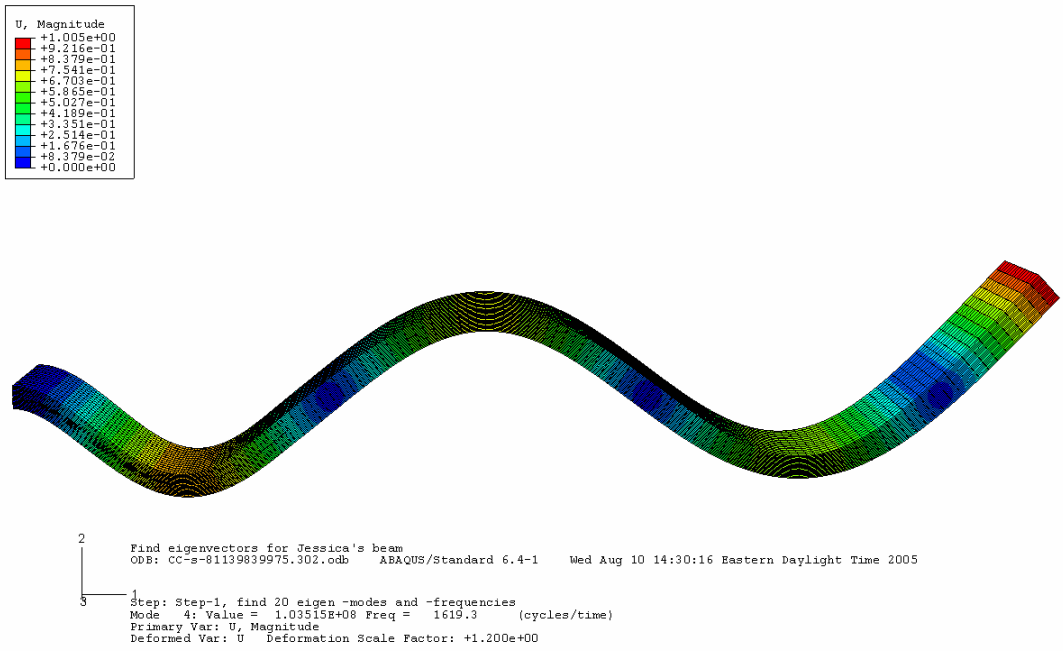

Figure 95. Fourth mode, 8 cm (3.150 in) clamped end notch

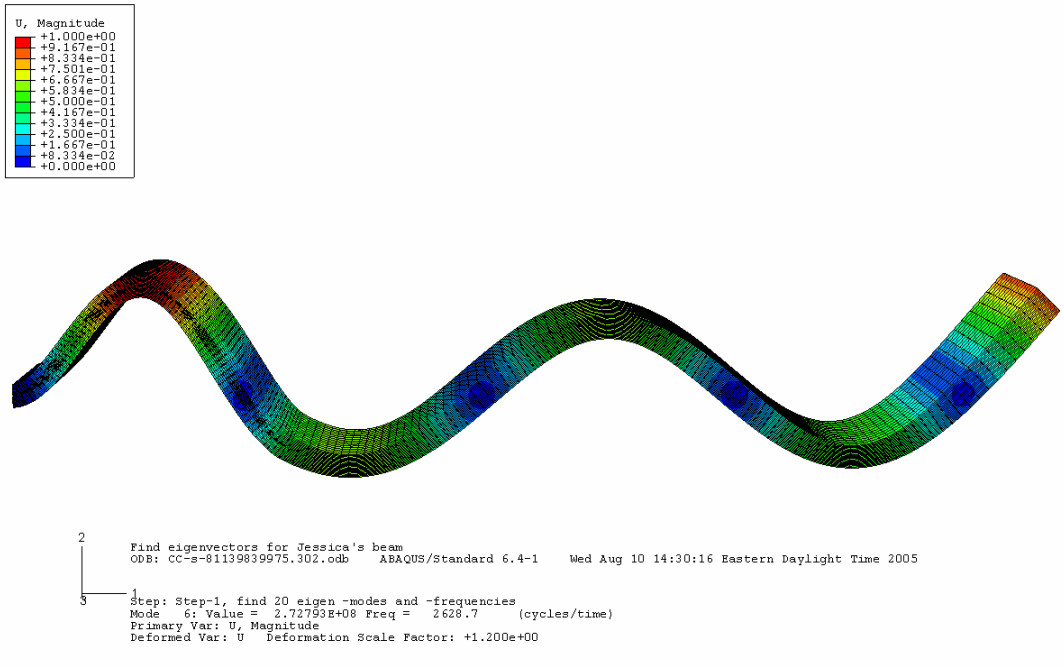

Figure 96. Fifth mode, 8 cm (3.150 in) clamped end notch

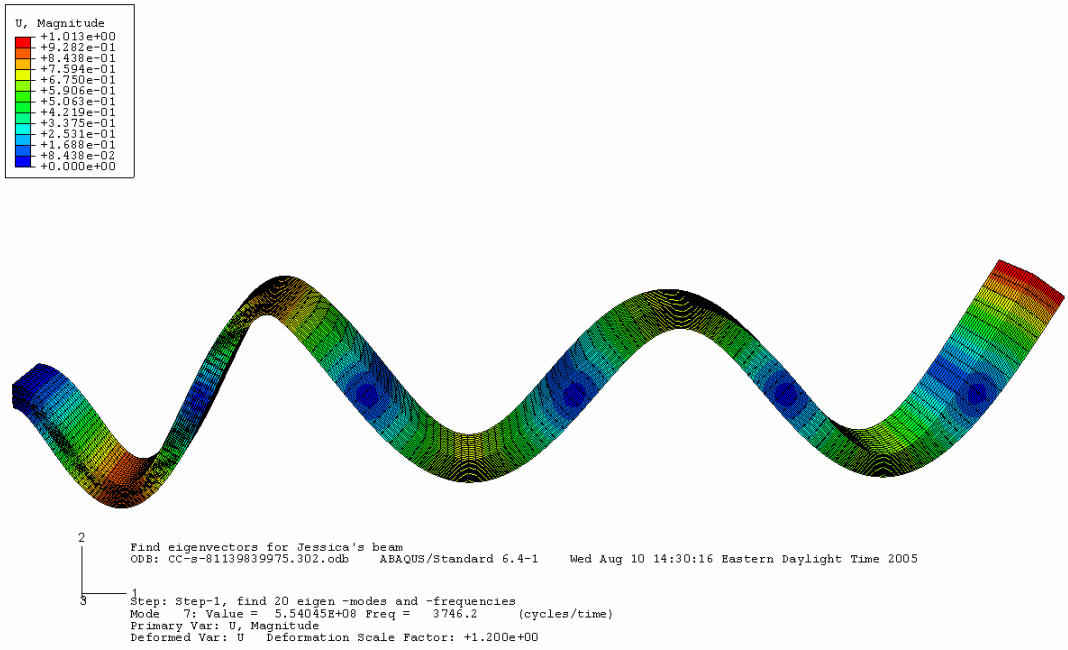

Figure 97. Sixth mode, 8 cm (3.150 in) clamped end notch

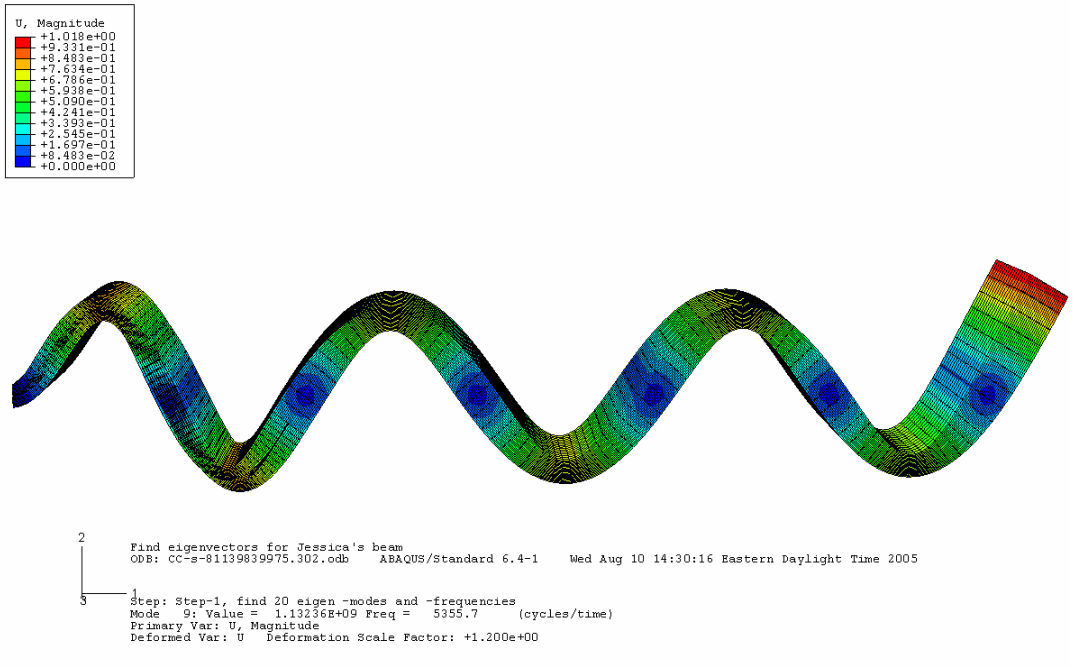

Figure 98. Seventh mode, 8 cm (3.150 in) clamped end notch

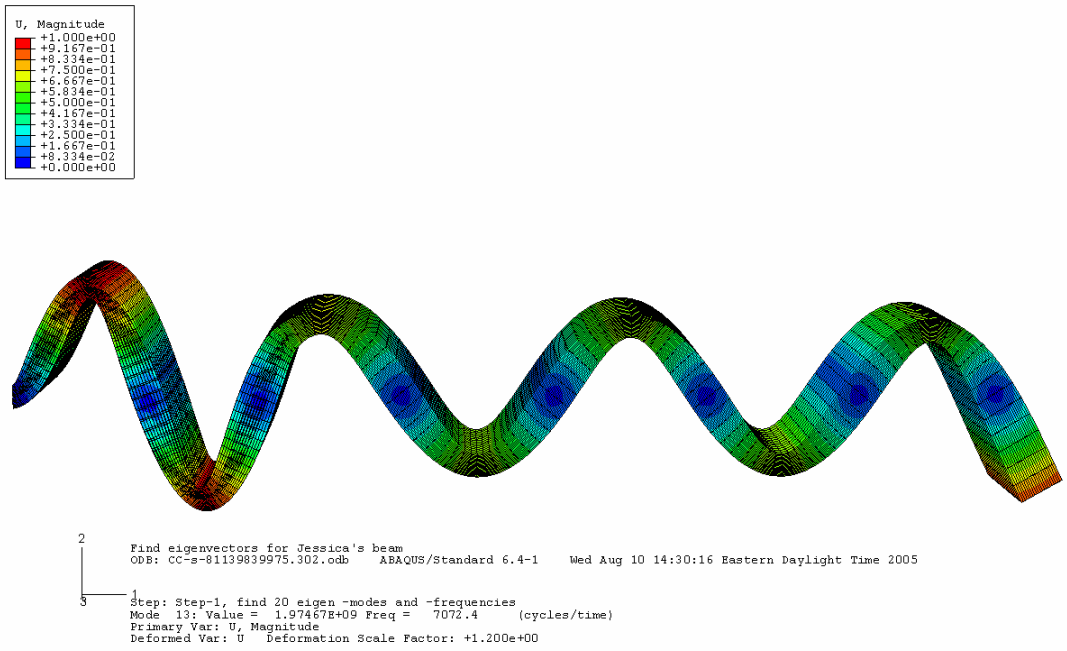

Figure 99. Eighth mode, 8 cm (3.150 in) clamped end notch

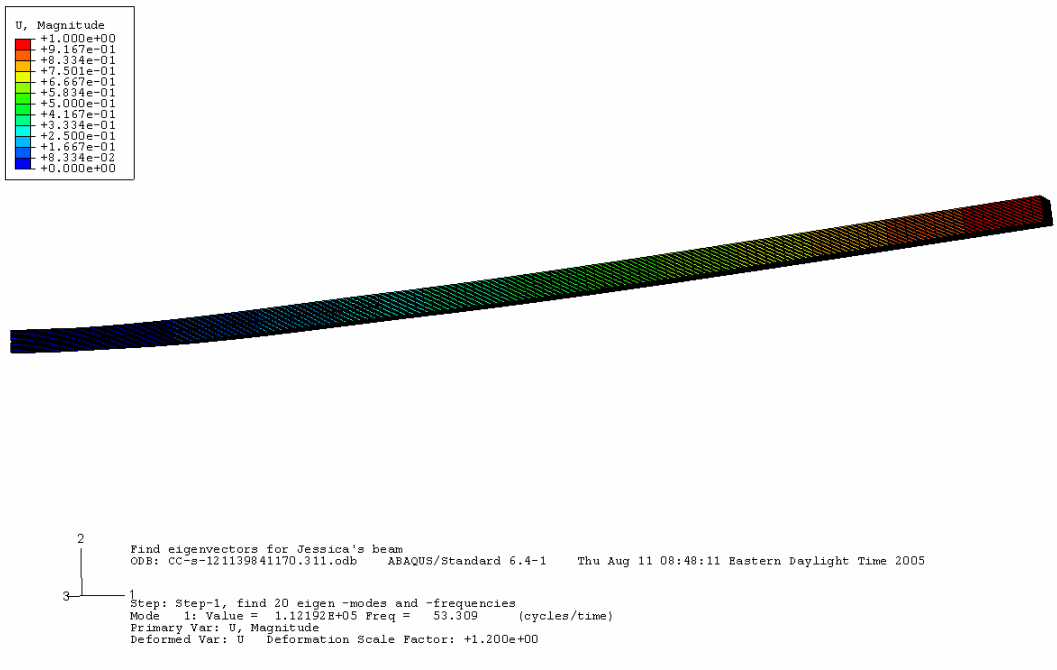

Figure 100. First mode, 12 cm (4.724 in) clamped end notch

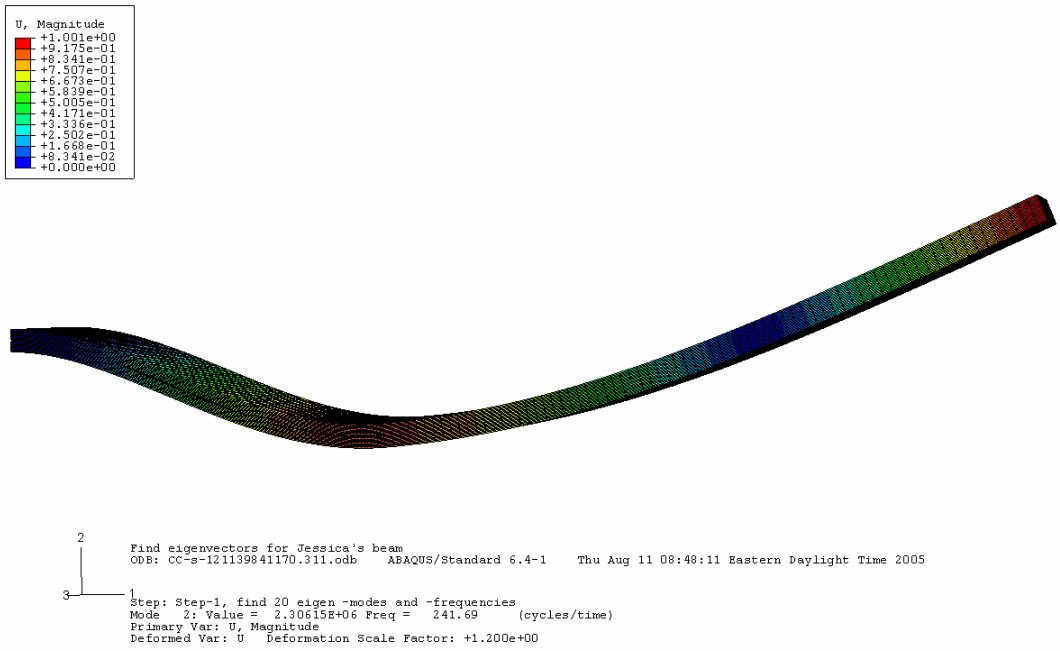

Figure 101. Second mode, 12 cm (4.724 in) clamped notch

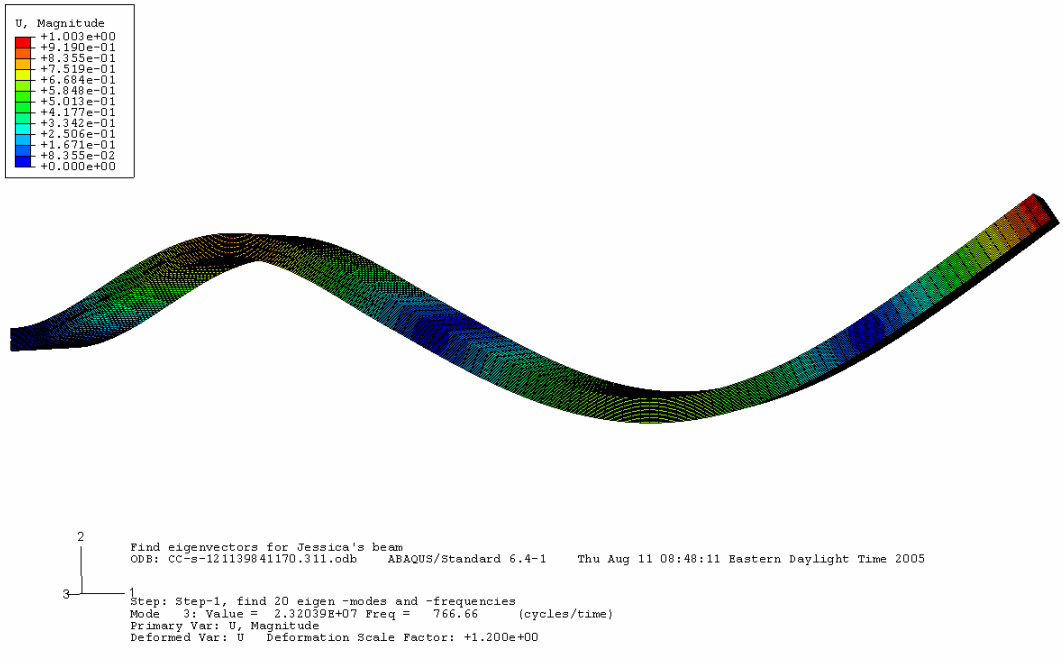

Figure 102. Third mode, 12 cm (4.724 in) clamped end notch

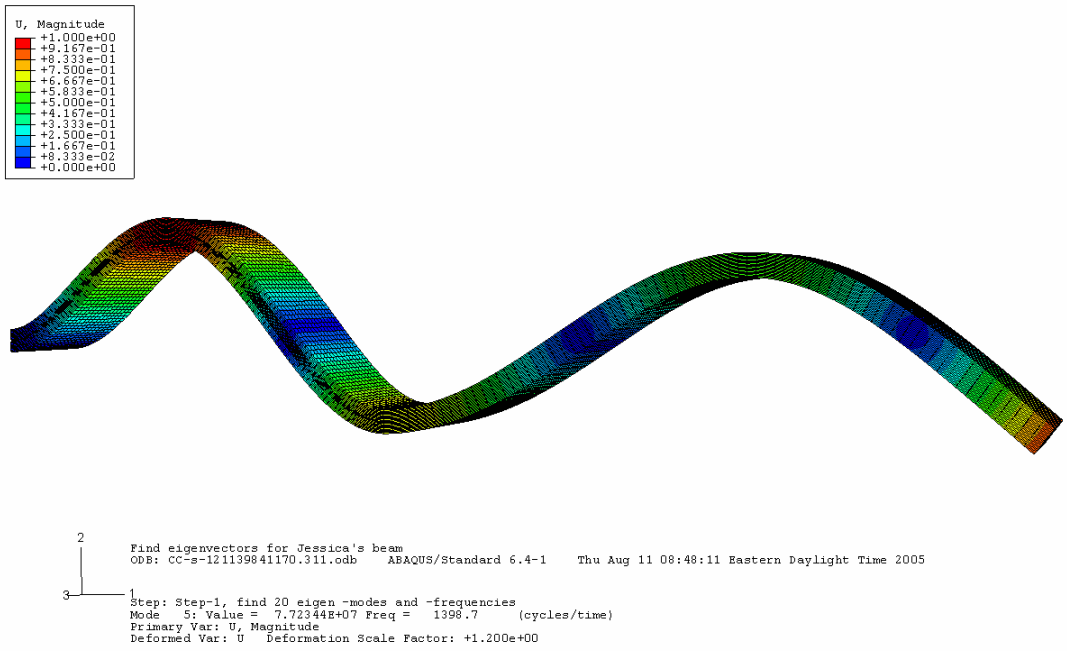

Figure 103. Fourth mode, 12 cm (4.724 in) clamped end notch

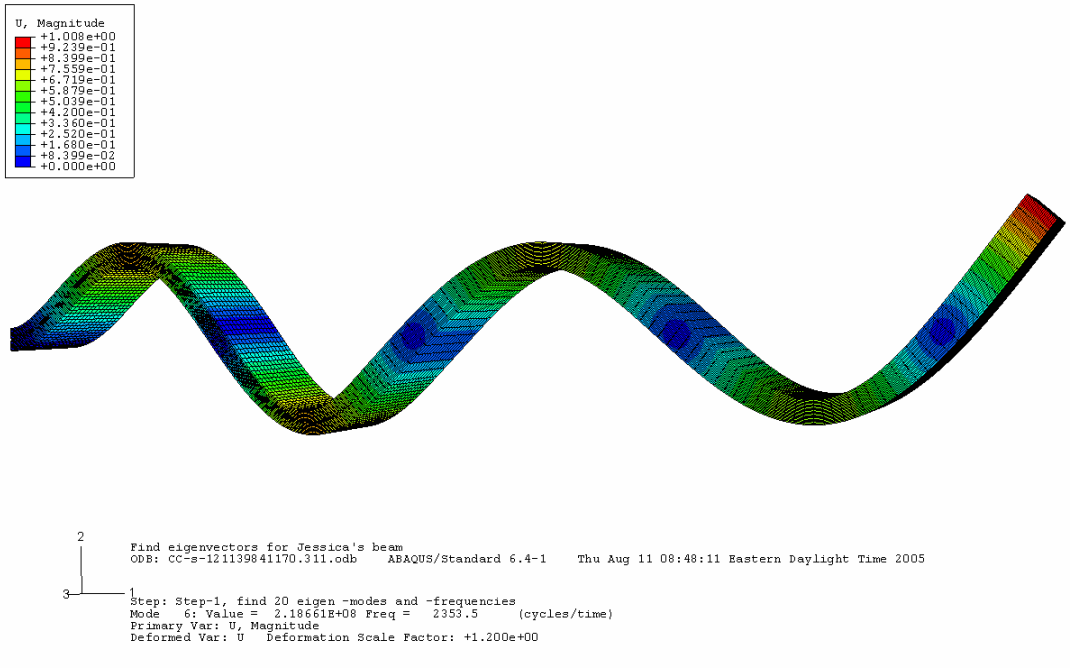

Figure 104. Fifth mode, 12 cm (4.724 in) clamped end notch

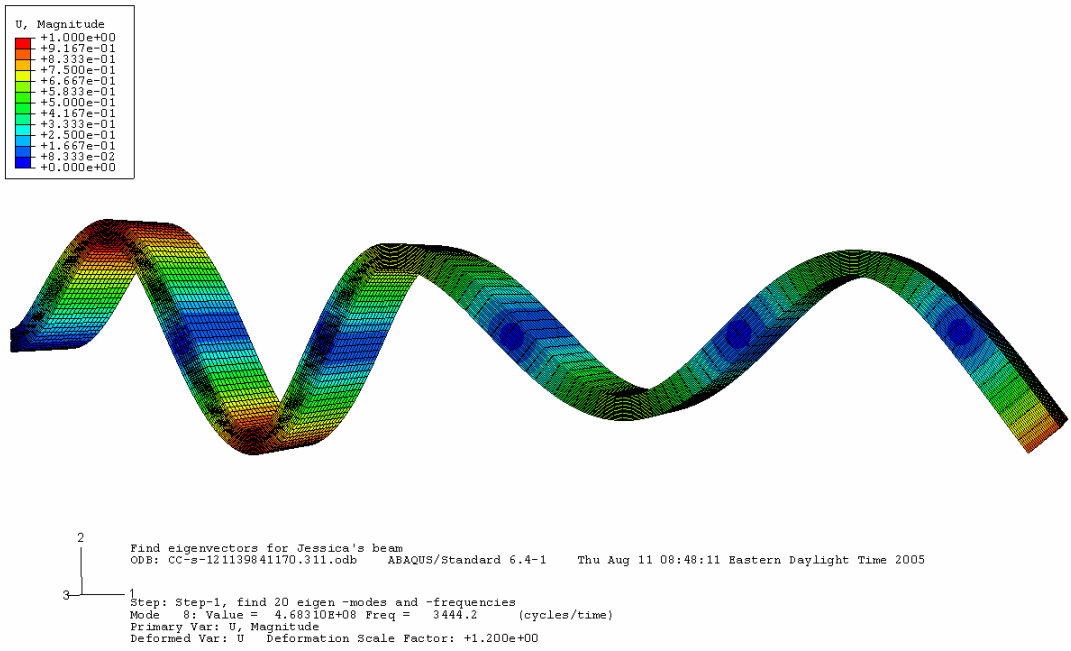

Figure 105. Sixth mode, 12 cm (4.724 in) clamped end notch

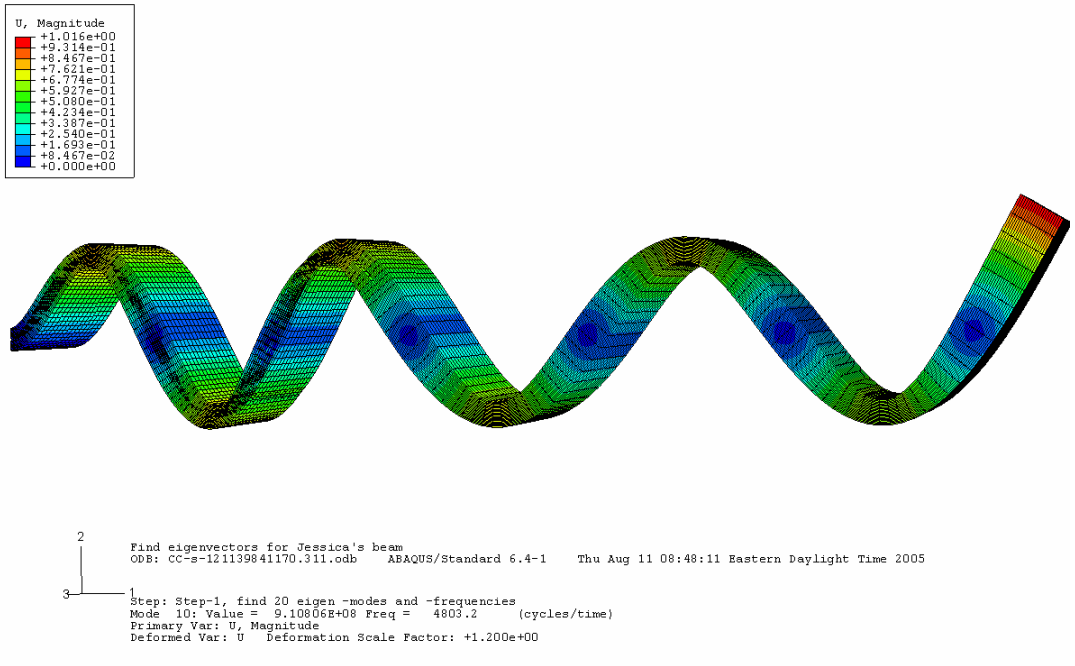

Figure 106. Seventh mode, 12 cm (4.724 in) clamped end notch

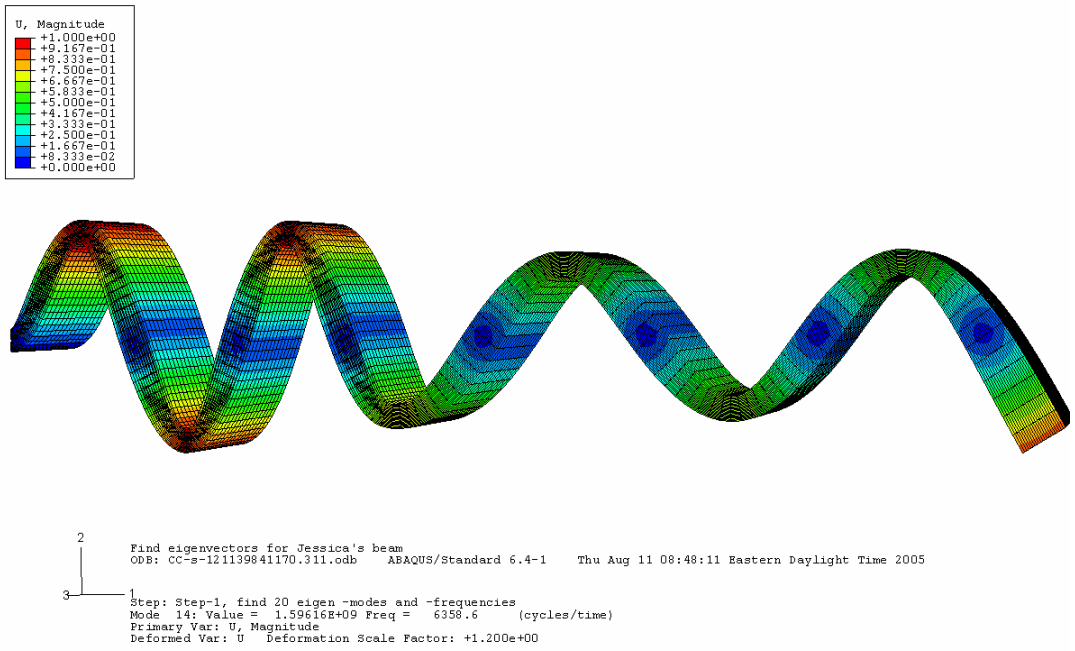

Figure 107. Eighth mode, 12 cm (4.724 in) clamped end notch

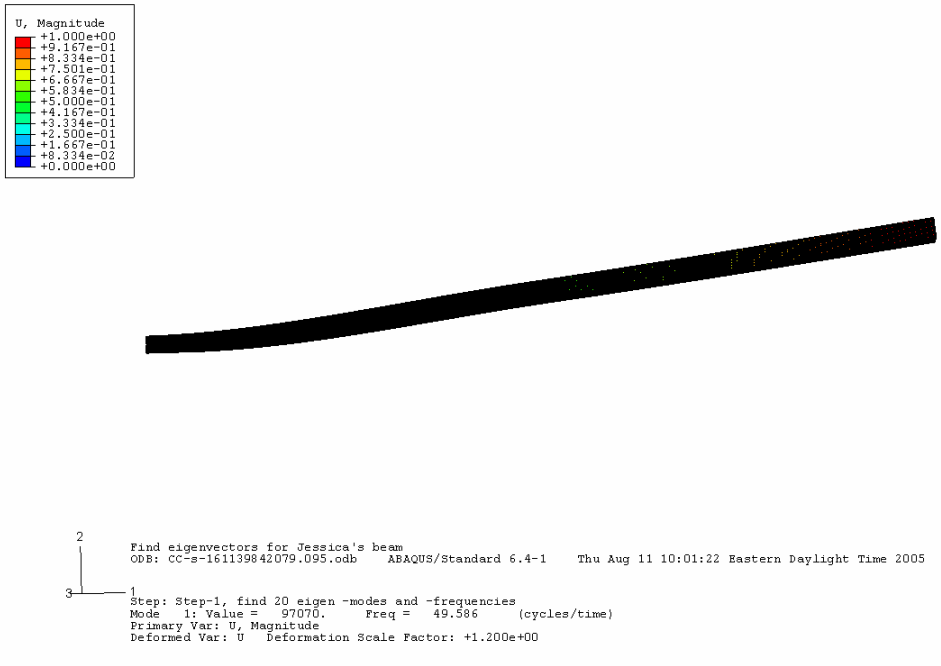

Figure 108. First mode, 16 cm (6.299 in) clamped end notch

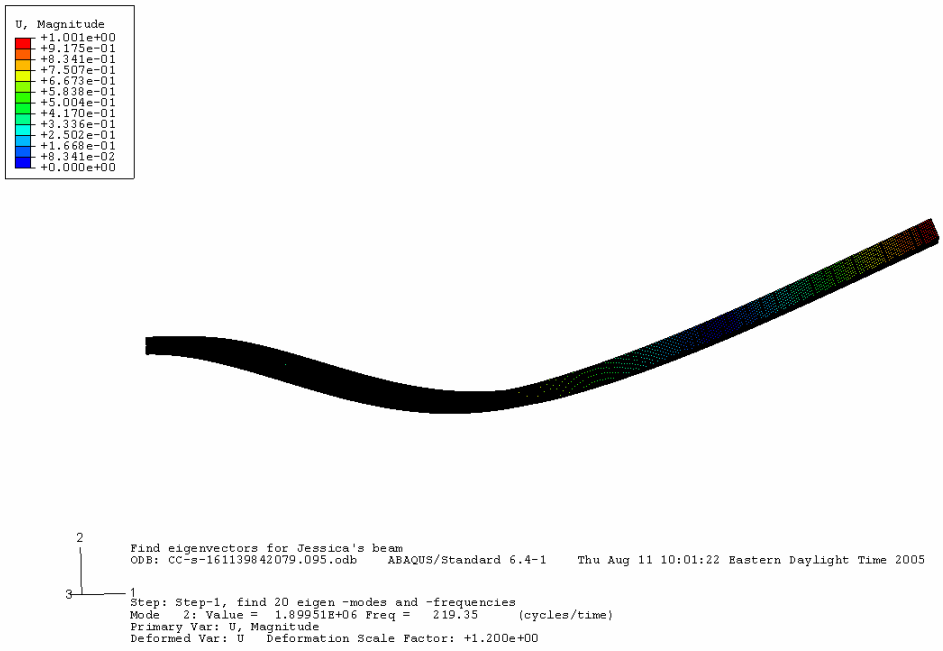

Figure 109. Second mode, 16 cm (6.299 in) clamped end notch

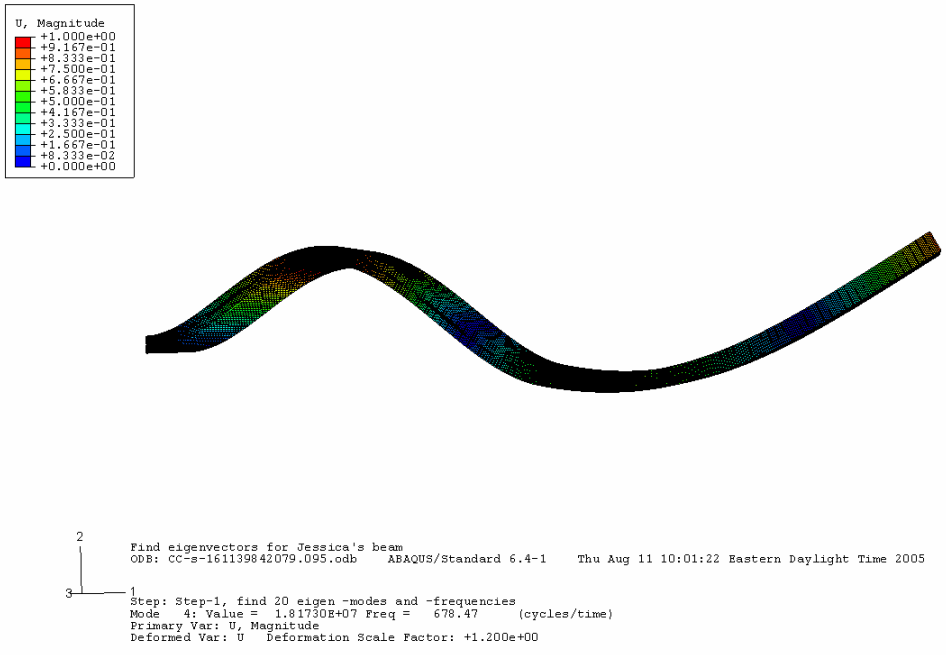

Figure 110. Third mode, 16 cm (6.299 in) clamped end notch

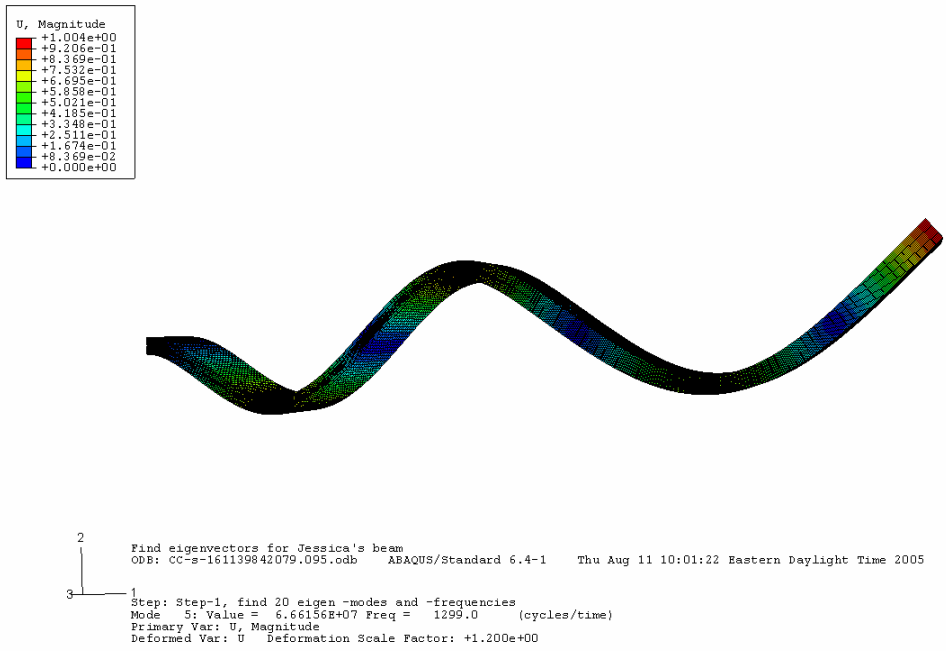

Figure 111. Fourth mode, 16 cm (6.299 in) clamped end notch

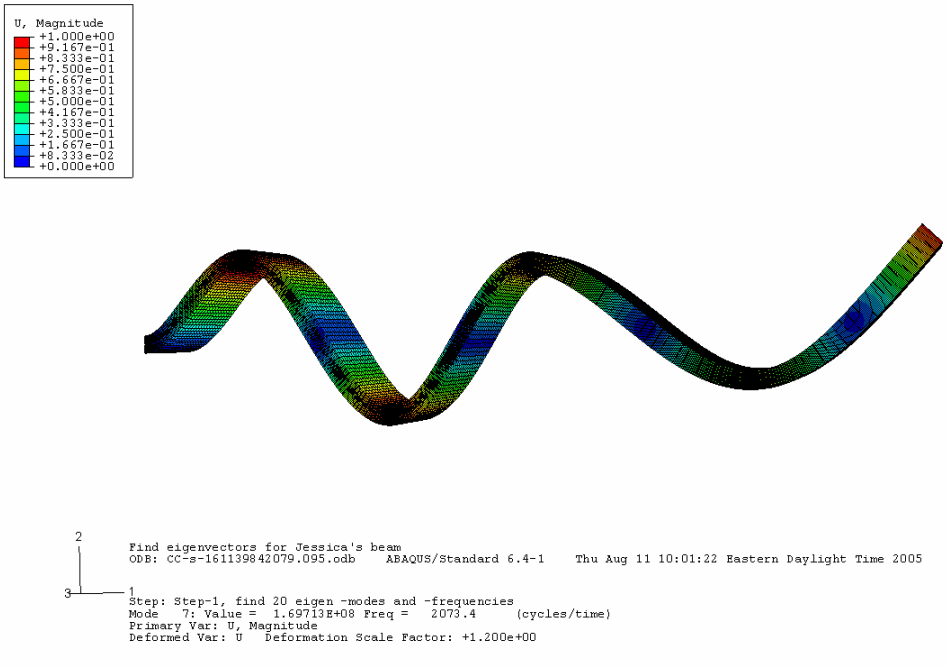

Figure 112. Fifth mode, 16 cm (6.299 in) clamped end notch

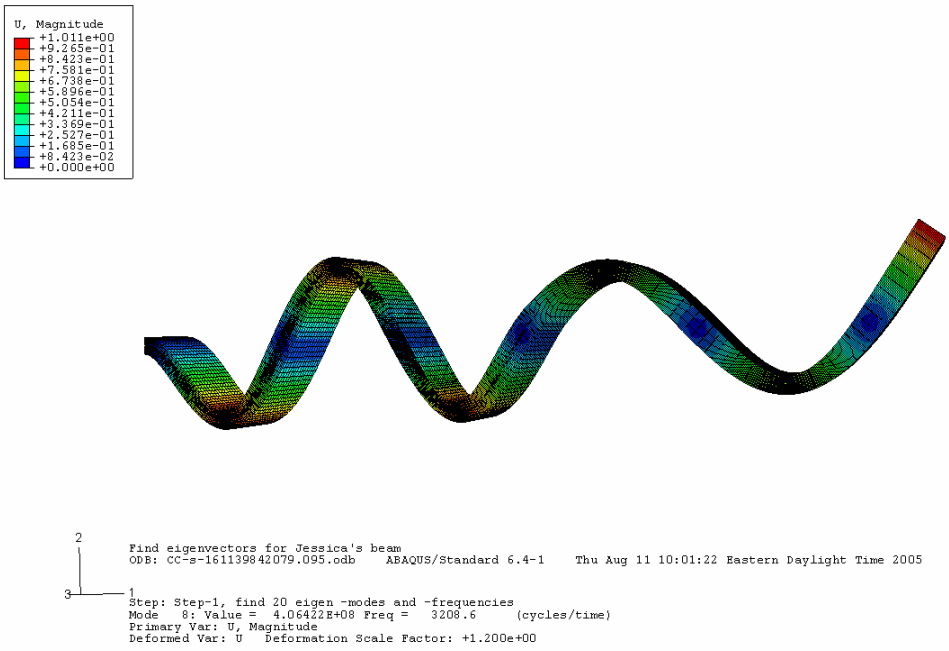

Figure 113. Sixth mode, 16 cm (6.299 in) clamped end notch

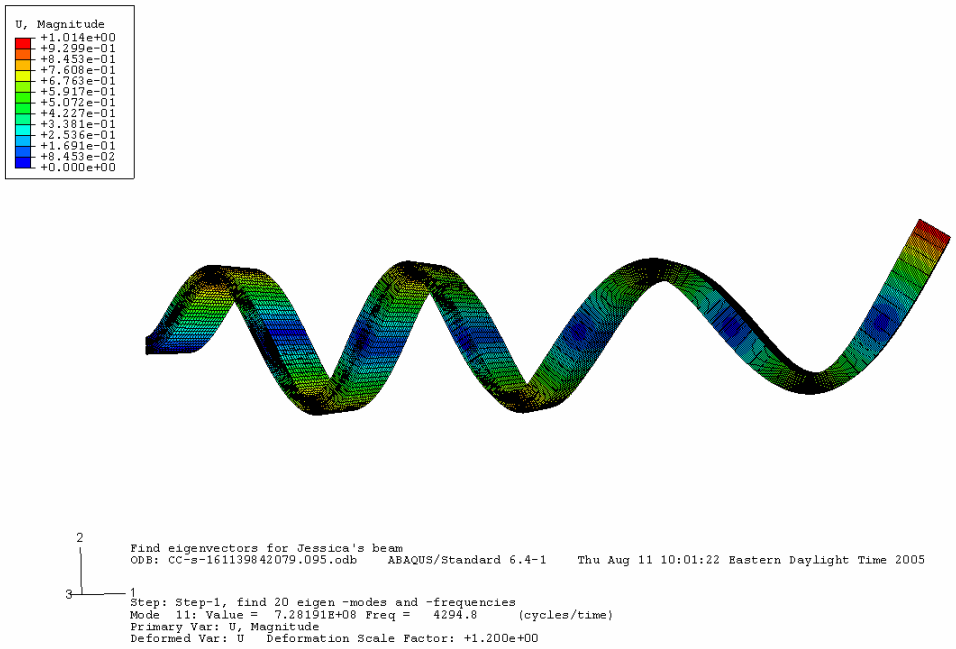

Figure 114. Seventh mode, 16 cm (6.299 in) clamped end notch

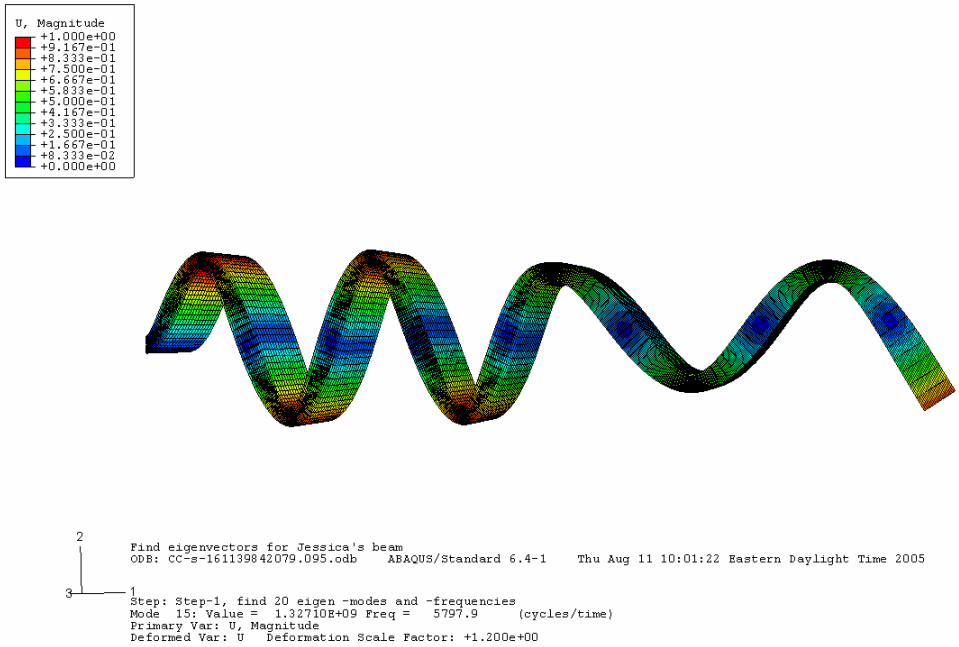

Figure 115. Eighth mode, 16 cm (6.299 in) clamped end notch

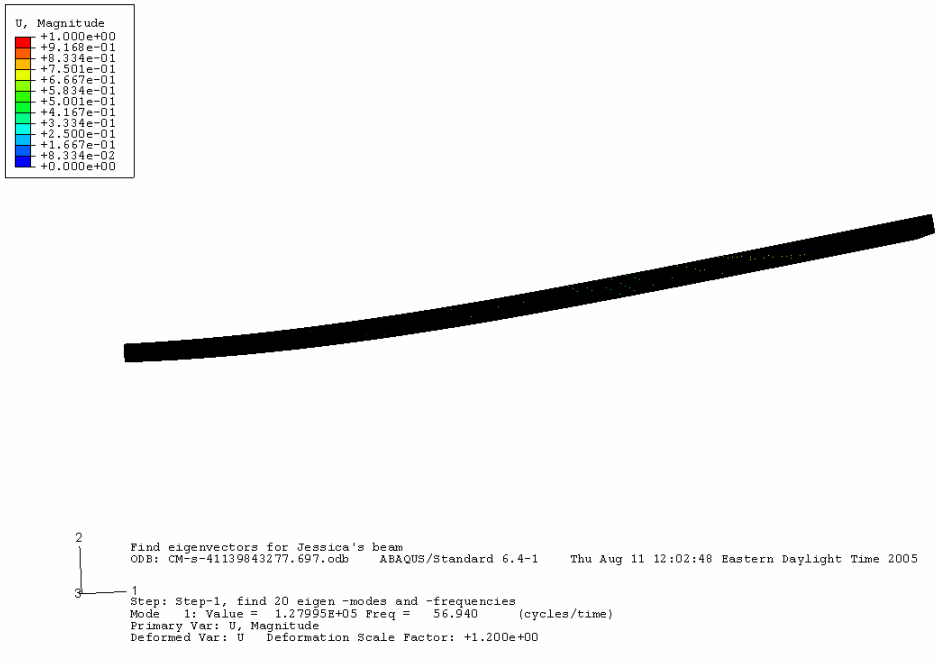

Figure 116. First mode, 4 cm (1.575 in) middle notch

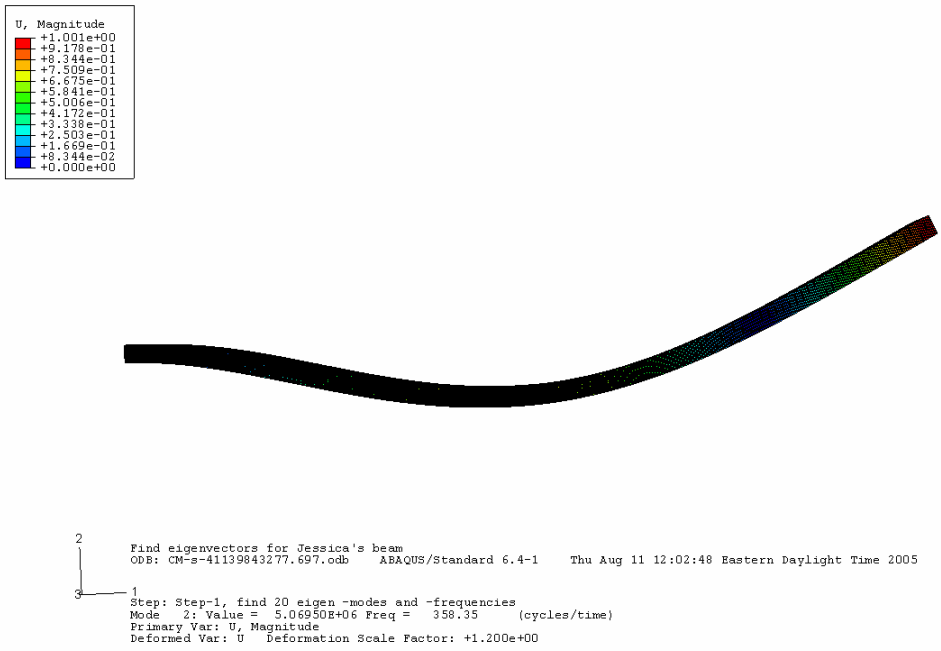

Figure 117. Second mode, 4 cm (1.575 in) middle notch

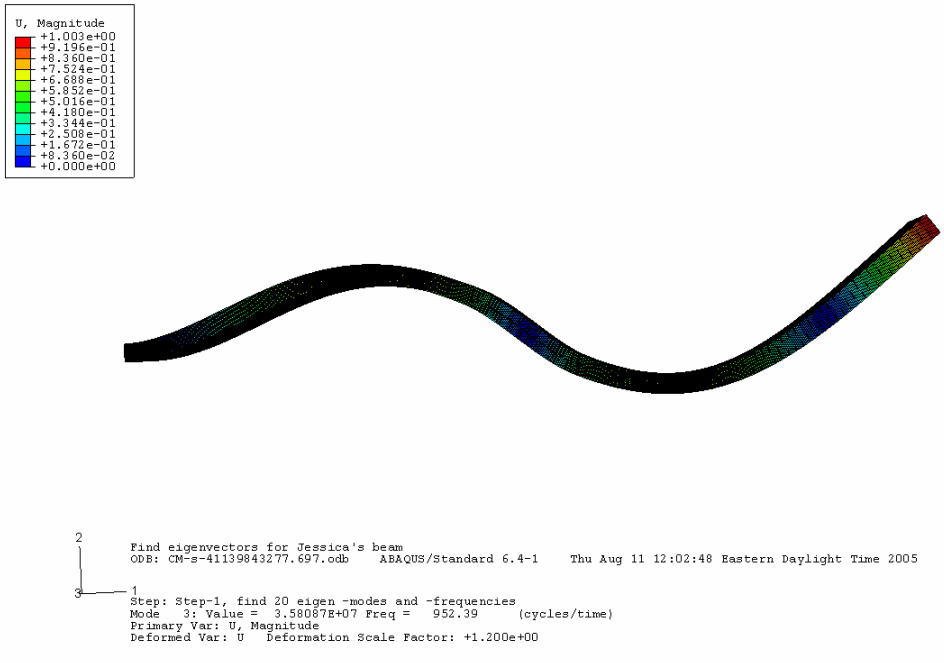

Figure 118. Third mode, 4 cm (1.575 in) middle notch

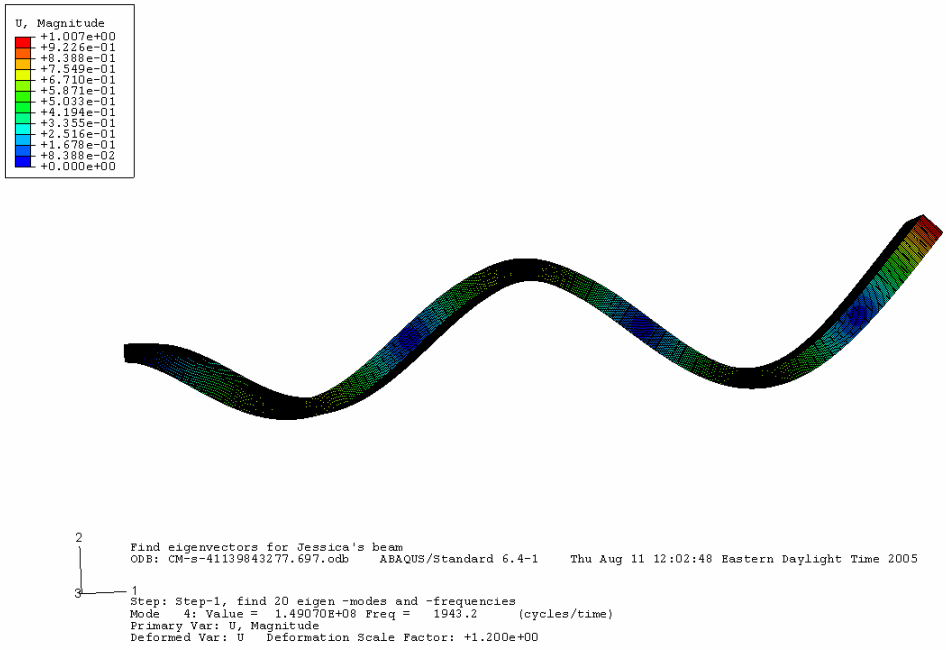

Figure 119. Fourth mode, 4 cm (1.575 in) middle notch

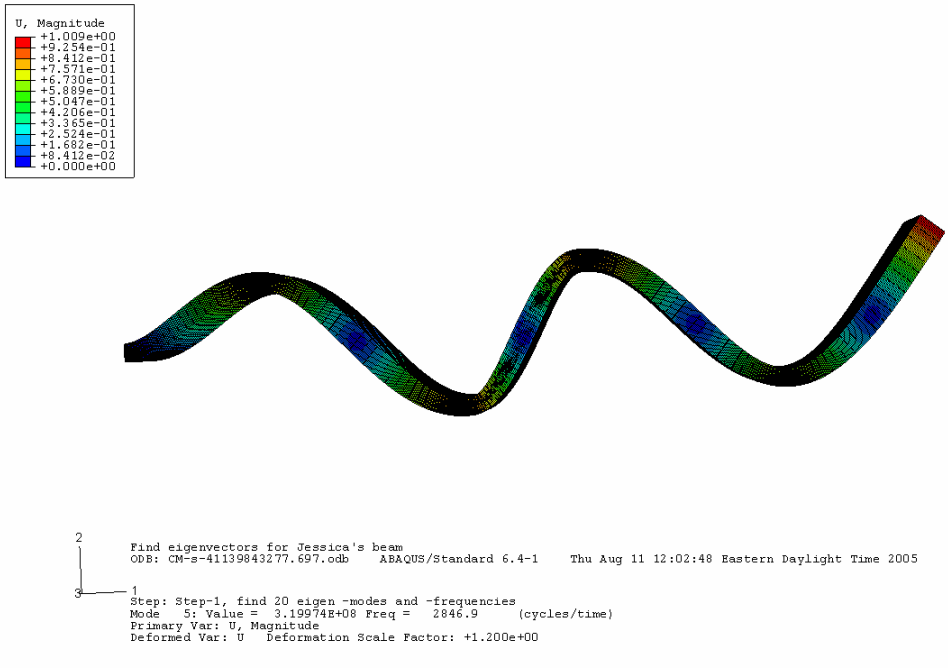

Figure 120. Fifth mode, 4 cm (1.575 in) middle notch

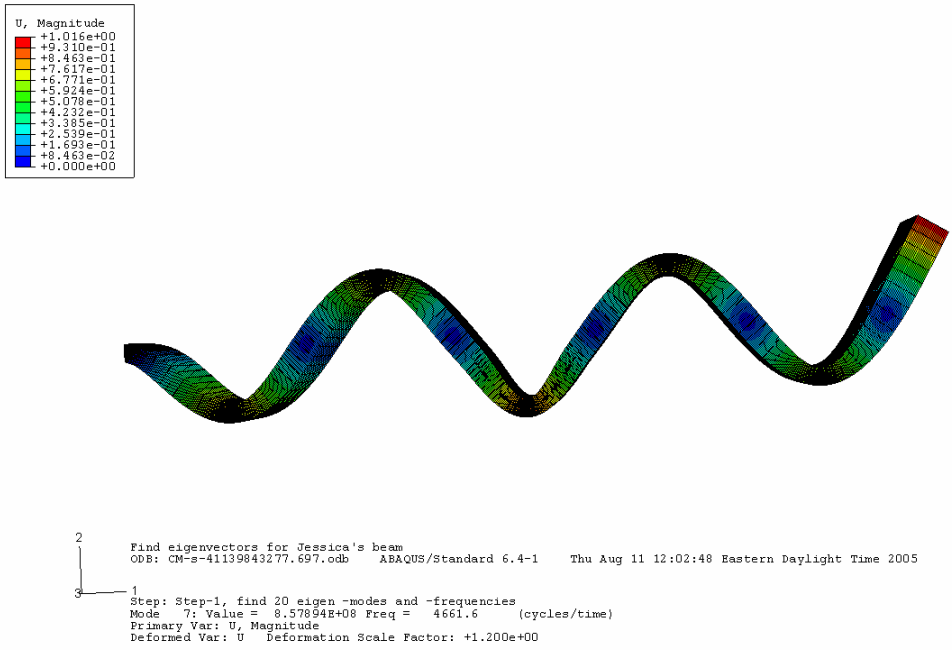

Figure 121. Sixth mode, 4 cm (1.575 in) middle notch

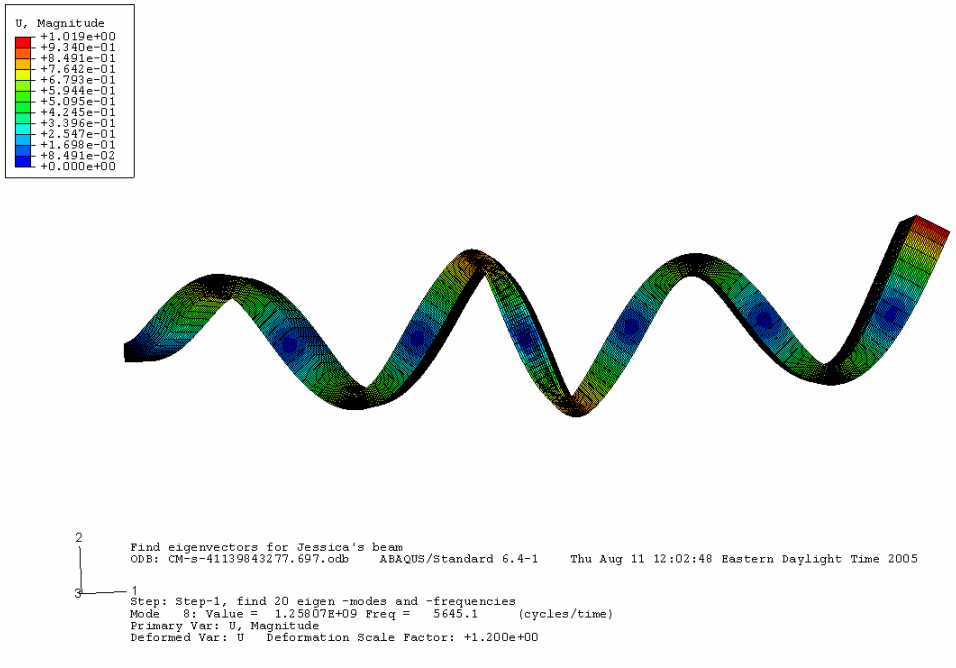

Figure 122. Seventh mode, 4 cm (1.575 in) middle notch

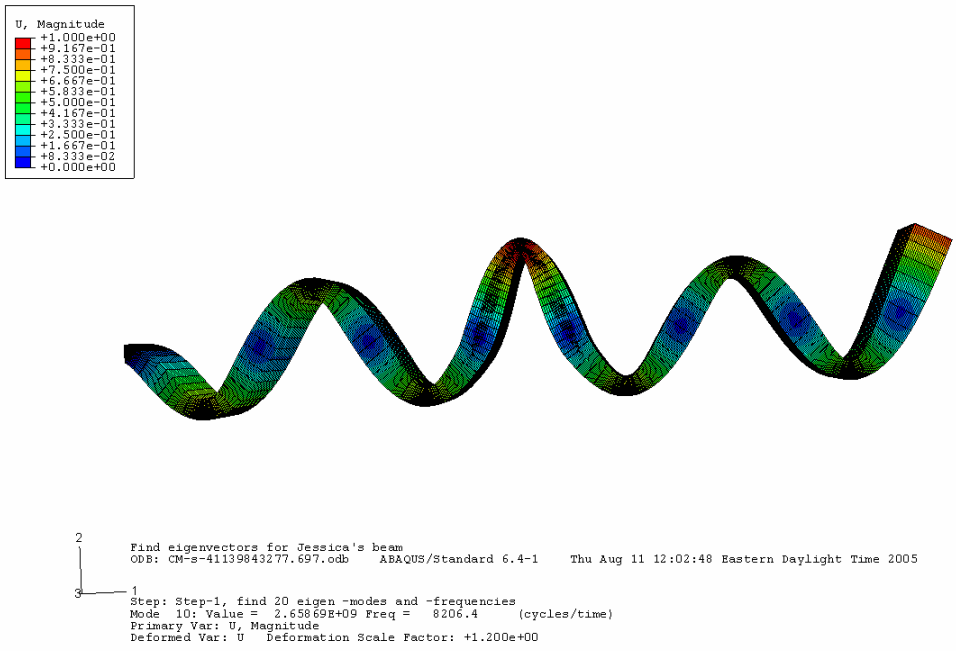

Figure 123. Eighth mode, 4 cm (1.575 in) middle notch

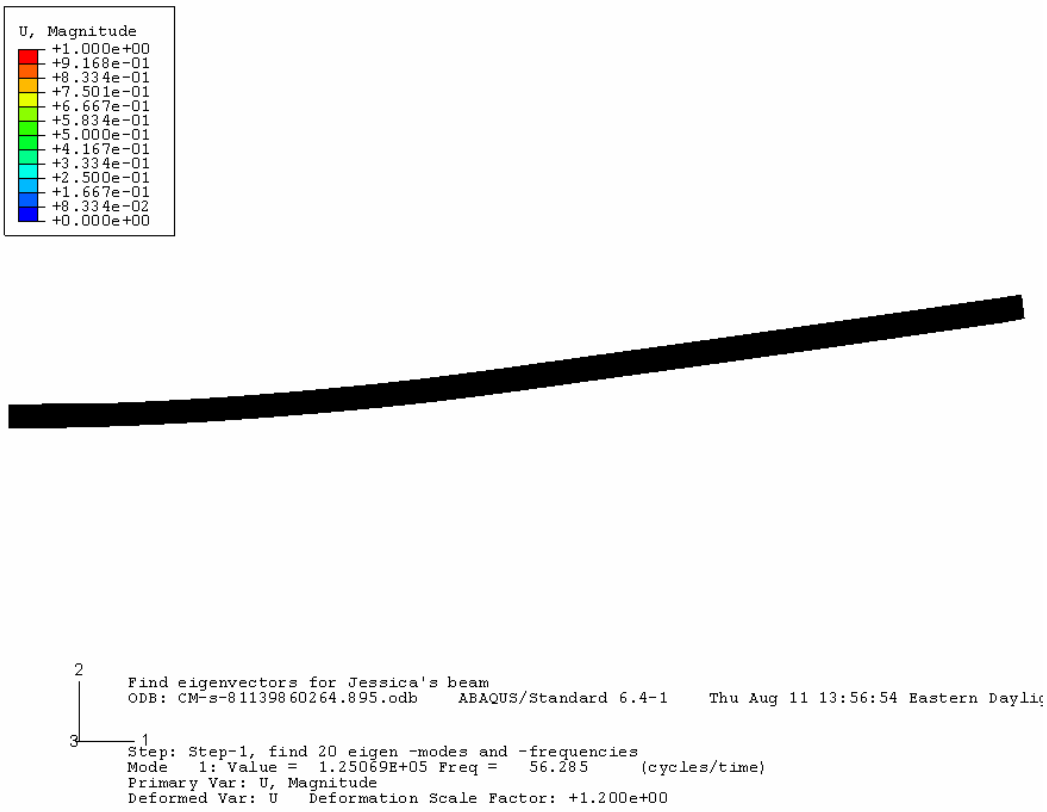

Figure 124. First mode, 8 cm (3.150 in) middle notch

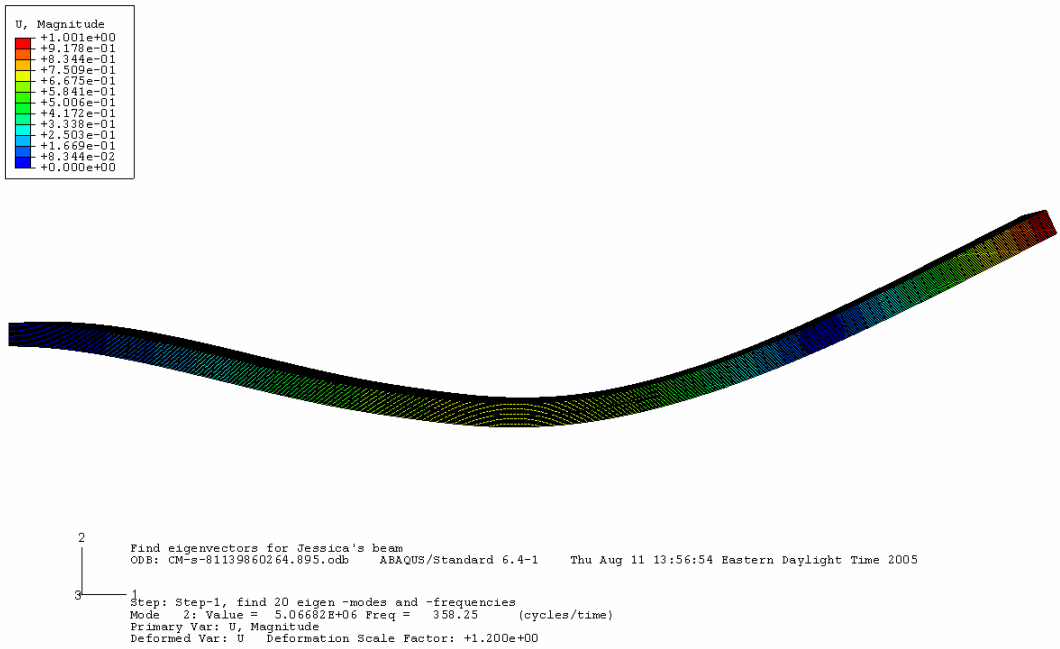

Figure 125. Second mode, 8 cm (3.150 in) middle notch

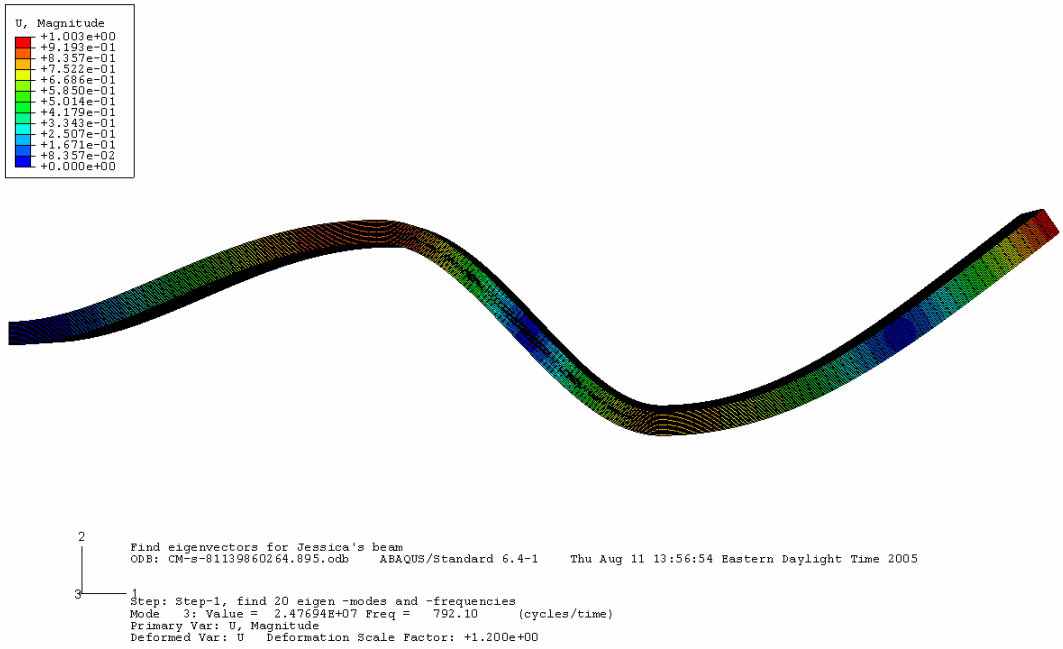

Figure 126. Third mode, 8 cm (3.150 in) middle notch

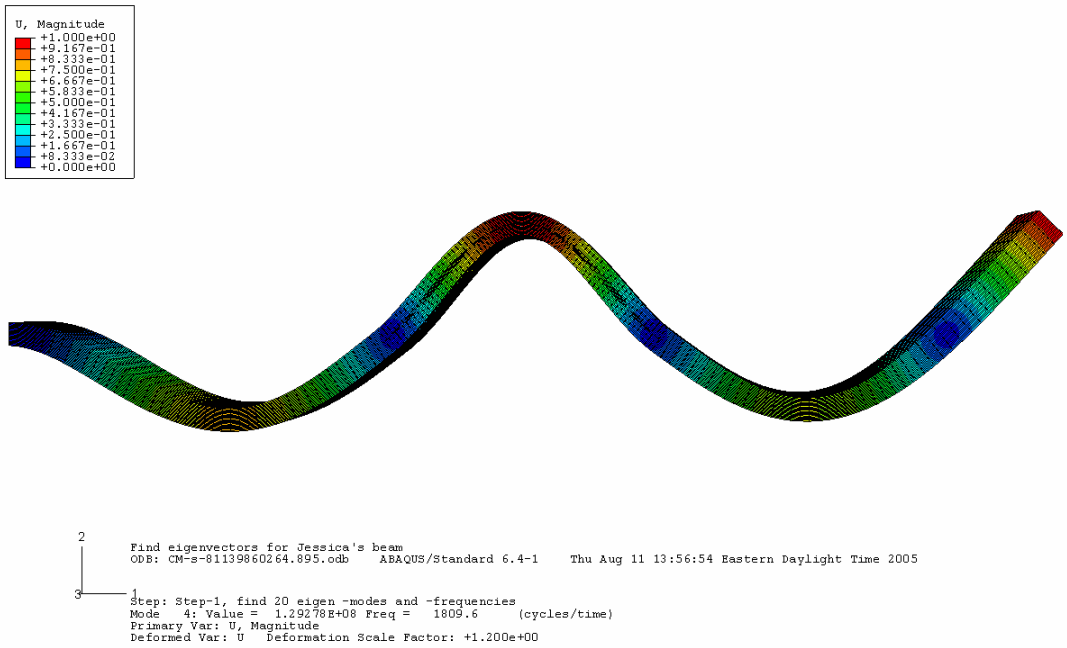

Figure 127. Fourth mode, 8 cm (3.150 in) middle notch

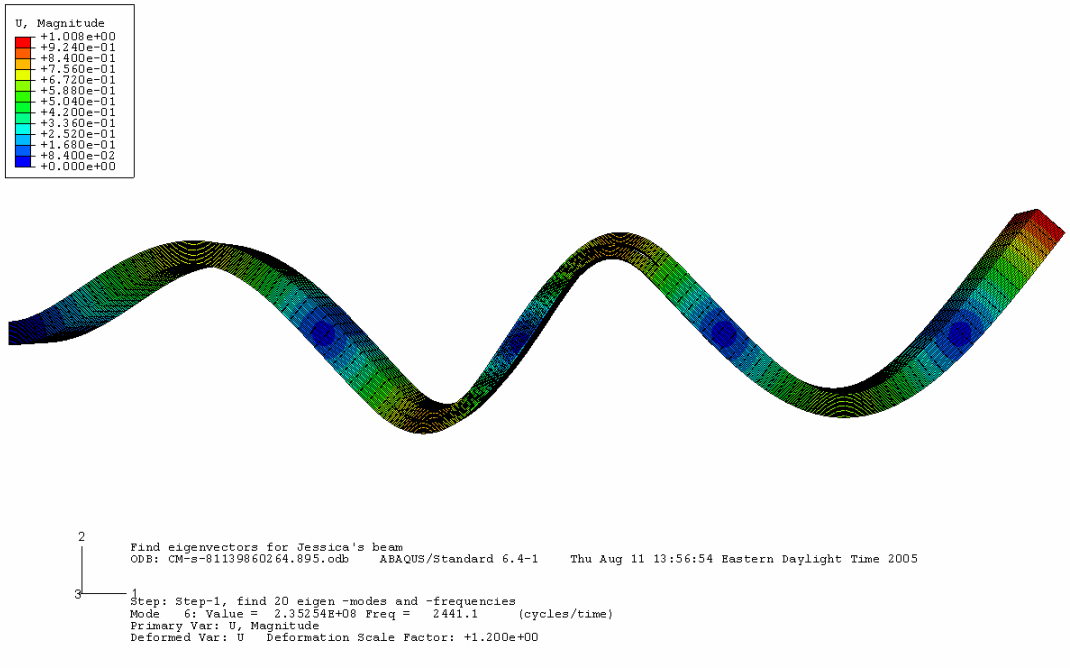

Figure 128. Fifth mode, 8 cm (3.150 in) middle notch

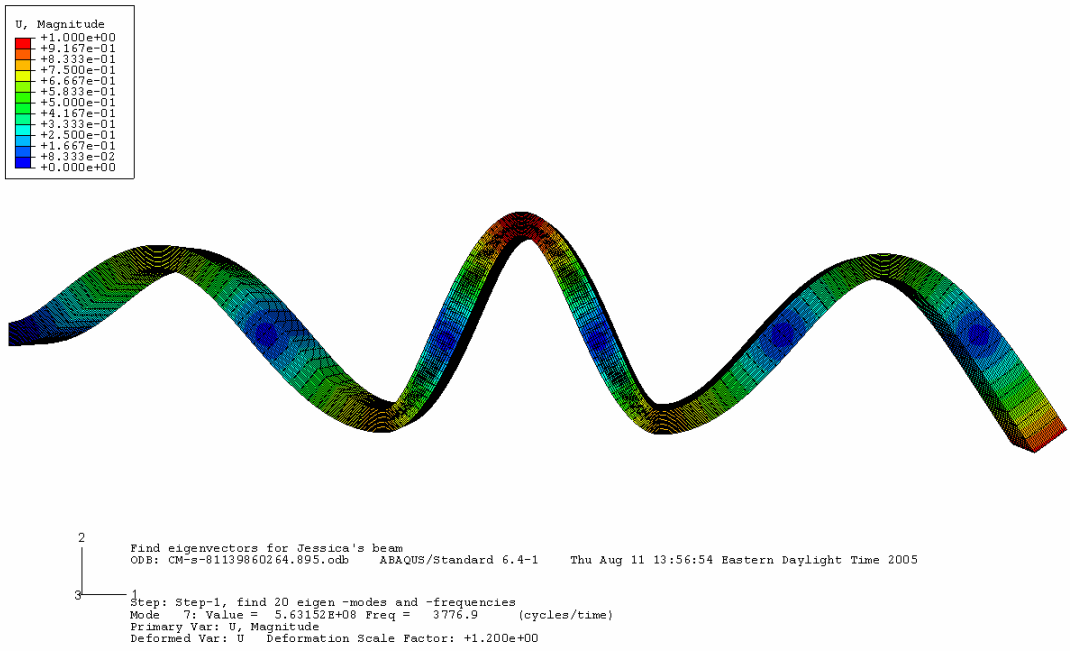

Figure 129. Sixth mode, 8 cm (3.150 in) middle notch

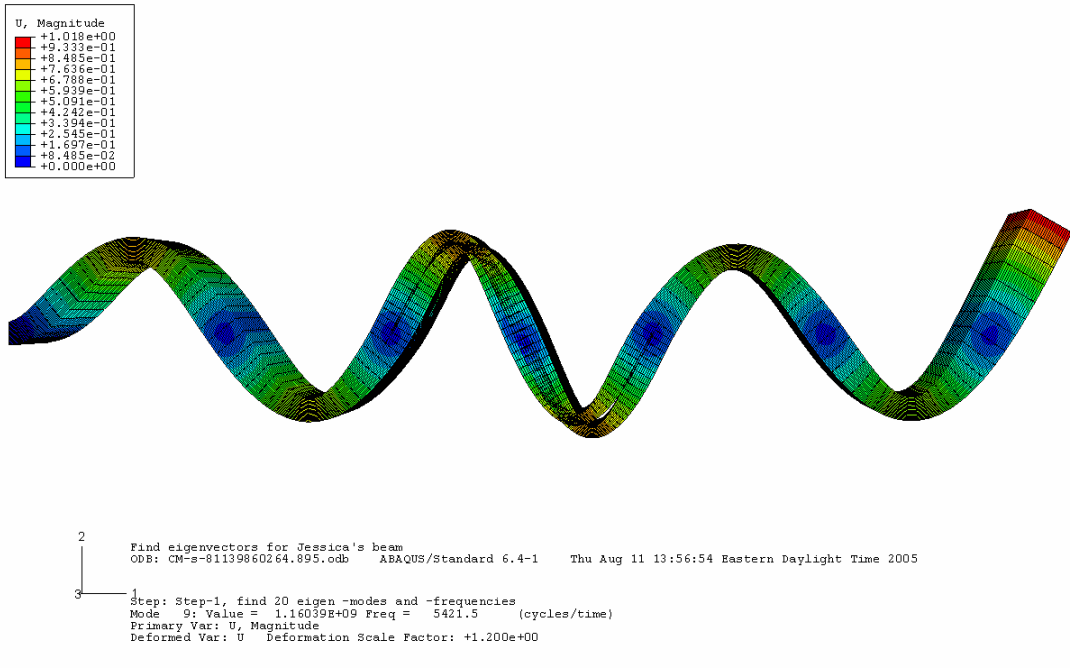

Figure 130. Seventh mode, 8 cm (3.150 in) middle notch

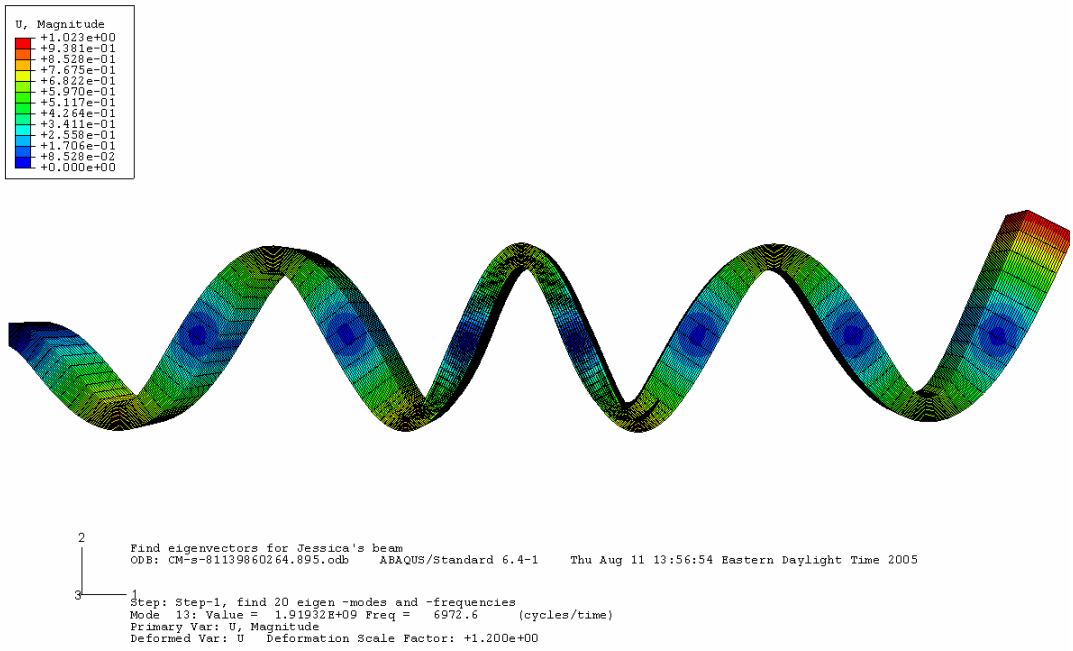

Figure 131. Eighth mode, 8 cm (3.150 in) middle notch

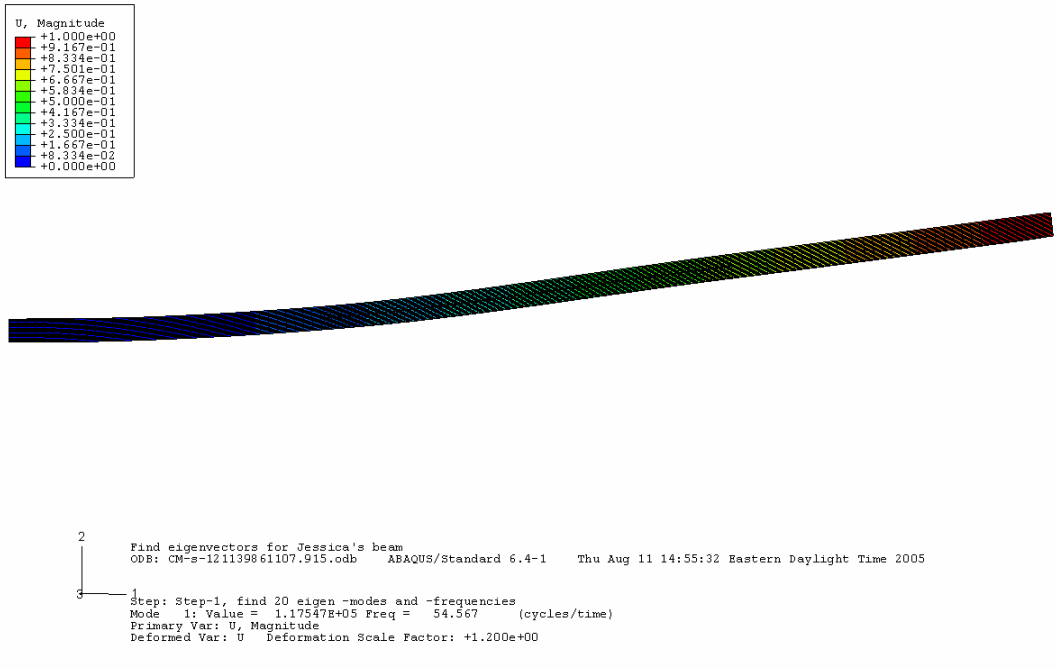

Figure 132. First mode, 12 cm (4.724 in) middle notch

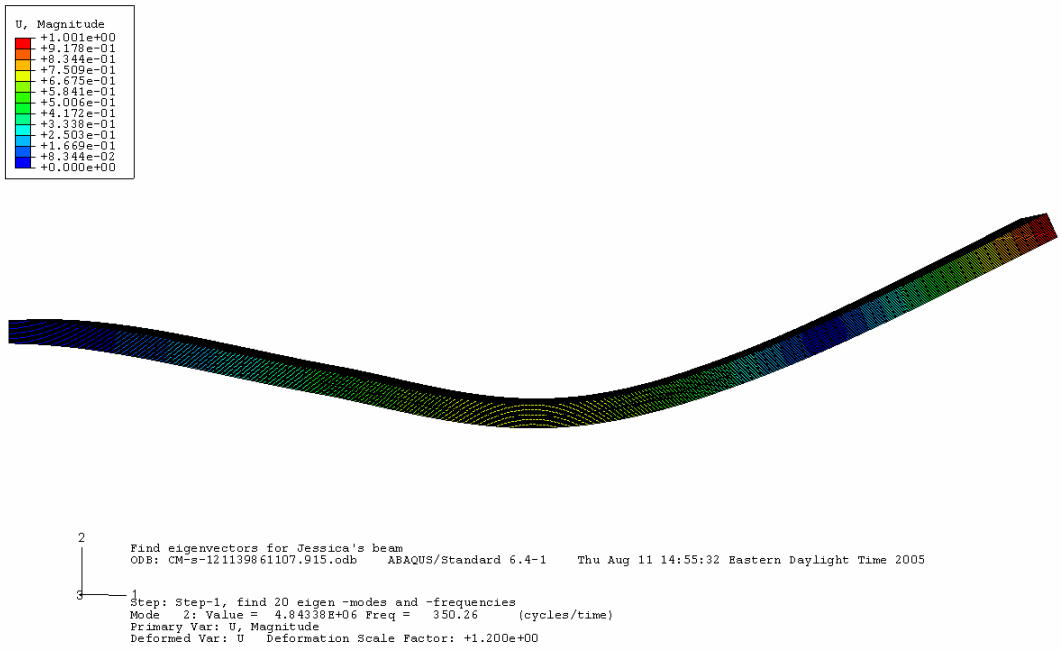

Figure 133. Second mode, 12 cm (4.724 in) middle notch

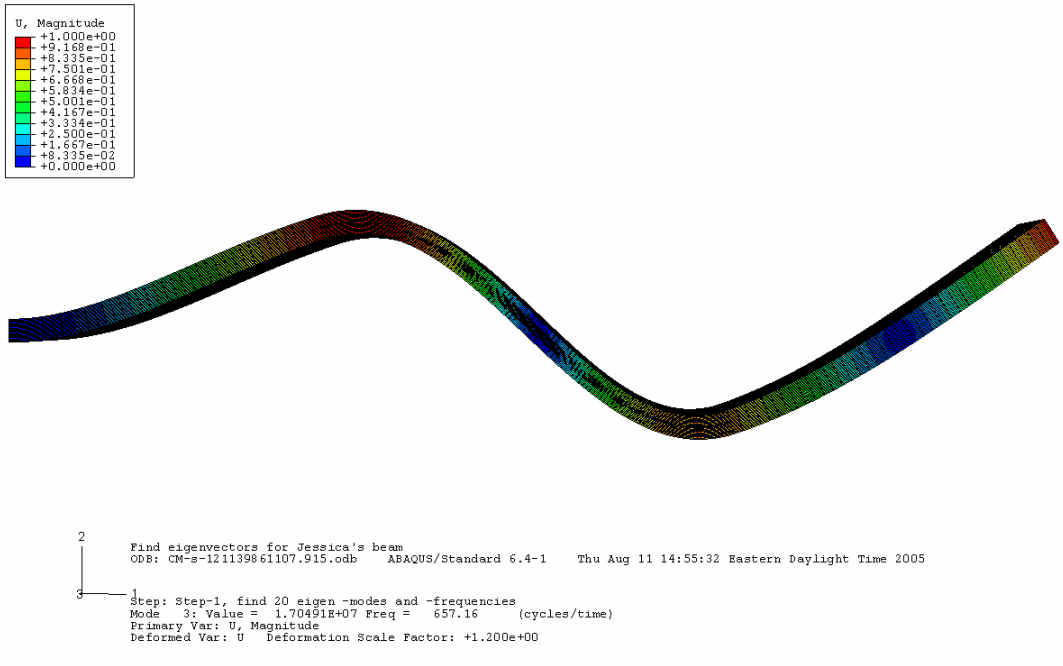

Figure 134. Third mode, 12 cm (4.724 in) middle notch

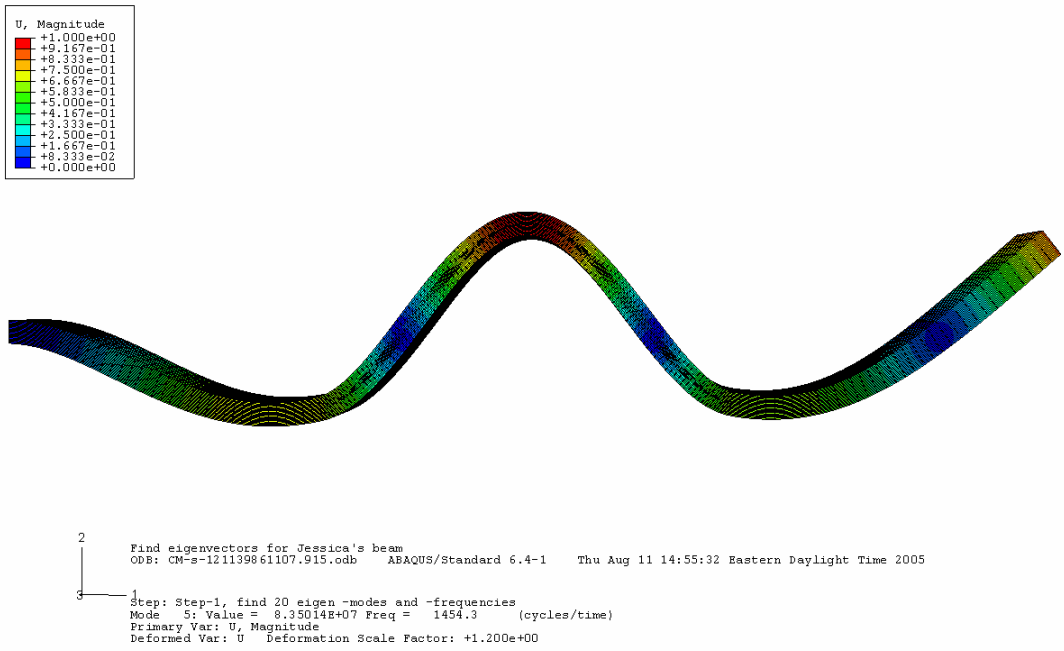

Figure 135. Fourth mode, 12 cm (4.724 in) middle notch

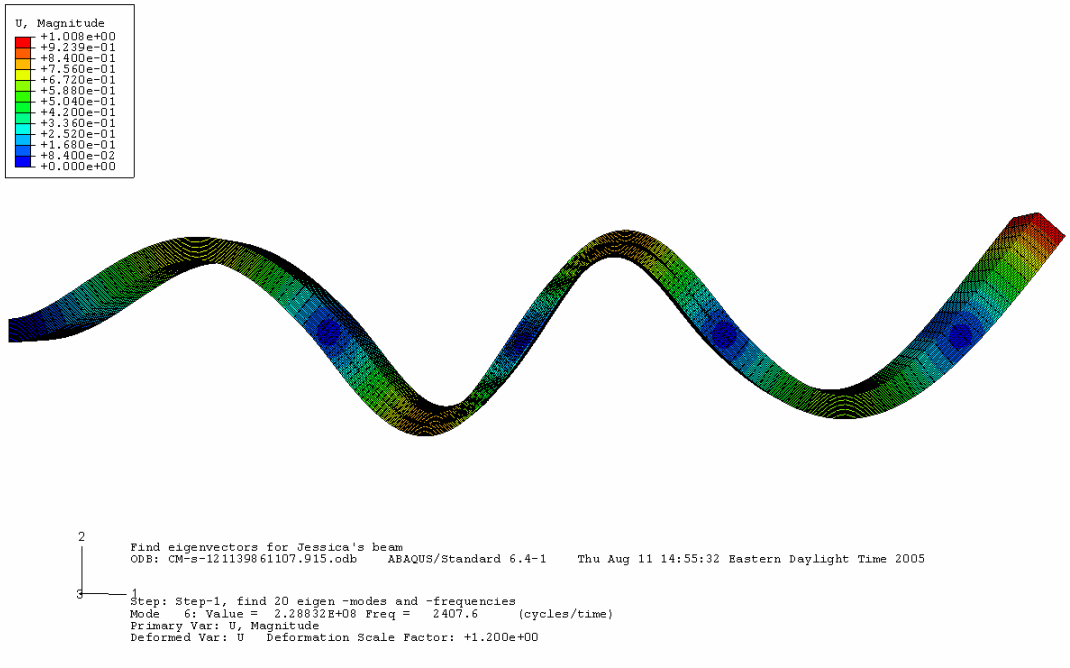

Figure 136. Fifth mode, 12 cm (4.724 in) middle notch

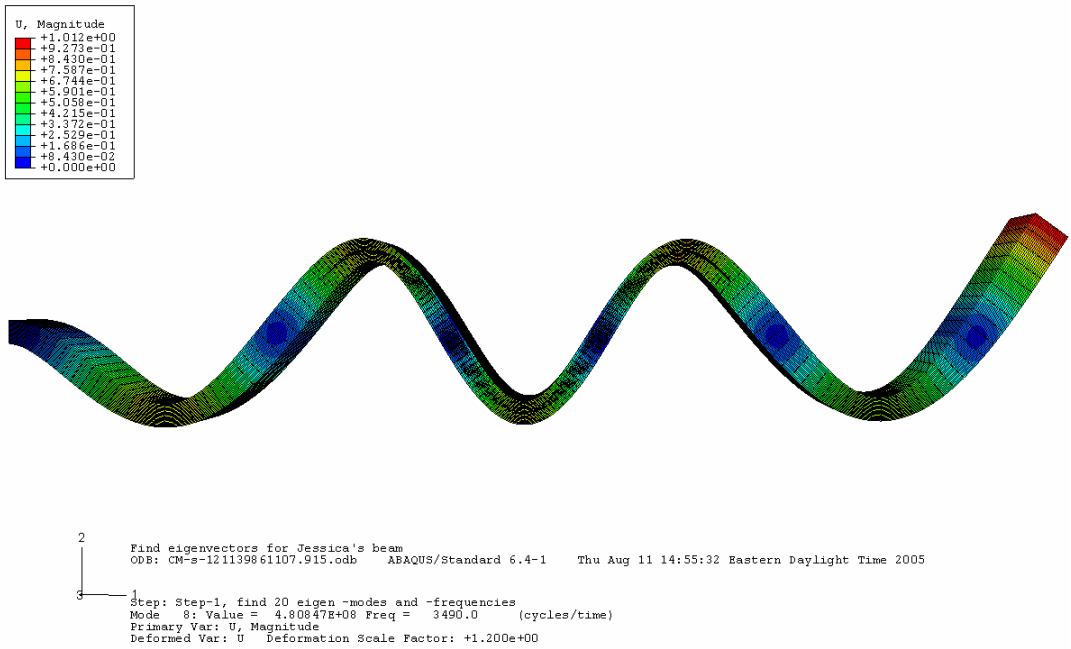

Figure 137. Sixth mode, 12 cm (4.724 in) middle notch

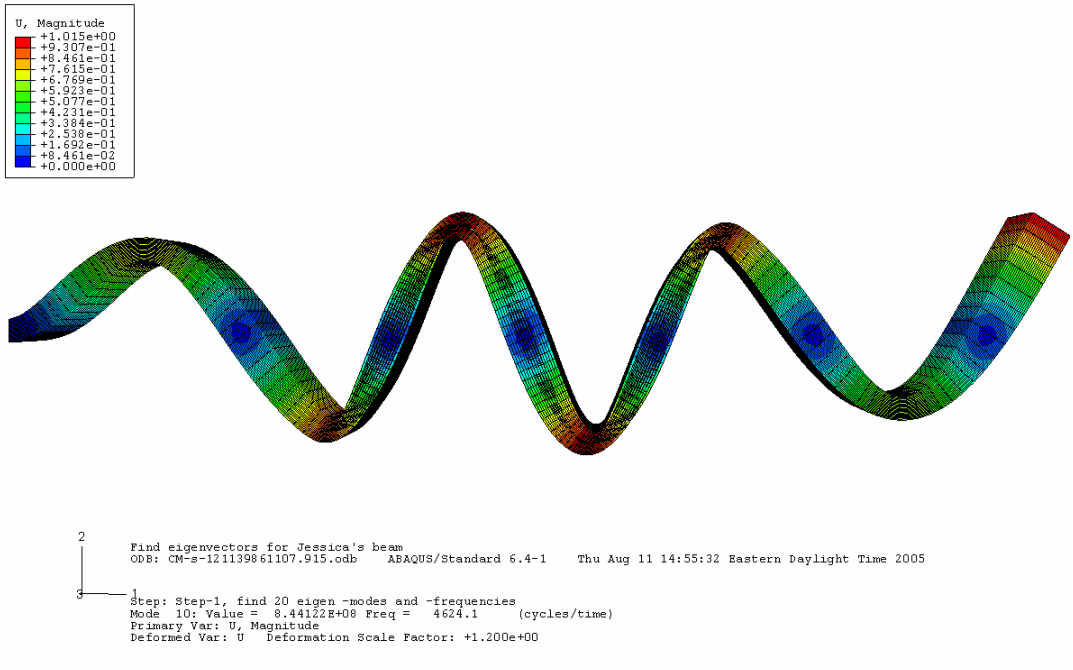

Figure 138. Seventh mode, 12 cm (4.724 in) middle notch

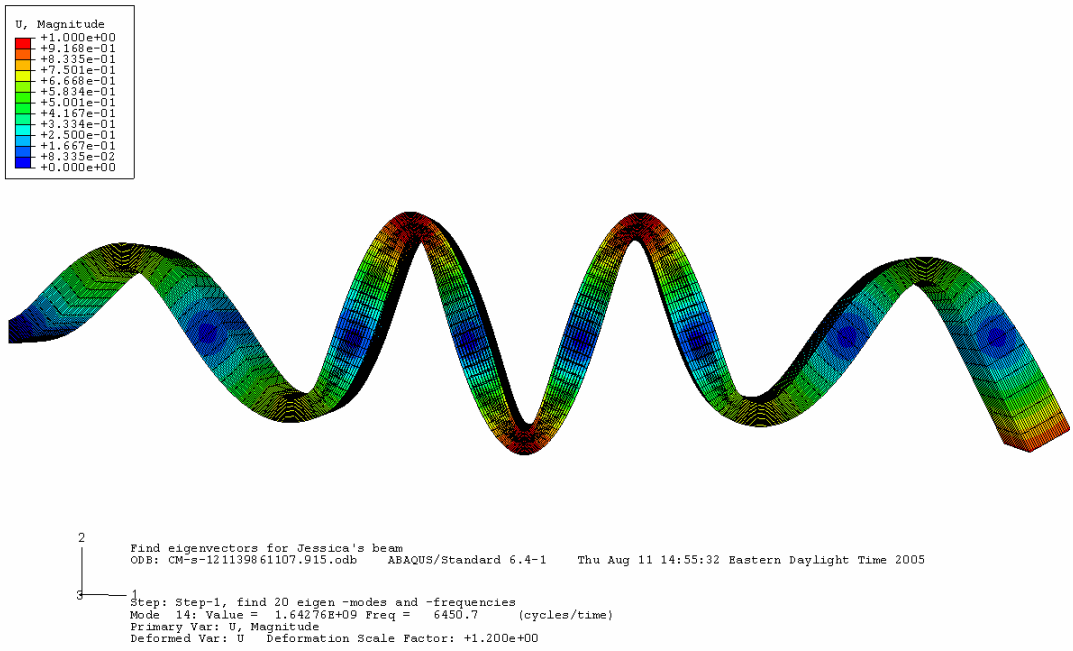

Figure 139. Eighth mode, 12 cm (4.724 in) middle notch

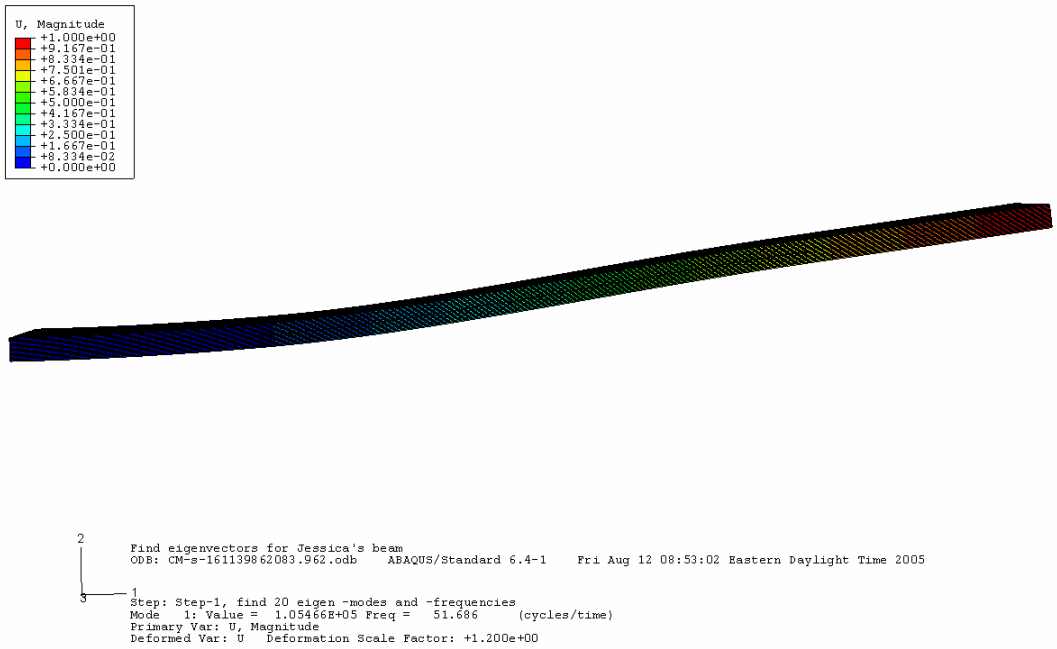

Figure 140. First mode, 16 cm (6.299 in) middle notch

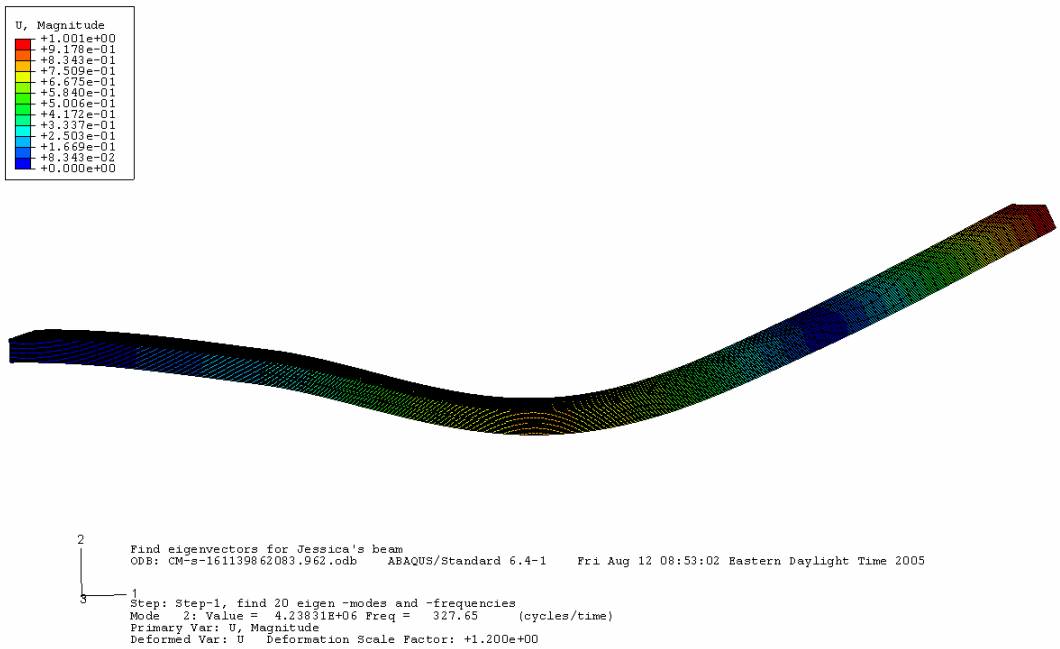

Figure 141. Second mode, 16 cm (6.299 in) middle notch

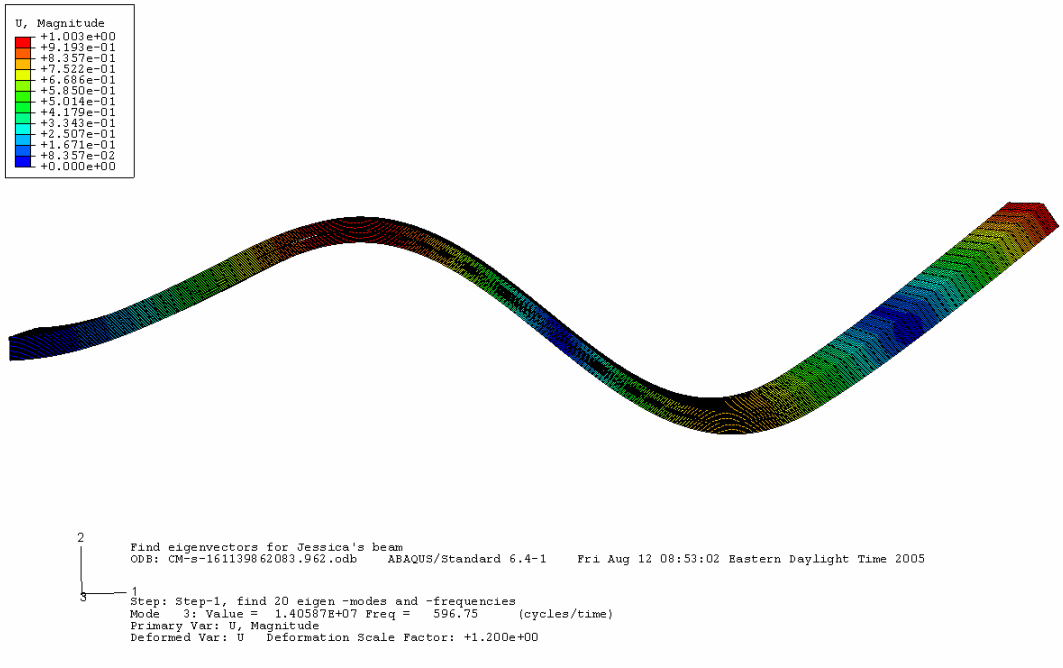

Figure 142. Third mode, 16 cm (6.299 in) middle notch

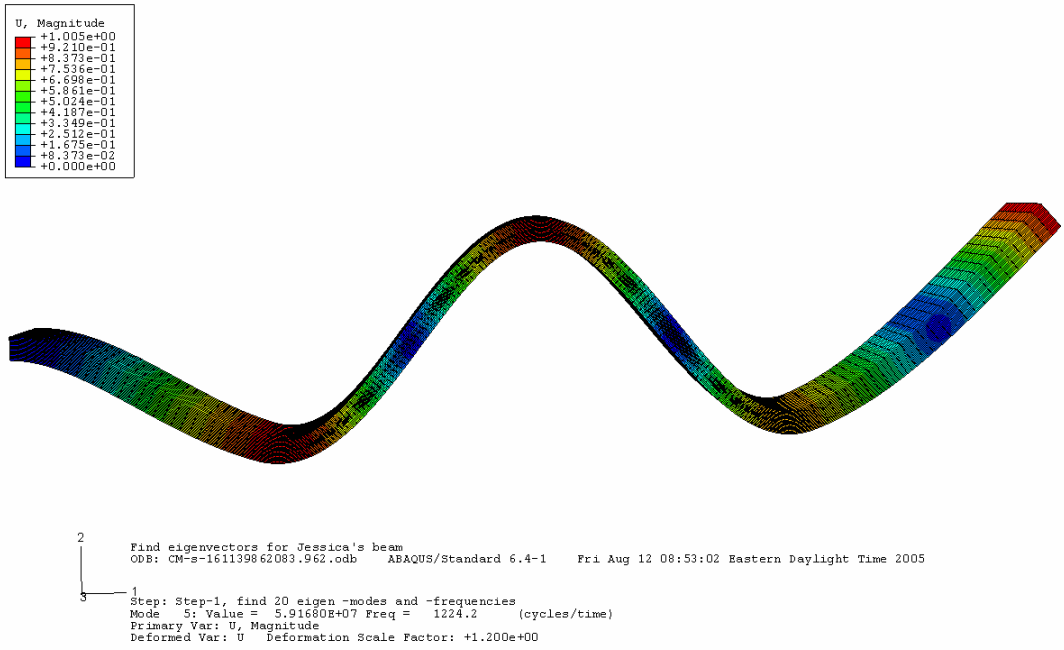

Figure 143. Fourth mode, 16 cm (6.299 in) middle notch

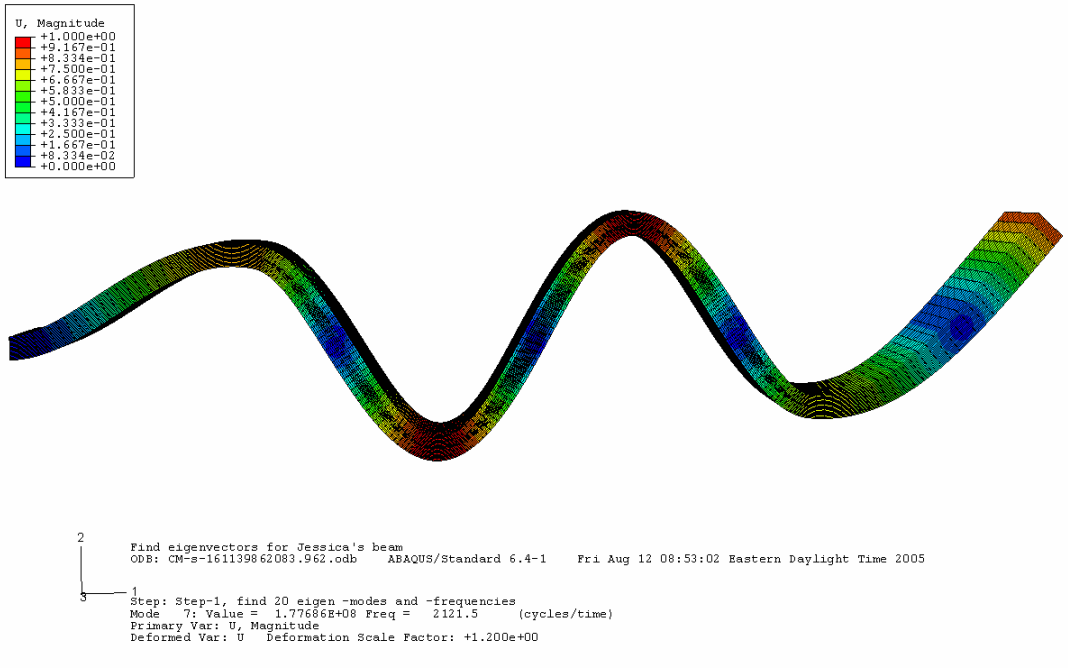

Figure 144. Fifth mode, 16 cm (6.299 in) middle notch

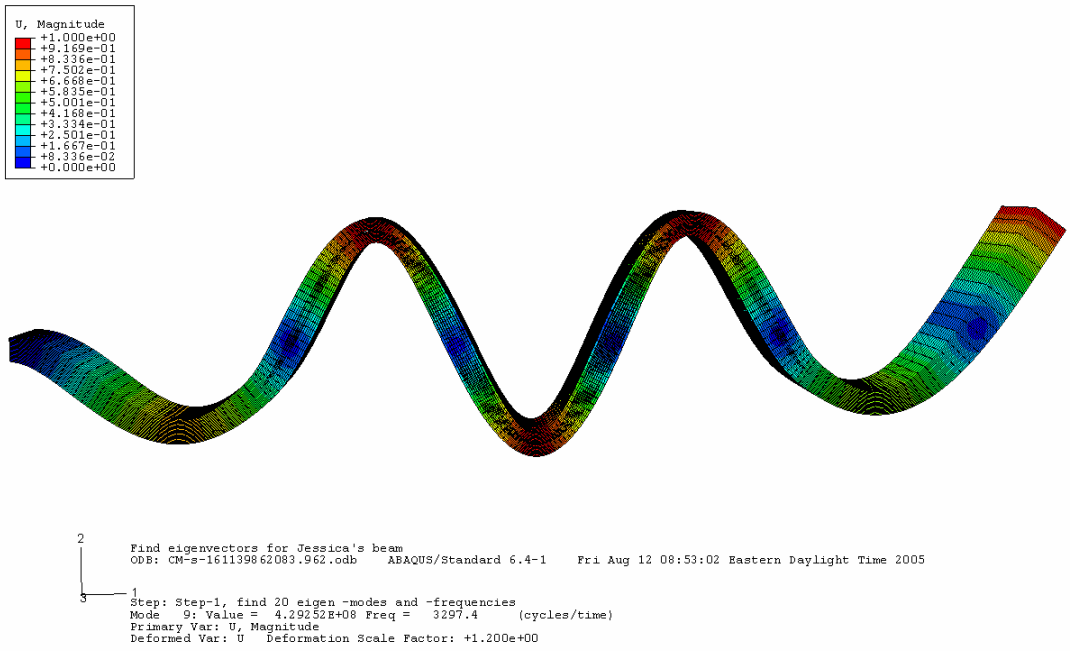

Figure 145. Sixth mode, 16 cm (6.299 in) middle notch

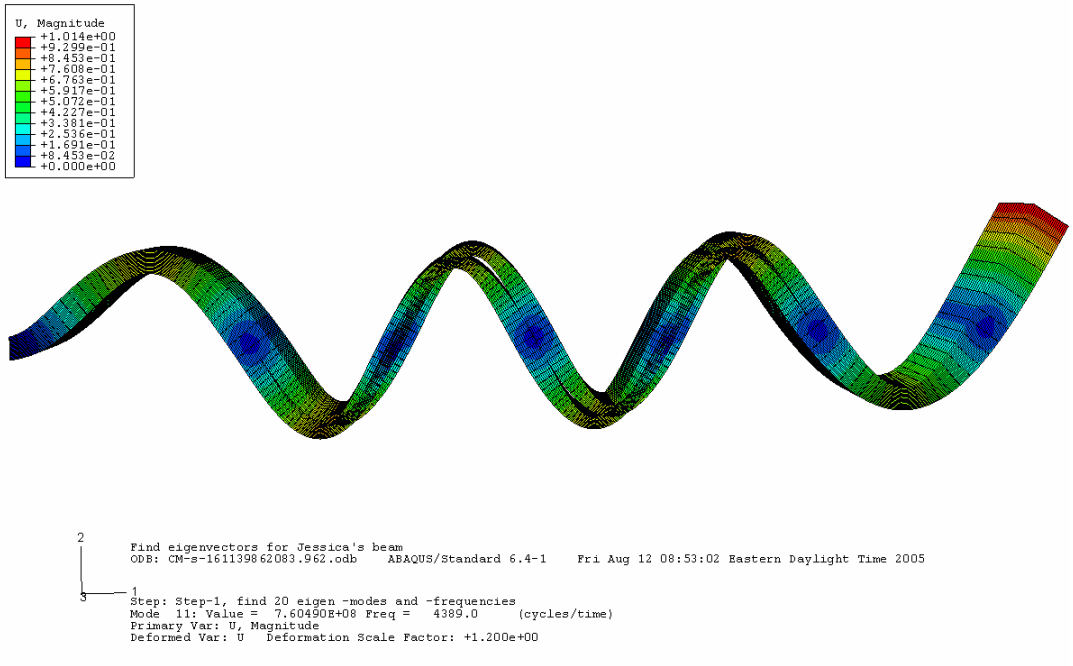

Figure 146. Seventh mode, 16 cm (6.299 in) middle notch

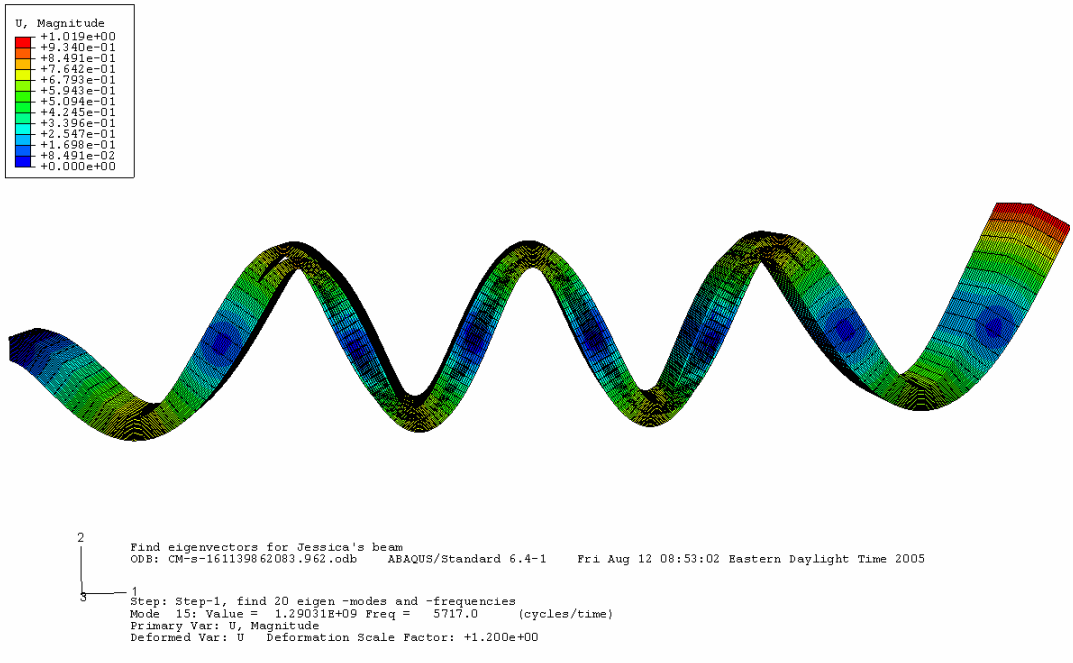

Figure 147. Eighth mode, 16 cm (6.299 in) middle notch

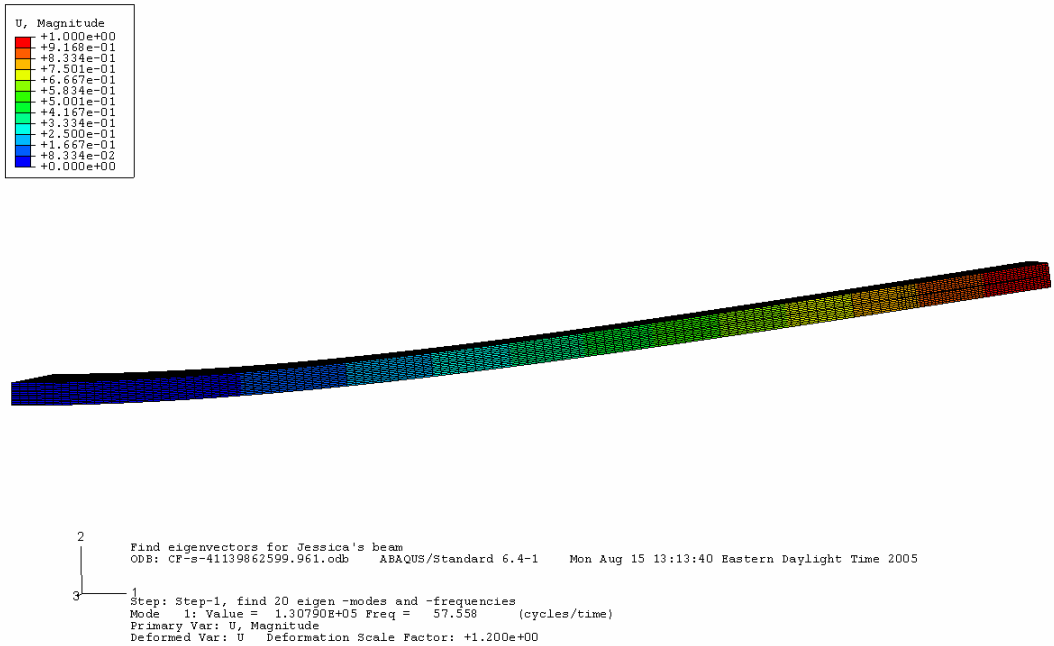

Figure 148. First mode, 4 cm (1.575 in) free end notch

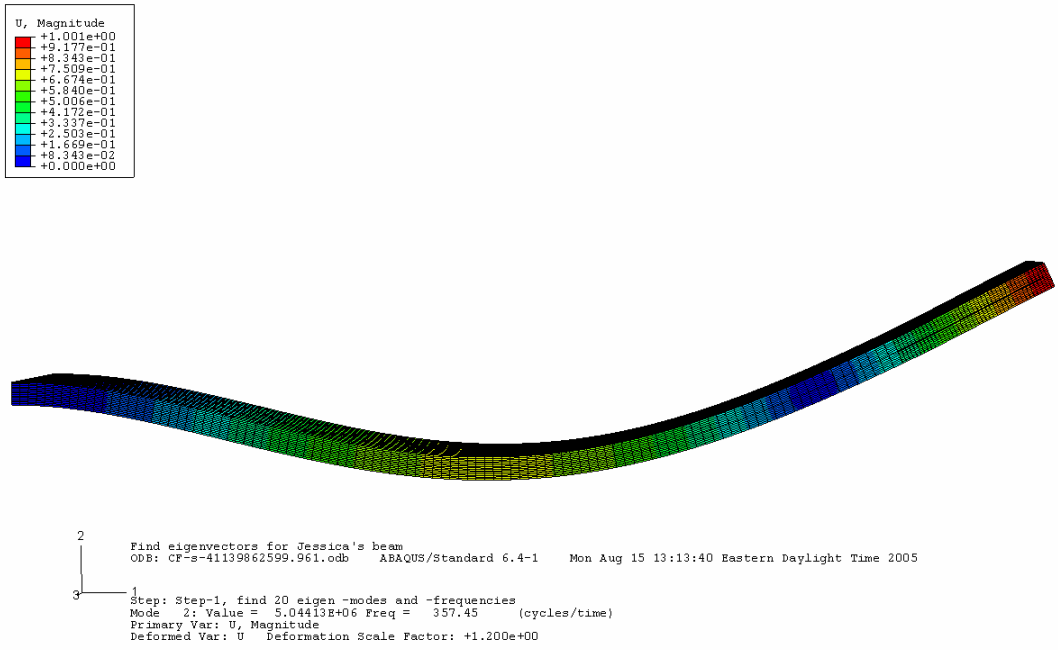

Figure 149. Second mode, 4 cm (1.575 in) free end notch

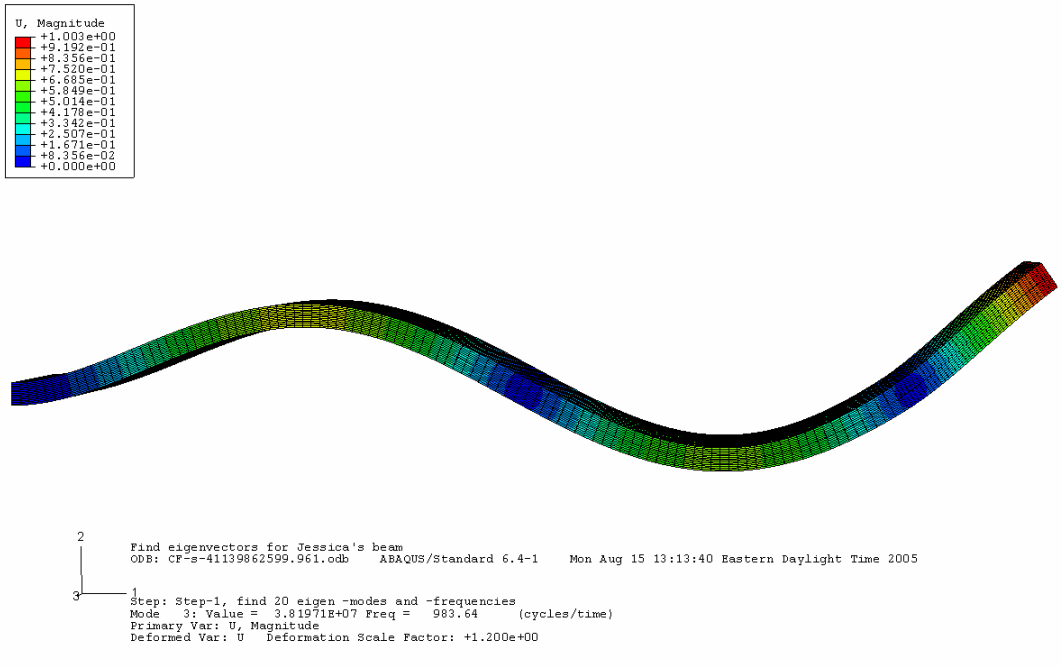

Figure 150. Third mode, 4 cm (1.575 in) free end notch

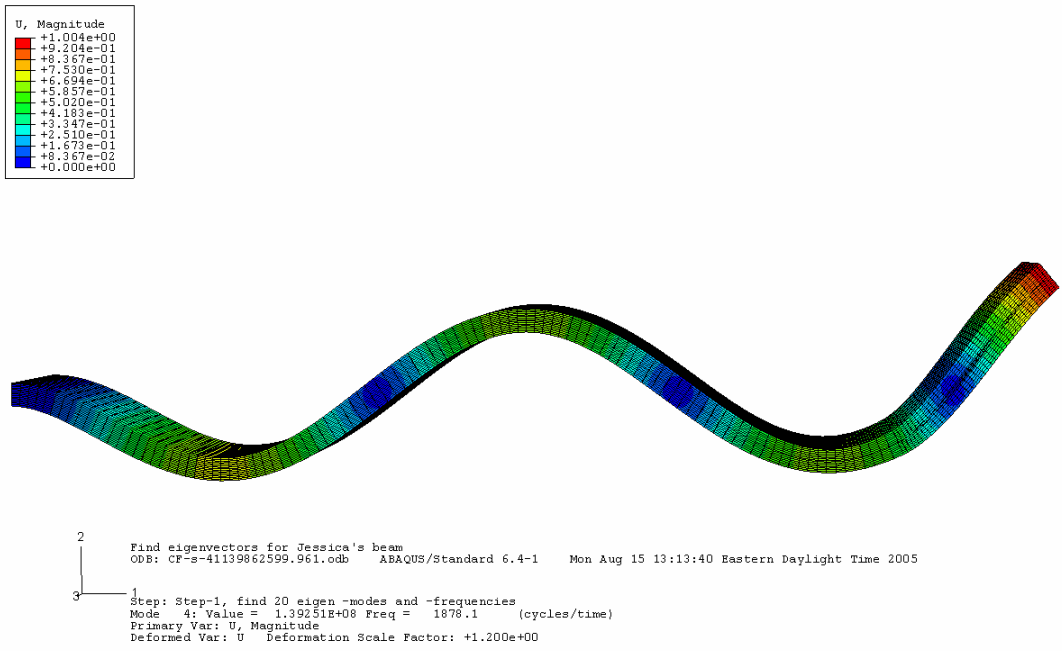

Figure 151. Fourth mode, 4 cm (1.575 in) free end mode

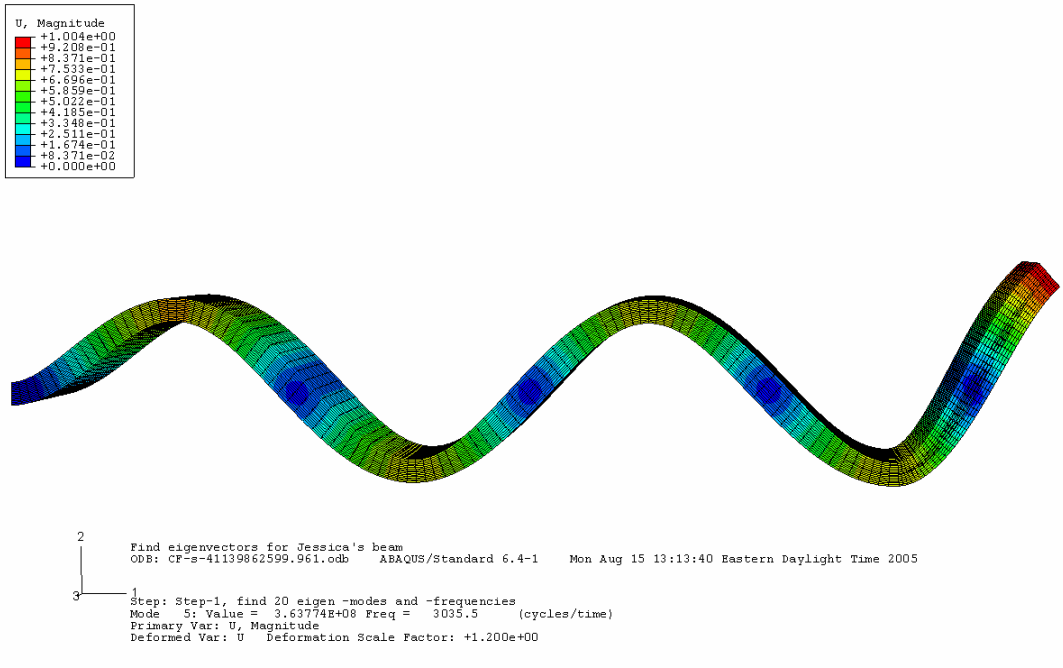

Figure 152. Fifth mode, 4 cm (1.575 in) free end notch

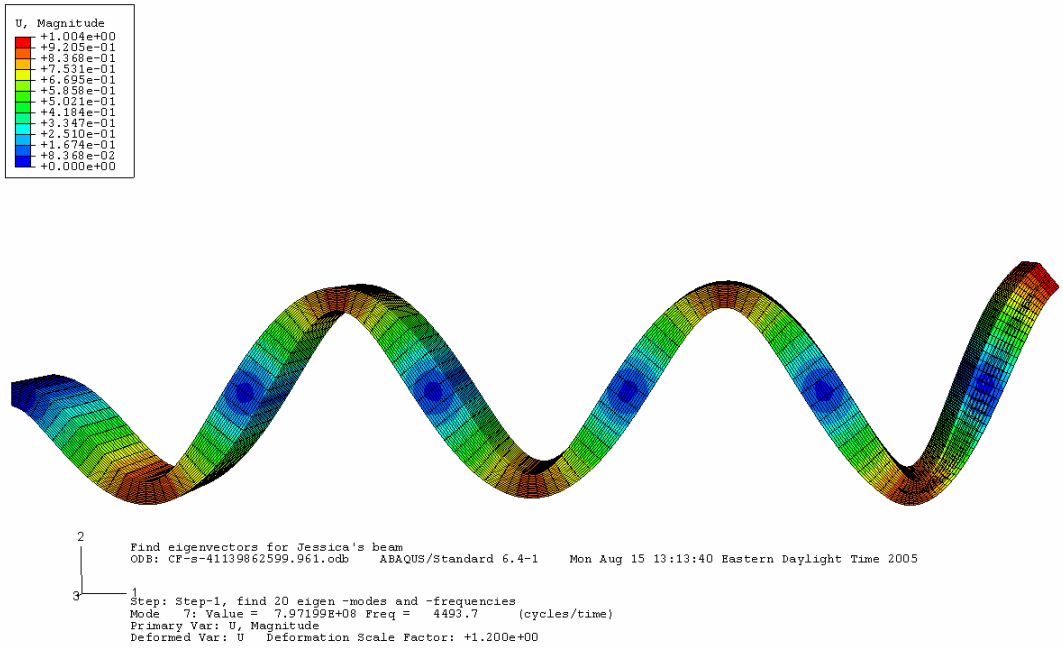

Figure 153. Sixth mode, 4 cm (1.575 in) free end notch

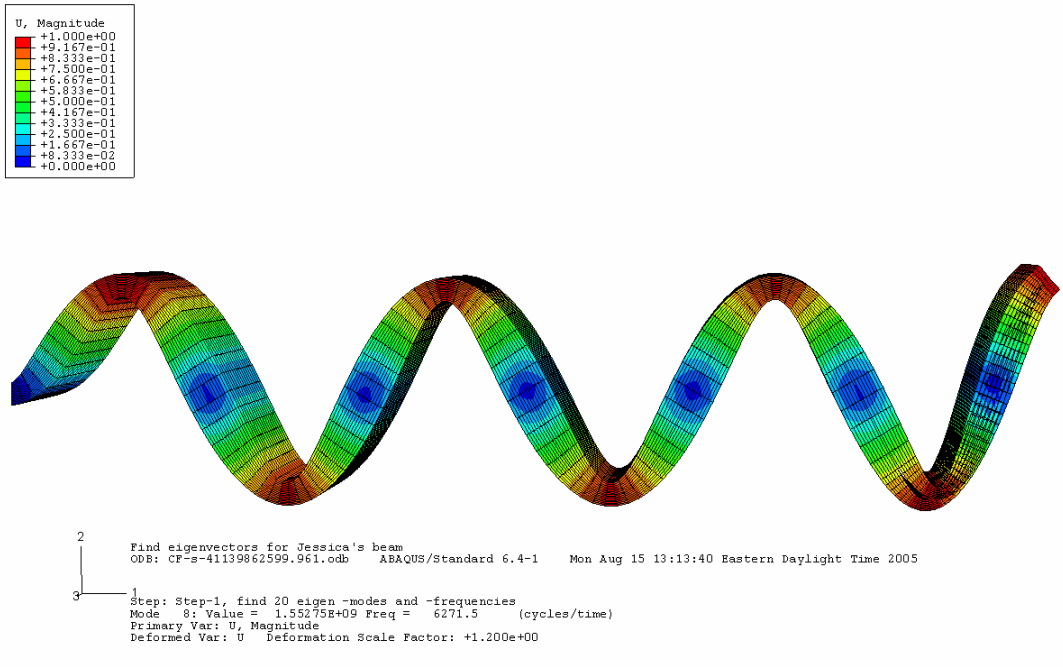

Figure 154. Seventh mode, 4 cm (1.575 in) free end notch

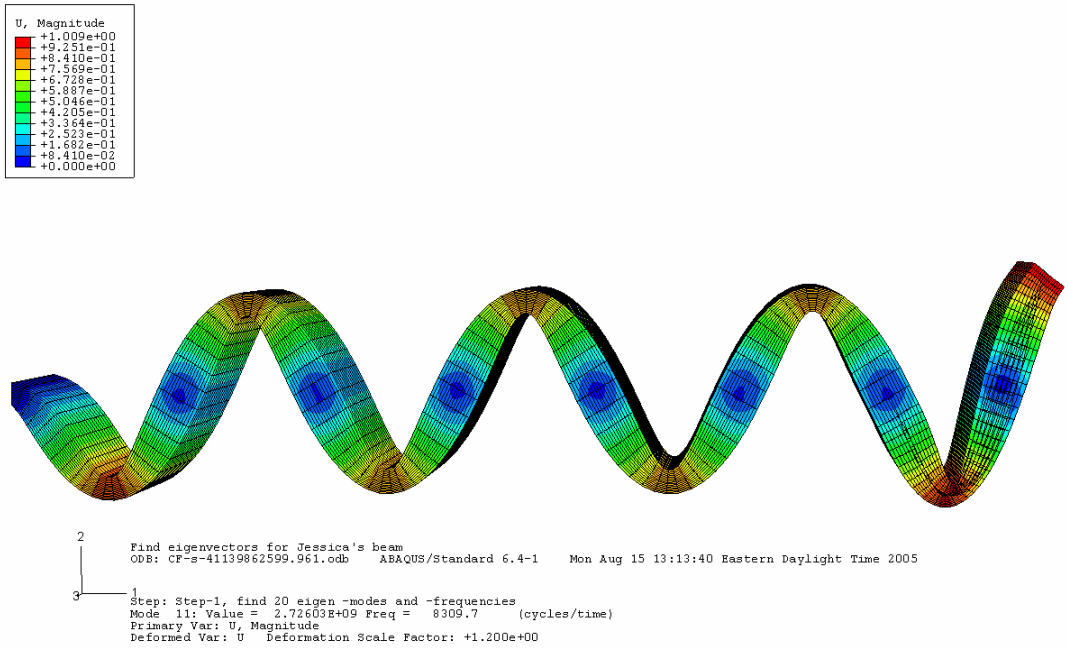

Figure 155. Eighth mode, 4 cm (1.575 in) free end notch

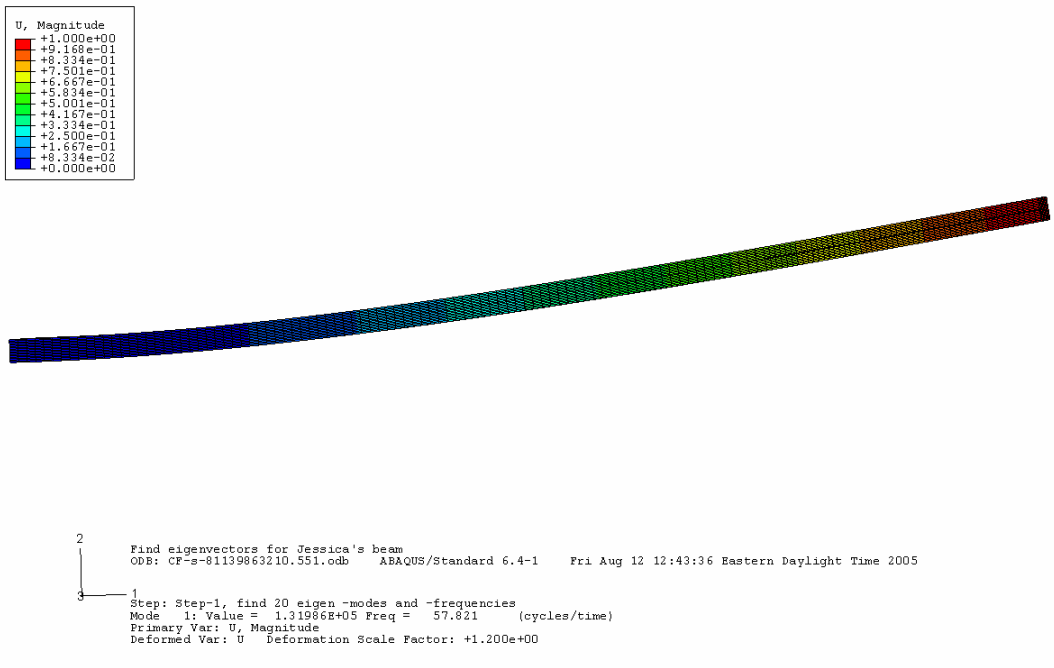

Figure 156. First mode, 8 cm (3.150 in) free end notch

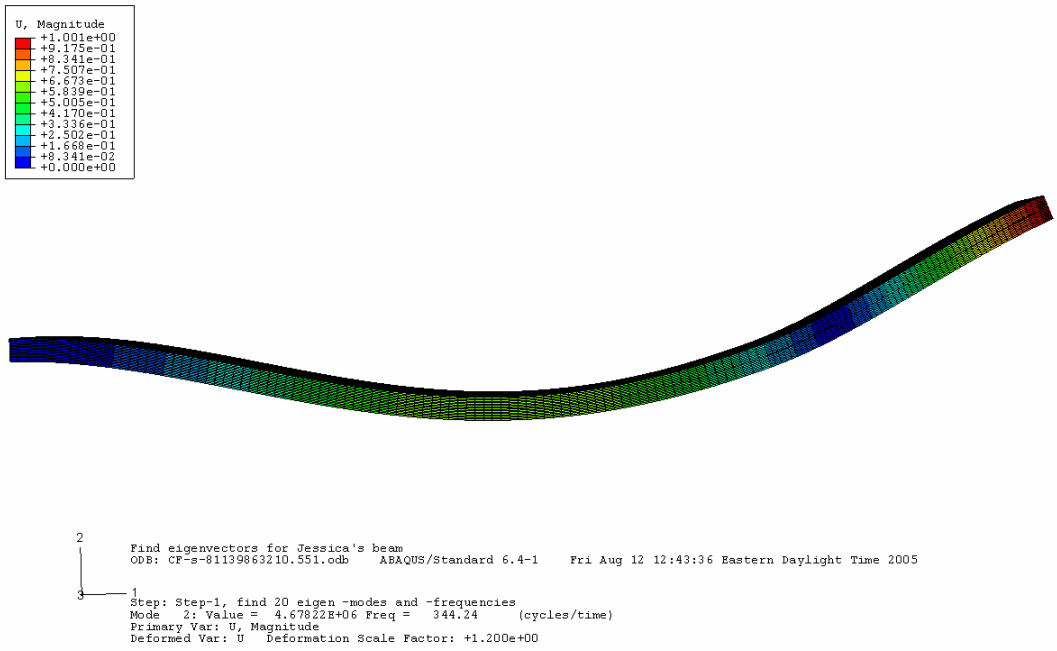

Figure 157. Second mode, 8 cm (3.150 in) free end notch

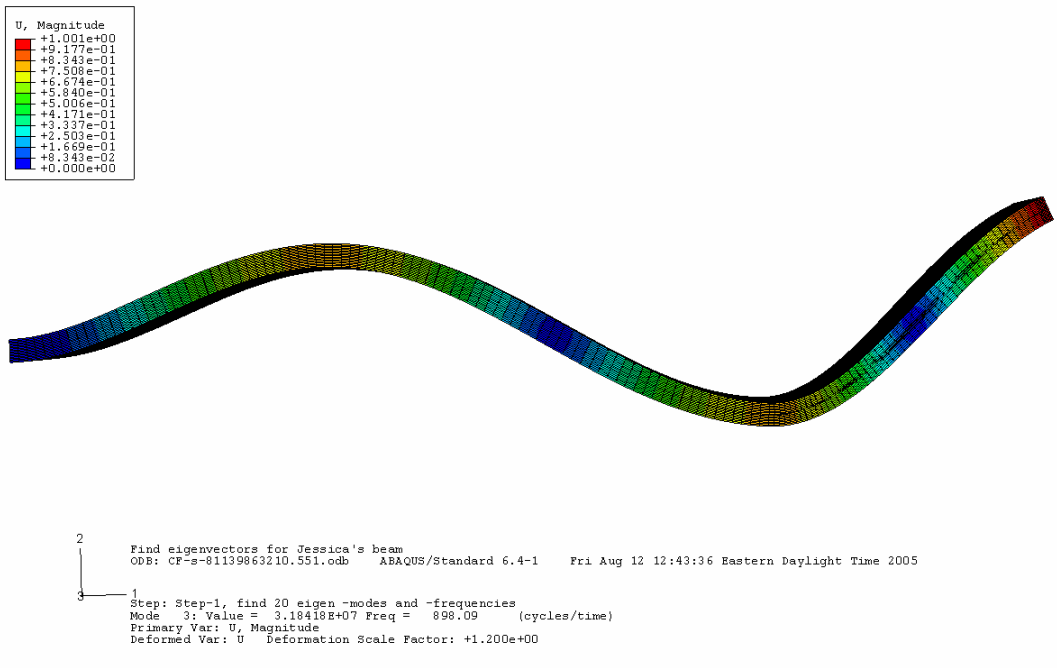

Figure 158. Third mode, 8 cm (3.150 in) free end notch

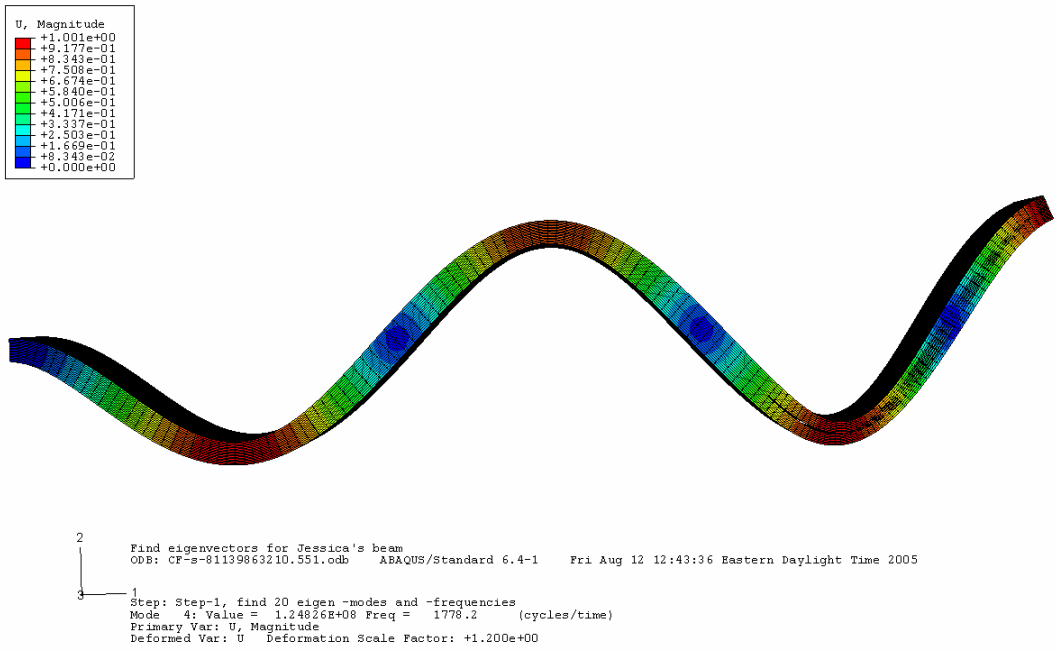

Figure 159. Fourth mode, 8 cm (3.150 in) free end notch

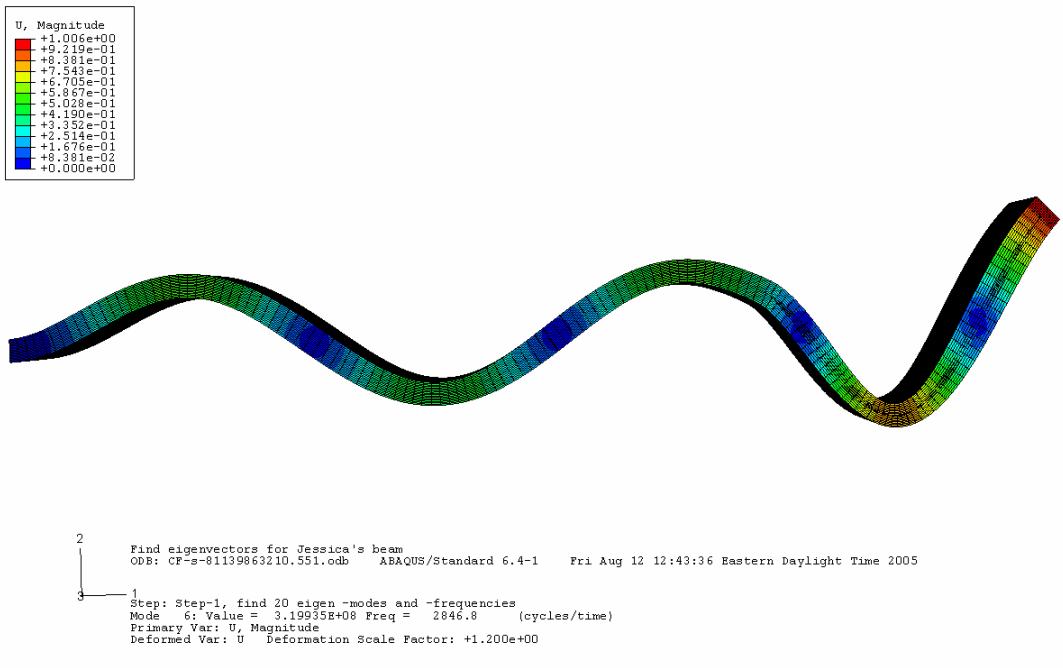

Figure 160. Fifth mode, 8 cm (3.150 in) free end notch

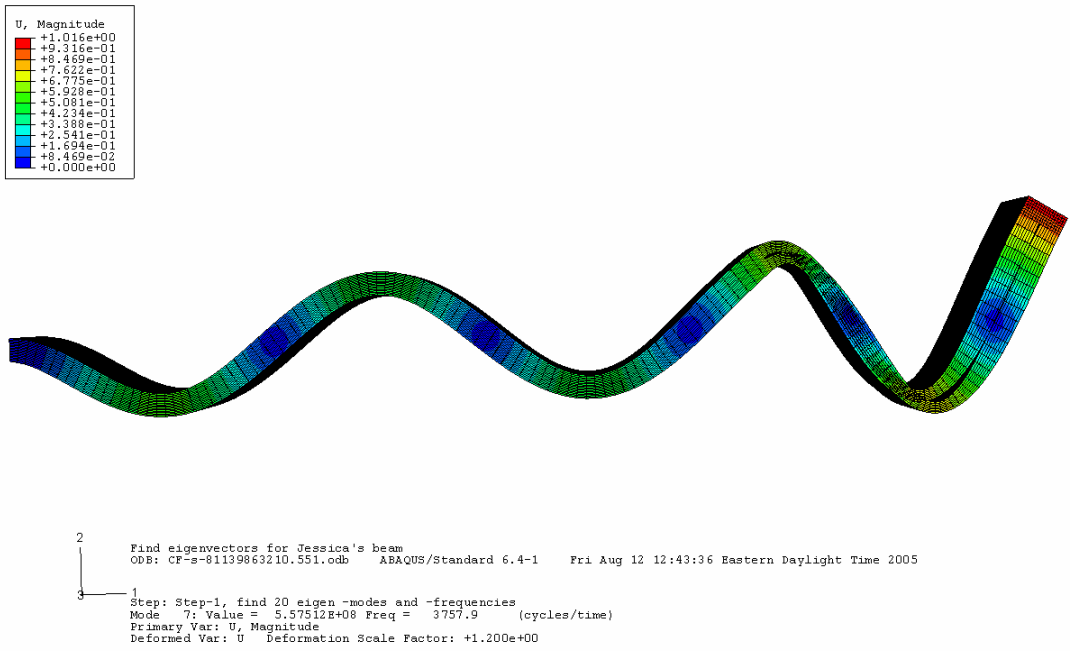

Figure 161. Sixth mode, 8 cm (3.150 in) free end

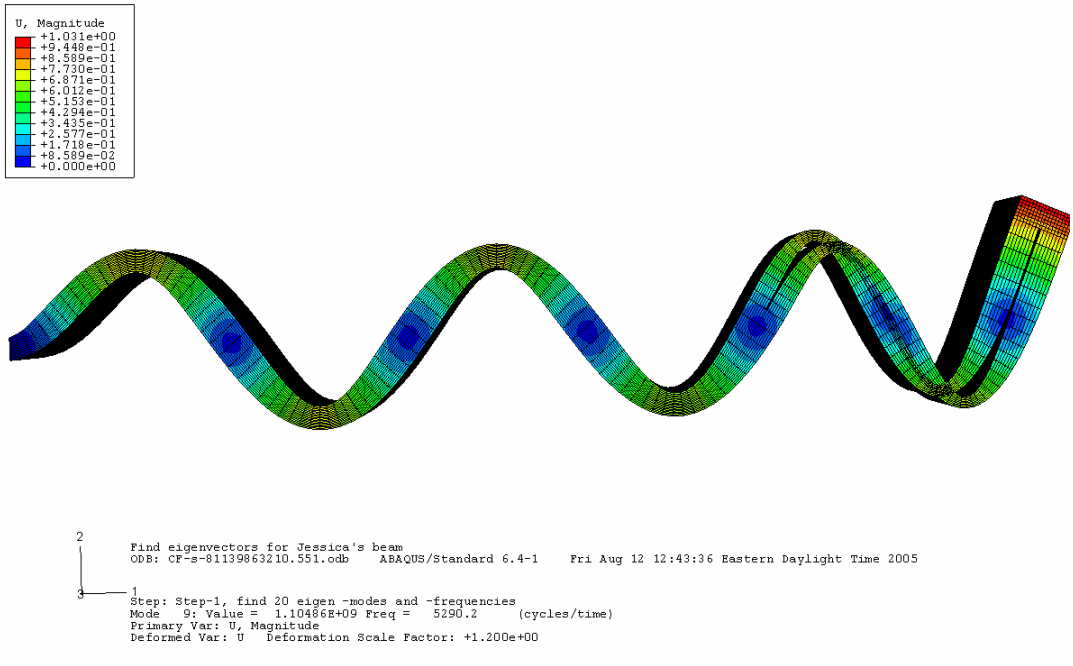

Figure 162. Seventh mode, 8 cm (3.150 in) free end notch

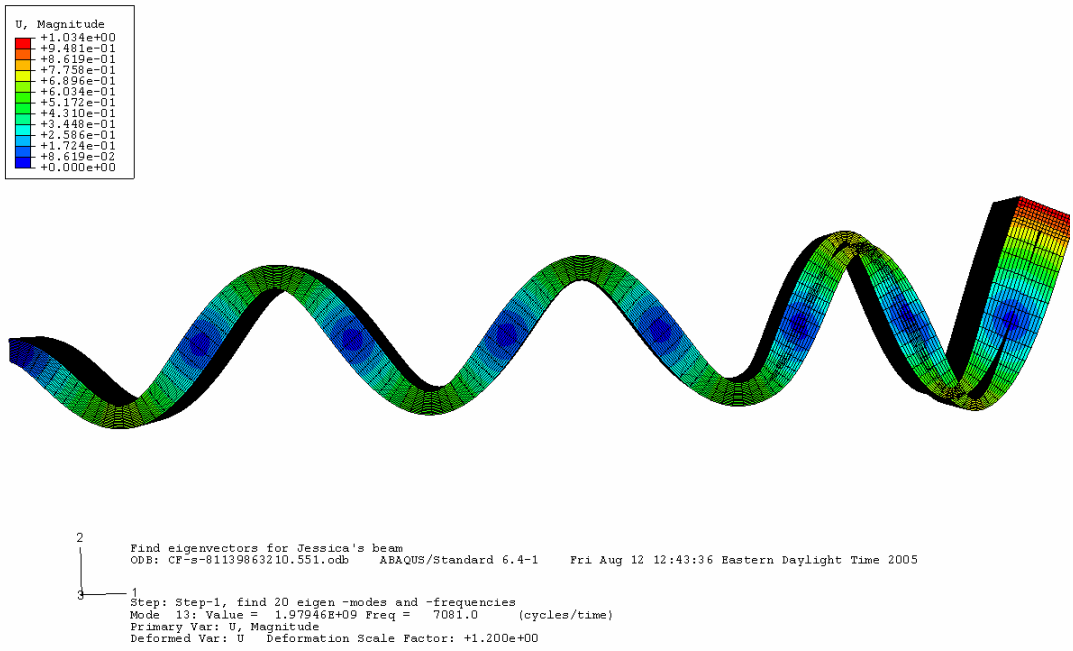

Figure 163. Eighth mode, 8 cm (3.150 in) free end notch

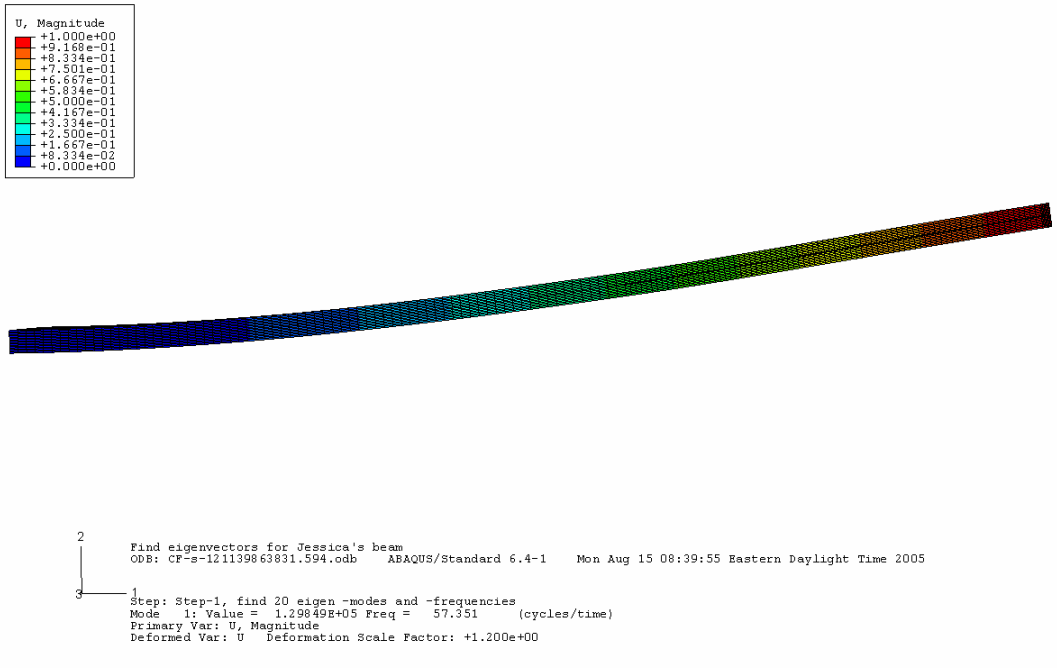

Figure 164. First mode, 12 cm (4.724 in) free end notch

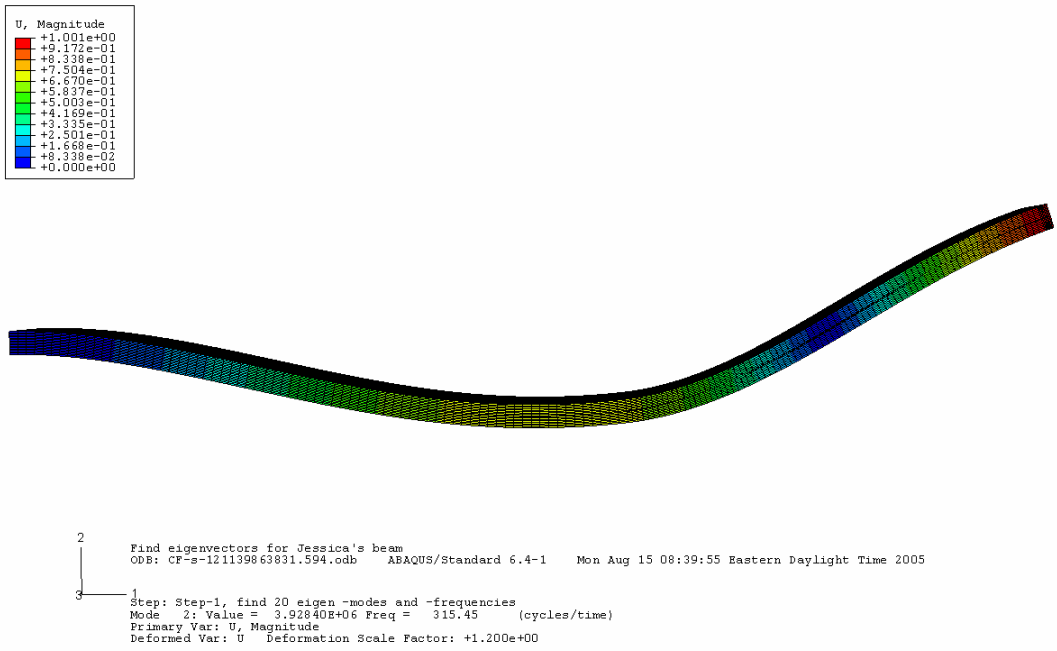

Figure 165. Second mode, 12 cm (4.724 in) free end notch

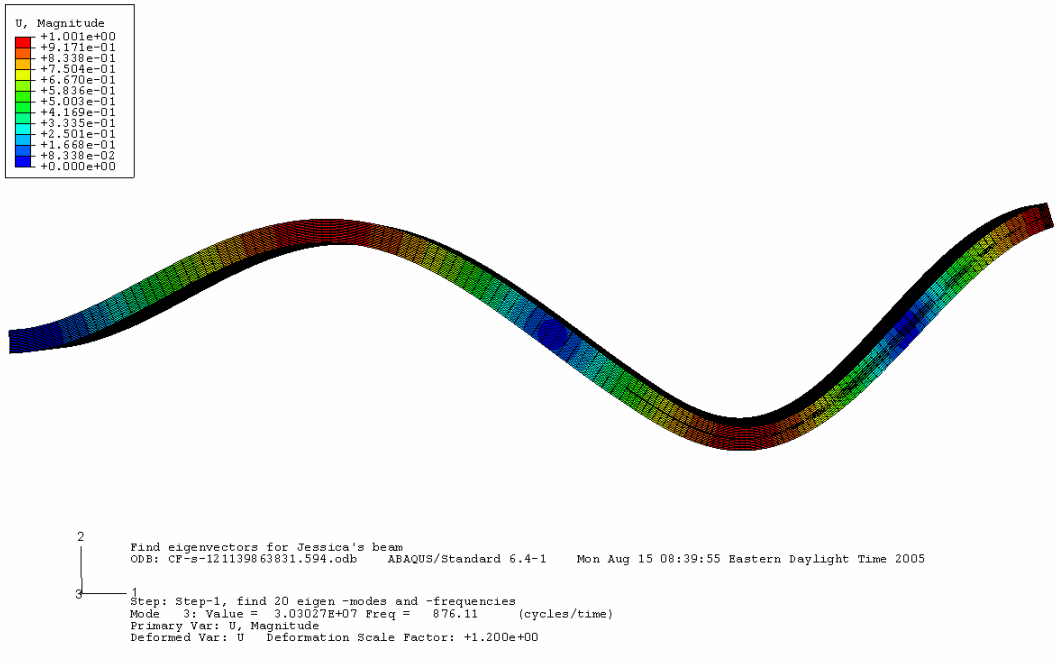

Figure 166. Third mode, 12 cm (4.724 in) free end notch

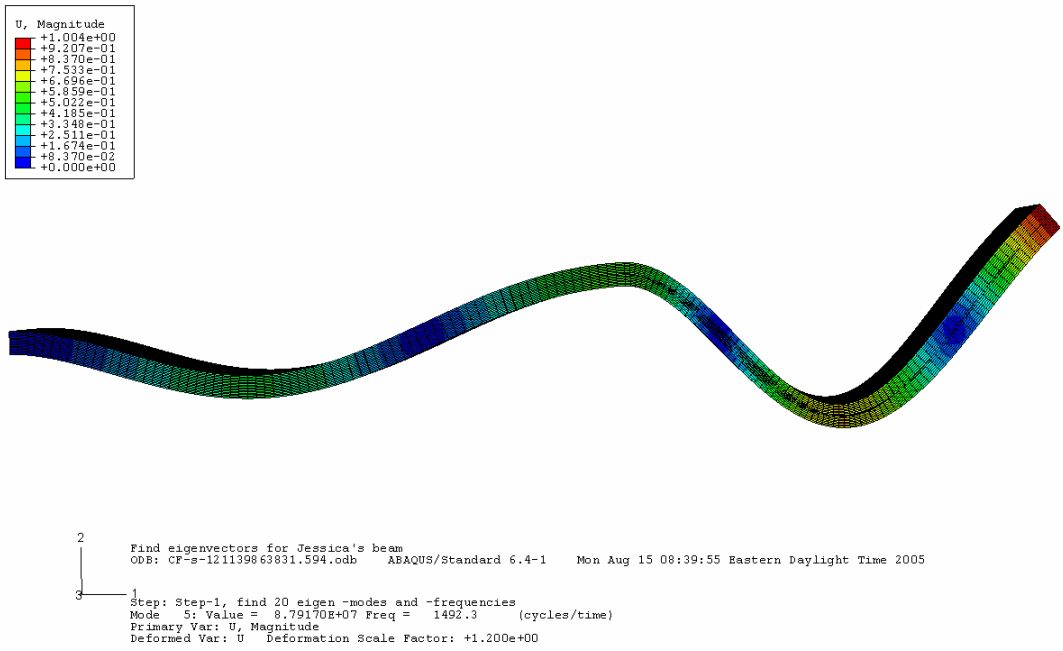

Figure 167. Fourth mode, 12 cm (4.724 in) free end notch

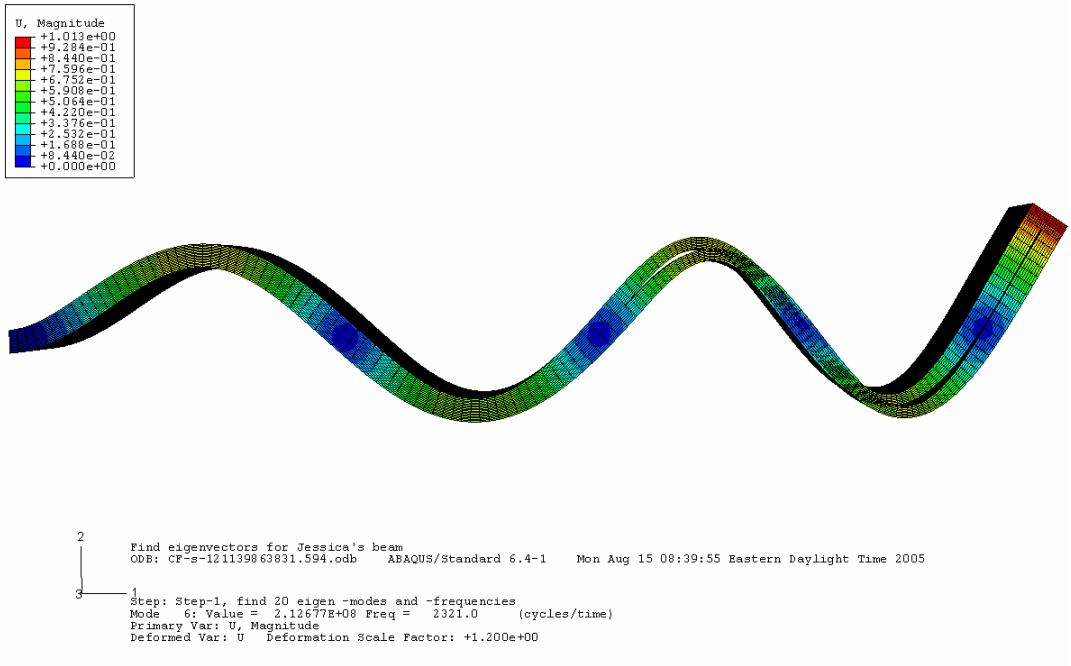

Figure 168. Fifth mode, 12 cm (4.724 in) free end notch

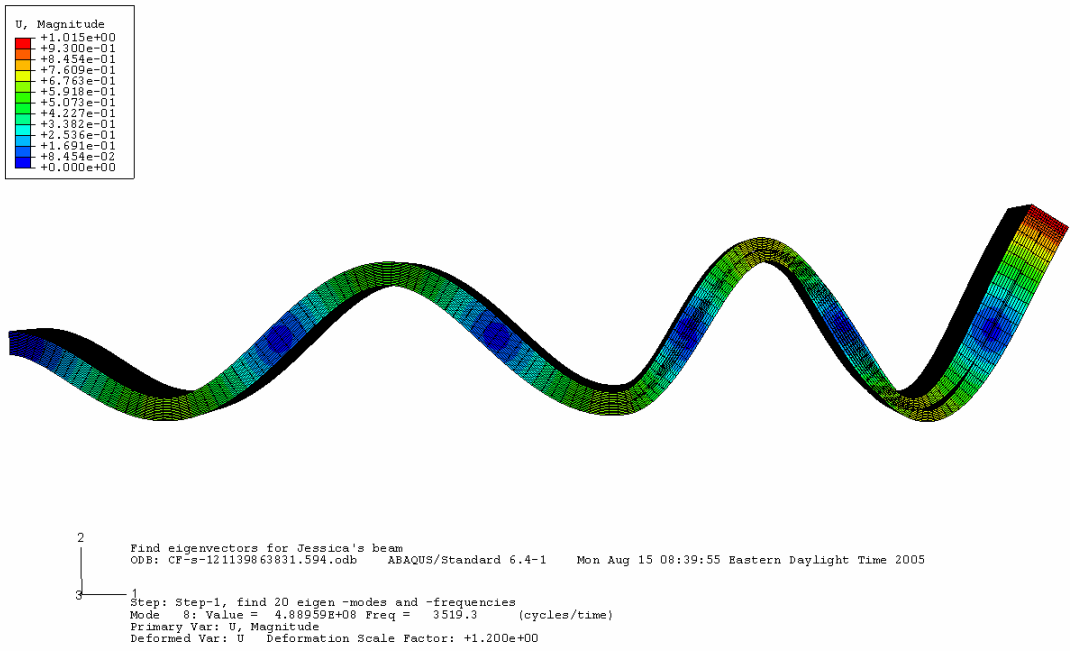

Figure 169. Sixth mode, 12 cm (4.724 in) free end notch

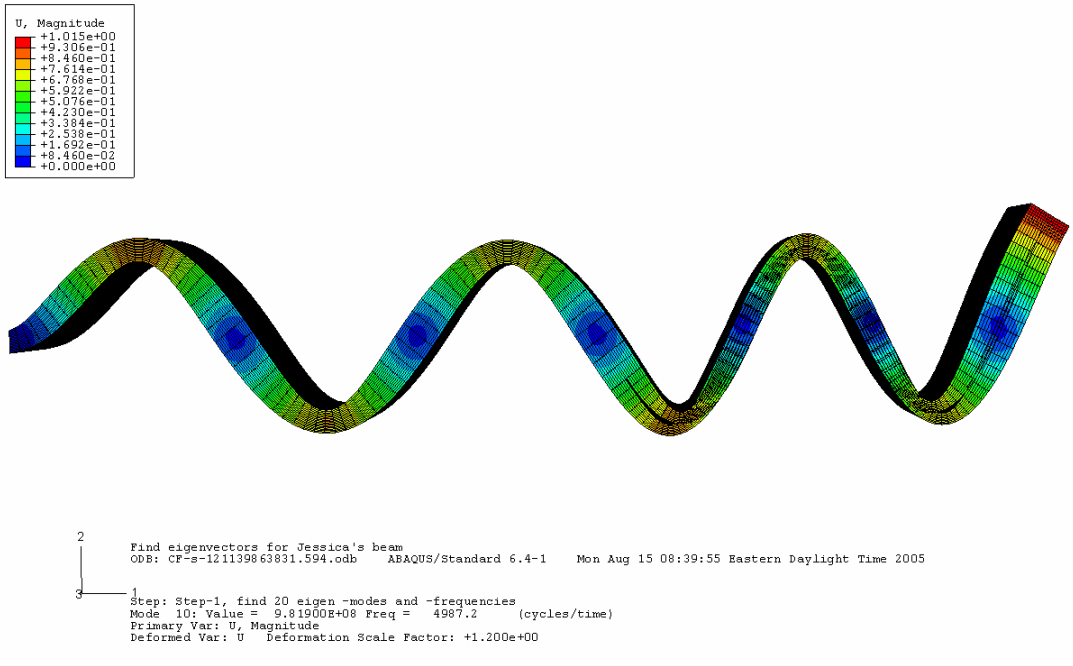

Figure 170. Seventh mode, 12 cm (4.724 in) free end notch

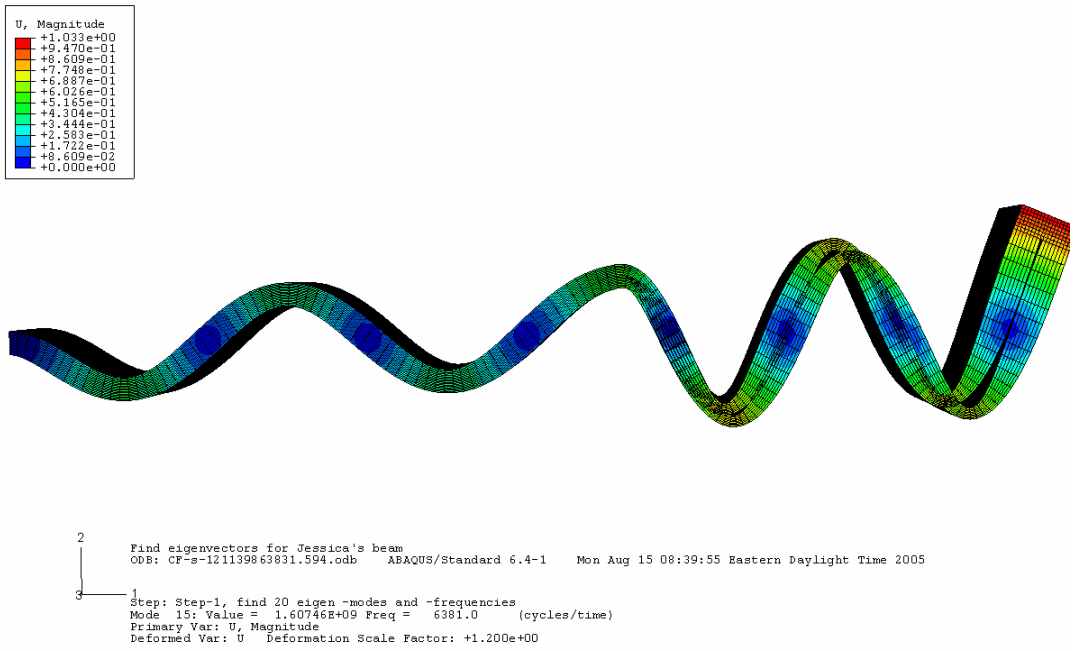

Figure 171. Eighth mode, 12 cm (4.724 in) free end notch

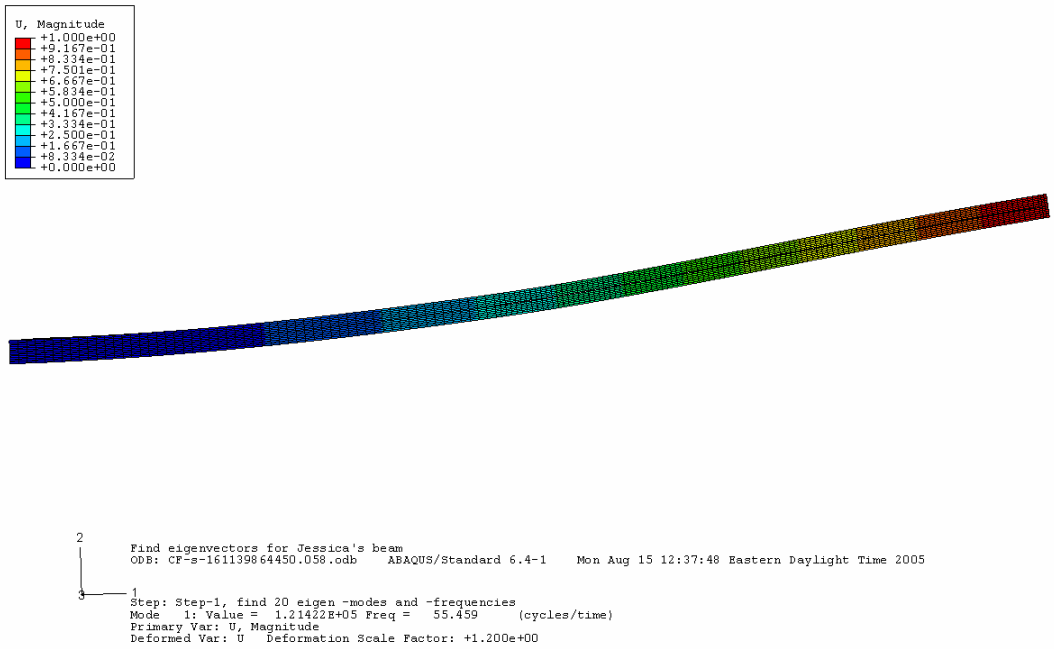

Figure 172. First mode, 16 cm (6.299 in) free end notch

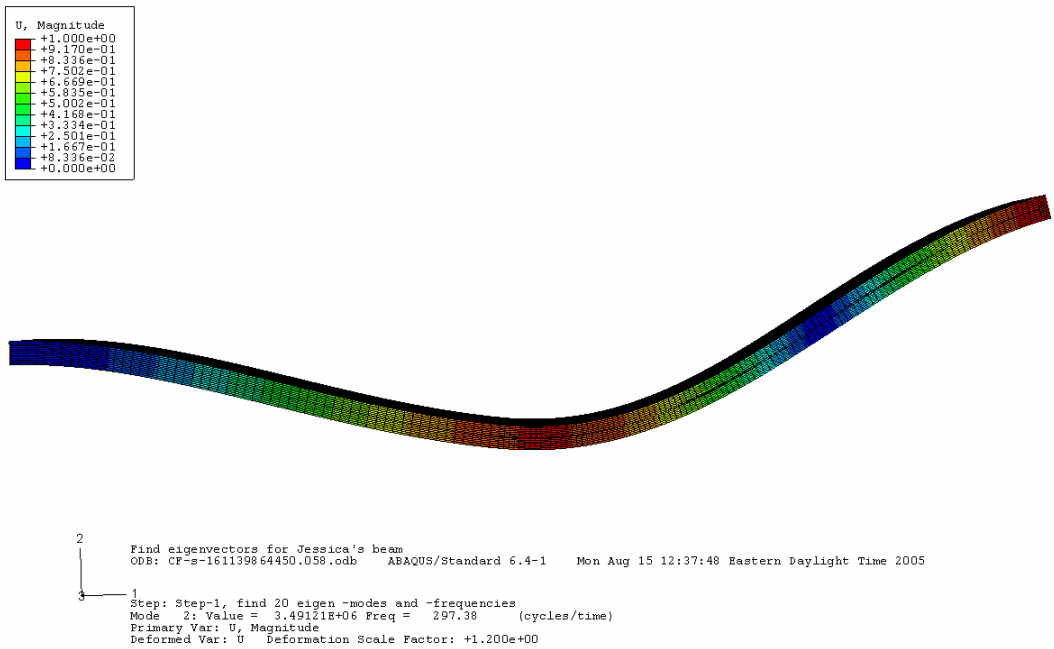

Figure 173. Second mode, 16 cm (6.299 in) free end notch

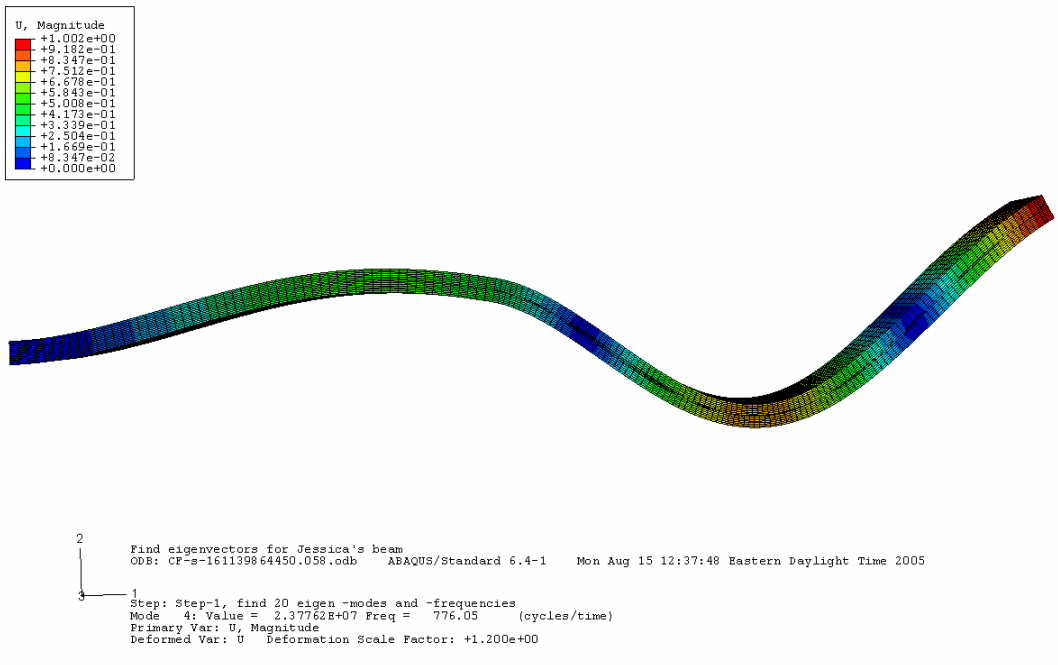

Figure 174. Third mode, 16 cm (6.299 in) free end notch

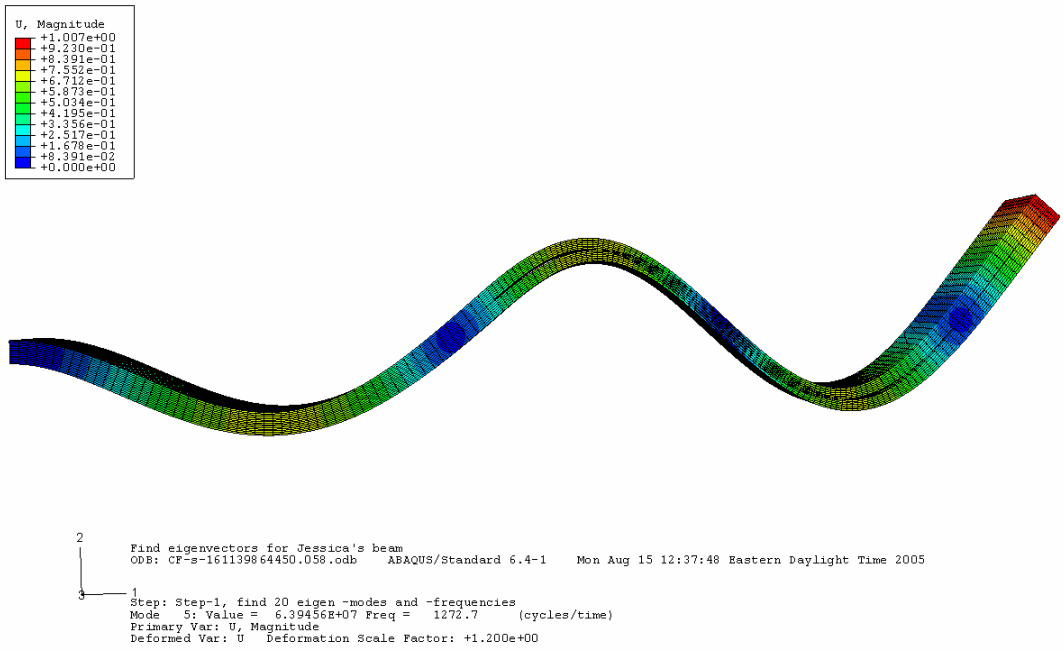

Figure 175. Fourth mode, 16 cm (6.299 in) free end notch

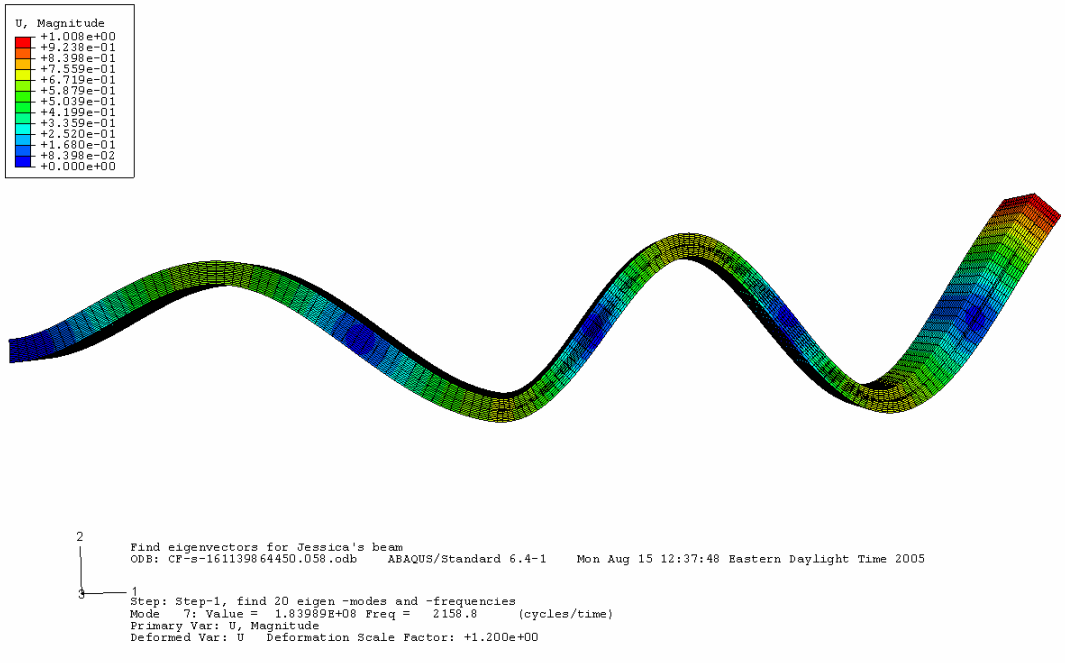

Figure 176. Fifth mode, 16 cm (6.299 in) free end notch

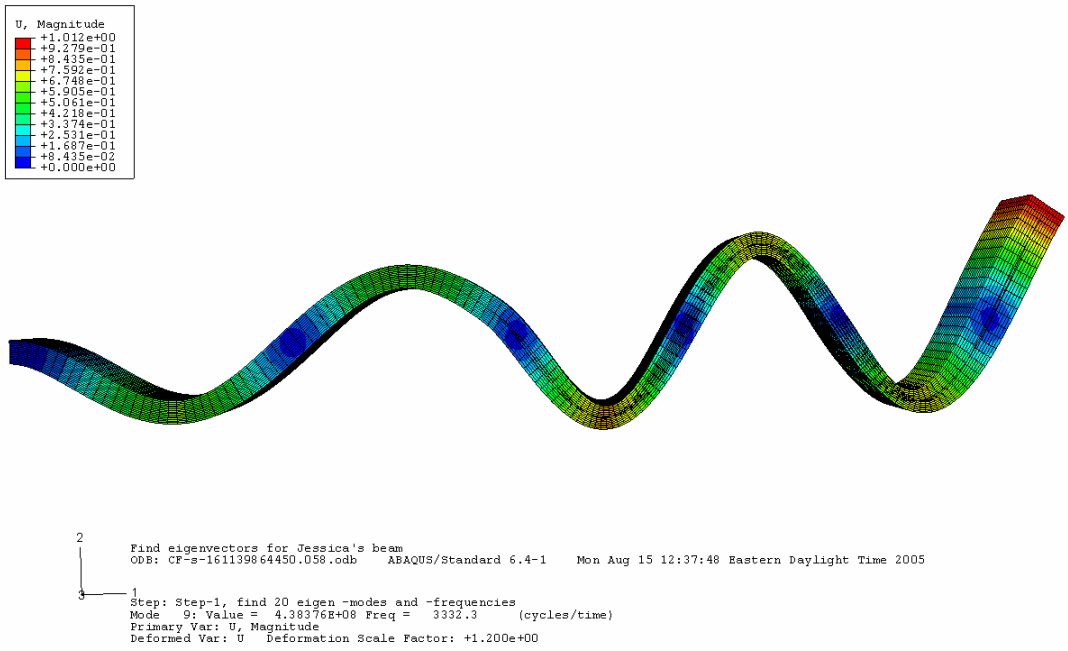

Figure 177. Sixth mode, 16 cm (6.299 in) free end notch

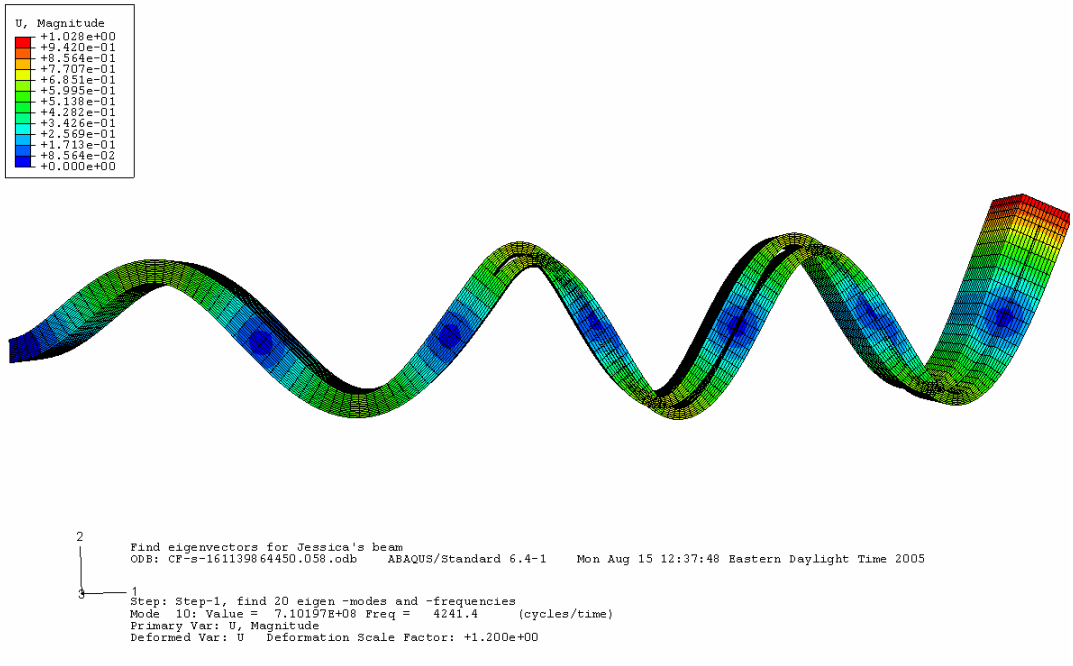

Figure 178. Seventh mode, 16 cm (6.299 in) free end notch

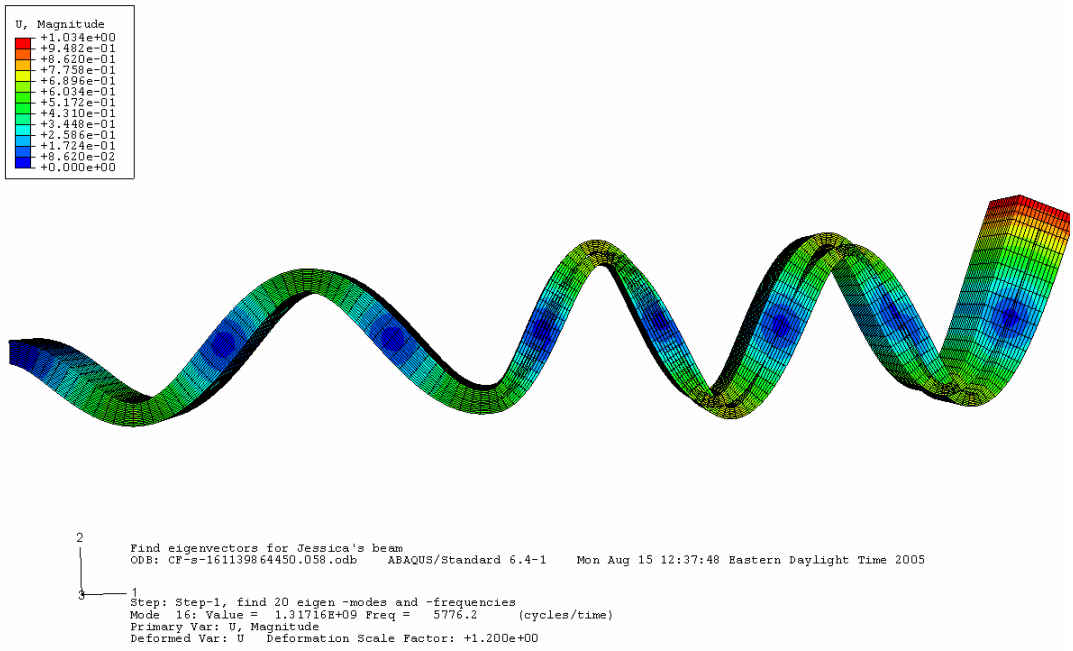

Figure 179. Eighth mode, 16 cm (6.299 in) free end notch

Appendix C: Damping Analysis

The method used for damping analysis is the half-power bandwidth method, in accordance with ASTM Standard Test Method for Measuring Vibration-Damping Properties of Materials (ASTM E756-05). In this method, a peak in the FRF is observed. The frequency at which the peak occurs is denoted ω_n. Next, measure the frequency at which the response is 3 dB down on either side. The lower value is referred to as ω_1 and the higher one is denoted ω_2. Another acceptable method of determining ω_1 and ω_2 is to multiply the peak amplitude by $\frac{1}{\sqrt{2}}$ and find the frequency at which this amplitude occurs.

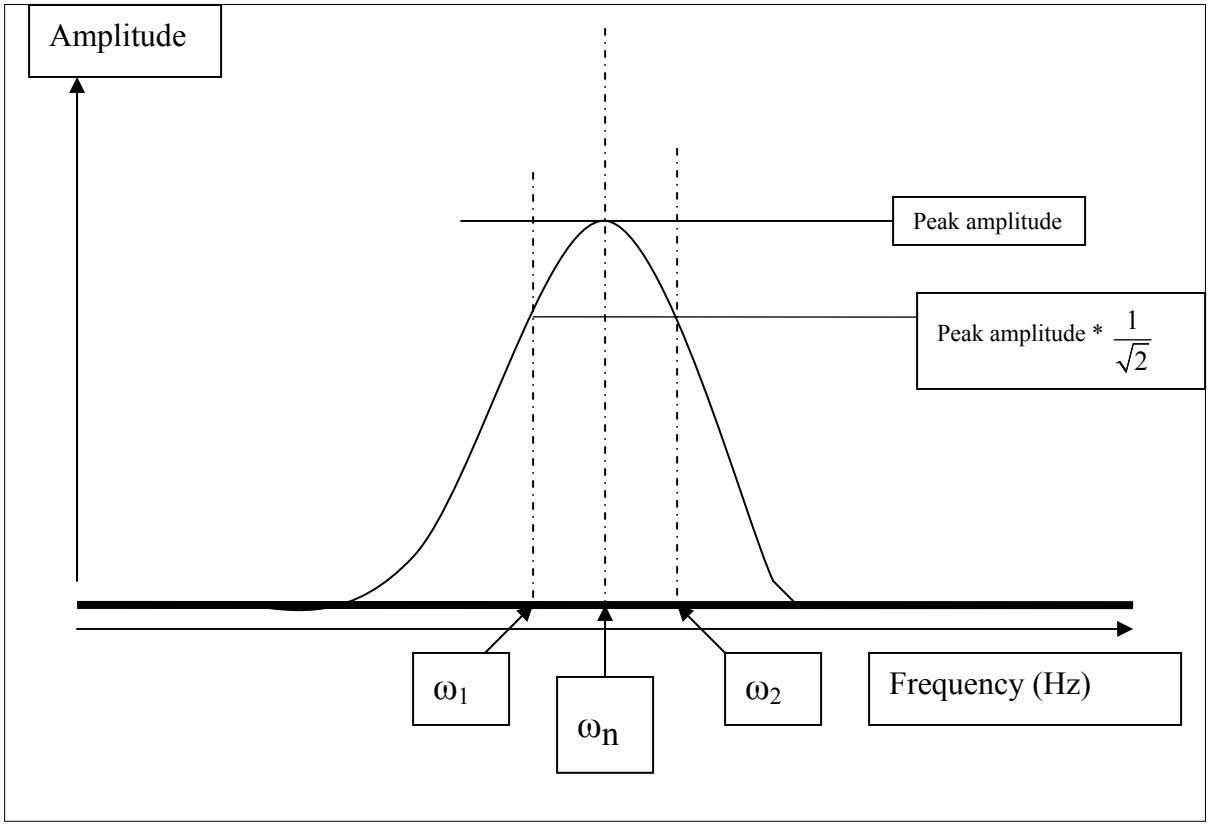

Figure 180. Half-power bandwidth method illustrated.

With this information, the damping ratio, ζ, can be found. Note that this method results in an approximation and is only valid for $\zeta < 0.35$. ζ is approximated as follows:

$$\zeta \approx \frac{\omega_2 - \omega_1}{2 * \omega_n} \tag{42}$$

As the spread of the peak increases, so does ζ, in agreement with the relationship stated above. Therefore, long, sharp peaks indicate low damping, while wider peaks indicate higher damping.

The final piece of information gleaned from this method is the quality factor, Q. Q is the measure of damping used in this study, and is inversely related to ζ.

$$Q = \frac{1}{2\zeta} \tag{43}$$

The original Q values obtained were a bit lower than expected, indicating that the Q of the entire system (table, test stand, clamp and beam) was captured. This data is still valuable, and comparisons can be made with the corroded beam Q values, but a normalization was undertaken to accomplish this. Ideally, the Q value of the beam could be isolated from the rest of the system's Q.

Appendix D: Technical Drawings of Beams

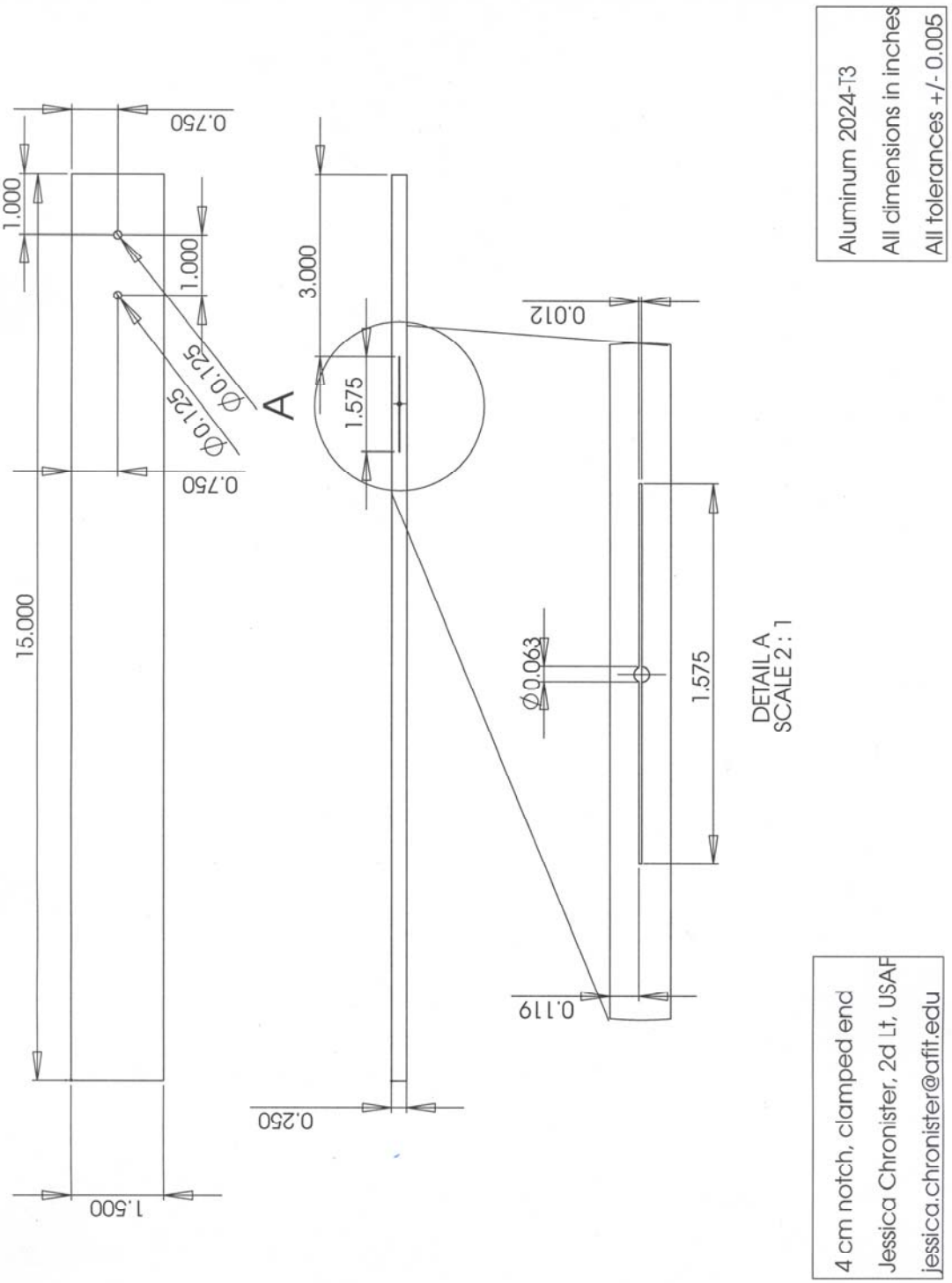

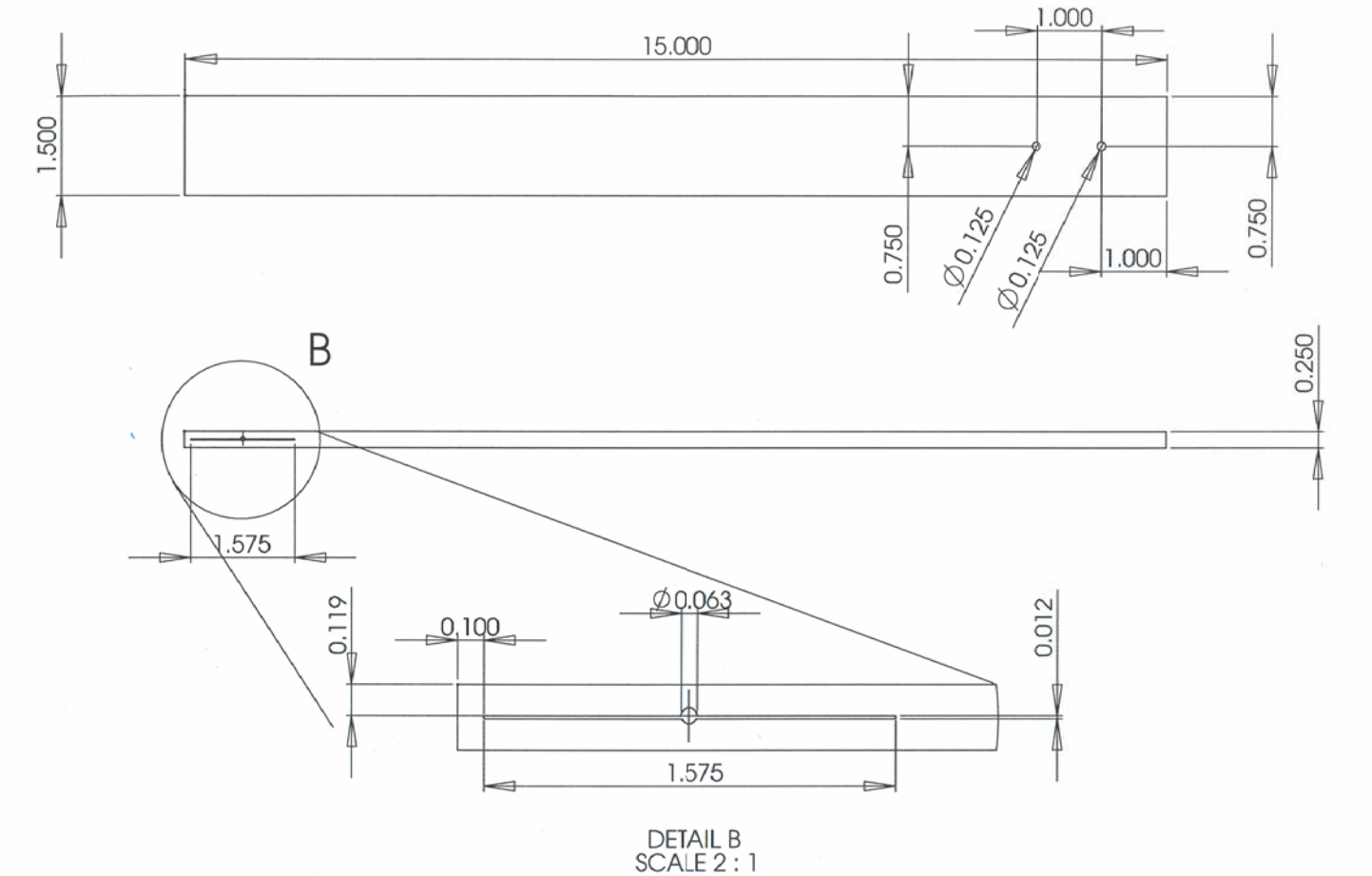

DETAIL B
SCALE 2 : 1

4 cm notch, free end

Jessica Chronister, 2d Lt, USAF
jessica.chronister@afit.edu

Aluminum 2024-T3
All dimensions in inches
All tolerances +/- 0.005

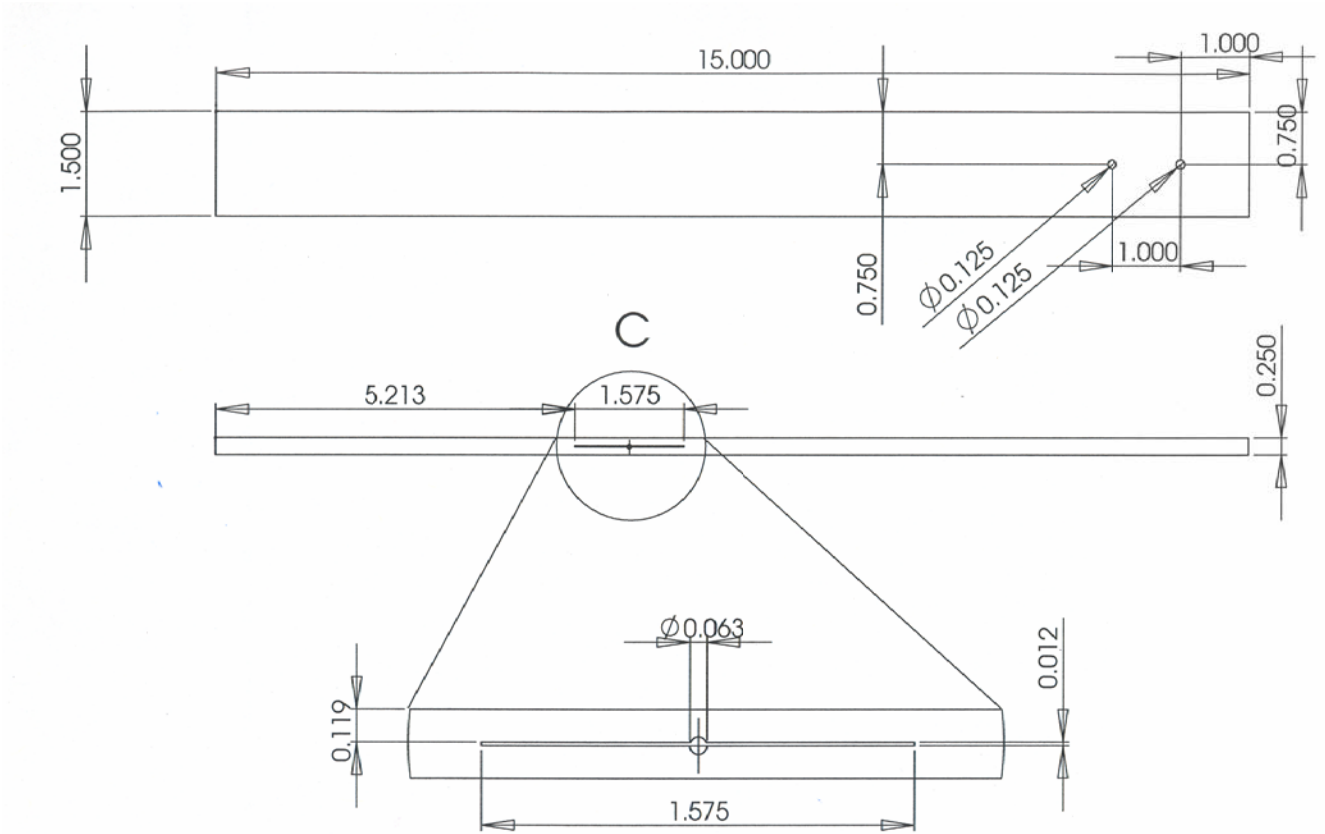

DETAIL C
SCALE 2 : 1

4 cm notch, middle
Jessica Chronister, 2d Lt, USAF
jessica.chronister@afit.edu

Aluminum 2024-T3
All dimensions in inches
All tolerances +/- 0.005

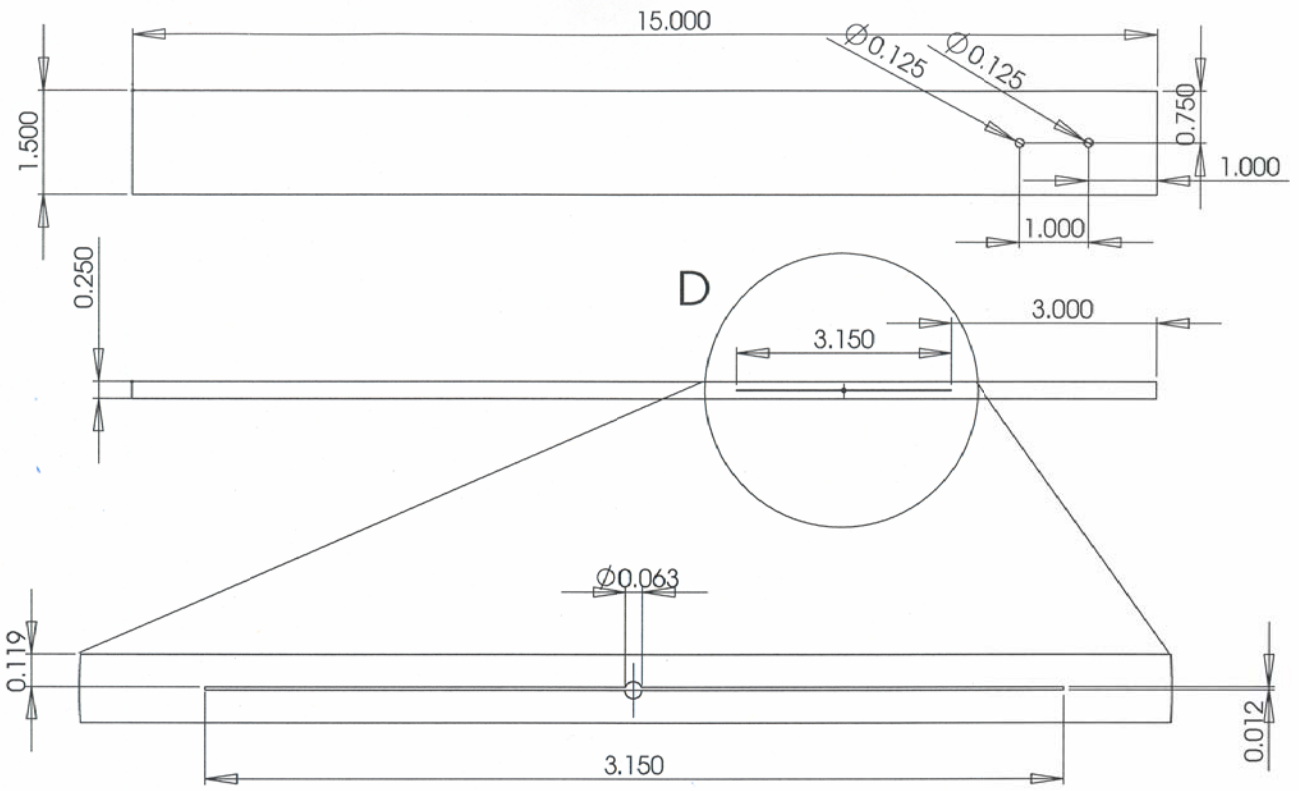

DETAIL D
SCALE 2 : 1

8 cm notch, clamped end
Jessica Chronister, 2d Lt, USAF
jessica.chronister@afit.edu

Aluminum 2024-T3
All dimensions in inches
All tolerances +/- 0.005

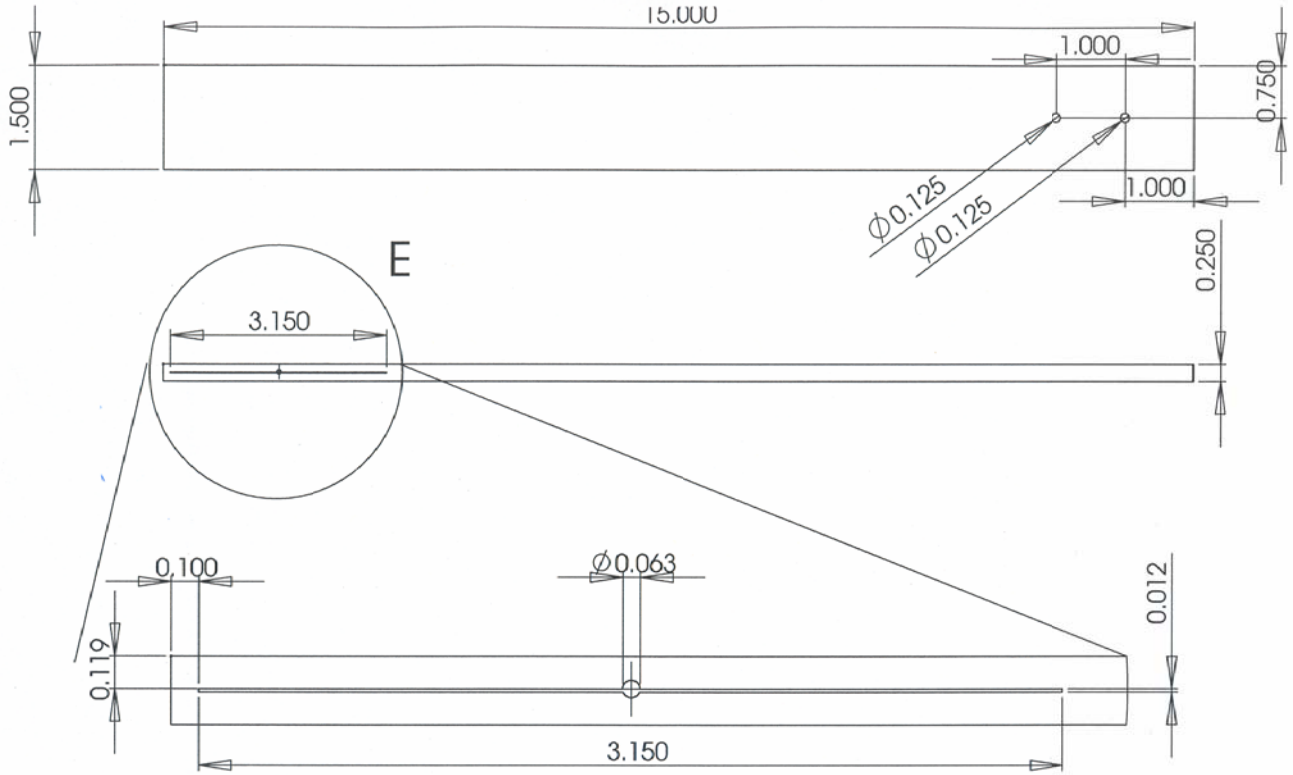

DETAIL E
SCALE 2 : 1

8 cm notch, free end
Jessica Chronister, 2d Lt, USAF
jessica.chronister@afit.edu

Aluminum 2024-T3
All dimensions in inches
All tolerances +/- 0.005

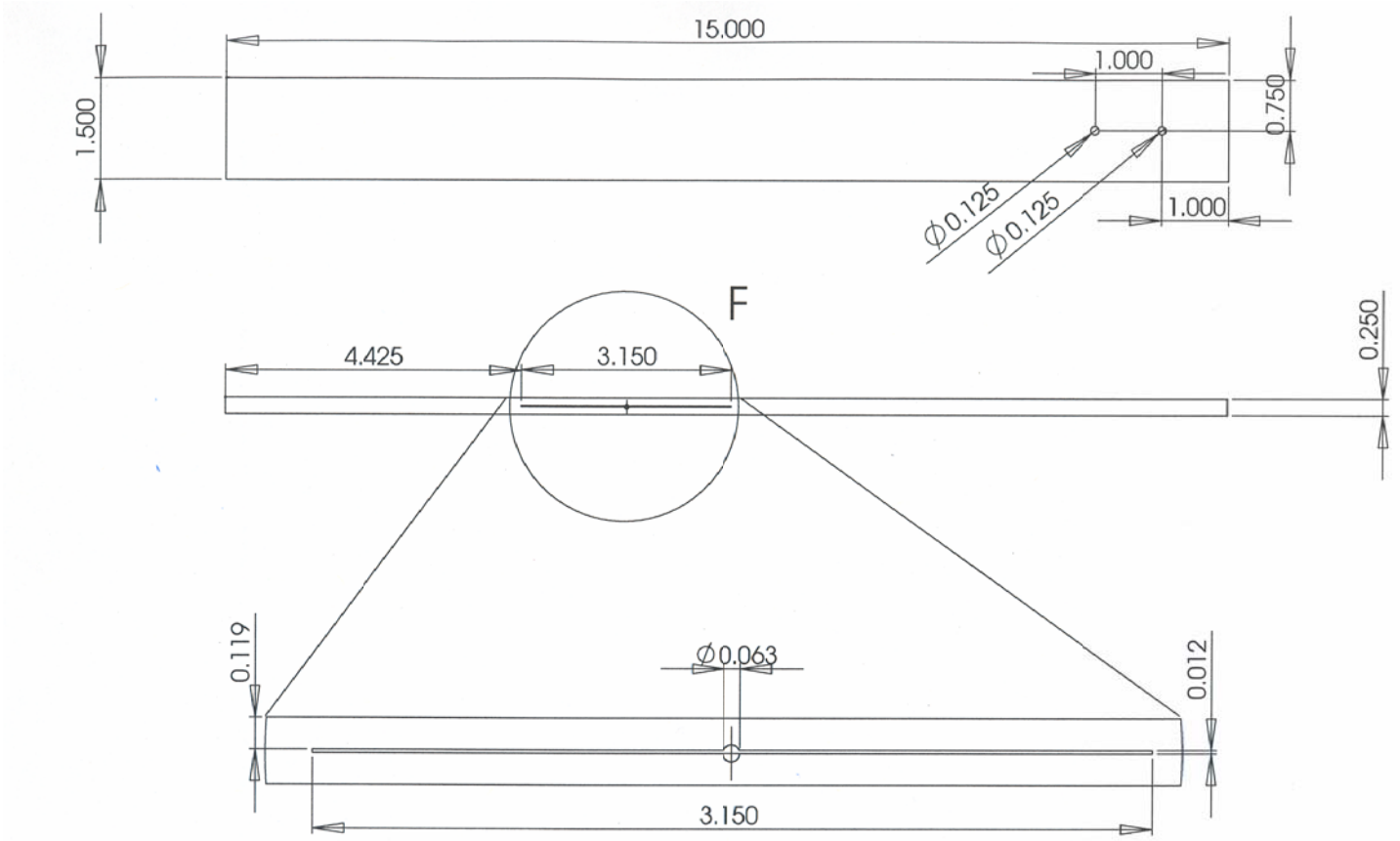

DETAIL F
SCALE 2 : 1

8 cm notch, middle
Jessica Chronister, 2d Lt, USAF
jessica.chronister@afit.edu

Aluminum 2024-T3
All dimensions in inches
All tolerances +/- 0.005

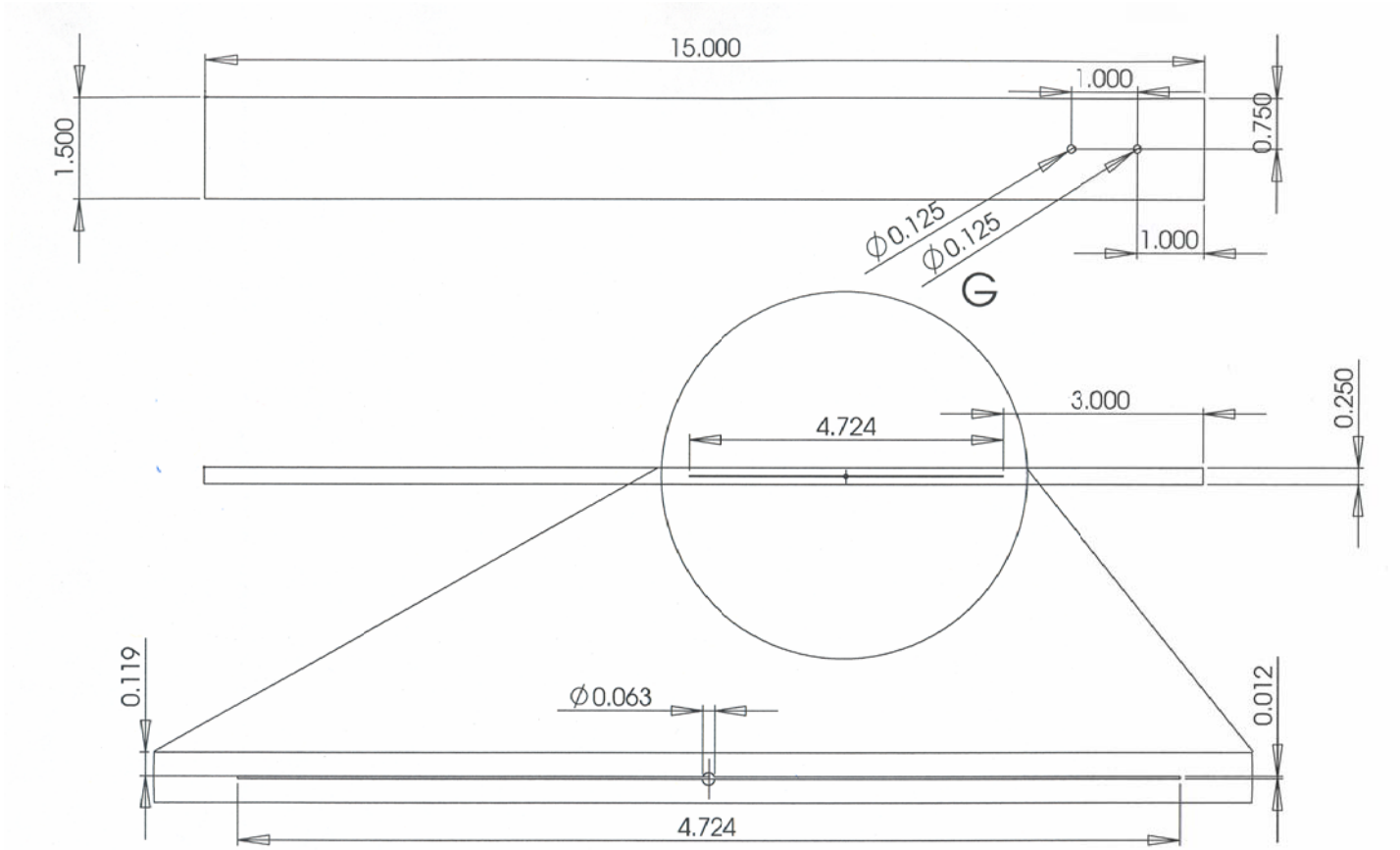

DETAIL G
SCALE 3 : 2

12 cm notch, clamped end

Jessica Chronister, 2d Lt, USAF
jessica.chronister@afit.edu

Aluminum 2024-T3
All dimensions in inches
All tolerances +/- 0.005

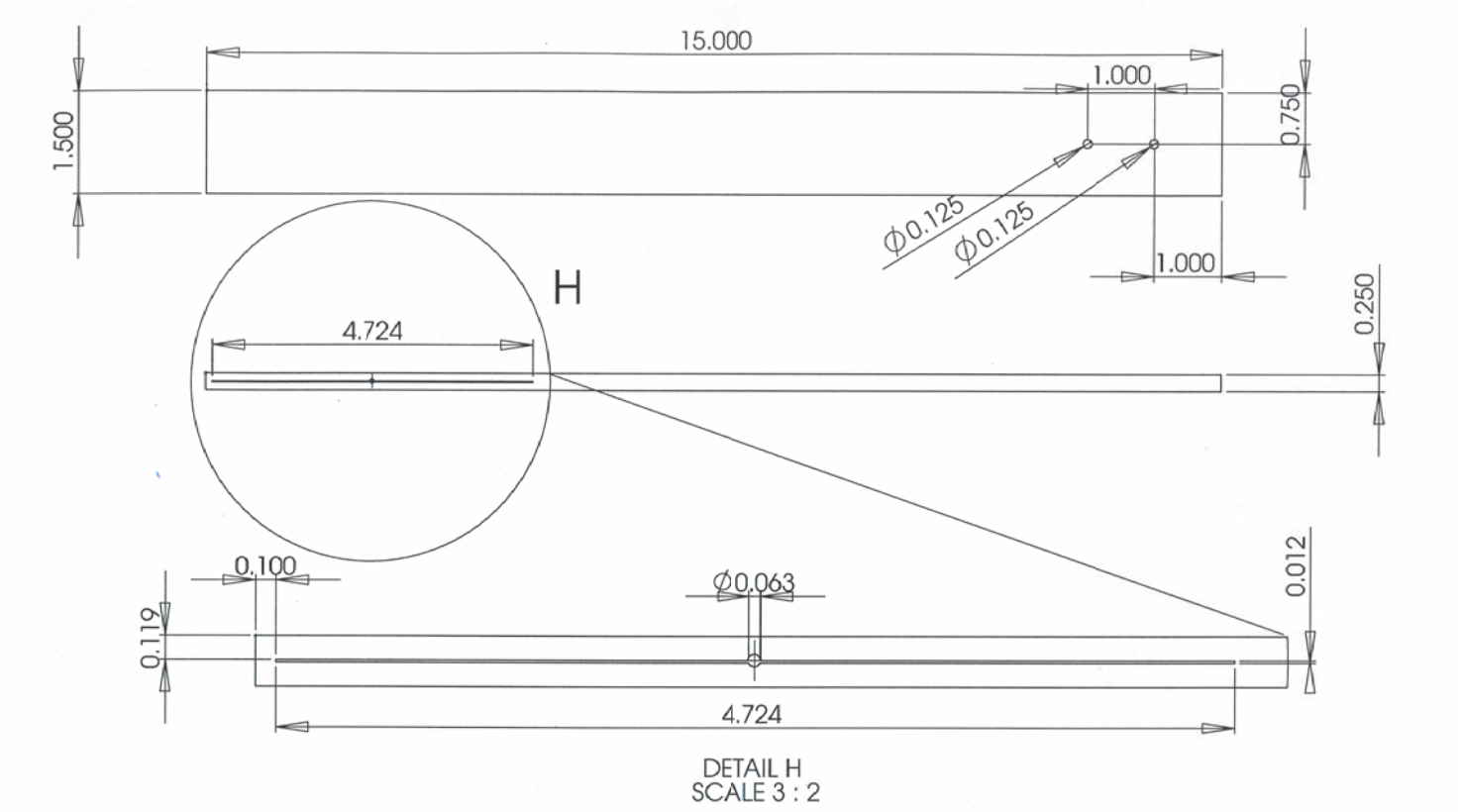

12 cm notch, free end

Jessica Chronister, 2d Lt, USAF
jessica.chronister@afit.edu

Aluminum 2024-T3

All dimensions in inches

All tolerances +/- 0.005

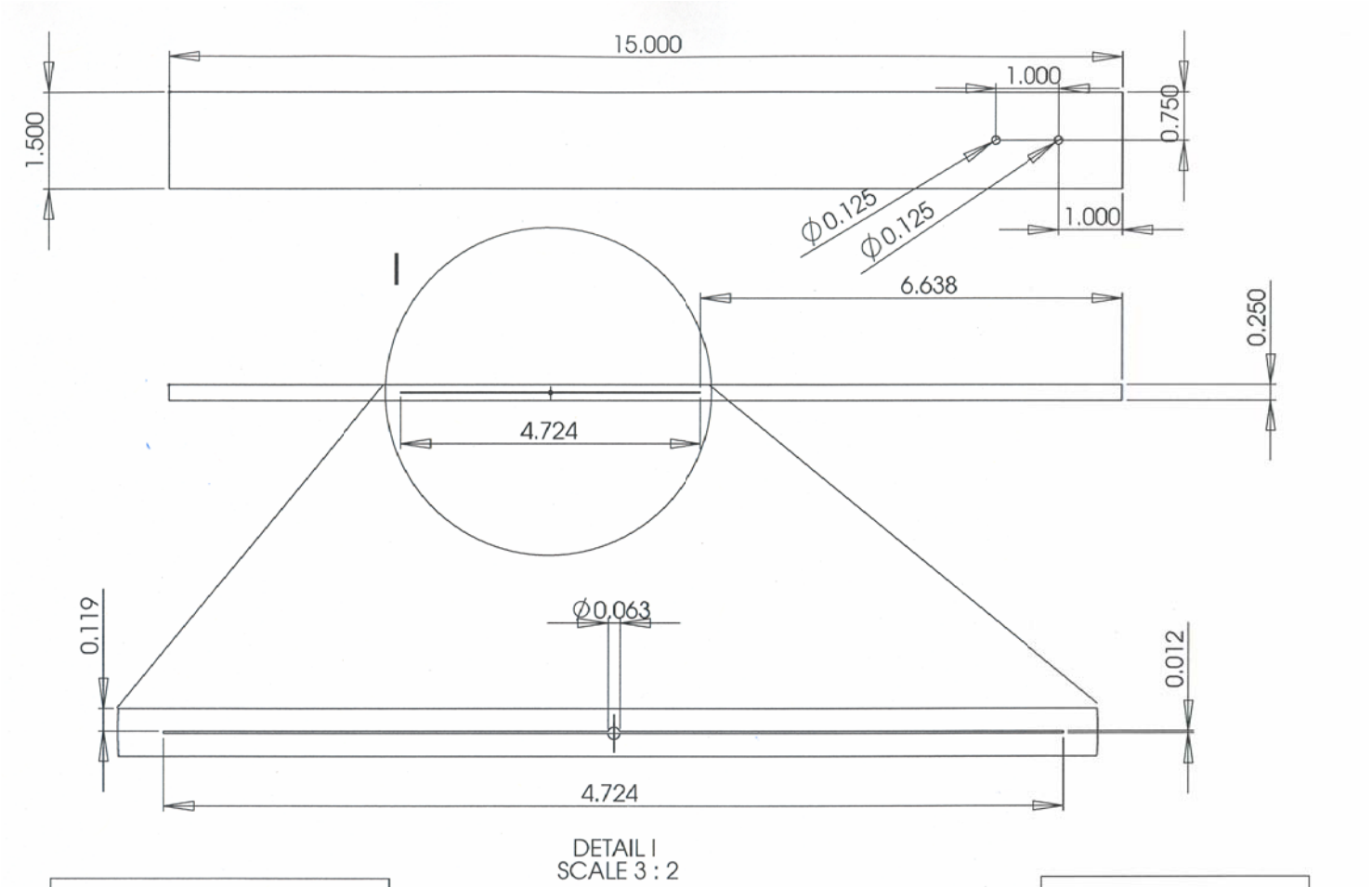

12 cm notch, middle

Jessica Chronister, 2d Lt, USAF

jessica.chronister@afit.edu

Aluminum 2024-T3

All dimensions in inches

All tolerances +/- 0.005

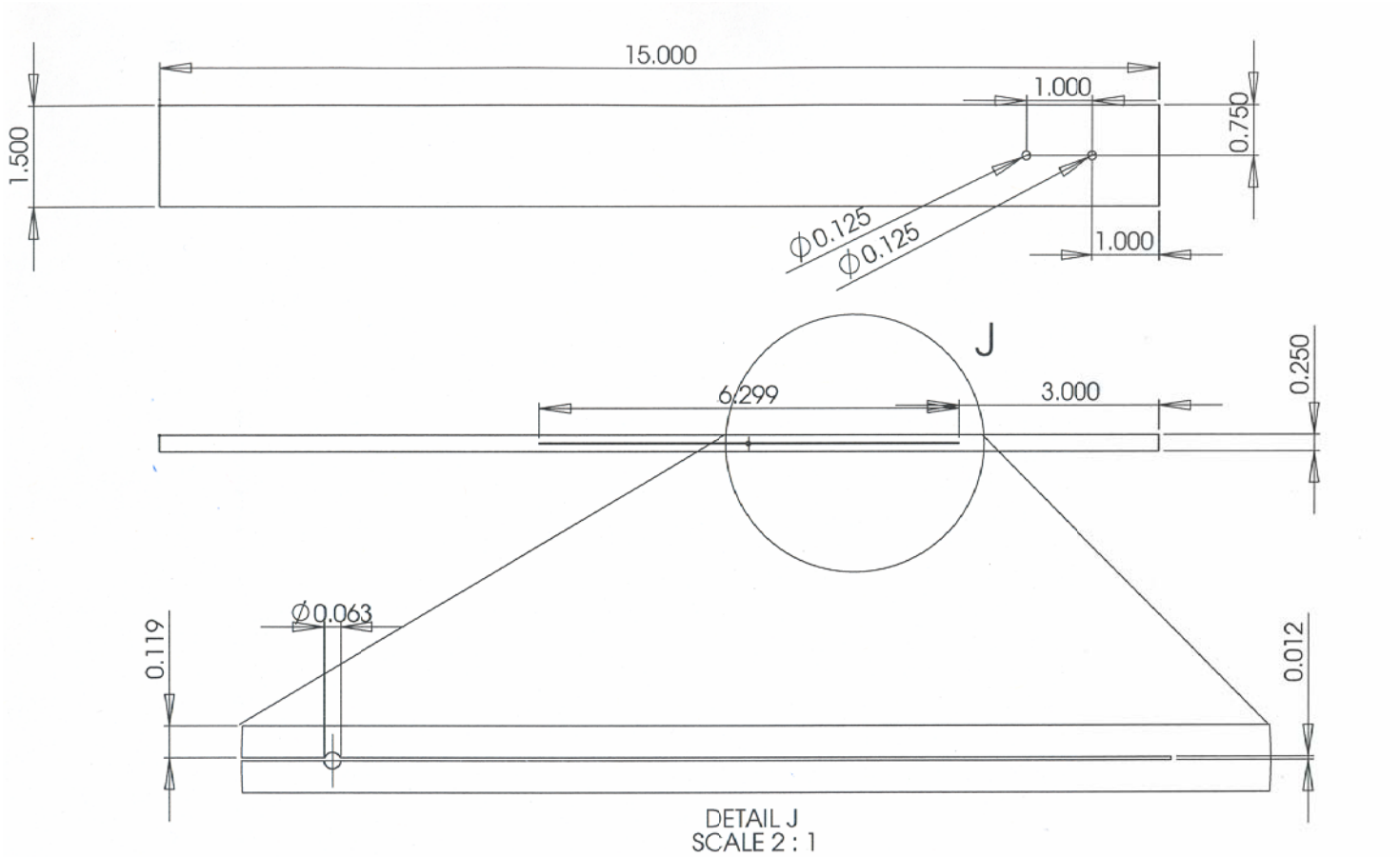

16 cm notch, clamped end

Jessica Chronister, 2d Lt, USAF
jessica.chronister@afit.edu

Aluminum 2024-T3

All dimensions in inches

All tolerances +/- 0.005

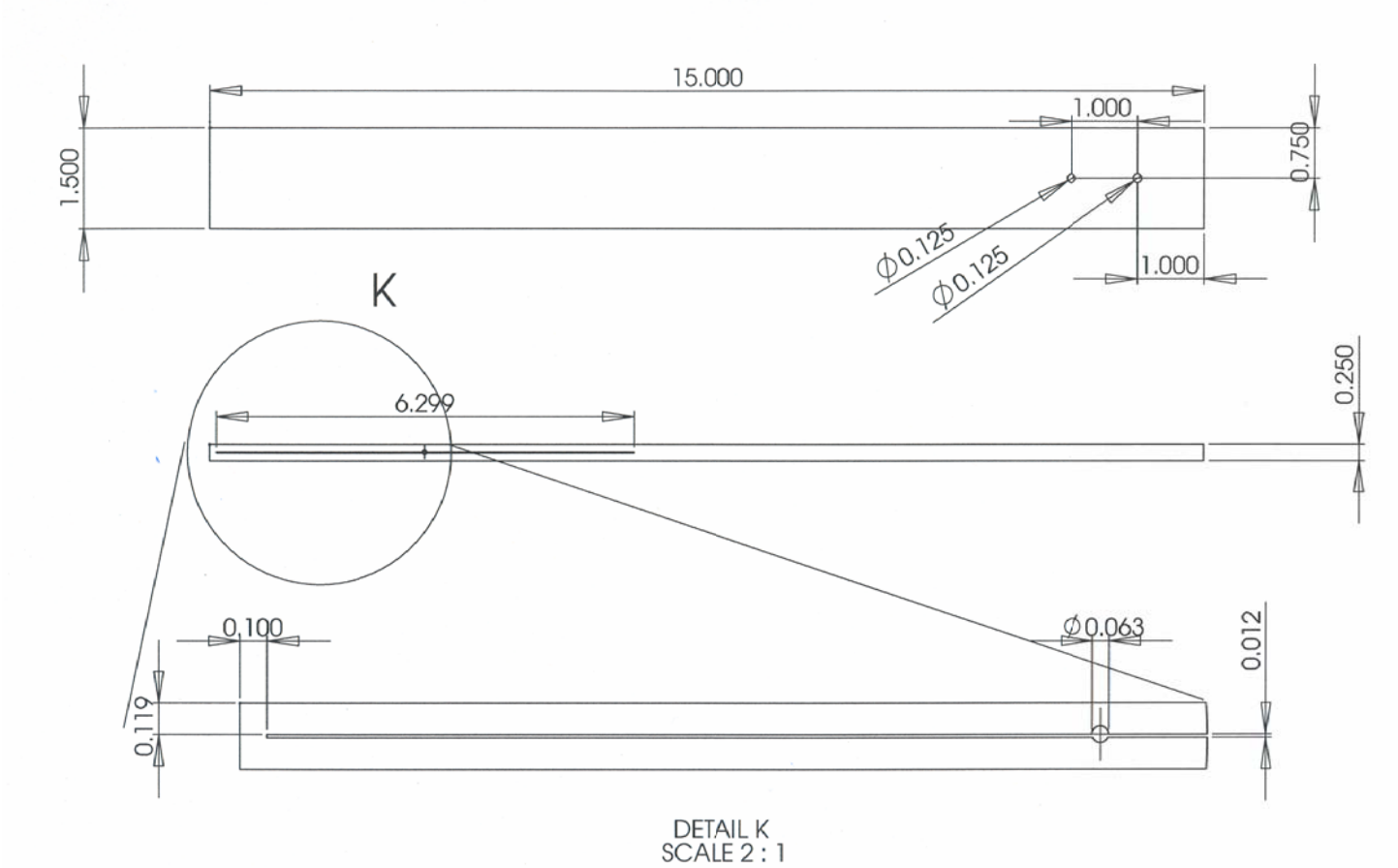

DETAIL K
SCALE 2 : 1

16 cm notch, free end
Jessica Chronister, 2d Lt, USAF
jessica.chronister@afit.edu

Aluminum 2024-T3
All dimensions in inches
All tolerances +/- 0.005

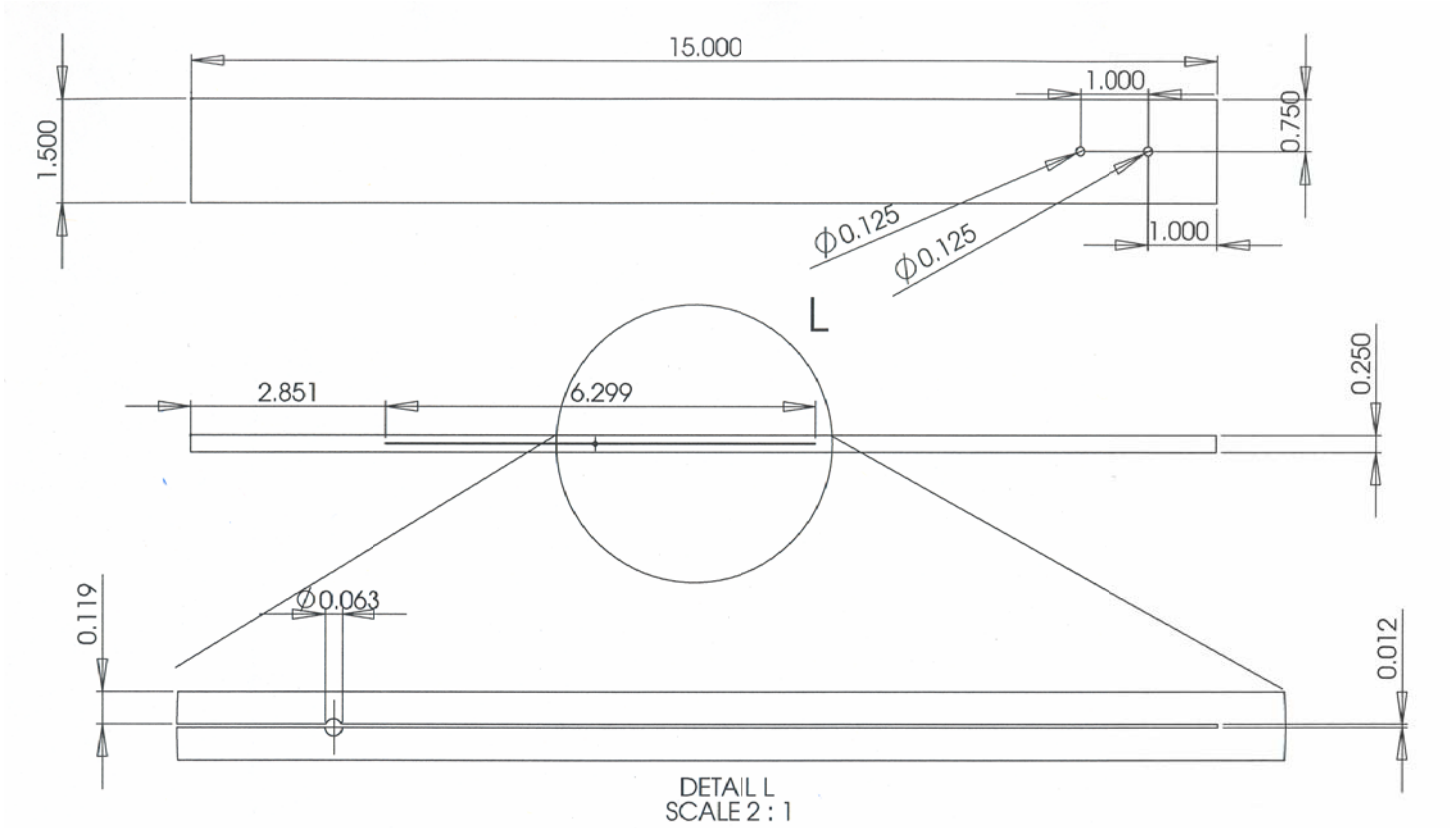

16 cm notch, middle
Jessica Chronister, 2d Lt, USAF
jessica.chronister@afit.edu

Aluminum 2024-T3
All dimensions in inches
All tolerances +/- 0.005

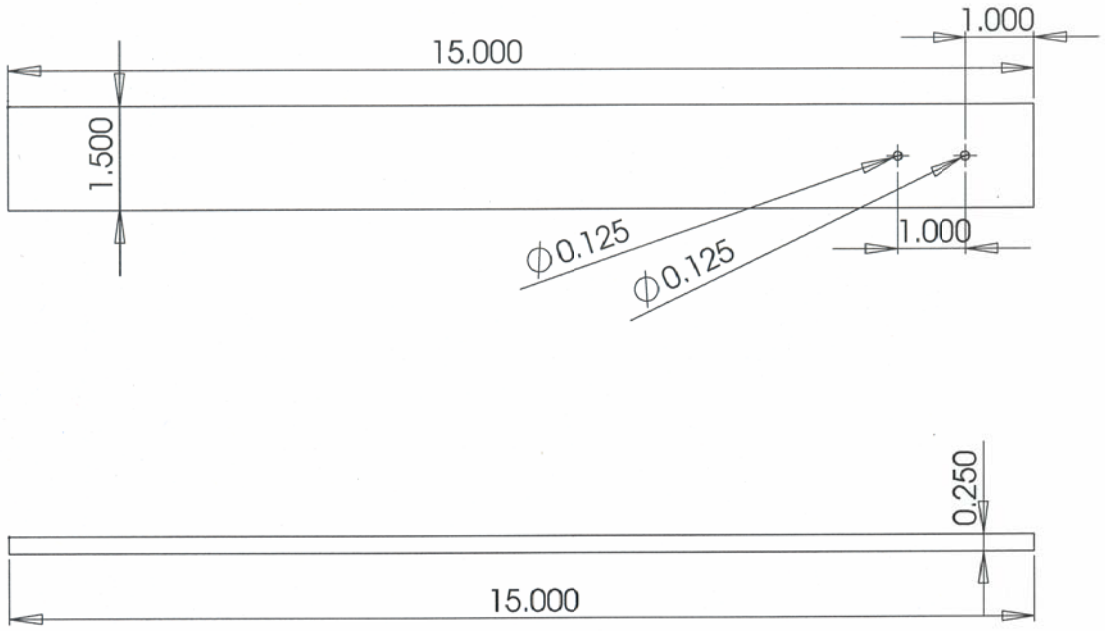

Notchless beam

Jessica Chronister, 2d Lt, USAF

jessica.chronister@afit.edu

Aluminum 2024-T3

All dimensions in inches

All tolerances +/- 0.005

Appendix E: User's Manual for Laser Vibrometer

Hardware

- Beam to be tested (with two holes, centered at 1" and 2" from the clamp end, each 1/8" diameter)
- Clamp with Newport Corporation model 100 magnetic base
- Plate with pins corresponding to holes in beam
- Four ¼" bolts
- Allen wrench (1/4" diameter)
- Polytec PSV-400 Scanning Head (top scan head) – to turn on, rotate the key on scanning vibrometer side of the large box under the computer
- Acoustic horn with amplifier and magnetic base stand
- Bogen amplifier (black box on floor)
- 2 connection cords – one from computer to amplifier, one from amplifier to horn
- Polytec OFV-5000 Vibrometric Controller – this is usually always on, if for some reason it's not, press the black button inside the door of the Junction Box
- Polytec PSV-400-3D Junction Box

Software

- PSV 8.2 program

Setup: Hardware

1. Place pins of the plate through the beam to be tested
2. Attach plate (and beam) to clamp with Allen wrench and bolts, starting with the upper right corner, then lower left corner, then upper left corner, finally the lower right. Use the torque wrench and tighten to 38.5 in-lb.
3. Ensure that legs of the tripod holding the top scanning head are all the same length. Make sure beam is perpendicular to the path of the laser beam (align with holes on table for a general idea of a straight line perpendicular to laser path) and that the laser beam hits roughly the middle of the aluminum beam when it is turned on. Beam should be approximately 5-10 feet from scanning head and at the same level (both 4 feet off the ground)
4. Place horn so the tip is 2-3 mm from the beam, centered on the width, ½" in from the free end (most beams have a dot to indicate this location)
5. The "SIGNAL 1" output from the "GENERATOR OUTPUTS" category on the Junction Box should be connected to the "HIZ INPUTS" inlet on the back of the Bogen amplifier in the upper right corner.
6. The output wires from "COM" and "25V 4-5Ω" on the back upper left of the Bogen amplifier should be connected to the horn input
7. Turn on all 3 lasers by turning the keys in the junction box. The top key is for the top scanning head, the bottom one and the second from the bottom control the left and right scan heads. Open the shutter of the top scanning head (laser should be turned on for 30 min before running an experiment to let it fully warm up)

Setup: Software

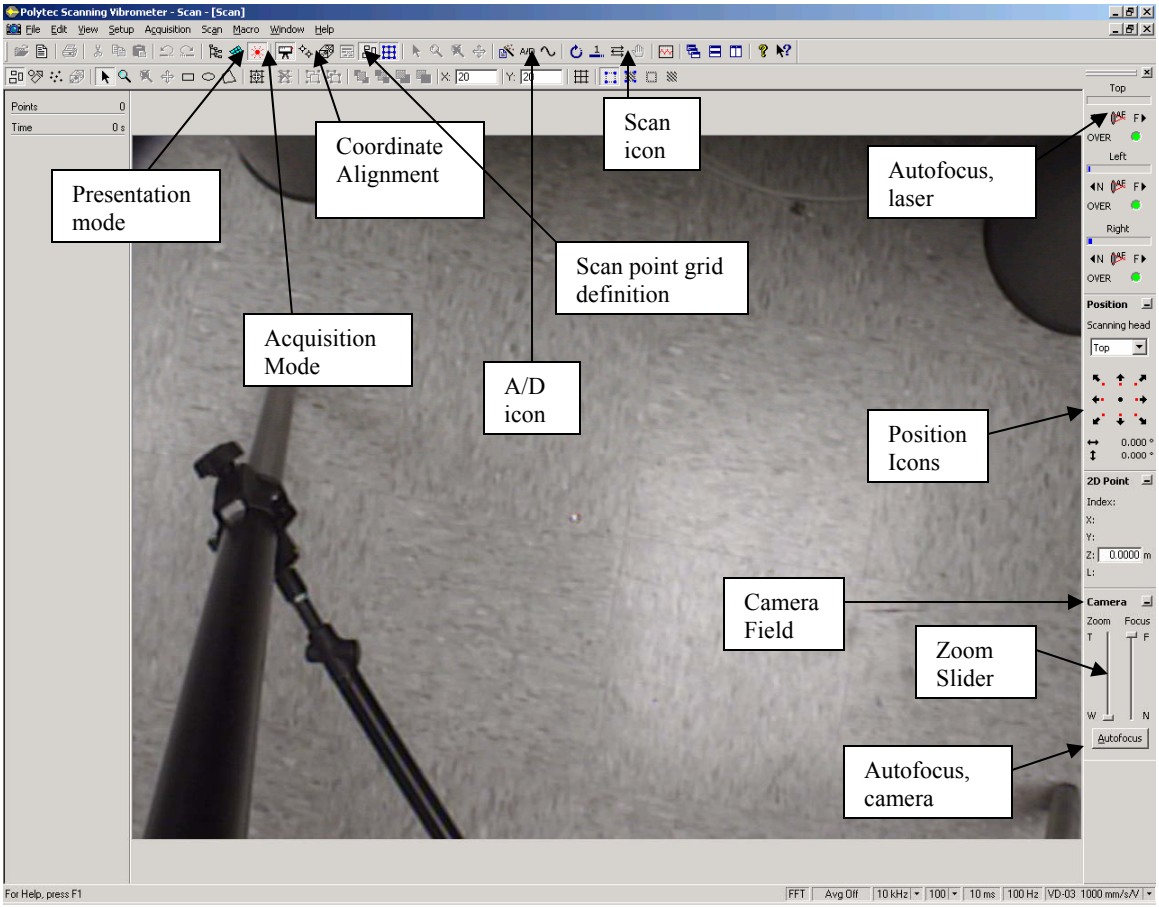

Figure 181. Screen capture of the PSV startup screen. Refer to this figure to locate icons.

1. The software used for data acquisition in this experiment is the PSV 8.2 program.
2. Once it is opened, the user must get into the acquisition mode by clicking the  icon. If the shutter is open and the camera is working, a large video feed of the intended object should appear on the screen.
3. While in acquisition mode, the user can select the device and generator for the experiment. Under the "Setup" menu, "Preferences" and then "Devices" should be chosen. Under the list for "Front End," the Junction Box can be selected. For the experiments in this study, PSV-E-400-3D(10) was used. For "Generator," "Internal" was chosen. Under the list for "Scanning Head," the Top Scanning Head, PSV-I-400-MR, was chosen.
4. Assuming the scanning head is already level and facing the beam perpendicularly, zoom in the camera so the beam is as large as possible in the screen. On the lower right of the screen, there should be a "Zoom" slider in the "Camera" field. After the camera has been zoomed, focus the image by pointing the laser in the upper left of the video screen by using the mouse, remote control, or "Position" icons,

then click “Autofocus” in the “Camera” field. After the camera is focused, point beam at the 0.0 location and focus the laser beam using the “Autofocus” icon (). Use the “Position” arrow icons to center the beam on the 0.0 location if needed.

5. The next step is the coordinate alignment. To do this, click the  icon. First, delete any existing points by right clicking on the point(s) to be deleted and choosing “delete” or “delete all.” To set alignment points, use the arrows to move the laser to the desired location and click the mouse once to set the point. To get a sufficient number of points, 4 points across the length by 3 points across the width were chosen, yielding a total of 12 evenly spaced points. After the alignment, click the  icon once more.
6. The next software setup step was to define a grid of scan points from which vibrational data would be collected. To define these, the  icon on the top row was selected and the same icon in the graphics toolbar was selected. A global grid then appears.
7. To replicate the tests used in the present study, a grid of X:24 and Y:17 should be chosen.
8. Ensure that the  icon is deselected, then click the  icon on the lower row and draw a large box over the beam image, completely covering it. The box should have a red edge with white quadrangles inside, and the prospective scan points should be blue. To end scan point definition, click the  icon on the upper row.
9. The remainder of the software preparation appears under the A/D tab in the middle of the upper row of icons. The first tab, General settings, presents measurement modes, averaging preferences and the re-measuring option. For the experiment presented, Fast Fourier Transfer (FFT) was the chosen measurement mode, complex averaging was chosen to average 11 measurements of each scan point, and the “Remeasure” box was checked in order to re-measure any potentially invalid or overrange scan points.
10. The second tab, entitled “Channels,” allows the user to select active channels. For this tab, Vibrometer Top and Reference 1 were selected as “Active,” while only Reference 1 was chosen as “Ref.” “Index” was left blank, “Direction” was chosen to be +Z for all, “Range” was 3.162 V for all, “Coupling” was DC for all and “ICP” remained unchecked. The quantity measured was velocity for all vibrometers, “Factor” was 0.002 for all three vibrometers and reference 1 while “Unit” was m/s/V for all.
11. The third tab, “Filters,” was “No Filter” for all data used in this study. Of course, a filter may be used if needed in future research. “Int/Diff Quantity” under this tab was Velocity (0) for all.
12. The fourth main tab, “Frequency,” will have differing contents for each case. For each test, the MATLAB code was used to predict the natural frequency mode of

the eighth bending mode. Using this frequency as the maximum frequency, a bandwidth of 8-10 kHz is chosen. For the number of FFT lines used, the maximum of 6400 was always used, and a 50% overlap was used. Overlapping is a method used to acquire data more quickly, particularly when the data acquisition time would be very long. In the case of a 50% overlap, a full data record would be taken over one period, then the next record (and each subsequent record) would reuse the last half of the previous record as its own, and only record the second half of the period's worth of data.

13. For the fifth main tab under the A/D settings, "Window," the "Function" should be Rectangle for all as no windowing was used. Windowing is sometimes necessary to minimize the effects of leakage, which is a source of error due to discontinuities across the beginning and end regions of a finite data record. A windowing function, when multiplied with a time signal, forces the resulting signal to zero at the beginning and end of the time period. No windowing was needed for this experiment. "Parameter" should be left blank under the "Window" tab.
14. The sixth tab, "Trigger" should be selected as "Off."
15. Under the seventh tab, "SE," Vibrometer Top and Reference 1 only should be checked. No speckle tracking was used, and the Standard mode was chosen.
16. The eighth tab is the "Vibrometer" information. Velocity was the measurement taken, with settings of VD-07 and a measurement range of 10 mm/s/V. The tracking filter and high pass filter were turned off with a low pass filter of 1.5 MHz and a maximum frequency set at 100 kHz, allowing all conceivable data to be recorded.
17. The generator chosen (ninth tab) was an active signal, a burst chirp, with a zero second wait and amplitudes ranging from 1 to 2.1 and an offset of 0 V. No amplitude correction file is needed.
18. Now it is time to run the scan. Click the  icon and name the scan as you would like it to be saved. After clicking save, the scan will proceed. In the upper left corner of the screen, you can track approximately how much longer the scan will last.

Analysis of Data

1. Go into presentation mode by clicking the  icon. Go to File, Open to open the desired scan.
2. To define frequency bands, click on the  icon and choose "Average Spectrum." Define bands by clicking the  icon and highlighting bands in the analyzer using the mouse. The software will determine the peaks. Close the frequency band analyzer by clicking  again (always save new frequency band definition after you have defined them).
3. If you would like to see the animation of the eigenvectors, click on the  button to "play" the animation. The window to the left tells which frequency band is being represented in the animation. You can rotate the view by clicking the  icon and "grabbing" the image with the mouse. If you flip the picture so you are seeing the top view, this will show you the eigenvector.

Appendix F: Corrosion Experiment Procedure

Specimen Preparation

1) Place identifying marks on the beams.[1] Use colored electrical tape. Mask off the three-inch end with holes with electrical tape.[2] This will prevent or hinder corrosion in the area that will be clamped.
2) Abrade with abrasive paper. The edges as well as the faces should be abraded to remove burrs.[1] Use No. 120 abrasive paper or cloth, or the equivalent.[3] No. 220 abrasive paper was used in this experiment because it was available in the laboratory.
3) Degrease with an organic solvent[1] or hot alkaline cleaner. Acetone was used for this experiment.
4) Rinse thoroughly, hot air dry, and store in a desiccator[1]. One desiccator is available in the lab, but it was in use for another project. If the use of a desiccator is not possible, simply clean and prepare the beams immediately before immersion.
5) Measure the specimen using calipers and weigh to as many significant figures as possible.[1]
6) Record surface area, accounting for mounting holes and notches. Also record all dimensions for all beams.
7) May want to take preliminary pictures with a digital camera.
8) Note and record any cosmetic differences (i.e. color changes, scratches, and surface roughness).[2]

Corrosion Bath

1) During the bath, periodically record temperature, salinity, and pH.[4]
2) Take pre-exposure photographs of assembled test rack
3) Make sure unmasked portion of beam is submerged, as well as the heater.
4) Hang the beams from the hooks using the nylon rope (rope may stretch, so make sure there is at least an inch between the bottom of the tank and the bottom of the beam).

Specimen Cleaning After Testing

1) First, clean by scrubbing and/or brushing the outside of the beam with a non-metallic bristle brush and a mild, abrasive-distilled water slurry.[1] Test with laser vibrometer.
2) After the laser vibrometer test, re-clean chemically to remove corrosion products for inside the notch. Submerge in room-temperature Nitric acid for 1 to 5 minutes to remove corrosion products from inside of the notch.[1] Re-test with laser vibrometer. The notch was not cleaned in the present experiment.

---

[1] ASTM International, Designation G1-03, Standard Practice for Preparing, Cleaning, and Evaluating Corrosion Test Specimens
[2] ASTM International, Designation G 112-92 (Reapproved 2003), Standard Guide for conduction Exfoliation Corrosion Tests in Aluminum Alloys
[3] ASTM International, Designation G 31-72 (Reapproved 2004), Standard Practice for Laboratory Immersion Corrosion Testing of Metals
[4] ASTM International, Designation G 52-00,
Standard Practice for Exposing and Evaluating Metals and Alloys in Surface Seawater

3) “Panels from immersion tests should be photographed as quickly as possible, since they will continue to corrode and change in appearance even though they have been removed from the test.” [2]
4) Cleaned exhibit specimens can be wrapped with a commercial plastic “cling-wrap” to help prevent corroded metal from being dislodged.[2]

Assessment of Corrosion Damage
1) Take pictures with a digital camera before and after the corrosion bath, as well as before and after cleaning. May want to try to zoom in on notch before and after notch cleaning. Try to use classification rankings from Test Method G34.[2] May want to photograph from an angle with side lighting, rather than straight down if it shows the corrosion better.
2) Calculate mass loss→weigh before bath, after bath but before cleaning, after first cleaning, then after second cleaning (total of four mass measurements). From this, one can determine corrosion rate.
3) Laser vibrometer should be used the same way as before to measure the frequency response. Evaluate any shift in natural frequencies and any damping changes.

Order of Testing
1) Test for a 24-hour period
2) Test for a 48-hour period[4]
3) Test for a 120-hour period
4) Test for a 7-day period (168 hr)[4]
5) Test for a 14-day period (336 hrs)—will use same beams as for uncorroded data
6) For each test, I will test 2 specimens at a time: one with a notch, one without. I will test each with the laser vibrometer immediately upon removal, without cleaning. After testing, I will clean mechanically (just the outside) and test again with the laser, then clean chemically (to remove deposits in the notch) and test a third time. Chemical cleaning will only be necessary for the notched beams.

Other Notes
Equipment list to clear through the lab:
~Organic solvent
~Abrasive paper
~Desiccator
~Calipers
~Mild, abrasive-distilled water slurry
~Non-metal bristle brush
~Nitric acid
~pH paper
~thermometer
~towels for drying
~rubber or latex gloves
~plastic pan or small tub for submerging the beams in Nitric acid

To determine mass loss due to cleaning, clean a replicate uncorroded control specimen by the same procedure. By weighing the control specimen before and after cleaning, the extent of metal loss resulting from cleaning can be recorded and used to correct the corrosion mass loss.[1]

It is advisable to start short term tests (24 hr and 48 hr) early in the day so specimens can be given an initial assessment before the end of the work day.

Additional Required Items:
~Hairdryer
~Plastic cling-wrap
~Digital camera

Appendix G: Photographs of Corroded Beams

24 Hour Corrosion

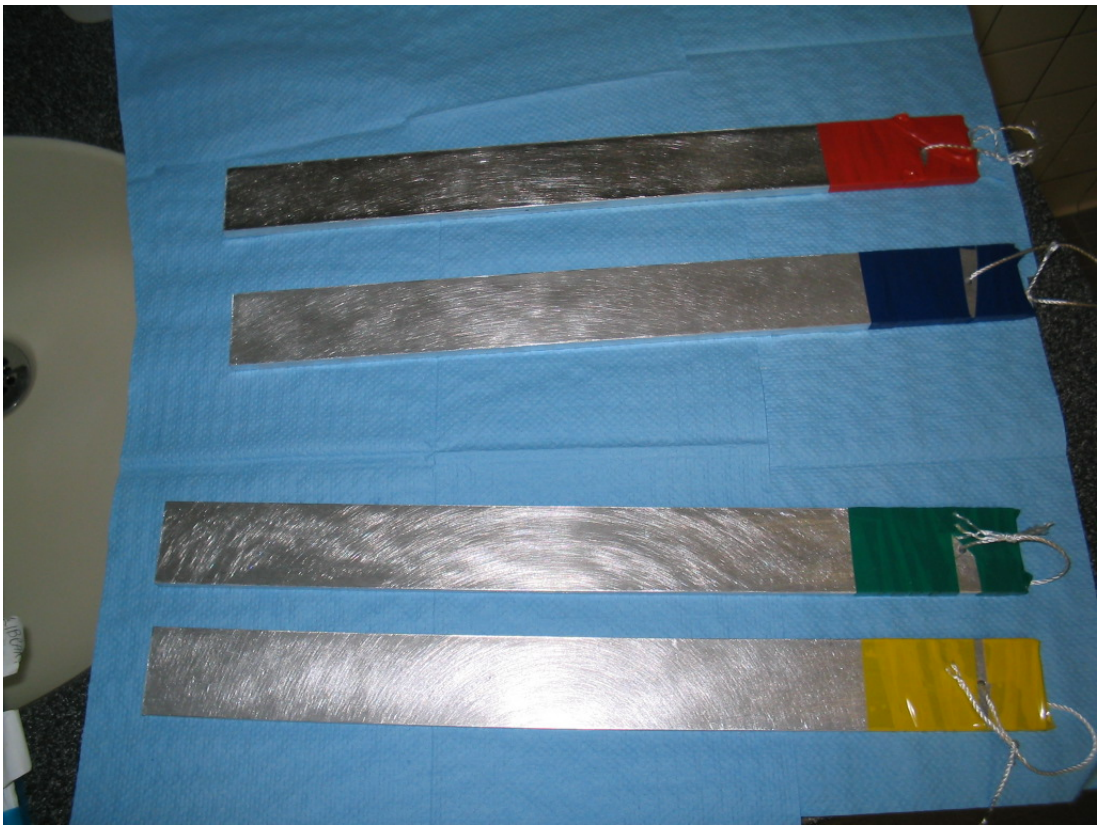

Figure 182. 24 hour and 48 hour beams before immersion. Yellow (notchless) and green (middle notched) beams will be corroded for 24 hours, blue (notchless) and red (middle notched) beams will be corroded for 48 hours.

Figure 183. Yellow notchless and green notched beam in the tank. Visible salt deposits in under 24 hours.

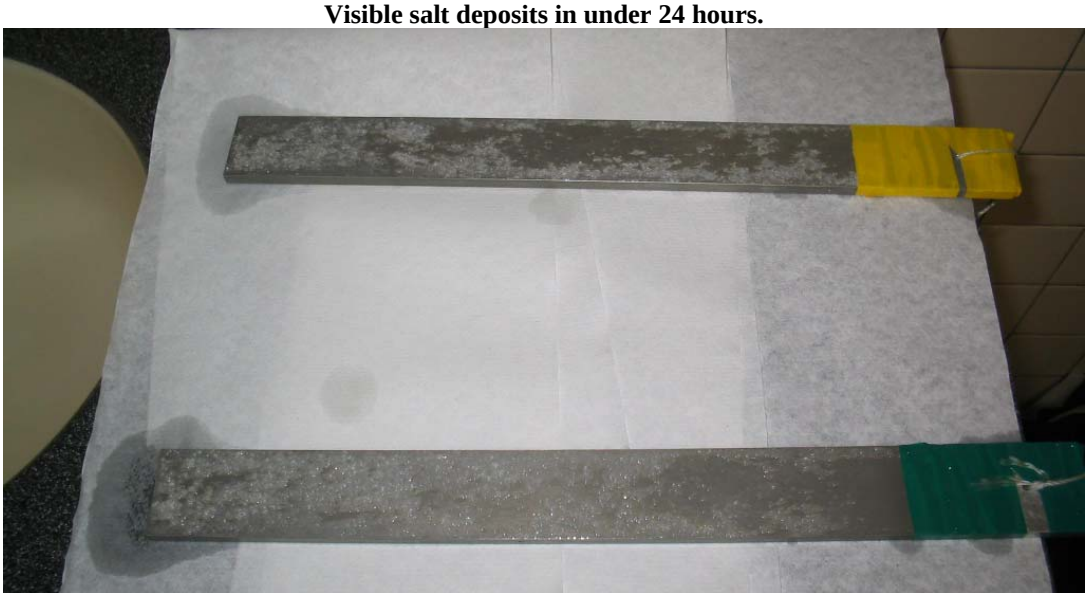

Figure 184. Fronts of green and yellow beams after corrosion. White markings are salt deposits.

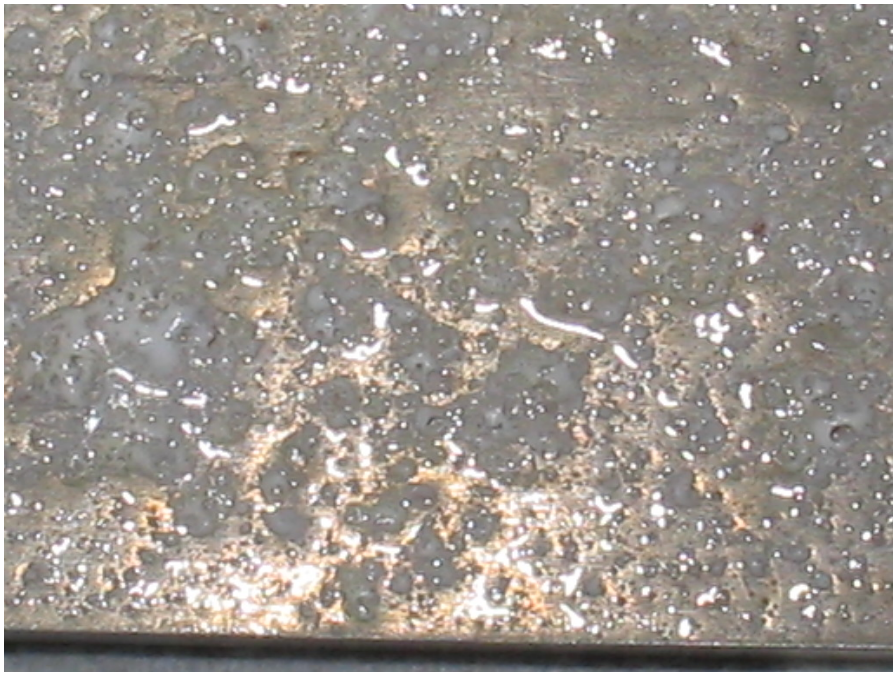

Figure 185. Close up of salt deposits

Figure 186. Front of yellow beam before cleaning

Figure 187. Back of green notched beam-no salt deposits present

Figure 188. Back of yellow notchless beam-not salt deposits evident

Figure 189. Zoom in on back of yellow cleaned beam. Overall corrosion and some apparent pitting despite the lack of salt deposits.

48 Hour Corrosion

Figure 190. Blue notchless and red middle notched beam before 48 hour corrosion

Figure 191. Blue notchless and red middle notched beam after 48 hour corrosion (before cleaning)

Figure 192. Salt deposits present on non-immersed portion of exposed beam

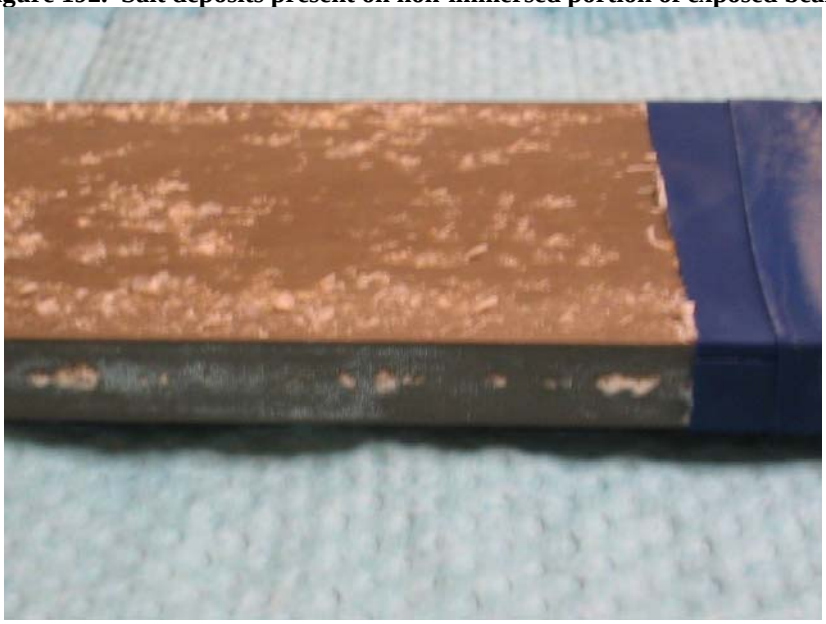

Figure 193. Salt deposits on blue notchless beam

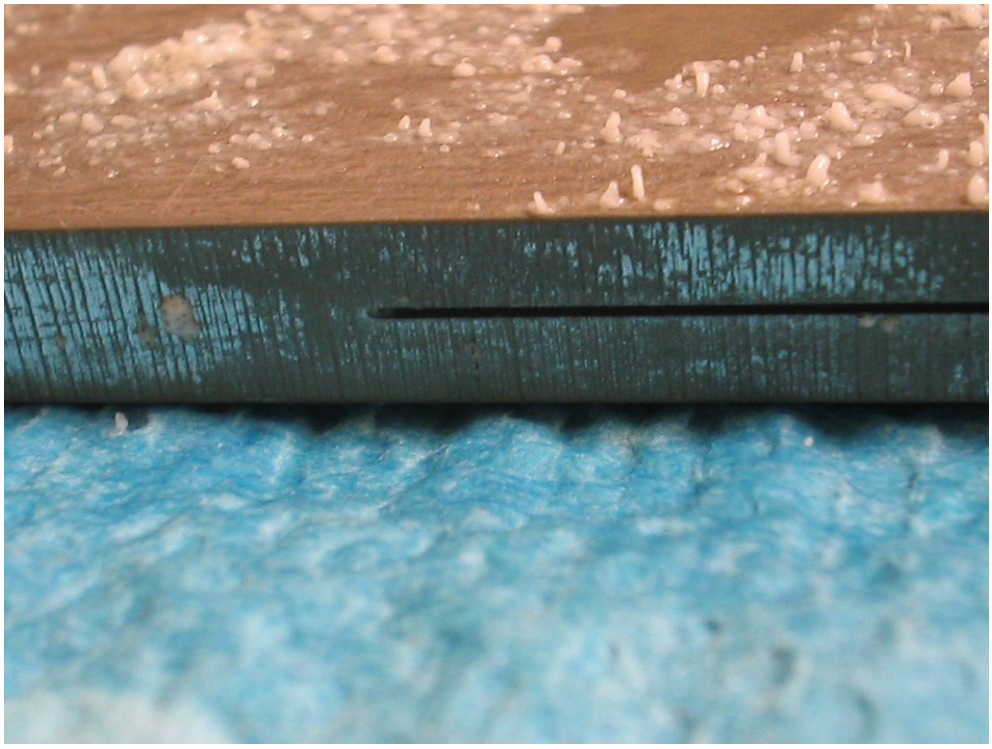

Figure 194. Salt deposits, discoloration of red notched beam

Figure 195. Back of corroded and cleaned red notched beam

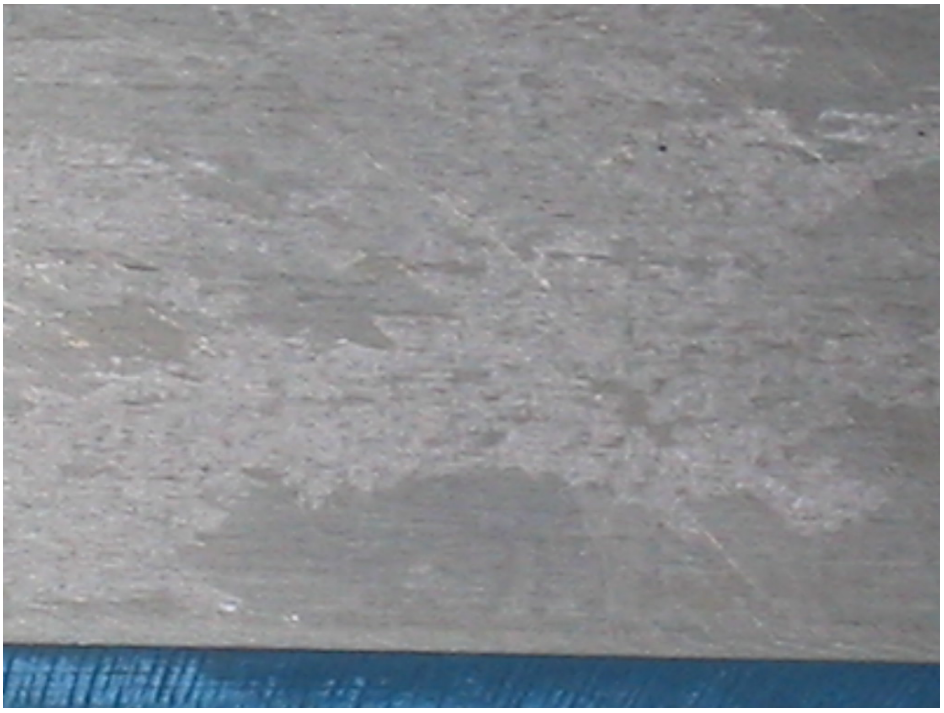

Figure 196. Close up of back of corroded and cleaned red notched beam

120 Hour Corrosion

Figure 197. Red notchless beam on top, white/red notched on bottom. Front surfaces before corrosion

Figure 198. White/red middle notched beam after corrosion and cleaning. Lighter gray areas represent where salt deposits were present, while darker gray areas indicate a larger extent of general corrosion, due to the absence of salt deposits.

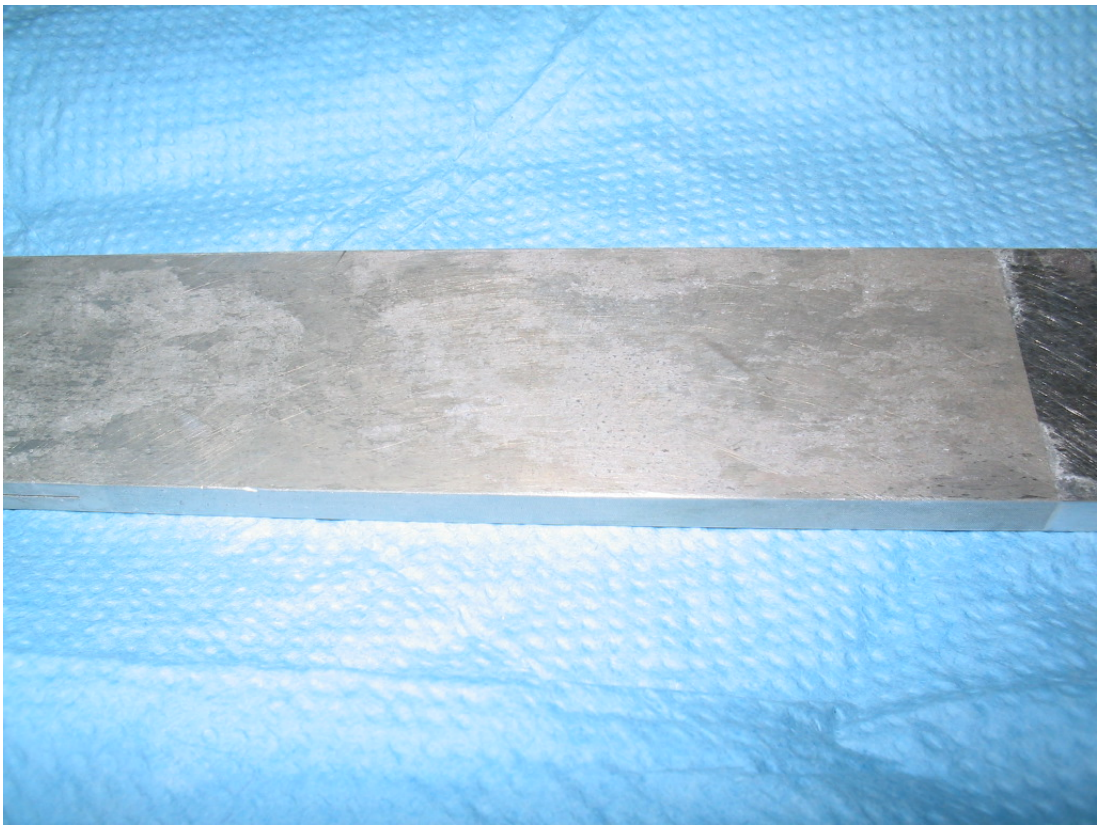

Figure 199. Back of white/red notched beam. Note the presence of pits contained in the lighter areas. Pitting appears to only occur under a region that has previously been covered with salt deposits.

One Week Corrosion

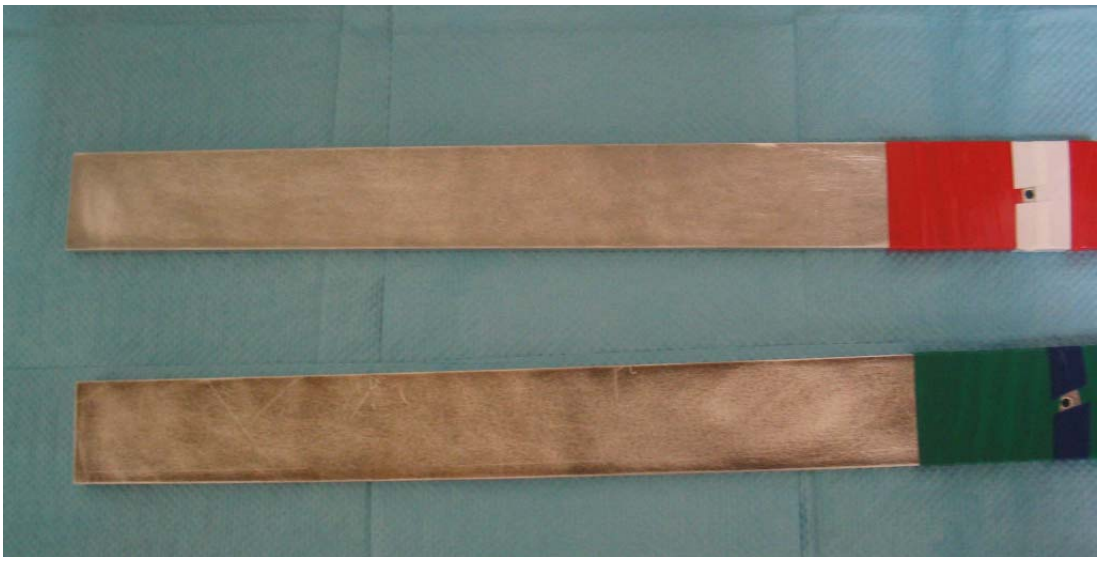

Figure 200. Front of white/red notchless and blue/green middle notched beams before corrosion.

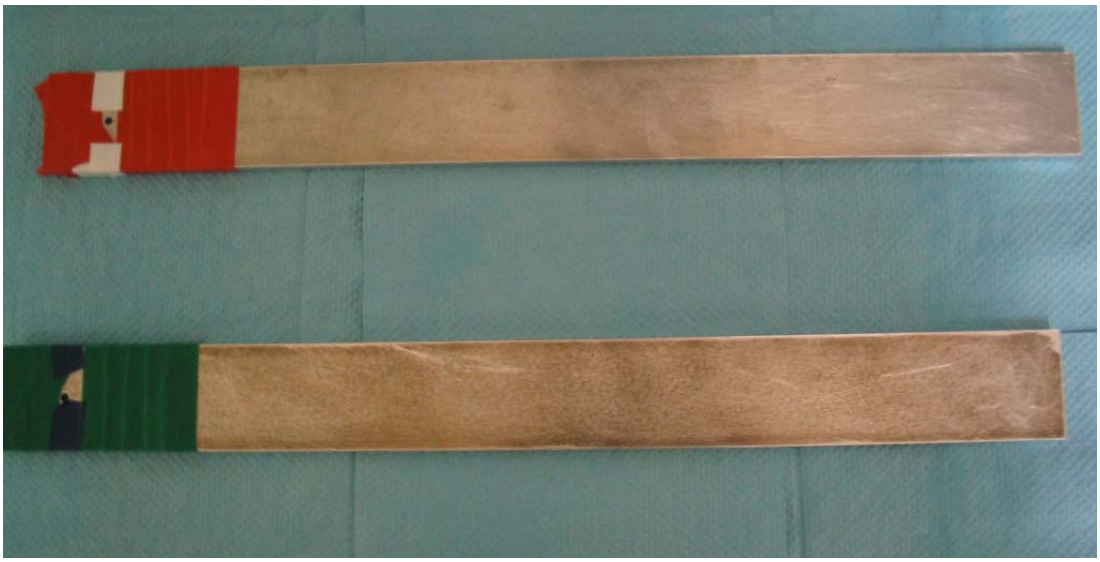

Figure 201. Back of white/red notchless and blue/green middle notched beams before corrosion.

Figure 202. Beams in the tank, salt deposits evident on this side

Figure 203. Very few salt deposits present on this side of both beams

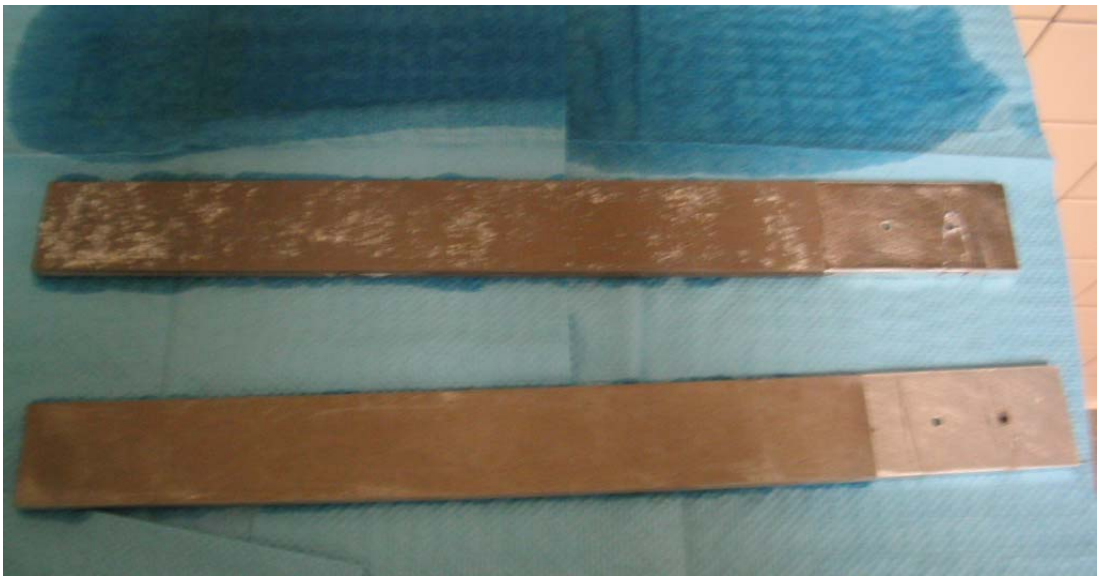

Figure 204. Front of beams after corrosion, before cleaning. Blue/green middle notched beam is on top, White/red notchless beam is on bottom

Figure 205. Back of beams after corrosion, before cleaning. Blue/green middle notched beam is on top, white/red notchless beam is on bottom.

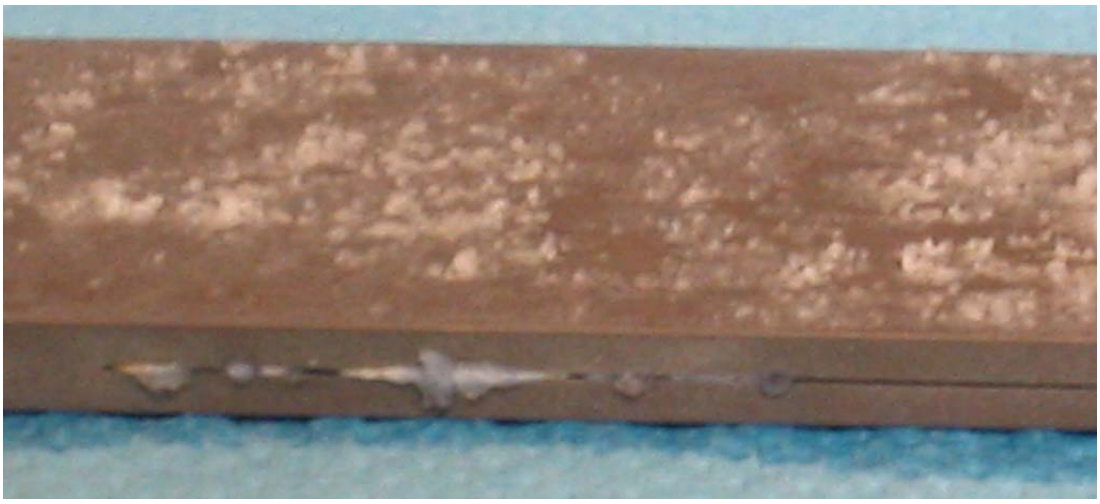

Figure 206. Zoom in on corrosion product in notch.

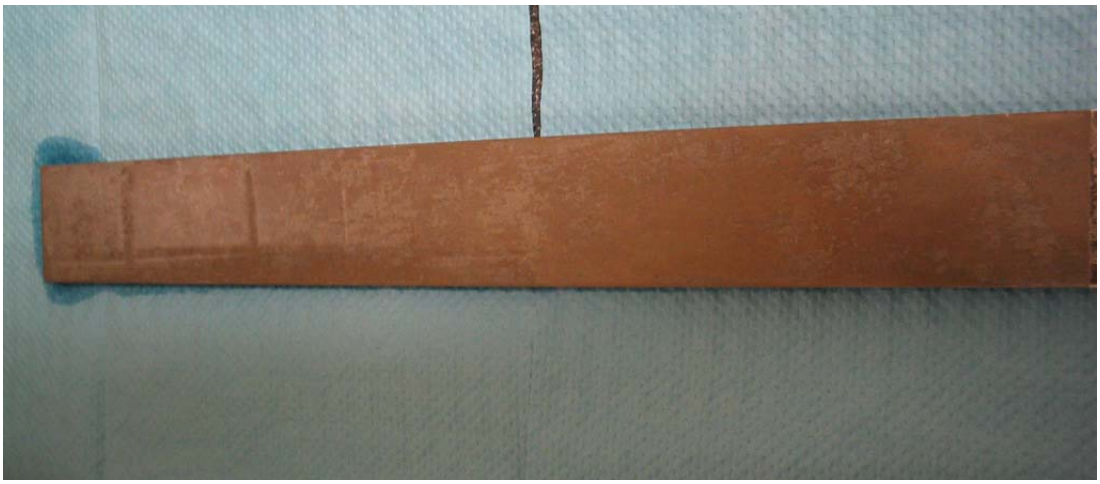

Figure 207. Front of blue/green notched beam after cleaning.

Figure 208. Back of blue/green notched beam after cleaning.

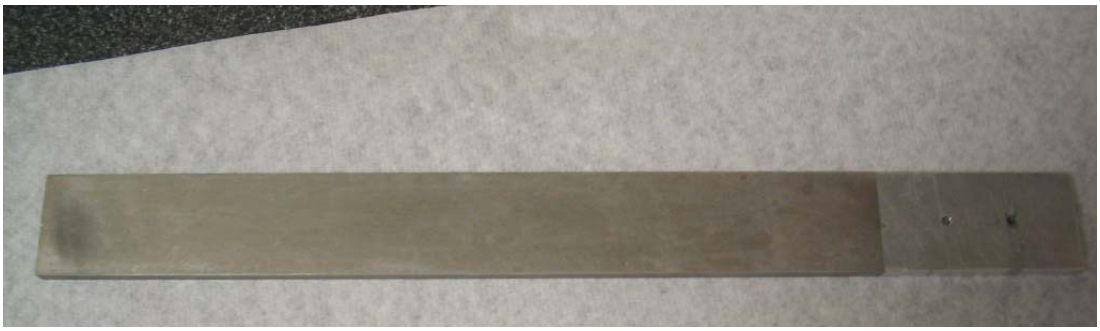

Figure 209. Front of white/red notchless beam after cleaning

Figure 210. Back of white/red notchless beam after cleaning.

Two Week Corrosion

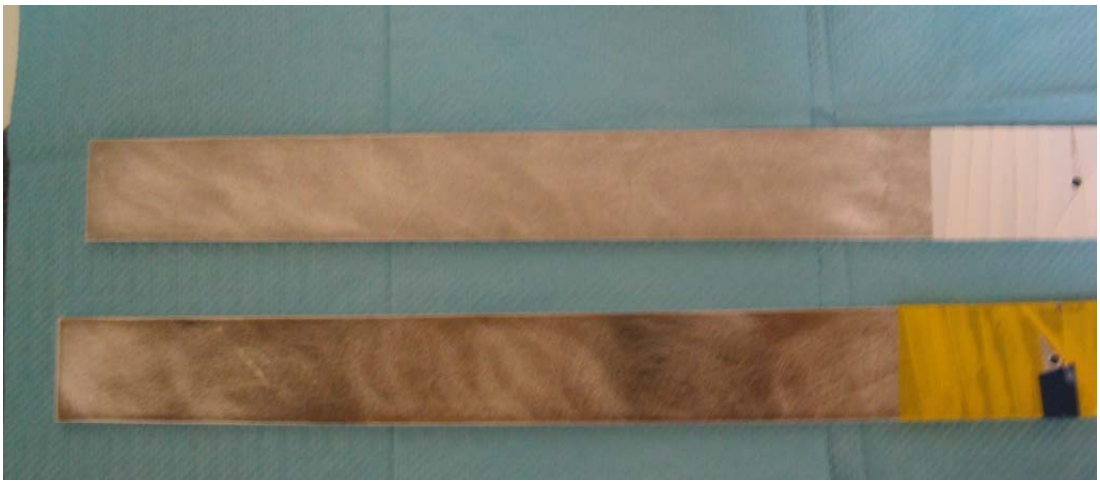

Figure 211. Front of white notchless and yellow/blue middle notched beams before corrosion

Figure 212. Back of white notchless and yellow/blue middle notched beams before corrosion

Figure 213. Two week immersion beams in the tank

Figure 214. Front of yellow/blue middle beam, back of white notchless beam after corrosion, before cleaning

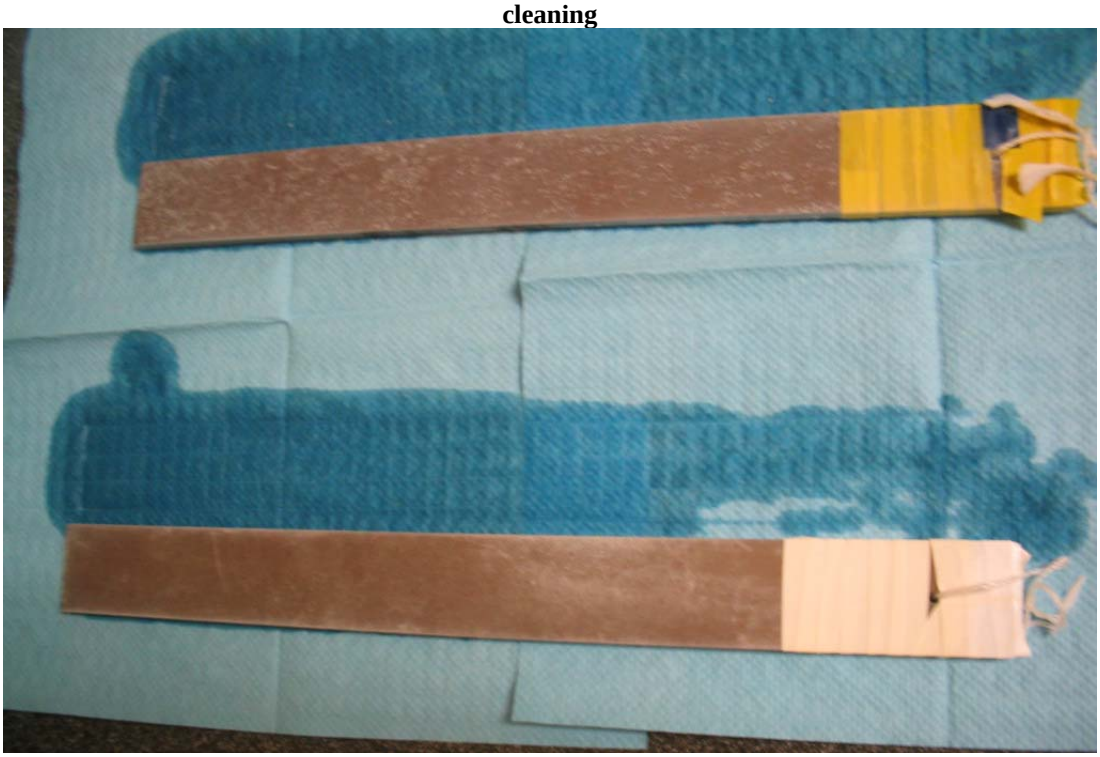

Figure 215. Back of yellow/blue middle beam, front of white notchless beam after corrosion, before cleaning

Figure 216. Front of yellow/blue notched beam (clamp end) after corrosion and cleaning

Figure 217. Front of yellow/blue notched beam after corrosion and cleaning

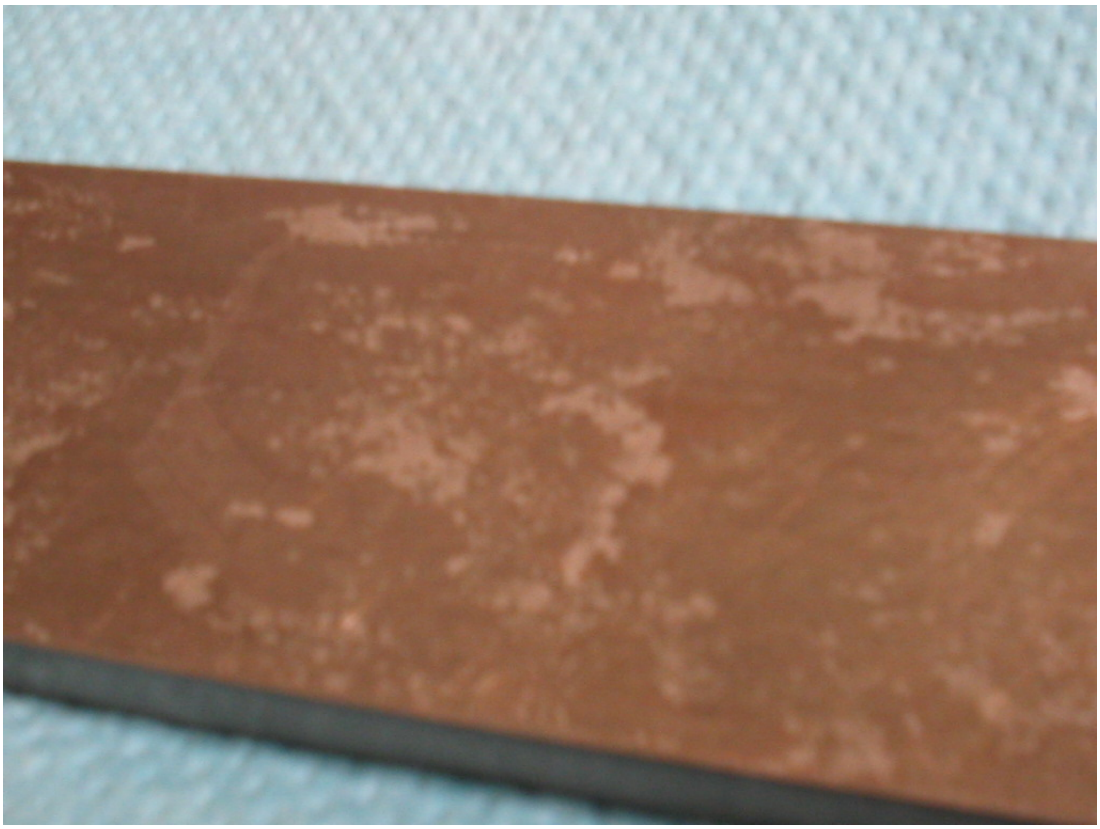

Figure 218. Zoom in on front of yellow/blue notched beam after corrosion and cleaning

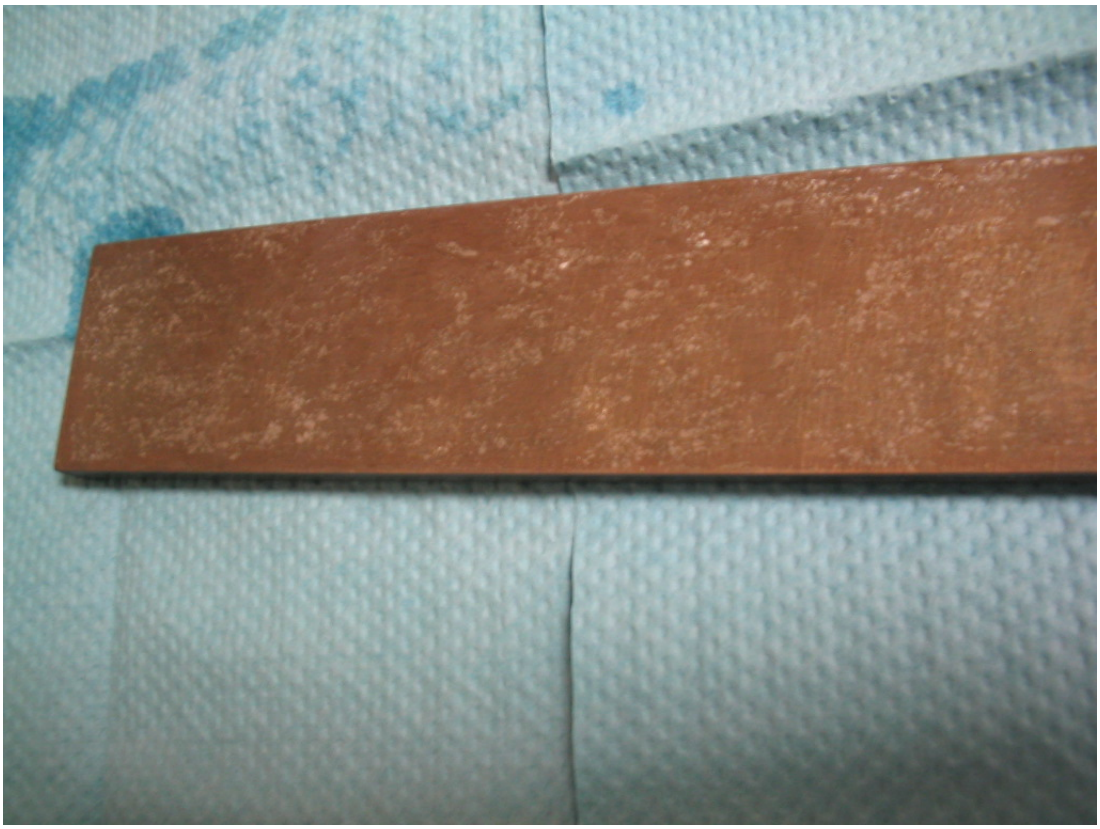

Figure 219. Back of yellow/blue notched beam after corrosion and cleaning

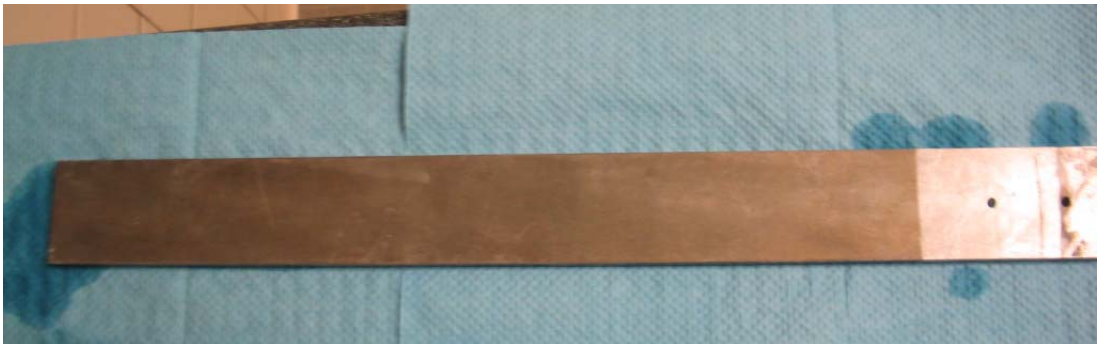

Figure 220. Front of white notchless beam after corrosion and cleaning. Note that mostly general corrosion is present.

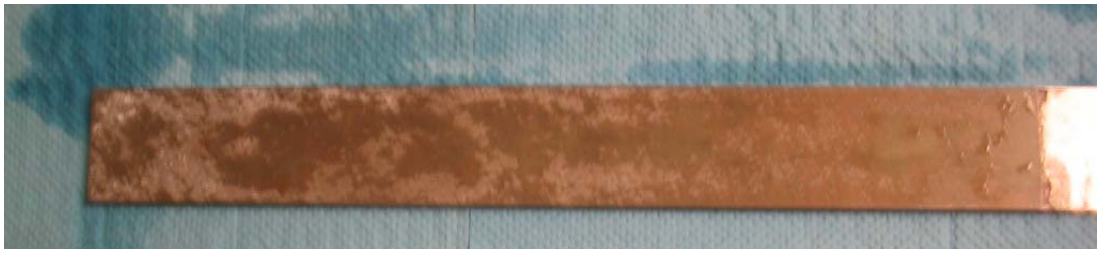

Figure 221. Back of white notchless beam after corrosion and cleaning. Lighter gray areas indicate former presence of alt deposits.

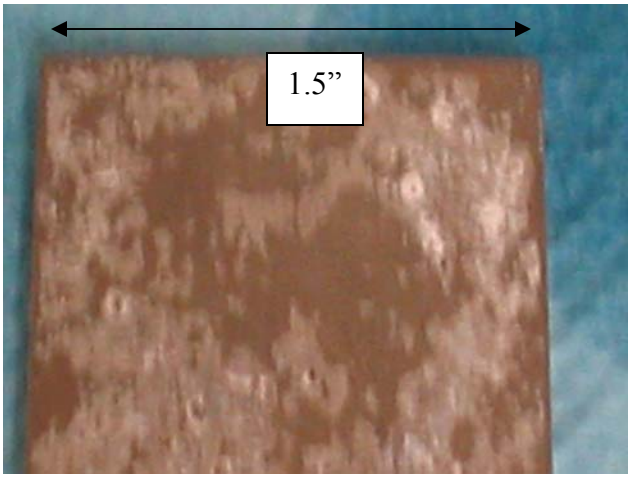

Figure 222. Zoom in on back of white notchless corroded and cleaned beam at free end.

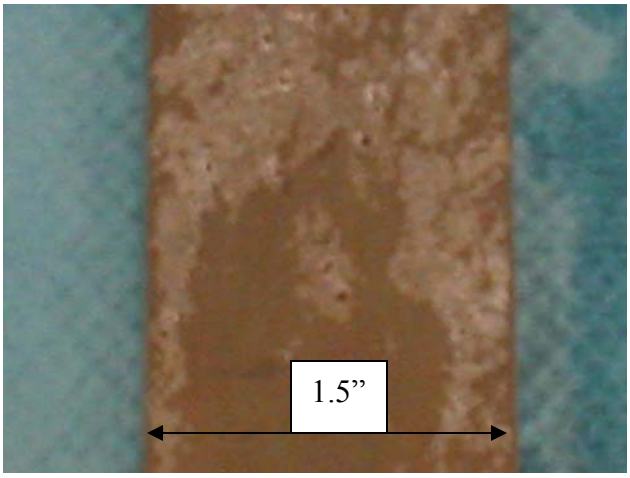

Figure 223. Zoom in on back of white notchless corroded and cleaned beam.

Appendix H: Lab Observations

24 Hour Corrosion

Yellow Notchless Beam Pre-Corrosion Observations: Small circular dent on middle front, scattered pits on back
Yellow Notchless Beam Post-Corrosion Observations: Entire exposed area shows evidence of corrosion. There are salt deposits suggesting localized corrosion on primarily one side (previously defined as back). These are more concentrated on free end and the edges of the back face. Some are also present on the thin edges of the beam.
After Cleaning: Overall darker color. Interesting to note that exposed area that was **not** immersed shows almost an equally dark color. On back, very interesting darker discolorations, look like pits. Area that was covered in salt looks lighter, but in some of these places there are these darker pits.

Green Middle Notched Beam Pre-Corrosion Observations: Front-faint dark discolorations on free end, scattered dents on clamp end. Back-scattered pits throughout.
Green Middle Notched Beam Post-Corrosion Observations: Entire exposed area is corroded. White salt deposits cover almost entire front, more concentrated closer to free end. Back shows no salt deposits. Some evidence of corrosion in notch, but it does not photograph well.
After Cleaning: Overall darker colored, but areas previously covered with salt deposits are not as dark. Hard to see any new pits on crevice.

48 Hour Corrosion

Blue Notchless Beam Pre-Corrosion Observations: 3 small dark discolorations on front free end. Faint vertical scratches 1" and 5" from front free end, scattered pits on back.
Blue Notchless Beam Post-Corrosion Observations: Salt deposits on front, especially around edges of flat face. Salt deposits on side edges as well. Salt deposits on non-immersed exposed area too. Few scattered salt deposits on back side, especially on bottom halfway down beam length.
After Cleaning: Overall darker in color except for where salt deposits were. There is pitting and some small, very dark gray spots which may or may not indicate further deep pitting. Corrosion is present in "cracks" between tape where beam was not exposed.

Red Middle Notched Beam Pre-Corrosion Observations: Darker all over in color. Three scattered lighter discolorations on back free end.
Red Middle Notched Beam Post-Corrosion Observations: Salt deposits scattered fairly evenly on front, NOT on edges of flat front. Darker discolorations in the middle surrounded by salt deposits. Back- scattered salt deposits. Side edges: patchy darker discoloration
After Cleaning: Overall darker in color, but not as dark in areas that were covered in salt. Areas covered in salt look "lighter" but there is pitting there. No obvious/visible corrosion product in crack.

120 Hour Corrosion

Red Notchless Beam Pre-Corrosion Observations: No identifying marks, overall darker in color. NOTE→ before corrosion, both beams are darker in color. Due to sanding, the edges are darker in color than the middle of the flat faces. We'll see if darker region becomes more or less corroded
Red Notchless Beam Post-Corrosion Observations: Salt deposits all over front and back, also on midlines of short edges
After Cleaning: Front-overall corrosion, scattered pitting. Especially deep scattered pits from free end to middle. Edges- some pits on centerline of edges. Back- Overall corrosion, overall scattered pits, especially deep pits concentrated 0-3 inches from clamp. Concentration of deep pits at free end too. There seems to be more concentration of deep pits than previously noted.

Red/White Middle Notched Beam Pre-Corrosion Observations: Diagonal scratch in front, 3-4 inches from free end, diagonal scratch in back 4-7 inches from free end. This beam is overall darker in color.
Red/White Middle Notched Beam Post-Corrosion Observations: More salt deposits on front, but quite a few on back as well. Not concentrated on edges. Some visible salt deposits on thin edges, evident corrosion product in crack.
After Cleaning: Front-pitting visible on free end, granular attack approximately 3 inches from clamp, localized pitting approximately 1 inch from clamp end. Back-deep pitting scattered 2 in (0-2 inches from clamp), pitting scattered throughout, especially deep last 3 inches to free end.

1 Week Corrosion

White/Red Notchless Beam Pre-Corrosion Observations: Front-scattered small pits. Back-scattered small pits and discoloration close to clamp end.
White/Red Notchless Beam Post-Corrosion Observations: Front-overall corrosion of exposed area. Back- scattered salt deposits, concentrated on edges, free end, and clamp end.
After Cleaning: Front-overall corrosion. Back- overall corrosion, pitting in former locations of salt deposits, scattered pitting overall, but especially deep pitting in these previously mentioned locations, traces of granular attack at free end and approximately 3 inches from clamped end.

Blue/Green Middle Notched Beam Pre-Corrosion Observations: Front-diagonal scratch 2-3 inches. Back-scattered pits, dent 3 inches from end, scattered scratches 0-3 inches from end. NOTE: Blue/Green beam is overall darker in color than the White/Red notchless beam.
Blue/Green Middle Notched Beam Post-Corrosion Observations: Front-scattered salt deposits, concentrated patch on free end, overall corrosion present, severe salt deposits in notch. Back-Overall corrosion, sparse salt deposits at free end.
After Cleaning: Front and back- scattered pitting, highly concentrated on free end.

2 Week Corrosion

White Notchless Beam Pre-Corrosion Observations: Front- scattered pits throughout, small dent and scratch at free end, series of small dents at clamp end. Back- scattered, sparse, small pits
White Notchless Beam Post-Corrosion Observations: Front- overall corrosion, faint salt deposits. Back-much larger salt deposits, concentrated on sides of larger, flat edges. Exposed, non-immersed area (in the tape area) is totally white with salt deposits too. Salt deposits on thin edges were all on centerline.
After Cleaning: Front-overall corrosion. Virtually no localized corrosion. Back- overall corrosion and severe localized attack where the salt deposits were (concentrated on edges of large front and back sides). What appears to me very deep, very wide pitting in some places.

Yellow/Blue Middle Notched Beam Pre-Corrosion Observations: No markings. Overall darker in color than white notchless beam.
Yellow/Blue Middle Notched Beam Post-Corrosion Observations: Overall corrosion, front and back salt deposits concentrated over whole beam, more on front than back. Lots of corrosion product seen in notch. Looks like it will be very hard to wash out. Salt deposits on thin edges were all on centerline.
After Cleaning: Front-overall corrosion, very wide intergranular attack in splotches all over, some deep pitting. Back-same as front but IGC not as severe

Table 27. Periodic temperature, salinity and pH recordings

Date	Time	Temp (˚F)	Salinity	pH
Start of 24 hour/48 hour tests				
5 Dec 05	1600	73.0	34.0%	n/a
5 Dec 05	1850	73.0	34.0%	n/a
6 Dec 05	1415	74.0	34.0%	8.4
6 Dec 05	1605	75.0	34.0%	8.4
6 Dec 05	1740	75.0	34.0%	8.4
7 Dec 05	1430	74.0	34.0%	8.4
Start of 120 hour test				
11 Dec 05	1830	75.0	34.5%	8.4
12 Dec 05	1600	74.0	34.0%	8.4
13 Dec 05	1635	75.0	34.0%	8.4
14 Dec 05	0905	75.0	34.0%	8.4
16 Dec 05	1830	75.0	34.0%	8.0
Start of 1 week/2 week tests				
20 Dec 05	1652	74.0	34.0%	8.2
21 Dec 05	1500	74.0	34.0%	8.2
27 Dec 05	1718	75.5	33.5%	8.0
3 Jan 06	1821	75.5	33.5%	8.0

Appendix I: All Experimental Mode Shapes

Uncorroded Mode Shape Curvature Comparisons

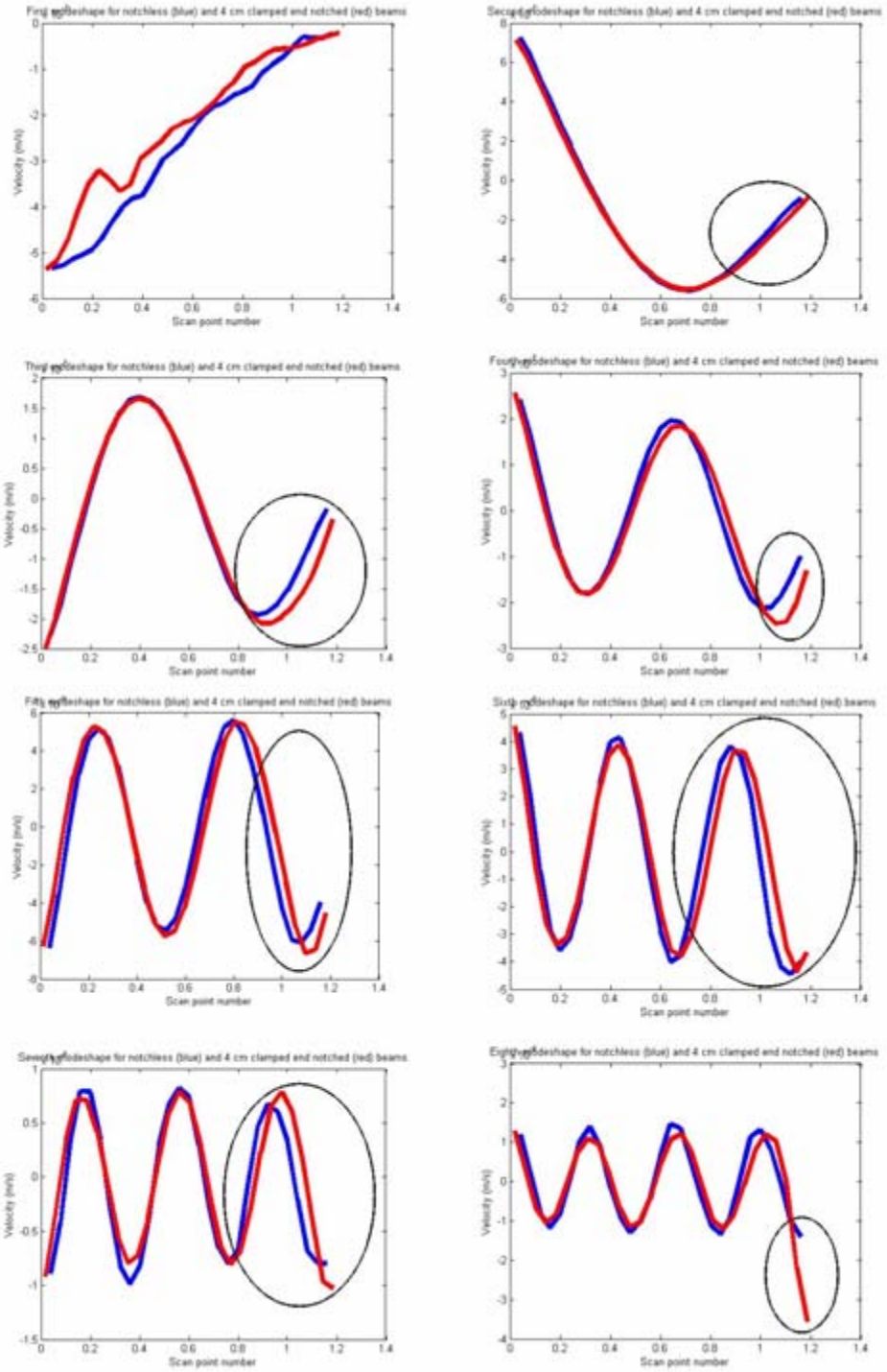

Figure 224. Four centimeter clamped end notch

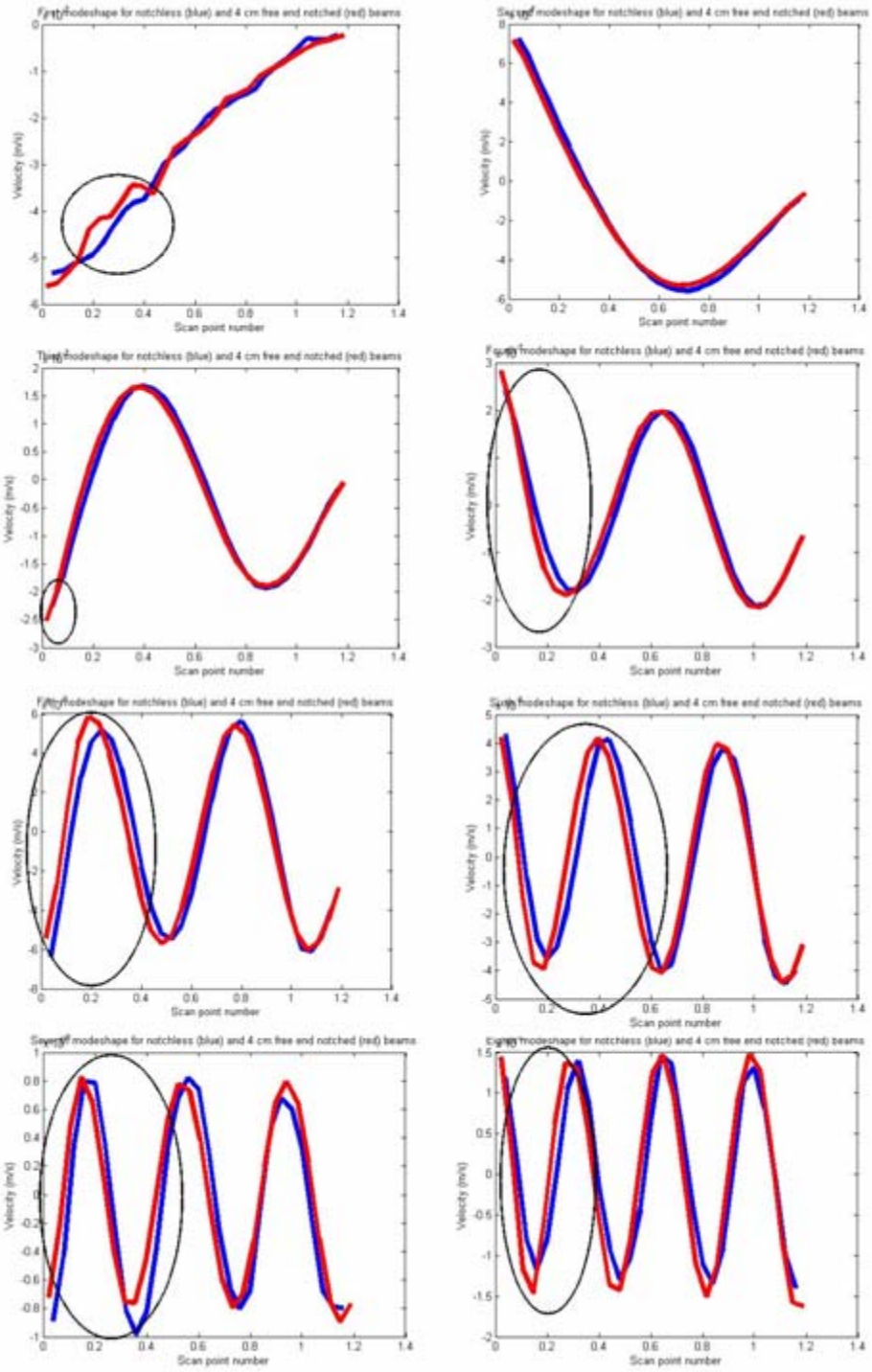

Figure 225. Four centimeter free end notch

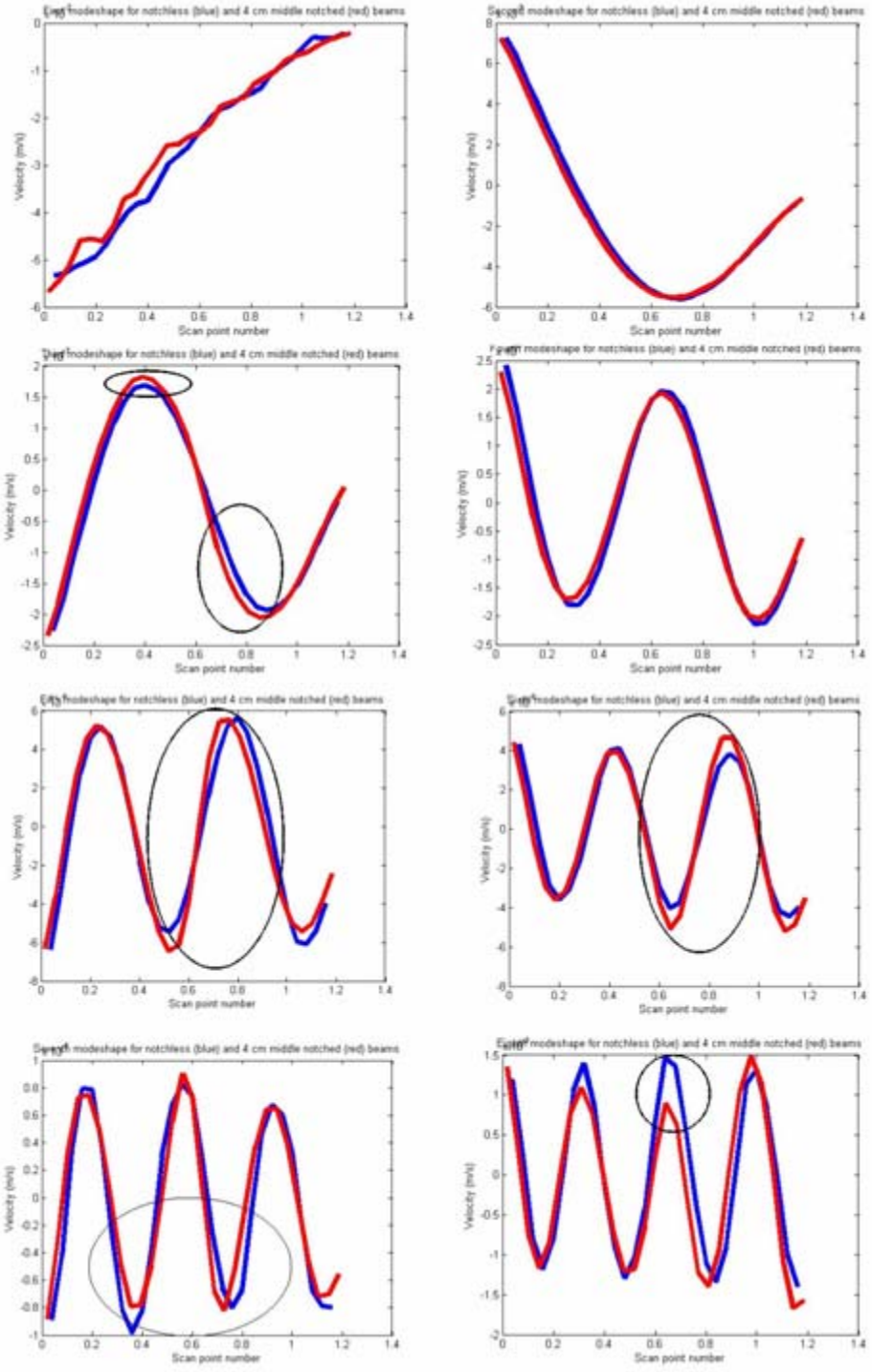

Figure 226. Four centimeter middle notch

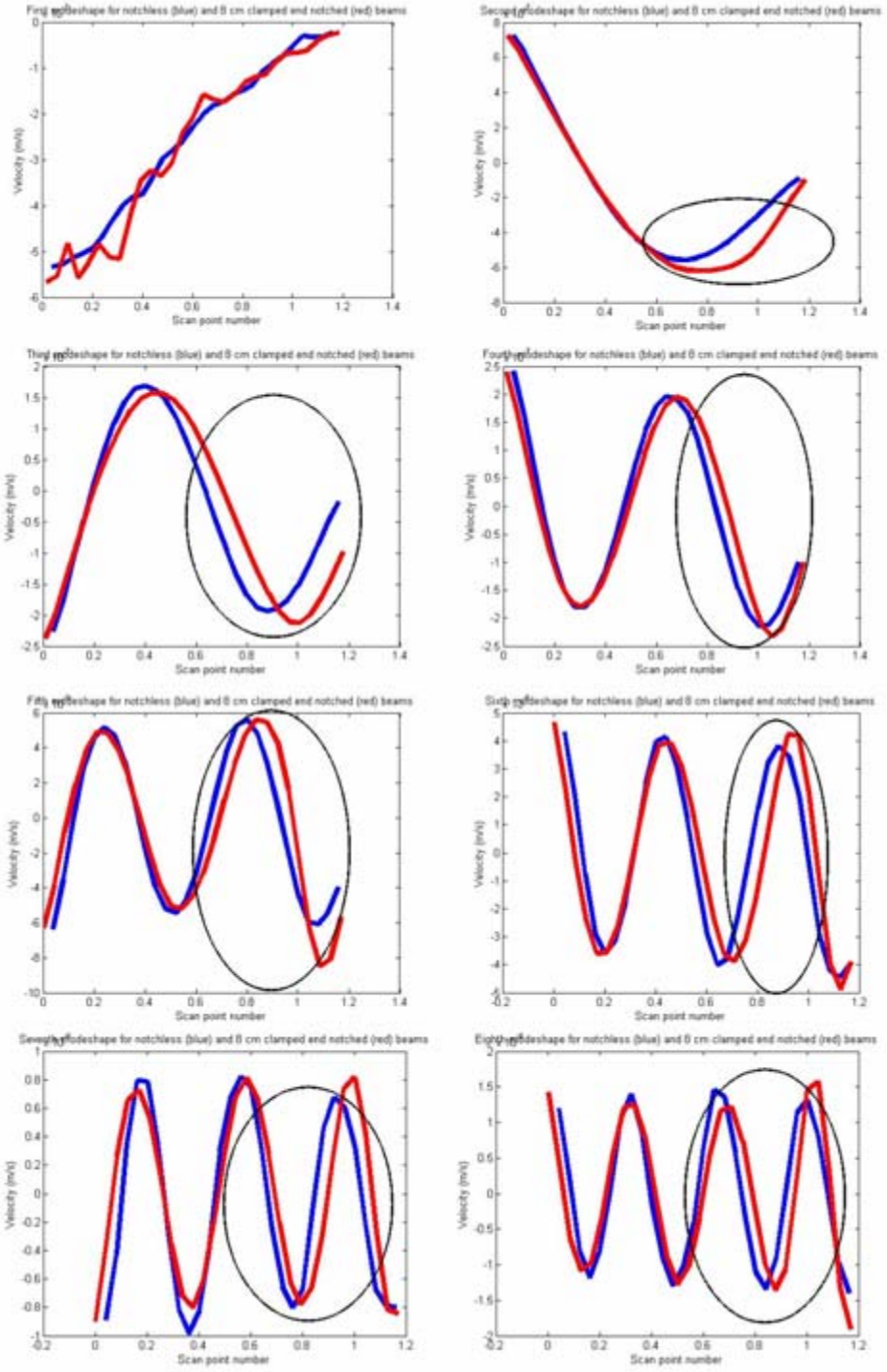

Figure 227. Eight centimeter clamped end notch

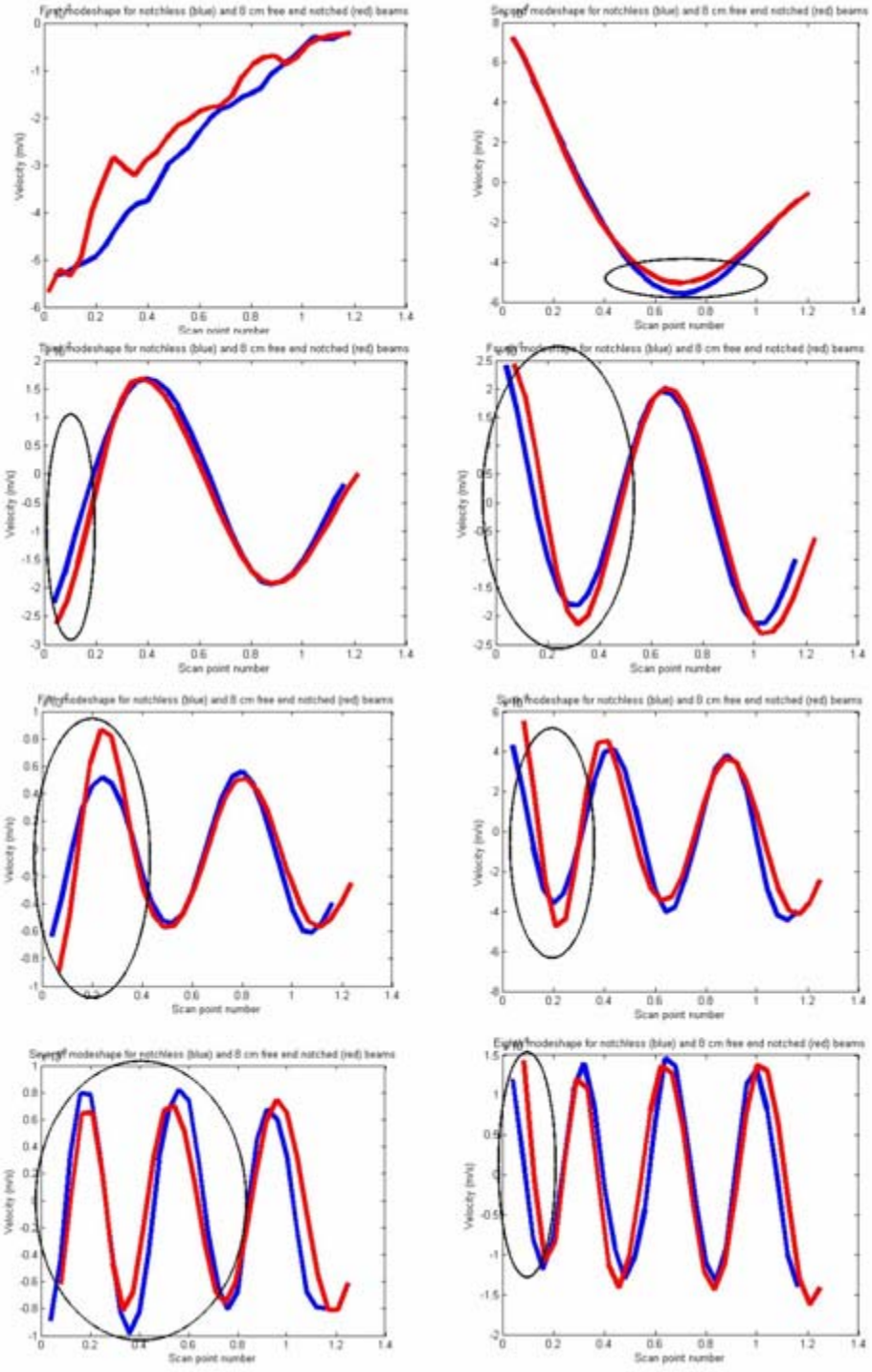

Figure 228. Eight centimeter free end notch

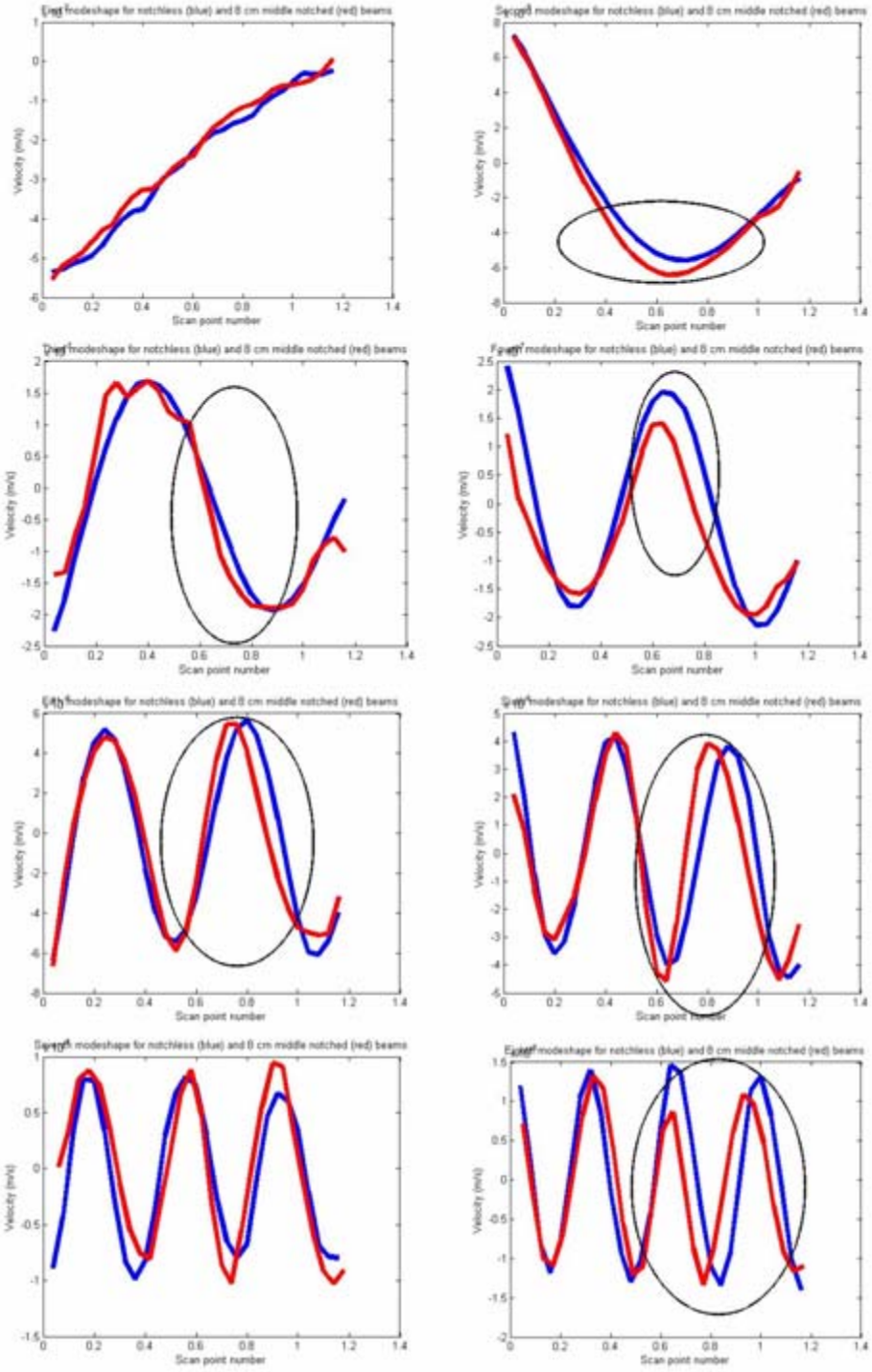

Figure 229. Eight centimeter middle notch

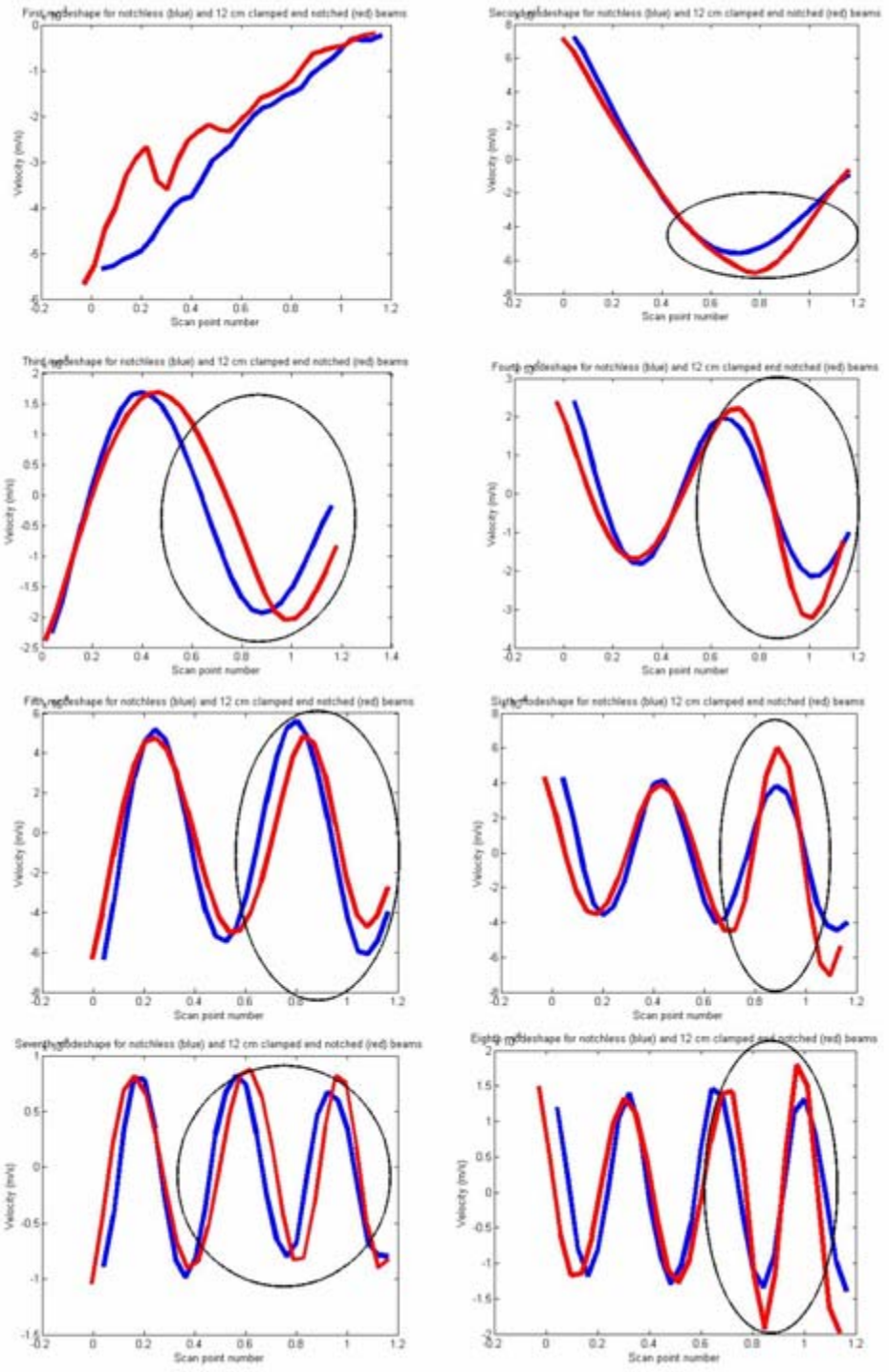

Figure 230. Twelve centimeter clamped end notch

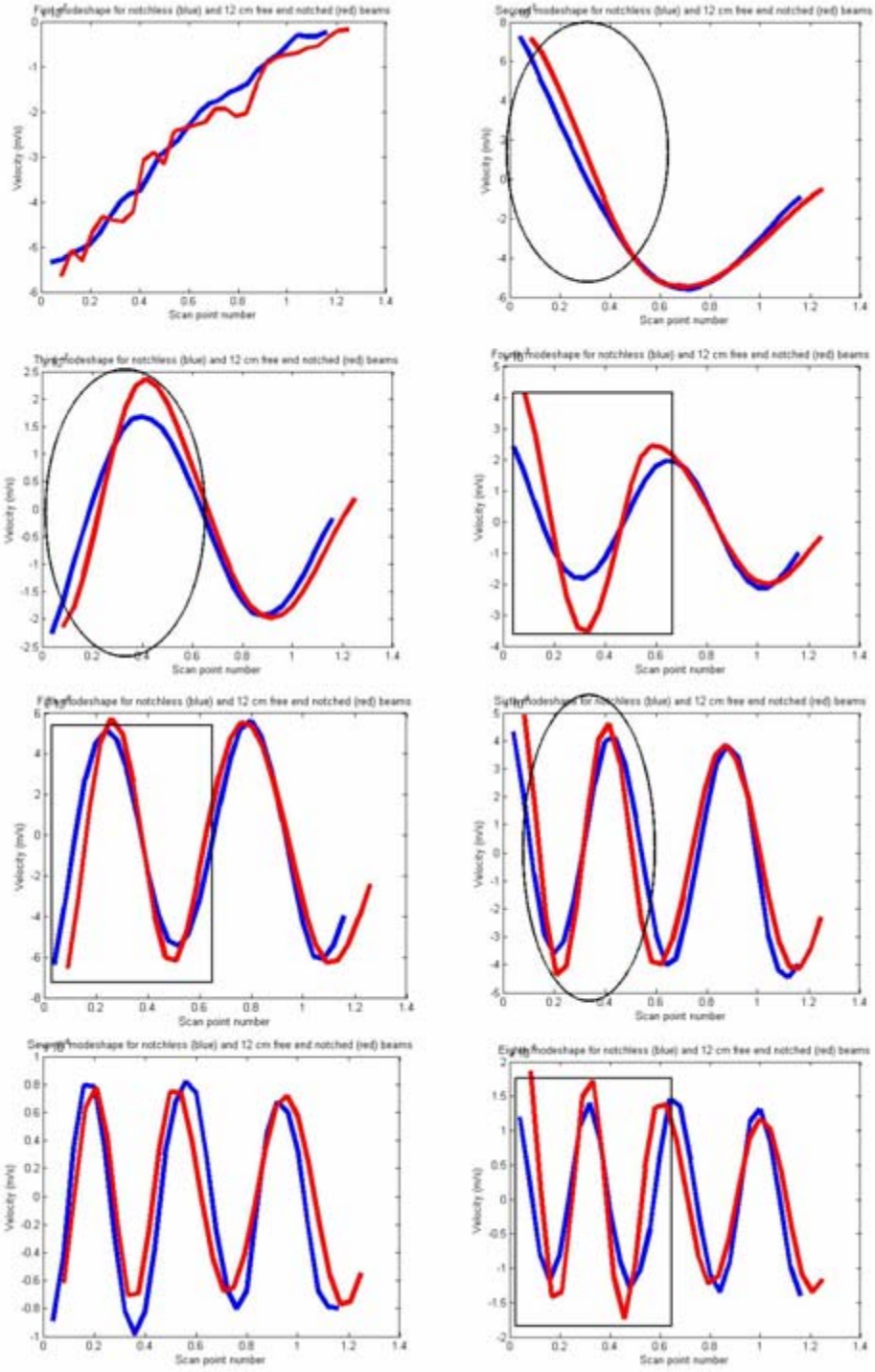

Figure 231. Twelve centimeter free end notch

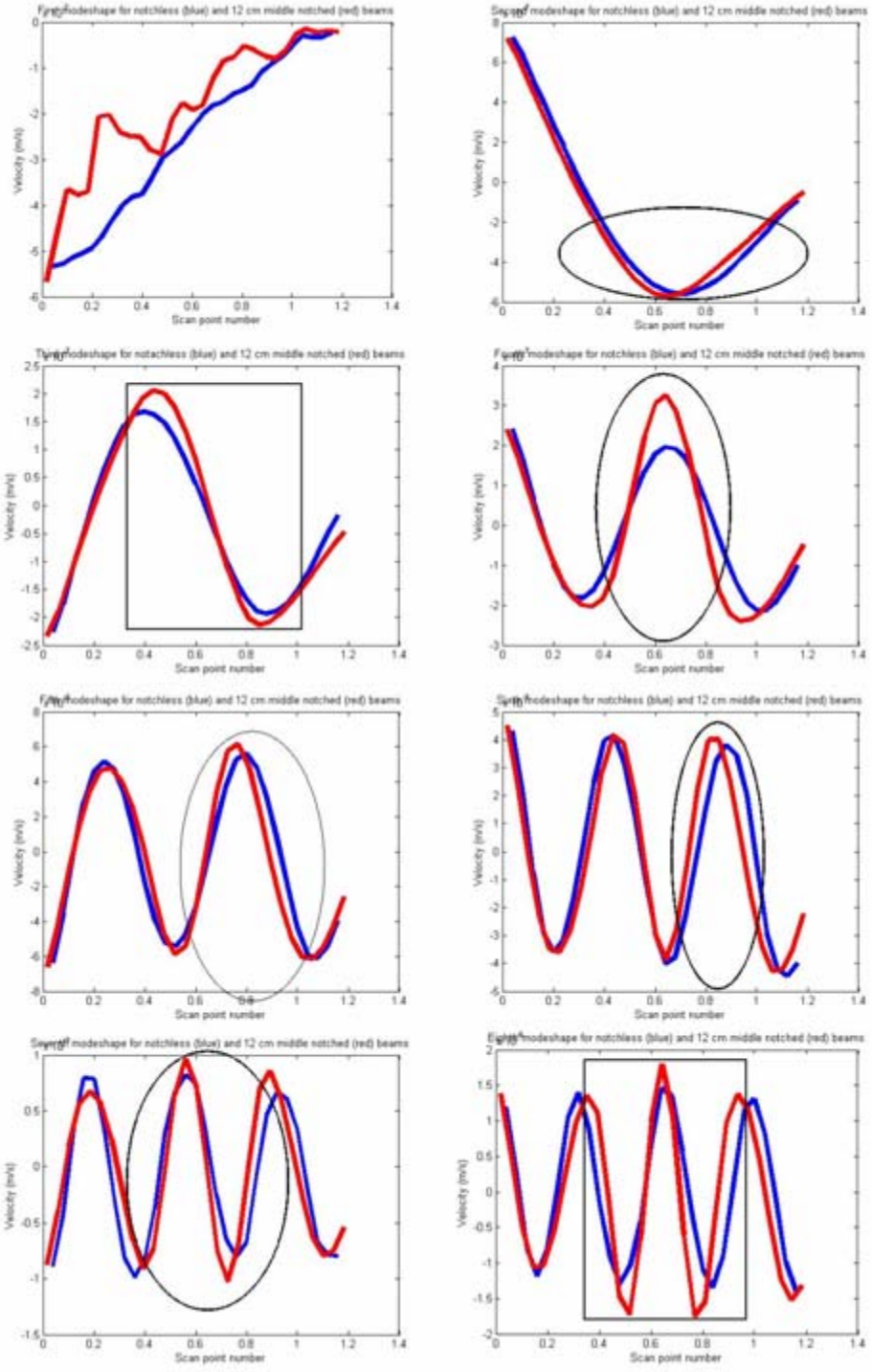

Figure 232. Twelve centimeter middle notch

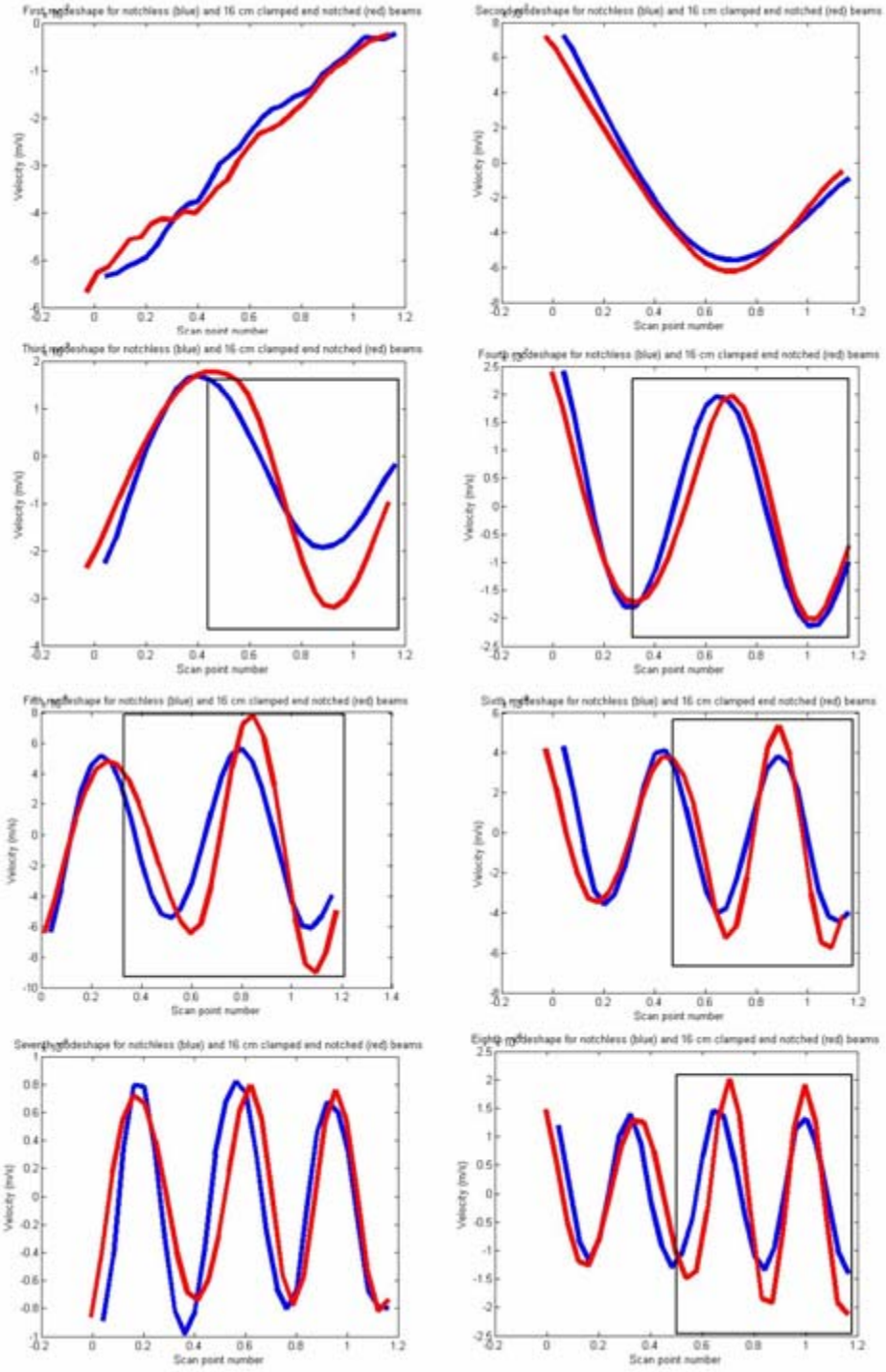

Figure 233. Sixteen centimeter clamped end notch

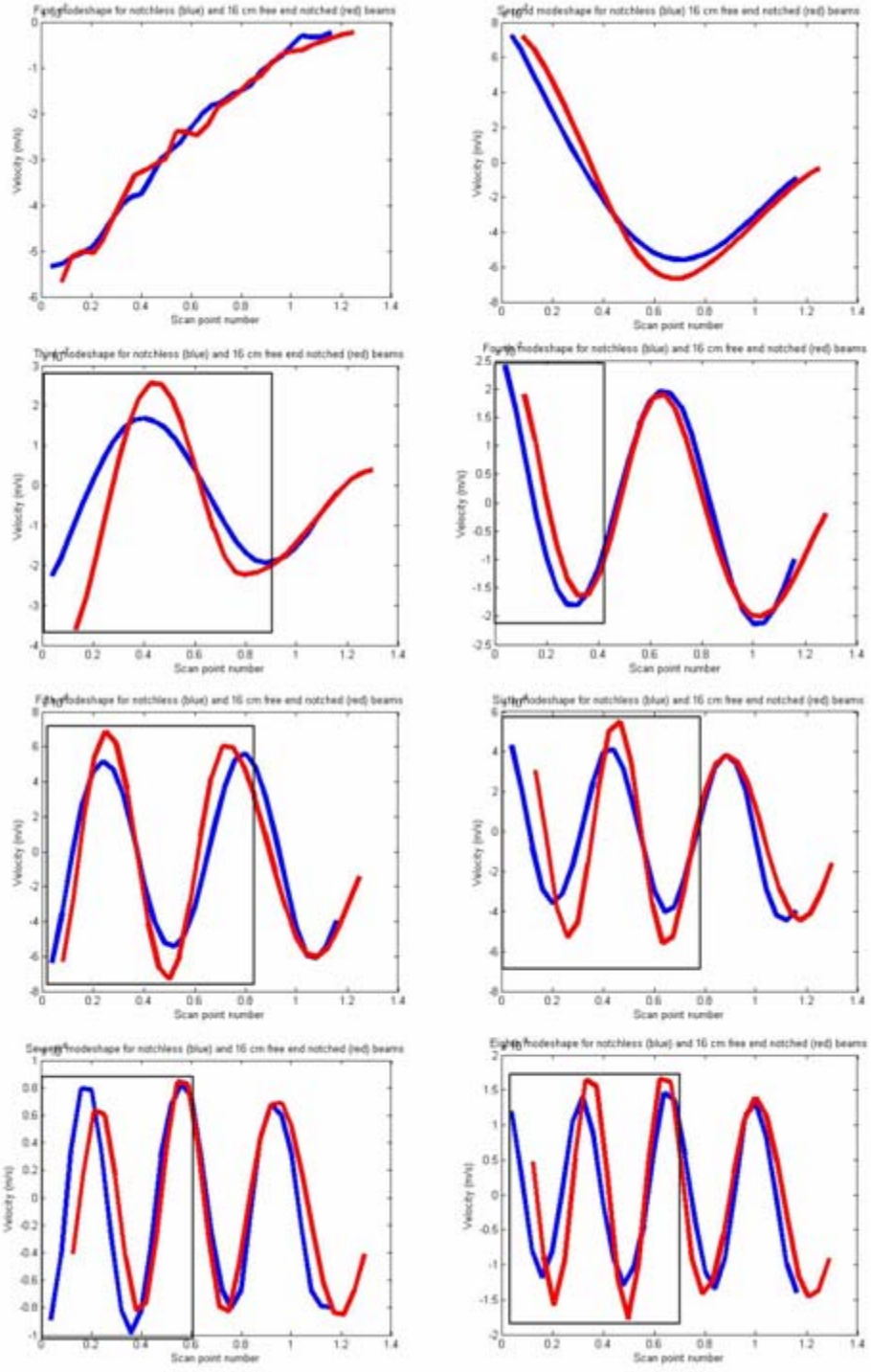

Figure 234. Sixteen centimeter free end notch

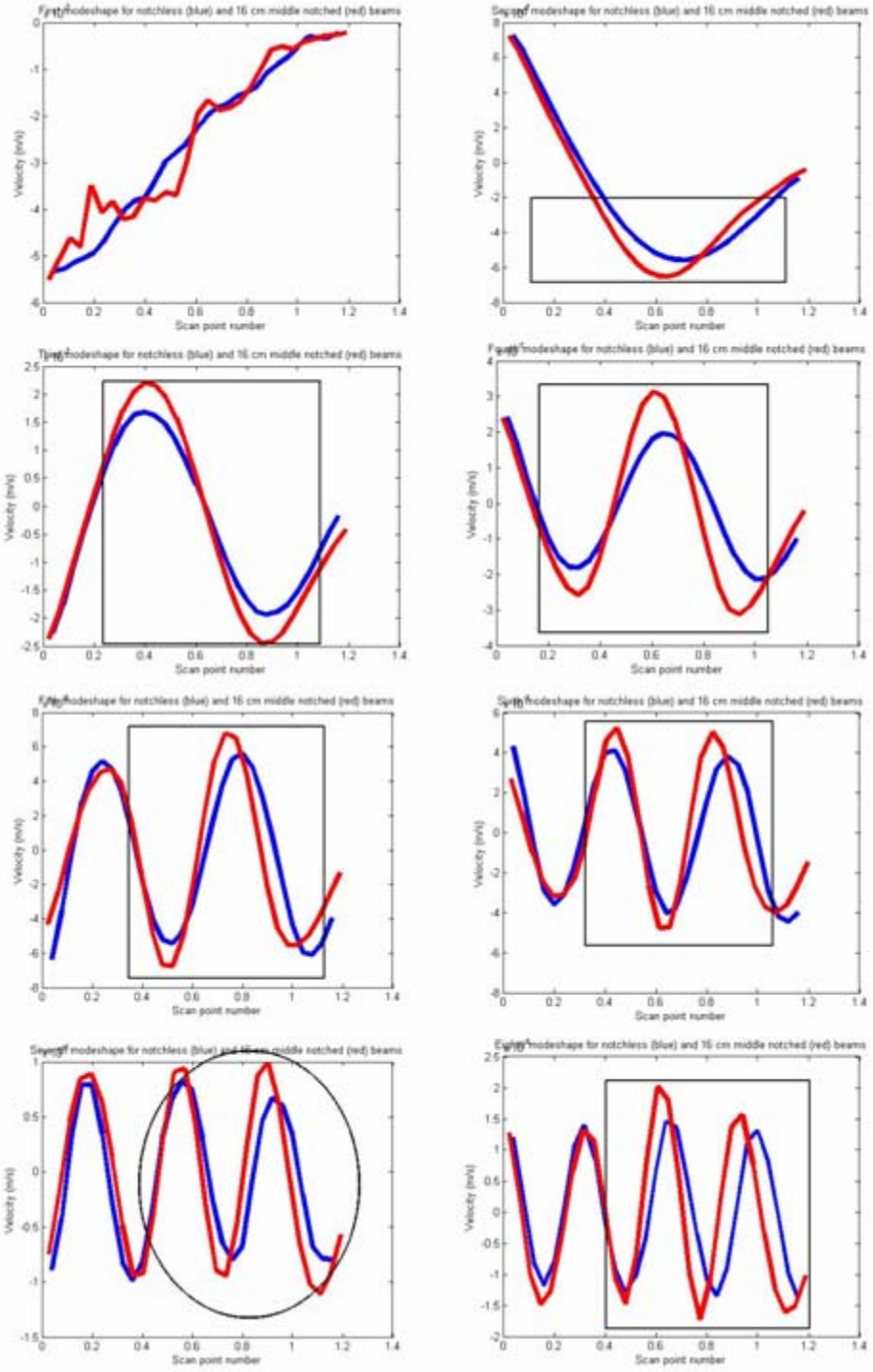

Figure 235. Sixteen centimeter middle notch

Corroded Mode Shapes

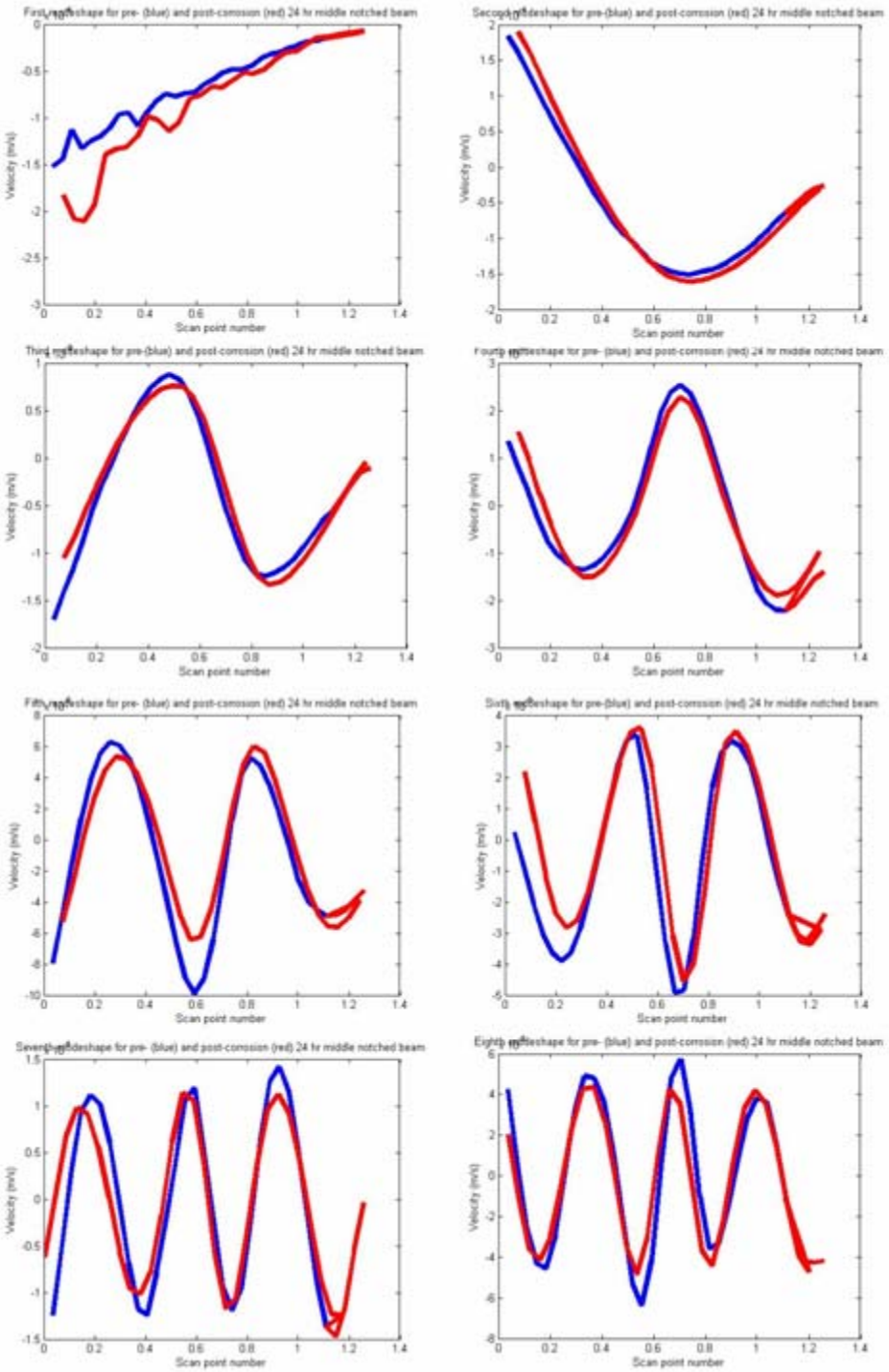

Figure 236. 24 hour corroded middle notched beam

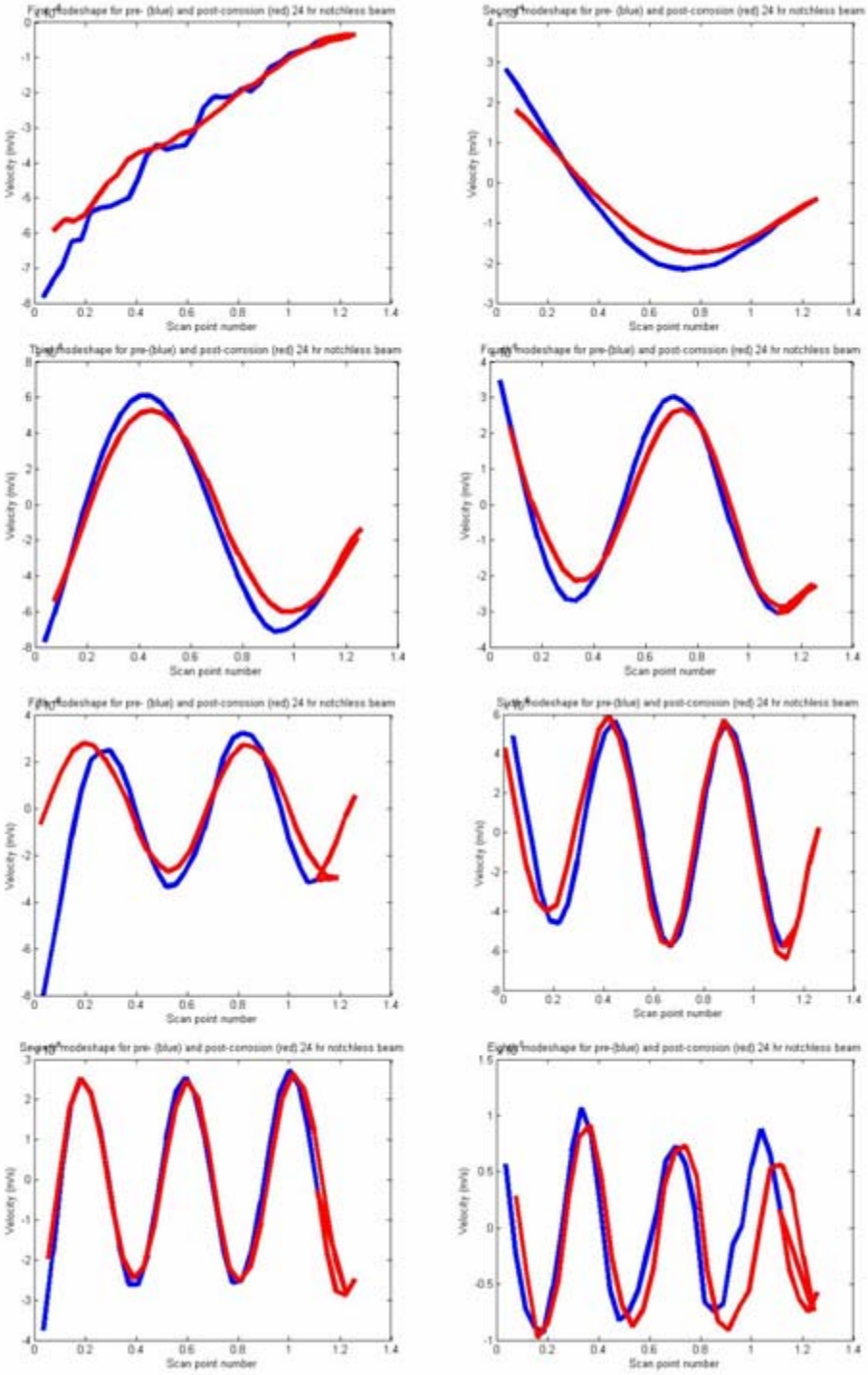

Figure 237. 24 hour corroded notchless beam

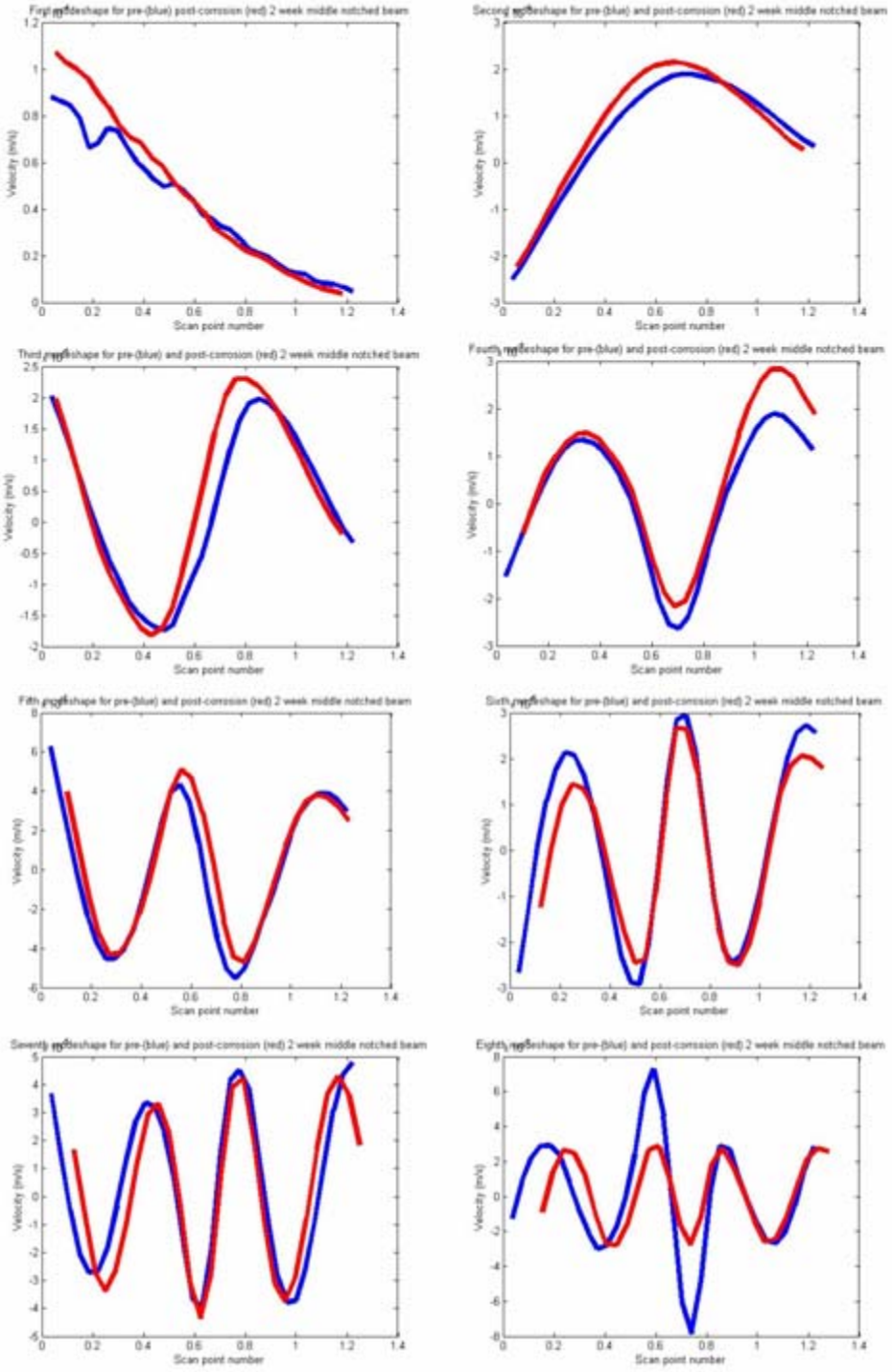

Figure 238. Two week corroded middle notched beam

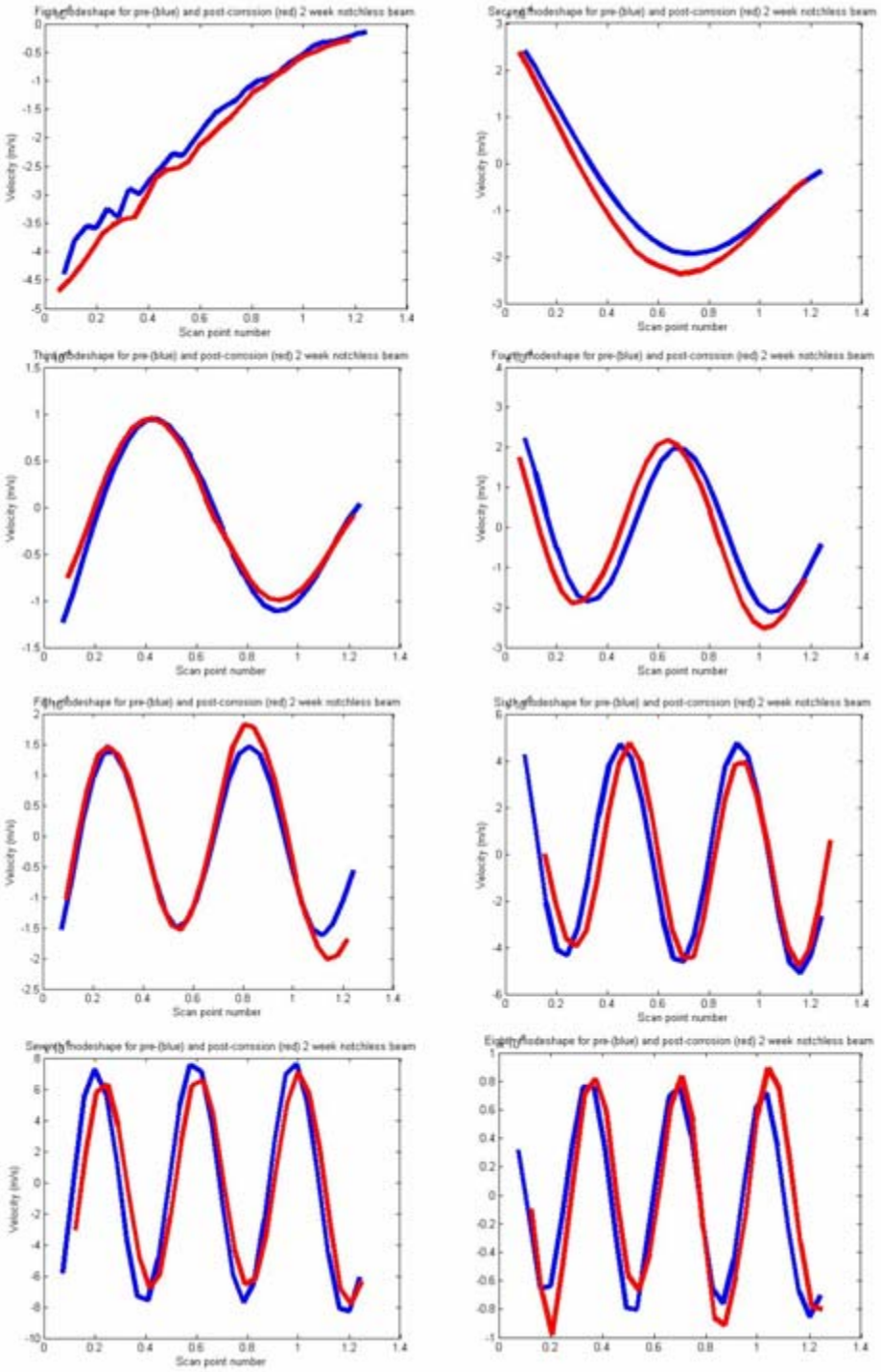

Figure 239. Two week corroded notchless beam

Bibliography

Adams, R. D. and P. Cawley. "The location of defects in structures from measurements of natural frequencies." *Journal of Strain Analysis*, 14:49-57.

ASTM International Designation E 756-05. "Standard Test Method for Measuring Vibration-Damping Properties of Materials." Date downloaded: 31 October 2005.

----. G1-03. "Standard Practice for Preparing, Cleaning, and Evaluating Corrosion Test Specimens." Date downloaded: 21 September 2005.

----. G4-01. "Standard Guide for Conducting Corrosion Tests in Field Applications." Date downloaded: 21 September 2005.

----. G 31-72 (Reapproved 2004). "Standard Practice for Laboratory Immersion Corrosion Testing of Metals." Date downloaded: 10 September 2005.

----. G 52-00. "Standard Practice for Exposing and Evaluating Metals and Alloys in Surface Seawater." Date downloaded: 21 September 2005.

----. G 112-92 (Reapproved 2003). "Standard Guide for Conducting Exfoliation Corrosion Tests in Aluminum Alloys." Date downloaded: 21 September 2005.

Cawley, P. and R. Ray. "A comparison of the natural frequency changed produces by cracks and slots." *Journal of Vibration, Acoustics, Stress, and Reliability in Design*, 110:366-370, 1988.

Chmiel, Aaron. "Finite Element Analysis of Notched Beams." Report to Dr. Anthony Palazotto, Air Force Institute of Technology, Dayton OH 2005.

Cobb, Richard. *Structural Damage Identification from Limited Measurement Data*. PhD thesis, Air Force Institute of Technology, Dayton OH, 1996.

Cobb, Richard. MECH 719 Vibration Damping and Control Class Notes. Air Force Institute of Technology, Dayton OH, Fall 2005.

Corporate Video on Vibrometers. http://www.polytec.com/usa 18 January 2005.

Corrosion Club. "Accelerated Corrosion Tests-Service Life Correlation." 10 August 2005 http://www.corrosion-club.com/testingcorrelate.htm

Corrosion Doctors. "Exposure Testing." 3 July 2005 http://corrosion-doctors.org/AtmCorros/Exposure.htm

Corrosion Testing Laboratories, Inc. *Electrochemistry: Corrosion and Electrochemical Basics*. 22 July, 2005 http://www.corrosionlab.com/ct/labresearch.htm

"Crevice Corrosion of Nickel-Based Alloys in Seawater." *The Hendrix Group Reporter*, 8(1):1-7, 1998.

Dimarogonas, Andrew D. "Vibration of cracked structures: A state of the art review." *Engineering Fracture Mechanics*, 55(5):831-857.

Dowling, Norman E. *Mechanical Behavior of Materials: Engineering Methods for Deformation, Fracture, and Fatigue, 2nd Ed*. Upper Saddle River NJ: Prentice Hall, 1999.

Doyle, James F. "Determining the size and location of transverse cracks in beams." *Experimental Mechanics*, 35:272-280, 1995.

Durham, Frances K. *Internal Damage Detection and Assessment in Beams Using Experimental Natural Frequencies*. Master's thesis, Air Force Institute of Technology, Dayton OH, 2004.

Ferrer, K. S. and R. G. Kelly. "Development of an Aircraft Lap Joint Simulant Environment." *Corrosion*, 58(5):452-459, 2002.

Fritzen, C. P. and K. Bohle. "Vibration-based global damage identification: A tool for rapid evaluation of structural safety." In Chang, editor, *Structural Health Monitoring*, 2004.

Inman, Daniel J. *Engineering Vibration, 2nd Ed*. Upper Saddle River NJ: Prentice Hall, 2001.

Juvinall, Robert C. and Kurt M. Marshek. *Fundamentals of Machine Component Design, 3rd Edition*. New York: John Wiley and Sons, Inc., 2000.

Kam, T. Y. and T. Y. Lee. "Detection of cracks in structures using modal test data." *Engineering Fracture Mechanics*, 42(2):381-387, 1992.

Kim, J. T and N. Stubbs. "Crack detection in beam-type structures using frequency data." *Journal of Sound and Vibration*, 259(1):145-160, 2003.

Leblanc, P. and G. S. Frankel. "A Study of Corrosion and Pitting Initiation of AA2024-T3 Using Atomic Force Microscopy." *Journal of the Electrochemical Society*, 149(6):B239-B247, 2002.

Mal, Ajit. "Structural Health Monitoring." *Mechanics*, 33(11-12):1-4, 2004.

Meirovitch, Leonard. *Elements of Vibration Analysis*. New York: McGraw-Hill, Inc., 1975.

Owolabi, G. M., A. S. J. Swanidas, and R. Seshadri. "Crack detection in beams using changes in frequencies and amplitudes of frequency response function." *Journal of Sound and Vibration*, 138:233-43, 2003.

Palacz, Magdalena, Marek Krawczuk, and Wiesaw Ostachowicz. "The spectral finite element model for analysis of flexural-shear coupled wave propagation." *Composite Structures*, 68:45-51, 2005.

Pandey, A. K., M. Biswas, and M.M. Samman. "Damage detection from changes in curvature mode shapes." *Journal of Sound and Vibration*, 145:321-332, 1991.

Polytec Scanning Vibrometer: Theory Manual. Version 8.1.

Reifsnyder, Aaron. *Vibrometric Detection of Beam Damage Due to Inclusions*. Master's thesis, Air Force Institute of Technology, Dayton OH, 2004.

Rizos, P. F., N. Aspragathos, and A. D. Dimarogonas. "Identification of crack location and magnitude in a cantilever beam from the vibration modes." *Journal of Sound and Vibration*, 138:381-388, 1990.

Salawu, O. S. "Detection of structural damage through changes in frequency: a review." *Engineering Structures*, 19:718-723, 1997.

Schmidt, H.-J. and B. Schmidt-Brandecker. "Structure design and maintenance benefits from health monitoring systems." In Chang, editor, *Structural Health Monitoring*, pages 80-101. 2003.

Shackelford, James F., William Alexander and Jun S. Park. *CRC Practical Handbbook of Materials Selection*. Boca Raton: CRC Press, 1995.

Sharma, V. K., S. Hanagud and M. Ruzzene. "Damage index estimation in beams and plates using laser vibrometry." Submitted to AIAA Journal, 2005.

Staszewski, W. J., B. C. Lee, L. Mallet, and F. Scarpa. "Structural health monitoring using scanning laser vibrometry: I. Lamb wave sensing." *Smart Materials and Structures*, 13:251-260, 2004.

Yuen, M. M. F. "A numerical study of the eigenparameters of a damaged cantilever." *Journal of Sound and Vibration*, 103:301-310, 1985.

Zhang, Weilong and G. S. Frankel. "Anisotropy of Localized Corrosion in AA2024-T3." *Electrochemical and Solid-State Letters*, 3(6):268-270, 2000.

Zhang, Weilong and G. S. Frankel. "Localized Corrosion Growth Kinetics in AA2024 Alloys." *Journal of The Electrochemical Society*, 149(11):B510-B519, 2002.

Vita

Second Lieutenant Jessica B. Chronister graduated from Sanford School in Hockessin, Delaware as a National Merit Finalist and AP Scholar. She commenced undergraduate studies at the United States Air Force Academy and upon completion of Basic Cadet Training, entered Cadet Squadron 25. She graduated with academic honors, earning a Bachelor's of Science degree in Astronautical Engineering.

While at the Academy, she also minored in German. She attended the *Offizierschule der Luftwaffe* in Fürstenfeldbruck, Germany her senior year, becoming the first female cadet in history to do so. In Germany, she was *Hörsaalleiter Üb* of *Hörsaal* 1.E (E-flight of Squadron One).

Jessica earned her commission through Cadet Squadron 04, USAFA. Her first assignment was to the Air Force Institute of Technology to study Astronautical Engineering. Upon completion of graduate studies, she will be assigned to the National Air and Space Intelligence Center, working under the Spaceflight Vehicles Branch.

REPORT DOCUMENTATION PAGE

Form Approved
OMB No. 074-0188

1. REPORT DATE *(DD-MM-YYYY)*	**2. REPORT TYPE**	**3. DATES COVERED** *(From – To)*
23-03-2006	**Master's Thesis**	Aug 2004 – Mar 2006

4. TITLE AND SUBTITLE

Structural Health Monitoring Considering Internal Beam Damage

5a. CONTRACT NUMBER

5b. GRANT NUMBER

5c. PROGRAM ELEMENT NUMBER

6. AUTHOR(S)

Chronister, Jessica, B., 2d Lt, USAF

5d. PROJECT NUMBER

5e. TASK NUMBER

5f. WORK UNIT NUMBER

7. PERFORMING ORGANIZATION NAMES(S) AND ADDRESS(S)
Air Force Institute of Technology
Graduate School of Engineering and Management (AFIT/EN)
2950 Hobson Way
WPAFB OH 45433-7765

8. PERFORMING ORGANIZATION REPORT NUMBER

AFIT/GA/ENY/06-M09

9. SPONSORING/MONITORING AGENCY NAME(S) AND ADDRESS(ES)
AFRL/VASA
Attn: Mr. Mark Derisso
2790 D Street
WPAFB OH 45433

10. SPONSOR/MONITOR'S ACRONYM(S)

11. SPONSOR/MONITOR'S REPORT NUMBER(S)

12. DISTRIBUTION/AVAILABILITY STATEMENT
APPROVED FOR PUBLIC RELEASE; DISTRIBUTION UNLIMITED.

13. SUPPLEMENTARY NOTES

14. ABSTRACT

The present study establishes a nondestructive method of damage detection and assessment in cantilever beams. The specimens used are twelve inch aluminum 2024-T3 beams with machined notches of varying lengths and locations. Laser Doppler vibrometry is used to obtain the frequency response of vibrating beams. Experimental methods are developed to detect the presence, location and extent of damage by direct observation of the eigenvector in the third through eighth modes. Models in MATLAB and ABAQUS are used to predict and validate the observed data. With this experimental method developed, the validity of the method is tested for specimens that have been exposed to a destructive corrosive environment. A corrosion experiment is developed and used to determine the validity of the damage detection method for corroded structures.

15. SUBJECT TERMS
Structural Health Monitoring, Laser Velocimeters, Vibration, Vibration Testing, Structural Analysis, Cantilever Beams, Modal Analysis, Natural Frequency, Frequency, Resonant Frequency, Frequency Response, Delamination, Finite Element Analysis, Corrosion, Damping Analysis

16. SECURITY CLASSIFICATION OF:			**17. LIMITATION OF ABSTRACT**	**18. NUMBER OF PAGES**	**19a. NAME OF RESPONSIBLE PERSON**
REPORT	**ABSTRACT**	**c. THIS PAGE**			Anthony N. Palazotto, Ph.D.
U	**U**	**U**	**UU**	283	**19b. TELEPHONE NUMBER** *(Include area code)* 937 255 3636 x4599

Standard Form 298 (Rev: 8-98)
Prescribed by ANSI Std. Z39-18